Properties of ceramic-matrix composites prepared by colloidal processing

Chant, Jason

Award date:
1996

Awarding institution:
University of Bath

PROPERTIES OF CERAMIC-MATRIX COMPOSITES PREPARED BY COLLOIDAL PROCESSING

submitted by

Jason Chant

for the degree of Ph. D.

of the University of Bath

1996

ProQuest LLC
789 East Eisenhower Parkway
P.O. Box 1346
Ann Arbor, MI 48106-1346

ABSTRACT

A method of fabricating continuous-fibre-reinforced, silica-matrix composites has been developed which exploits the ability of a colloidal silica sol to form a stable gel when rapidly frozen ("freeze-gelation"). Carbon fibres were impregnated with slurries comprising colloidal silica and filler particles prior to filament winding, freeze-gelation and sintering. The process is cheap, consistent, essentially shrinkage-free and requires relatively low sintering temperatures.

The most prominent microstructural feature in all samples was the complex pattern of open, coarse porosity which replicated the ice crystals which grew during the freeze-gelation process. Scanning electron microscopy (SEM), transmission electron microscopy and x-ray diffraction revealed that the incorporation of lithium-aluminosilicate glass-ceramic filler particles assisted the densification of the colloidal silica particles and encouraged such amorphous regions to crystallise to quartz in samples sintered at 630 °C and above. The incorporation of quartz filler particles caused the colloidal silica to crystallise to cristobalite when the composites were sintered at 900 °C and above. Unfilled matrix systems remained amorphous.

A comprehensive program of mechanical testing was complemented by SEM analysis of fracture surfaces. Mechanical properties and damage modes were related to microstructural features and processing conditions, and this permitted the optimisation of different composite systems. Acoustic emission measurement was employed successfully to detect the onset of damage during testing and could differentiate between different damage mechanisms.

Values of tensile modulus were satisfactorily described by a rule of mixtures treatment; the highest measured value was 120 GPa. The highest measured values of tensile and flexural strength were 630 MPa and 250 MPa respectively. Under appropriate conditions, flexural

specimens failed gracefully by extensive delamination and exhibited works of fracture up to 20 kJm^{-2}. Similarly, tensile specimens were notch-insensitive, and fibre-related damage processes contributed to measured works of fracture up to 60 kJm^{-2}.

ACKNOWLEDGEMENTS

I am grateful to all those who contributed to make my time at Bath so rewarding and enjoyable. In particular, I acknowledge the supervision and encouragement offered by Professor Bryan Harris during this project. Special thanks also to Frank Hammett and Richard Russell-Floyd for their enthusiastic help with specimen fabrication, Mark Deven for assistance with microscopy, Drs. Robin Cooke and Neil McCartney (NPL) for their useful discussions, and the staff of the Electron Optics Centre. Finally, I would like to express my warm gratitude to family and friends for their continued support and interest.

Financial support for this project was provided by the Engineering and Physical Science Research Council and the National Physical Laboratory.

CONTENTS

Chapter 4
PROPERTIES OF COMPOSITES WITH UNFILLED SILICA AND ß-SPODUMENE / SiO_2 MATRICES

Chapter 1

REVIEW OF LITERATURE

1.1 INTRODUCTION

The Materials Scientist has long been enticed by ceramics, eager to exploit their potential as engineering materials. Their intrinsic high stiffness, high hardness, chemical inertness and refractoriness derive from the strength of their ionic and covalent bonding [1]. Unfortunately this same bonding permits little or no movement of dislocations, even at modest temperatures, and leads ultimately to that property of ceramics which has restricted their greater exploitation in engineering applications: brittleness, or the tendency to fail catastrophically by the growth of a single crack that emanates from a minute flaw. Moreover, the stress levels at which failures occur are a tiny percentage of those theoretically achievable. Sensitivity of strength to defect size is enshrined in Griffith's now classical treatment of brittle fracture. Since a distribution of flaw sizes is evident in real materials, so then do ceramics exhibit a distribution of strength values; from a design engineer's perspective, ceramics are disconcertingly unreliable.

The concept of toughening and strengthening weak, brittle materials by incorporating fibres was established in antiquity - a reference to clay bricks reinforced with straw occurs in *Exodus* 5(6-7). The building industry returned to this theme in more modern times; probably the first examples of mass-produced, fibre-toughened composites were asbestos-filled cement sheets manufactured by the Hatschek process in the 1900s [2-3]. More recently, advances in several areas have permitted the exploration of fibre-reinforced glasses and ceramics for engineering applications. Phillips [4] summarised potential application areas thus:

- highly stressed, high-temperature applications *e.g.* in aircraft engine environments;
- moderately stressed, high-temperature components *e.g.* in metal processing industries;
- cutting tools and dies.

Several methods of toughening ceramics have been considered. Following a deeper understanding of crack growth processes in brittle materials, crack interaction and crack shielding mechanisms in monolithic ceramics have been invoked through engineering of their microstructures [5-7]. Addition of second phase particles such as whiskers or transformation toughening particles of zirconia, for example, has produced modest increases in toughness, typically by a factor of 2-3.

By far the most impressive increases in toughness, however, are seen when ceramic fibres are incorporated into brittle, ceramic matrices. Some two decades ago the potential of ceramic matrix composites was demonstrated [8,9]. The incorporation of carbon fibres into glass and glass ceramic matrices led to composite materials having a toughness some 20 times greater than the monolithic matrix materials. These composites can withstand large tensile strains prior to final failure and exhibit a significant degree of damage tolerance. Moreover, they also give 'warning' prior to failure, an important psychological attribute if this class of materials is to become widely used.

The huge advances which have been made in the area of ceramic-matrix composites (cmc) over the past two or three decades may be attributed in part to the development of appropriate fabrication technologies. Since the principal motivating force behind this progress has come from the aerospace industry, most of the research has been focussed on the development of materials and components which exhibit excellent mechanical properties at high temperatures; the cost of materials and processes has not been a first priority.

In contrast, a SERC ACME project carried out at Bath University (of which this thesis forms an adjunct) examined how *low-cost* cmc components could be fabricated by sol-gel techniques. The feature of sol-gel processing which has historically prevented its exploitation

in the fabrication of monolithic and reinforced components is the very high degree of shrinkage, and associated cracking, which occurs as gels are dried and later sintered. The Bath ACME project rediscovered that colloidal silica sols can form shrinkage-free gels if gelation is caused by rapid freezing, and, moreover, that the "freeze-gelation" process is unaffected by the presence of fillers or fibres in the starting sol. The objectives of the project were therefore refined when it was decided to concentrate exclusively on silica-matrix composites fabricated by freeze-gelation.

The remainder of this chapter is divided into three sections:

1.2 A review of toughening mechanisms in ceramic-matrix composites and underlying composites science principles provides guidance on the selection of appropriate fibre/matrix combinations. Test methods appropriate to this class of material are discussed briefly. This is followed by an appraisal of current fabrication technology.

1.3 Review of sol-gel technology, with particular emphasis on applications. The limitations of conventional sol-gel processing for the fabrication of ceramic-matrix composites are discussed.

1.4 Description of the freeze-gelation process and how it may be applied to the fabrication of ceramic-matrix composites. The data and experience acquired during the ACME project's investigation into freeze-gelled, short-fibre-reinforced composites provides a basis for developing a freeze-gelation route to continuous-fibre-reinforced composites, the subject of this thesis.

In the light of the comments made in these sections, Chapter 2 will then define the objectives of this thesis.

1.2 CERAMIC-MATRIX COMPOSITES

1.2.1 Toughening mechanisms and composite mechanics

Since the strain to failure of the fibres in a typical ceramic-matrix composite is significantly greater than that of the matrix, the onset of damage in such materials is signified by matrix cracking. In the case of a unidirectionally reinforced composite loaded in tension along its fibre axis, this generally results in a matrix crack (or series of cracks) transverse to the fibre direction, and bridged by the fibres. In a successful ceramic-matrix composite the fibres perform two principal rôles:

(i) they provide a means of transferring stresses across matrix cracks, thereby enhancing the strength of the composite and;

(ii) they provide energy-absorbing mechanisms which act against crack growth and contribute to the toughness of the composite.

Figure 1.1 illustrates the damage processes which have been reported for effective, unidirectional ceramic-matrix composites tested in tension and flexure [5,10-16]; such data have most typically been obtained from SiC/glass-ceramic composites. The advance of a crack through such a composite typically involves the following steps:

(i) fibre-matrix debonding;

(ii) bridging of cracks by intact fibres (this involves frictional resistance);

(iii) fibre fracture;

(iv) fibre pullout.

Composite toughness may be considered to be the net effect of the energy expended during such processes.

It is convenient to consider an idealised stress-strain curve, such as that presented in figure 1.2, as comprising three distinct stages:

(i) an elastic range which extends to the point where the first matrix cracking occurs;

(ii) a 'multiple cracking' range during which the matrix becomes saturated by an array of transverse cracks which are bridged by the fibres and;

(iii) a post-cracking stage during which the fibre-related toughening processes described above are active.

Numerous authors have analysed the features of this curve both experimentally and analytically, and the subject has been the focus of many reviews [6, 17-19]. Probably the first complete description of the mechanical response of such materials was provided by Aveston, Cooper and Kelly [12, 20]; the so-called ACK model uses an energy-balance criterion to predict matrix-cracking strain, crack separation and increase in failure strain for the case of a composite where the bonding between fibres and matrix is purely frictional. More recent models have considered other interfacial conditions and have applied fracture mechanics concepts [*e.g.* see 21, 22]. Features of the mechanical behaviour of ceramic-matrix composites relevant to the design of new materials will now be discussed.

Within the elastic range, the composite is assumed to remain undamaged and the composite's elastic modulus, E_c, may be described satisfactorily by an isostrain "rule-of-mixtures":

$$E_c = E_f V_f + E_m V_m \qquad \text{Equation 1.1}$$

where E and V represent the elastic moduli and volume fractions of the fibres (subscript f) and matrix (subscript m) respectively.

The ACK model predicts that matrix cracking will commence at stress σ_{mc} given by:

$$\sigma_{mc} = \left[\frac{12 \gamma_m \tau E_f V_f^2}{r E_c E_m^2 V_m} \right]^{1/3} \qquad \text{Equation 1.2}$$

where γ_m is the fracture energy of the matrix, r is the radius of the reinforcing fibres and τ is the interfacial shear stress (assumed to be constant and frictional in origin). Similar expressions have been published for other interfacial conditions. The onset of matrix cracking is of considerable practical importance since it is accompanied by decreases in composite

elastic modulus and it permits the potentially deleterious ingress of the environment to the fibre-matrix interface. Once the matrix cracking stress is reached (point A in figure 1.2), either saturation matrix cracking may occur immediately and the stress-strain curve will follow the path ACD or the matrix cracking will occur gradually and the stress-strain curve will follow the path ABD. The shape of the stress-strain curve for a particular composite will depend on a number of factors *e.g.* the presence of matrix flaws and the degree of fibre-matrix bonding and/or interaction. According to the ACK theory, the matrix will eventually fracture into segments of lengths between x and 2x where x is determined by the rate of stress transfer between matrix and fibres. For the case of constant interfacial (frictional) shear stress τ :

$$x = \left(\frac{V_m}{V_f}\right)\frac{\sigma'_{mu}\, r}{2\tau} \qquad \text{Equation 1.3}$$

where σ'_{mu} is the tensile strength of the matrix in the absence of reinforcing fibres. Thus, it is theoretically possible to estimate interfacial bond strength from saturation crack spacing.

The effective composite elastic modulus decreases with the formation of each matrix crack. When matrix cracking is complete, one can assume that the load in the composite is carried exclusively by the fibres and that the final composite modulus may then be given by:

$$E_{c(final)} = E_f V_f \qquad \text{Equation 1.4}$$

It is reasonable to assume that with the generation of each matrix crack, the load once borne by the matrix is thrown onto the surrounding fibres. If there are insufficient fibres to withstand this additional load, the composite will fail. This failure stress (σ_{cu}) may be predicted by using a "rule-of-mixtures" approach:

$$\sigma_{cu} = \sigma'_f V_f + \sigma_{mu} V_m = \varepsilon_{mu} E_f V_f + \sigma_{mu} V_m \qquad \text{Equation 1.5}$$

where σ'_f is the stress in the fibre at the matrix cracking strain and σ_{mu} is the tensile strength of the matrix (in the absence of fibres). Alternatively, if there is a sufficient fibre volume

fraction to accommodate the additional load imposed when the matrix cracks, then the composite's failure stress (σ_{cu}) may be predicted approximately from:

$$\sigma_{cu} = \sigma_{fu} V_f \qquad \text{Equation 1.6}$$

where σ_{fu} corresponds to ultimate fibre strength. This is a simplistic relationship which ignores, for example, any contributions to strength from the matrix or the statistical nature of fibre strength. Figure 1.3 demonstrates diagramatically how the crossover point between matrix-dominated and fibre-dominated composite failure occurs at a value of fibre volume fraction $V_{f(crit)}$ given by [1]:

$$V_{f(crit)} = \frac{\sigma_{mu}}{\sigma_{mu} + (\sigma_{fu} - \sigma'_f)} \qquad \text{Equation 1.7}$$

This expression is obtained by equating equations 1.5 and 1.6, and defines a condition for a useful composite. In most practical systems $V_{f(crit)}$ is low, typically in the region 0.005- 0.05.

1.2.2 Considerations for cmc development

1.2.2.a Fibres

Developments in ceramic-matrix composites have been facilitated in part by advances in fibre technology. Several reviews have been published [*e.g.* see 24-26]. Early fibre-reinforced glasses and ceramics were restricted to low temperature applications (up to ~ 450 °C) by the poor oxidation resistance of the carbon fibres they employed. In recent years, much effort has been invested in producing ceramic fibres which retain their properties at high temperatures. Table 1.1 summarises the physical and mechanical properties of fibres suitable for incorporation into ceramic-matrix composites. In particular, composites containing silicon carbide (*e.g.* Tyranno) and silicon oxycarbide (*e.g.* Nicalon) fibres have been extensively studied. Also, several manufacturers now produce alumina- and mullite-based fibres by sol-gel routes (see table 1.5 and section 1.3.7.d).

1.2.2.b *Matrix materials*

Davidge [28] notes that the matrix phase in a practical ceramic-matrix composite system is likely to be an existing engineering ceramic (or glass or glass-ceramic) which would profit from the incorporation of a second, fibrous phase. Early work considered glassy matrices principally because of the ease with which they could be processed; examples include soda-lime-silica and Pyrex (borosilicate) (see table 1.2).

Glass-ceramics retain the advantages of being processed whilst in the glassy state, but are converted to a polycrystalline body by appropriate heat treatment [29-31]. This controlled devitrification results in a fine-grained ceramic body which may contain between 2-50 volume% residual amorphous material and which generally offers mechanical properties superior to those of the parent glass. Table 1.2 presents examples of glass-ceramic systems which have been considered as candidate matrix materials for ceramic-matrix composites. A useful characteristic of some systems is that thermal expansion coefficients can be altered through composition changes, and that ceramics with near-zero thermal expansion coefficient can be prepared. Important examples include $Li_2O \cdot Al_2O_3 \cdot 4SiO_2$ (LAS, spodumene) and $2MgO \cdot 2Al_2O_3 \cdot 5SiO_2$ (MAS, cordierite).

Matrix phase changes which occur during processing or later during service may affect the composite's properties. Figure 1.4 summarises the transitions between the crystalline forms of silica (SiO_2) [32]. The three basic polymorphs (quartz, tridymite and cristobalite) have distinct crystal structures with well defined fields of stability under equilibrium conditions. Additionally, each basic structure has one or two low-temperature modifications (designated low- or α-) which are essentially distortions of the parent structure (designated high- or β-). Since converting from one basic structure involves substantial atomic rearrangement, this process is slow and requires a significant energy input. In contrast, converting between modifications requires only a distortion of the crystal lattice and so occurs more quickly.

The different thermal expansion coefficients of these silica polymorphs can have important practical consequences. In particular, the formation of cristobalite is generally to be avoided because its high thermal expansion coefficient ($27 \times 10^{-6} K^{-1}$) often causes residual stresses and cracking on cooling from processing temperatures.

1.2.2.c Fibre and matrix compatibility

If candidate fibre/matrix combinations are to form successful composites, it is necessary that different types of compatibility criteria be satisfied. Of particular importance are thermal expansion mismatches, chemical compatibility between fibres and matrix and the properties of the fibre/matrix interface.

The difference in thermal expansion coefficient of the fibres (α_f) and of the matrix (α_m) plays an important rôle in determining the mechanical properties of the composite. Any fabrication procedure will invariably involve some processing at an elevated temperature, $T_{process}$. The differential strain between the fibre and matrix, $\Delta\varepsilon$, will then be given by:

$$\Delta\varepsilon = \Delta\alpha\,\Delta T = \Delta\alpha\left(T_{process} - T_{ambient}\right) \qquad \text{Equation 1.8}$$

where $\Delta\alpha$ is the difference between α_f and α_m. This gives rise to residual stresses within the composite.

One can envisage two types of behaviour – figure 1.5 shows schematically the idealised radial residual stress systems. If $\alpha_f < \alpha_m$ then the matrix will contract more than the fibres on cooling and, gripping the fibres tightly, generate residual tensile stresses within the matrix. In the axial direction, the magnitude of these tensile stresses may well be sufficiently high to cause matrix cracking even before the composite is mechanically loaded. On the other hand, if $\alpha_f > \alpha_m$ then the fibres will be subject to residual tensile stresses and the matrix will be in residual compression; this may increase the stress at which the matrix cracks when the

composite is loaded. In the radial direction, if $\alpha_f > \alpha_m$ then debonding between fibre and matrix is encouraged.

Several analytical solutions, of varying complexity, have been published which describe the residual stress state in composites. Sambell *et al* [8] presented the following expression for axial residual stresses in the matrix:

$$\sigma_{axial} = \frac{E_f V_f \Delta\alpha \Delta T}{1 + V_f(E_f/E_m - 1)} \qquad \text{Equation 1.9}$$

Whilst α_f and α_m should ideally be kept as close as possible, in practice this is rarely possible. The case where $\alpha_f > \alpha_m$ is then preferred since the fibres are more capable of withstanding tensile strains than the matrix. Even then, some of the useful load-bearing ability of the fibres may be consumed just by these residual thermal stresses. The most effective composites are therefore recognised to be those where $\Delta\alpha$ is of the order 1-2 x 10^{-6} K^{-1}, with $\alpha_f > \alpha_m$. It is important to appreciate that some fibres are very anisotropic, exhibiting different expansion coefficients in the axial and radial directions. In particular, carbon fibres have expansion coefficients of about 0 and 10 x 10^{-6} K^{-1} respectively in these directions (see table 1.1).

The properties of the fibre/matrix interface, particularly interfacial bond strength, are recognised as being central to the performance of ceramic-matrix composites, and have consequently received a great deal of attention [34-35]. There are two conflicting requirements which must be optimised.

Firstly, the fibre/matrix interfacial shear strength should be sufficiently strong for applied mechanical stresses to be transferred by shear from matrix to fibres, thereby exploiting the load-carrying potential of the fibres. If a ceramic-matrix composite is to be effective, however, the stress field ahead of an advancing matrix crack should be able to induce interfacial debonding in front of the crack tip and thereby facilitate the fibre-related toughening processes described in the previous section (*i.e.* matrix crack bridging, fibre

pullout *etc.*). Note that the condition $\alpha_f > \alpha_m$ mentioned above encourages this. In this way, energy is consumed, the effects of the matrix crack are delocalised away from the crack tip and the composite behaves in a tough manner. Conversely, a strong fibre/matrix interface which does not permit interfacial debonding will result in a brittle composite. The effects of weak and strong interfacial bond strengths on mechanical performance are summarised in figure 1.6.

Chemical interactions between fibres and matrix may alter or control interfacial properties, either during processing or during service. In like-like composites where there is a natural tendency for strong interfacial bonds to form, barrier layers may be introduced *e.g.* by chemical vapour deposition or sol-gel techniques. In other composite systems, desirable interfacial layers may form during processing, *e.g.* weak carbon interlayers form during heat treatment of SiC/glass-ceramic composites [36, 23].

1.2.3 Test methods

1.2.3.a Flexural versus tensile strength

The problems associated with the mechanical testing of ceramic-matrix composites have been discussed in a number of reviews [*e.g.* see 37, 38]. Test methods have evolved partly from techniques employed previously for monlithic ceramics, and partly from methods conceived originally for other types of composite, particularly polymer-matrix composites. Whilst many test methods for this latter class of material have been standardised [*e.g.* 39], methods for ceramic-matrix composites have not yet reached that level of maturity.

The problems of obtaining reliable tensile data are well documented. Since the shear strength of unidirectional, ceramic-matrix composites is typically two orders of magnitude lower than the tensile strength [40], care must be taken to avoid shear failure. Soft (*e.g.* aluminium) end tabs must be bonded to specimens in order to provide protection against possible compression and/or shear damage [41]. Slight misalignments in the loading axis or slight bending of

specimens during tensile testing can lead to the development of shear stresses which may cause splitting parallel to the fibres.

For the purposes of materials/process development, values of "strength" have often been obtained with flexural measurements because of the ease with which such measurements can be performed. Once again, the low shear strength of many ceramic-matrix composites means that test geometries must be carefully defined if shear failure is to be avoided and tensile failure promoted; the ratio of loading span to specimen thickness must be large, typically greater than 25. Values of flexural peak stress are calculated from beam-bending formulae which assume linear elastic behaviour in the specimens; such data are commonly referred to as "modulus of rupture" (MOR) values.

The first permanent damage during flexural testing of a unidirectional composite is usually the formation of transverse cracks on the tensile side of the specimen. One might expect a reasonable correlation between values of elastic modulus and matrix cracking stress determined from flexural and tensile tests because the beam-bending formulae used to calculate flexural stresses and strains apply (in theory) to the point where damage just commences. As the test proceeds and the neutral axis moves down the specimen towards the compression side, several different damage modes are possible, including extension of a bridged matrix crack, delamination within a plane near to the neutral axis, and compression damage on or near the compressive face of the specimen. The lack of correlation between flexural and tensile strength data may be attributed to the different failure modes in the two types of specimens, and to a lesser extent to the lack of validity of the equations used to calculate flexural strength. For composite samples which fail in the same mode in tension and flexure, stressed-volume effects predict that MOR values would exceed tensile data [*e.g.* see 1].

1.2.3.b Toughness

It is recognised that toughness measurements based on the concept of linear elastic fracture mechanics are not applicable to ceramic-matrix composites for three principal reasons:

- Failure in these materials is a complex, delocalised process involving damage away from the major macroscopic crack growth zone;
- Failure from a pre-existing crack does not occur by self-similar crack growth;
- The delocalised nature of the damage process makes it difficult to define crack length.

However, this has not prevented the application of conventional fracture mechanics test techniques (notched bend tests, compact tension *etc.*) to composites, although the wisdom of accepting results obtained from such techniques has been questioned [*e.g.* 42]. Despite these comments, there is a recognised need for quantitatively describing crack growth resistance. Integration of force-displacement curves yields the energy consumed during a test. Whilst these data cannot be related in a straightforward way to microstructural damage processes, the method is nevertheless useful for comparative studies and general characterisations as long as one remains aware of its limitations. Such measurements should be accompanied by microstructural evaluation of damage. Various notched tensile and flexural test geometries have been recommended for their ability to provide a controlled form of crack growth. The work of fracture, which can be approximated to the fracture surface energy, is then given by the area under the force-displacement curve divided by the area of the fracture surface created. Whilst such approaches to obtaining a quantitative description of toughness will not be suitable for engineering design purposes, they have some utility in comparative assessments as long as the warnings mentioned above are heeded.

1.2.3.c Acoustic emission analysis

Acoustic emission may be defined as: *"the class of phenomena whereby transient elastic waves are generated by the rapid release of energy from a localised source or sources*

within a material, or the transient elastic wave(s) so-generated" [43]. The displacements caused when such waves reach the surface of a specimen may be detected with an appropriate transducer (*e.g.* a piezoelectric device) and suitable amplification and signal processing electronics [*e.g.* see 44].

A common measure of acoustic emission activity is a running total of the number of amplified pulses which exceed a predefined voltage threshold. Individual excursions above this threshold are referred to as *ringdowns* (figure 1.7). Alternatively, the ringdowns from such a single source may be registered as an *event*. Signals may be further distinguished on the basis of their amplitude or energy – histograms of number of counts versus amplitude (referred to as amplitude distributions) are a convenient way of presenting these data.

The utility of acoustic emission analysis during the mechanical testing of composites is well established [45, 46]. At the simplest level, the onset of acoustic emission activity is indicative of the commencement of permanent damage within a specimen and may coincide with a mechanically determined proportional limit. Alternatively, the detection of significant acoustic emission activity before a proportional limit is reached (as has been reported for some ceramic-matrix composites [47]) may indicate that sub-critical cracking is occurring. Several authors have attempted to correlate amplitude distribution histograms with damage modes, either in different samples or at different stages of tests [48-50]. The rationale here is that some microstructural processes, such as fibre/matrix slippage, generate more energetic stress waves than, say, a single matrix cracking event.

1.2.4 Processing of ceramic-matrix composites

Several authors have reviewed the advances in processing technology which have facilitated the development of ceramic-matrix composites [4, 51-54]. A useful fabrication process must fulfil several requirements: the fibres should not be degraded during processing either mechanically or chemically; the fibres should retain their intended alignments in the final

composite; fibre-matrix interface properties should satisfy the criteria described in preceding sections and should ideally be controllable; the matrix should be completely densified and matrix porosity should be minimised. Further requirements are that the method should be applicable to a wide variety of fiber and matrix combinations, that complex shapes can be produced with minimal post-fabrication machining requirements, and that the process be economically viable. There exists also the desire to use shaping technologies which are already well understood in other areas, particularly polymer-matrix composites. While Phillips [4] observes that successful routes to ceramic-matrix composites typically involve processing at temperatures in excess of 1000 °C, there are advantages to be gained through reducing temperatures: thermal expansion effects between fibre and matrix are diminished; possible phase changes or chemical reactions are avoided; the process will be cheaper.

Table 1.3 summarises possible methods of preparing dense ceramics. The following sections review how these methods may be applied to the fabrication of ceramic-matrix composites. Attention will be given to flexibility regarding materials and component geometries.

Several methods share common ideas or principles. The ceramic matrix material may be introduced in powder form (hot-pressing, sintering, slurry techniques) or be synthesised chemically *in situ* (sol-gel, polymer pyrolysis, CVD/CVI). The latter are generally achieved by the liquid- or vapour-phase infiltration of a fibre preform in manner akin to resin transfer moulding (RTM) in polymer-matrix composites. Despite the sophistication of many of the ideas which will be described, it is worth noting that slurry techniques have probably been the most successful to date in terms of quantity of published work.

1.2.4.a Hot-pressing

Perhaps the simplest method of fabricating ceramic-matrix composites is to mix matrix powders intimately with fibres or whiskers and then consolidate the matrix using heat and pressure, typically by uniaxial hot-pressing or by hot-isostatic pressing (HIPing). Solid-state sintering conditions are generally severe; for example, temperatures of 1800-2100 °C and

pressures of nearly 100 MPa are required to densify silicon nitride matrices. Lange *et al* [52] discussed the requirements for preparing efficient powder compacts with emphasis on strength and stability during processing. Although continuous fibre composites can be fabricated using hot pressing, the high processing temperatures lead typically to problems such as fibre degradation and high residual thermal stresses. Moreover, the range of shapes which can be formed is extremely limited. The approach is, therefore, generally limited to small, simply-shaped, whisker-toughened ceramic components.

1.2.4.b Slurry techniques

During the late 1960s Sambell *et al* [8] introduced a method in which fibre tows are passed through a colloidal suspension of matrix particles to which has been added organic binders and surfactants (this is usually referred to as a slurry). The coated fibres can be wound onto mandrels and dried to form pre-preg sheets which can subsequently be stacked and hot-pressed to consolidate the composites and drive off any organic species not removed during drying. The shaping process is directly analogous to the layup methods used to prepare polymer-matrix composite laminates from prepreg sheets.

The first composites prepared by this method comprised carbon fibres in a variety of glass and glass-ceramic matrices [8, 33]. Prewo, Brennan and coworkers responded to the perceived need for high-temperature engineering materials by incorporating SiC yarns and monofilaments, selected for their higher temperature capability, into borosilicate, "Vycor" (boron-leached borosilicate), high-silica and aluminosilicate glasses [16, 27, 55-57]. Glass-ceramic matrix systems studied include lithium aluminosilicate (LAS), calcium aluminosilicate (CAS) and magnesium aluminosilcate (MAS). Hegeler and Brückner modified the slurry process by introducing an alkoxide sol as a processing aid [58].

Viscous phase consolidation of the glassy matrix is achieved by hot pressing at a temperature above the softening point of the glass, typically in the range 1000-1400 °C. Glass-ceramic matrices are then converted to their crystalline form by further heating. Slurry processing is

generally ineffective in crystalline-ceramic-matrix systems because of the lack of viscous flow and the high sintering temperatures which are required. At elevated temperatures there are potential problems of fibre degradation, undesirable fibre-matrix interface reactions and phase changes within the fibres or matrix. Sintering additives may be used to depress hot-pressing temperatures and avoid these problems, *e.g.* Guo *et al* [59] employed fluxing agents to prepare carbon-fibre reinforced Si_3N_4 composites.

The principal limitations of slurry processing are that only one- or two-dimensional reinforcement geometries may be produced and that component forms are restricted to flat plates or tubes. Further, the excess matrix material which inevitably accumulates on the exterior faces of tapes causes matrix-rich regions to be formed when tapes are stacked and hot-pressed. This inhomogeneity is worse when viscous flow of the matrix is absent *e.g.* in the case of refractory, ceramic matrices.

Cornie *et al* [53] conclude that slurry infiltration techniques are best-suited to glassy or low-melting-point ceramic matrices and limited to simple fibre geometries. It is worth noting that this fabrication route has received enormous exposure in the literature over the past decade or so. In particular, the experimental data gained from SiC-reinforced glass-ceramics has been extensively cited in mechanical property modelling for continuous fibre-reinforced ceramic-matrix composites.

1.2.4.c Sol-gel methods

Sol-gel technology and its applicability to processing ceramic-matrix composites are explored in some depth in a later section. The main attractions of the approach are low sintering temperatures, excellent homogeneity and purity of materials, and the ability to prepare compositions and phases that are impossible to achieve by conventional methods. It will be shown that although an enormous amount of interest has been shown in sol-gel processing, various problems have restricted its wider exploitation, including very high levels of shrinkage, shrinkage cracking; high volume fractions of residual porosity; and low yields. The

main contributions have therefore been in the form of "supporting rôles" *e.g.* in the preparation of glass-ceramic powders for slurry processing or hot pressing, as an efficient binder system in slurry processing, or as a means of applying fibre coatings to modify interfacial properties. The fabrication of ceramic fibres by sol-gel methods will be discussed in section 1.3.7.d.

1.2.4.d Polymer pyrolysis

Research on the production of ceramic fibres by pyrolysing preceramic polymers stimulated interest in the use of a similar approach to prepare dense, ceramic matrices. The polymer pyrolysis route offers similar potential advantages to the sol-gel approach: excellent compositional control of the ceramic can be achieved via the composition and molecular weight of the polymer; unique, multiphase ceramic compositions can be attained; processing temperatures are lower than those required in solid-state sintering; and fibre preforms can be readily infiltrated to achieve complicated composite shapes. Also, polymeric materials are easily shaped by conventional methods. The technique also shares the principal drawbacks of sol-gel methods, *e.g.* high levels of residual porosity (large volumes of gases which are evolved during the pyrolysis step); high shrinkage; and low yield.

In his review of the subject, Sheppard [54] describes several composite systems prepared by polymer pyrolysis. Precursors exist for SiC, Si_3N_4 and Si-C-N. The commercial manufacture of ceramic fibres for reinforcement (*e.g.* Nicalon SiC) was described in a previous section. One approach to manufacturing ceramic-matrix composites is to replace the ceramic particles with polymer particles in the slurry method described above. Alternatively, a fibre preform may be infiltrated with a thermoplastic polymer precursor in a process similar to resin transfer moulding (RTM). Pyrolysis is usually performed in the temperature range 800-900 °C, although further heat treatment is required to convert the amorphous products into a crystalline form (*e.g.* ~1300 °C for Si_3N_4). Yield rates are low, so repeated polymer impregnation/pyrolysis cycles are required to build up a useful matrix density. Nicalon (SiC)

woven, continuous fabrics have been impregnated and pyrolysed to obtain composites that retain reasonable mechanical properties to ~1000 °C in oxidising environments. Short fibre SiC-SiC composites have also been prepared by this route. However, the disadvantages described above have limited the amount of interest shown in polymer pyrolysis.

1.2.4.e Gas-metal reaction

In the Lanxide™ or directed metal oxidation process a molten metal is reacted with a gas to form a ceramic, *e.g.* Al_2O_3 and AlN have been prepared by reacting molten aluminium with oxygen and nitrogen respectively [60]. Alloying elements are used to disrupt the formation of any passivating films which would normally occur. Growth of the ceramic occurs *away* from the original metal surface. If a fibre preform is in close proximity to the molten alloy then the ceramic phase will grow around the fibres and a ceramic-matrix composite will result; Nicalon SiC-reinforced Al_2O_3 and AlN composites have been produced in this way, for example. Particulate composites have also been prepared. If the metal is not completely reacted or if the alloy contains solute elements which will not react, then the result may be a two-phase structure comprising interpenetrating networks of ceramic and metal [61]. Such ceramic-metal materials may have interesting properties.

1.2.4.f Melt infiltration

Infiltration of fibre preforms by liquid phase ceramics appears attractive superficially: the prospect is offered of fully-dense, flaw-free matrices formed in a single processing step with no great restrictions on component shape. The technique has been frequently used to manufacture metal-matrix composites [62]. The principal obstacles to applying the technique to ceramic-matrix composites are the likelihood of fibre degradation and undesirable interface reactions at the high temperatures involved, difficulties in infiltrating preforms with high viscosity melts, and high residual thermal stresses. Low-melting-point glass and glass-ceramic systems seem to be the most likely candidates for consideration. Some success has been achieved with silicon infiltration followed by controlled reaction with carbon to

produce SiC *e.g.* Fitzer and Gadow [63] created carbon-fibre-reinforced SiC by infiltrating C-C preforms with molten silicon.

1.2.4.g Gas phase reactions

Numerous ceramic and glass compositions can be prepared by the reaction of gaseous precursors. Naslain & Langlais [64] summarise reaction chemistries which can be used to prepare carbon, oxides, carbides, nitrides and borides. The deposition of powder products (a "soot") onto a substrate is referred to as Chemical Vapour Deposition (CVD). This is a mature technology which is used, for example, to manufacture monofilament reinforcements and preforms for drawing optical glass fibres.

If the reactive gas mixture is permitted to infiltrate a preform of reinforcement fibres, the reaction products will deposit on the fibres and will hopefully form a dense, ceramic matrix. Such Chemical Vapour Infiltration (CVI) was exploited originally for the manufacture of carbon-carbon composites and later by Société Européene de Propulsion (SEP), France, for SiC-SiC composites. Workers at Oak Ridge National Laboratory, USA, describe how CVI may be "forced" by pressure and thermal gradients to reduce infiltration times from weeks to hours and permit the densification of thicker sections [65, 66]. Forced CVI has been used successfully to prepare SiC- and Al_2O_3-reinforced SiC and Si_3N_4 composites.

It is widely considered [54] that of all the possible processing routes to ceramic-matrix composites for aerospace applications, CVI has achieved the most industrial success. CVI is a near-net-shape process, can produce many ceramic matrix compositions, is very flexible in the geometry/layup of reinforcing fibres and has fewer limitations on component size than other fabrication methods. SEP's SiC-SiC and C-SiC have been used to manufacture a variety of high-temperature components *e.g.* gas turbine engine nozzle petals and rotors, leading edges for re-entry applications, thermal protection shingles and rocket nozzles.

1.3 THE SOL-GEL PROCESS

1.3.1 Background

The label "sol-gel" refers to a family of methods for producing an amorphous, inorganic network from the low-temperature reaction of chemical species in solution. A ***colloidal sol*** may be defined as comprising a disperse, solid phase having a dimension between 1 nm and 1 μm in a liquid dispersion medium [67]. If the inter-particle forces which control sol stability are disturbed in a controlled manner, then a continuous network of solid material entwined with an inter-penetrating network of solvent-filled, continuous porosity may be formed, a ***gel***. Alternatively, a macromolecular sol may be created by encouraging monomeric species (e.g. metal alkoxides) to "polymerise"; continued growth of the macromolecules so formed also leads to gel formation. Figure 1.8 presents a schematic overview of the possible routes a gel (however formed) can follow to attain its final state.

Comprehensive reviews of the subject include those by Colomban [68], Hench and West [69], Mackenzie [70], Wilson and Patel [71], Schmidt [72], James [73] and Scherer [74]. Brinker and Scherer [75] recently published a book which considers each step in the sol-gel process in detail. Segal's monograph [76] has useful chapters on colloidal and macromolecular methods of ceramic processing. Although the majority of published work is concerned with macromolecular sol-gel routes (and silica in particular), many of the experimental data and physical principles are equally applicable to colloidal gels.

The current status of sol-gel technology will now be reviewed, and several of the steps described in figure 1.8 will be discussed. Following reviews of the properties of both macromolecular and colloidal sols, the nature of silica sols will be explored. The phenomenon of gelation is discussed and subsequent sections consider the microstructural changes which occur as gels are aged, dried and sintered. The potential benefits and disadvantages of sol-gel processing routes are then examined in a survey of application areas. Particular emphasis is

given to the utility of sol-gel technology in fabricating composite materials, including fibres, interfacial coatings and glass- or ceramic-matrix materials.

1.3.2 The precursors

1.3.2.a Macromolecular sols

Most of the work in this area has been performed on metal alkoxides as these provide a convenient source for the "inorganic monomers" which are stable in many common solvents and which can be encouraged to polymerise to give gels. Metal alkoxides have the general formula $M(OR)_x$ where M is a metal with valence state *x* and R is an alkyl group, typically methyl ($-CH_3$) or ethyl ($-C_2H_5$). Such an alkoxide is essentially an ester resulting from the reaction between either an oxide, $(MO)_x$, or a hydroxide, $M(OH)_x$, and an appropriate alcohol, ROH:

$$(MO)_x + 2xROH \leftrightarrow M(OR)_{2x} + xH_2O \qquad \text{Equation 1.9}$$

$$M(OH)_x + xROH \leftrightarrow M(OR)_x + xH_2O \qquad \text{Equation 1.10}$$

A commonly-quoted example is that of tetraethoxysilane (TEOS), $Si(OC_2H_5)_2$. The following equations give a simplified description of the steps involved:

$$\equiv Si\text{-}OEth + H_2O \rightarrow \equiv Si\text{-}OH + Eth\ OH \qquad \textit{partial hydrolysis} \qquad \text{Equation 1.11}$$

$$Si(OEth)4 + 4H_2O \rightarrow Si(OH)_4 + 4Eth\ OH \qquad \textit{complete hydrolysis} \qquad \text{Equation 1.12}$$

$$\equiv Si\text{-}OH + HO\text{-}Si\equiv \rightarrow \equiv Si\text{-}O\text{-}Si\equiv + H_2O \qquad \textit{condensation 1} \qquad \text{Equation 1.13}$$

$$\equiv Si\text{-}OH + Eth\ O\text{-}Si\equiv \rightarrow \equiv Si\text{-}O\text{-}Si\equiv + Eth\ OH \qquad \textit{condensation 2} \qquad \text{Equation 1.14}$$

The hydrolysis reactions (equations 1.11 and 1.12) and the condensation reactions (1.13 and 1.14) will generally occur simultaneously and will not be complete. The initial hydrolysis may be partial (1.11) or complete (1.12); a mixture is most likely. The condensation steps may involve reactions between two hydroxyl groups or between a hydroxyl and an alkyl group (equations 1.13 and 1.14 respectively). These reactions may be

carried out in organic solvents; alcohols are particularly convenient because they are miscible with water to start the process according to equation 1.11. The structure and properties of the polymer units and of the macromolecular gel (when links form eventually between these polymer particles) are dictated by a number of parameters. These include pH, $R = [H_2O]/[M(OR)_x]$, temperature and the presence of salts or other ions. The behaviour of macromolecular silica sols is explored in more depth in a later section.

The metal alkoxide route is flexible because all metals can form alkoxides [71]. Two or more alkoxides can be mixed according to the appropriate molar ratios to obtain chemically pure, highly homogeneous products which may be impossible to produce by conventional means.

1.3.2.b Colloidal sols

The science of colloids is an interdisciplinary one and draws heavily from areas of physical and surface chemistry. There are several text books in these areas which give useful insights into the nature of colloids, *e.g.* see Shaw [67].

A colloid may be defined as a system comprising a dispersed phase, having at least one dimension in the range 1 nm to 1 μm, in a dispersion medium. A sol was introduced earlier as a colloid whose dispersed phase is solid and whose dispersion medium is liquid.

Colloidal particles are sufficiently large for tangible interfaces to exist between them and the dispersion medium. The origins of colloid stability lie in the interface between the dispersed particles and the dispersion medium, and particularly in the nature and magnitude of the particle-particle and particle-dispersion medium interactions. It should be appreciated that even though the area-to-volume ratio of the colloidal particles is very large, such interactions are most strongly influenced by the outermost molecular layers at the interface; consequently, quite small material additions to the system can provide sufficient molecular coverage at the interface for the overall properties of the colloid to be changed markedly.

The very high surface area of colloidal particles is accompanied by a correspondingly high surface free energy and hence a large thermodynamic driving force for aggregation of the

barrier which must be overcome for aggregation to occur. The colloidal particles are in constant thermal motion (witness Brownian motion) and whether or not one of the frequent chance encounters between two particles results in aggregation is dictated by the balance of the attractive forces and the repulsive forces which act between the particles.

Attraction between particles is generally due to van der Waals-type interactions. Stability against aggregation may be due to repulsion between similarly-charged electric double layers, to steric effects (large, adsorbed molecules may inhibit particles coming together) or, in the case of lyophilic (solvent-loving) sols, to high particle-solvent affinity.

The first of these mechanisms is considered to be the most important for true colloidal sols. Preferential adsorption of ions from solution or dissolution of ions from the particle's surface will result in a net surface charge on the particle. Counter-ions (*i.e.* ions of opposite charge) are attracted towards the surface, and co-ions (*i.e.* ions of like charge) are repelled from the surface. The distribution of the different ionic species is such that electrical neutrality is maintained, and the two-layered nature of this distribution has earned the label 'double layer'.

Deryagin, Landau, Verwey and Overbeek (DLVO) developed a quantitative theory based on the energy changes which occur when charged particles are brought together. The total potential energy between two particles, V_T, may be written as the sum of terms representing attractive interactions (V_A) and repulsive interactions (V_R). The stability of colloids may then be interpreted in terms of a curve which shows the variation of interaction energy with inter-particle distance. A simplified example of such a curve is shown in figure 1.9.

The strong repulsion between particles at very small interparticle separations is attributed to Born repulsion. Potential energy minima at small and large interparticle separations are due to Van der Waals attractions [67]; these may be referred to as primary and secondary minima. Primary minima are markedly deeper than the secondary minima. Double-layer repulsion between particles dominates at intermediate distances and so gives rise to the potential energy maximum shown in figure 1.9.

The tendency of colloids to aggregate in order to minimise their very high surface energy was mentioned above. ***Aggregation*** is a general term used to describe the joining of colloidal particles. Figure 1.9 permits a more informative description of how these particles might join into clusters, chains and three-dimensional networks, and these are summarised schematically in figure 1.10.

Coagulation refers to the irreversible aggregation one sees when particles are forced closely together such that the particles are 'stuck' in the primary minimum of the potential energy well (labelled 'i' in figure 1.9). The particles generally form into relatively dense clusters which may then precipitate out. ***Flocculation***, by contrast, is a reversible aggregation at the secondary minimum ('ii' in figure 1.9). Flocculated particles are more open and less dense than coagulated particles. ***Gelation*** describes the formation of a three-dimensional, porous network of colloidal particles with no change in volume from the that of the original sol. The properties of gels are discussed in more depth in the following sections.

1.3.3 Colloidal silica

Iler [77] provides a definitive review of the chemistry of silica which embraces the preparation, stability and applications of colloidal silica sols. Commercially available silica sols typically contain particles 5-50 nm in diameter and 30-50% by weight of silica. Most are base-stabilised (*e.g.* with sodium hydroxide or ammonia) and have a pH between 8 and 10. Acid-stabilised sols (pH ~ 2) are available, typically by giving the silica surface a positive charge with alumina. A number of industrially-practicable processes for producing stable, silica colloids of controlled particle size have been developed:

- Polycondensation of silicic acid, $Si(OH)_4$. This is the most important and extensively studied route. Control of pH and electrolyte concentrations permit the preparation of sols with particle sizes beween ~ 5 nm and > 100 nm
- Dilute solutions of sodium silicate, Na_2SiO_4, may be partially neutralised with acid to a pH of 8-9. At low Na^+ concentrations, aggregation is avoided and the formation of a sol is promoted. Suitably low values of Na^+ concentration may also be attained by ion-exchange methods and by electrodialysis.
- Methods utilising base-catalysed polycondensation of stoichiometrically-controlled alkyl-silicate/alcohol/water systems have been extensively studied. Frequently attributed to Stöber, Fink and Bohn [78], the approach permits the fabrication of large (*e.g.* up to 1000 nm), monodisperse, spherical particles and is widely used industrially.
- Pyrogenic (or "fumed") silica powders are formed by the flame hydrolysis of, typically, silicon tetrachloride. Dispersion in water or polar organic liquids is difficult to achieve because of the hydrophobicity of the surfaces. This may be overcome by surfactancy (*i.e.* adsorbing species onto the silica surfaces which present hydrophilic "tails" into the solvent) or, more commonly, by incorporating small quantities of TiO_2 or Al_2O_3 into the solid structure (via $TiCl_4$ or $AlCl_3$ in the precursor).

Once formed, sols may be purified by ion exchange, dialysis or electrodialysis methods. Concentration of the sols to obtain higher weight fractions of solids may be achieved by evaporation of water, by centrifugation or by ultrafiltration. Table 1.4 presents manufacturer's data on the materials which are studied in this thesis.

1.3.4 Gelation

Whilst the physical reasons behind the gelation of colloidal sols and macromolecular sols are different, the outward appearance of their gelation is sufficiently similar phenomenologically that they may be discussed together. A gel was described above as a rigid, continuous network of solid material entwined with an inter-penetrating network of solvent-filled, continuous porosity. Both the solid material and the porosity are of colloidal dimensions and the total volume occupied is identical to that of the starting sol. Gelation is characterised by a marked increase in sol viscosity and by the sudden ability of the structure to support an elastic stress.

Colloidal (or physical) gels are formed when the repulsive forces between the electric double layer fields of neighbouring colloid particles are overcome. This is most commonly achieved by altering the electrolyte chemistry (particularly pH) to diminish the repulsive double layer interactions. Aggregation may also be achieved by the introduction of ions (or, indeed, of molecular species) having opposite charge to the particles. Polymer chains whose ends are attractive to the particles have also been used to induce aggregation.

Aggregation of the particles, however inspired, causes clusters to form and link, and gelation is considered to have occurred when sufficient clusters have linked that the vessel holding the sol is completely bridged. The gelation of colloidal sols is often a reversible process.

Macromolecular (or chemical) gelation occurs when the polymerisation described in the previous section leads to the formation of a three-dimensional network which spans the vessel. The experimental parameters which control the morphology of polycondensation

products (including whether or not a gel will form) were discussed earlier. The products of inorganic polymerisation, in which monomers (*e.g.* metal alkoxides) form particles which may eventually link, should be distinguished from organic polymers.

In both the colloidal and the macromolecular routes, gelation may be considered to be a statistical event corresponding to the formation of the last link necessary to form the spanning cluster. As such, gelation is accompanied by no exotherm or endotherm.

The precise point at which gelation occurs is generally difficult to determine. The marked increase in sol viscosity at gelation may be used to define a time of gelation, t_{gel}, as the time taken for the viscosity to attain a predefined value. Another approach is to measure the viscoelastic properties (*e.g.* the loss and storage components of the sol's complex shear modulus).

1.3.5 Ageing

The structure of the gel at the gel point is dependent on the arrangement of the sol particles prior to gelation, and is therefore a function of the characteristics of the sol. However, the structure and properties of the gel continue to evolve long after gelation by a series of mechanisms which are usually grouped together under the heading "ageing". These phenomena, which may act singly or in concert, have been extensively studied [68, 69] and attempts have been made to develop theoretical models for different aspects of the ageing process [74]. However, Hench and West [69] assert that current understanding of the mechanisms and kinetics of ageing is limited and that few quantitative descriptions of the effects of ageing on gel properties and structures exist.

After gelation, other particle clusters will eventually become linked to the original spanning network. In macromolecular gels this may be attributed to the density of bridging bonds between clusters increasing as polycondensation reactions continue to occur (*cf* equations 1.13 and 1.14). In colloidal gels, regions of aggregated particles will join

eventually with the primary network as van der Waals attractive interactions overcome repulsive double layer effects; this may be promoted by adjusting the electrolyte properties. In both cases, the resultant contraction of the gel will cause solvent to be expelled from the pores in a process known as ***syneresis***. Scherer [74] has suggested that syneresis is driven by the thermodynamic advantage to be gained by reducing the huge solid-liquid interfacial area in a gel. Volume shrinkages can be very high; values of greater than 50 volume% have been reported for TEOS-derived silica.

Coarsening or ***Ostwald ripening*** is discussed at length by Iler [77]. Convex surfaces (having positive radii of curvature) are more soluble than concave surfaces (negative radii of curvature), so continual dissolution and reprecipitation of particles will tend to cause the growth of necks between particles and small pores to be filled in at the expense of material loss from particles' "exterior" surfaces (figure 1.11). This results in an overall increase in the average pore size and a decrease in solid-liquid interfacial area. Iler also reviewed the factors which affect the dissolution of and subsequent coarsening of silica gels [77]. Silica becomes more soluble at high values of pH, and the rate of coarsening of silica gels is similarly pH dependent. Other critical parameters which affect the properties of the gel prior to drying include time, temperature, solvent type and the presence of and concentration of stabilising salts in the electrolyte.

The growth of necks between particles, whether due to coarsening or to continuing condensation, causes the stiffness, strength (*e.g.* modulus of rupture) and toughness (*e.g.* K_{IC}) of the gel to increase. These are all desirable if cracking is to be avoided during drying.

1.3.6 Drying and sintering

This stage may be considered the most problematic in sol-gel processing and is considered to be responsible for the conspicuous lack of success in producing monolithic components by sol-gel routes. The high shrinkage and capillary stresses which develop during syneresis and

drying are often too great for the solid network to withstand and lead inevitably to dimensional instability or to catastrophic fracture of the specimen.

The mechanisms of drying (*i.e.* the removal of physically adsorbed solvent) in SiO_2 gels have been extensively studied by (among others) Brinker and Scherer [75]. Large capillary stresses can develop when the gel pores are small, *e.g.* < 20 nm. The conventional view is that cracking is the result of the variation of pore sizes in the gel (figure 1.12); the higher capillary pressure in a smaller pore could fracture the solid wall separating it from a neighbouring larger pore. Although Scherer has propounded several reasons why this explanation of experimental data is flawed, it is widely accepted that large pores and small variation in pore size are desirable if cracking during drying is to be avoided. The occurrences of syneresis and coarsening during ageing are therefore advantageous, and long ageing times are often necessary for monolithic components. Hench [69] has demonstrated the utility of drying chemical control additives (***DCCA***s) in achieving uniform, large pore-size gels from alkoxide routes.

One approach to avoiding capillary stresses is to avoid the solid-liquid interface altogether and remove the pore liquid in its gas phase. This can be achieved by heating under pressure to a point above the critical temperature and pressure of the solvent. Under such hypercritical conditions the pore structure does not collapse and a low density ***aerogel*** is produced, the porosity of which may reach 98 % by volume. When the pore liquid is removed at or near ambient conditions the gel network will shrink considerably and a ***xerogel*** results. The addition of surfactants to depress the solid-liquid interfacial energy has also been shown to reduce cracking.

The final process is the conversion of the dry gel into a densified glass. Heating at elevated temperatures causes pores to be eliminated by further shrinkage, and the ultimate density is often equivalent to that of fused silica. The driving force for densification is a reduction in the very high surface free energy of the gel, and so the densification temperature is a function of

the gel pore characteristics (dimensions, connectivity, surface area). James [73] has provided a comprehensive review of the processes which occur during sintering. Sintering is usually performed at temperatures well below the melting temperature of conventionally-derived glasses, and often lower than the glass transition temperature. Colloidal gels usually require a sintering temperature of 1500-1700°C, although temperatures as low as 1000°C have been reported for systems where the packing density of the colloid particles has been very carefully controlled [73]. Significant crystallisation of the glass may occur once the dry gel has been fully densified.

1.3.7 Applications

The potential advantages of sol-gel processing over conventional methods of fabricating glass and ceramic structures have been summarised in other reviews of the subject [*e.g.* see 71]. Among the benefits are excellent homogeneity and purity of materials (precursors are prepared chemically and intimately mixed on a fine scale), the ability to prepare compositions and phases which are impossible to achieve by conventional methods (phase changes and reactions which occur at high temperatures are avoided) and low sintering temperatures (the very high surface area of gels gives rise to a large thermodynamic driving force for densification). However, these advantages have been tempered historically by a number of problems which have restricted the wider adoption of the approach: very high levels of shrinkage (and associated shrinkage cracking) which arise during drying and sintering, residual fine porosity, high cost and impractically long processing times. The potential for producing dense, homogeneous, near-net-shape ceramic components (or matrices for composite materials) via the sol-gel route has not been realised principally because of shrinkage cracking.

The possible ways sol-gel processing can be applied to make different shapes and components may be seen from figure 1.13. For a new product or process to be successful, it must either

improve significantly on the previous state of the art, or it must introduce entirely new features [79]. On this basis, it appears that few sol-gel products have moved from being feasible, laboratory demonstrators to being commercially successful. The literature shows a discernible bias towards chemical sol-gel routes over colloidal routes and towards the production of glasses over the production of polycrystalline ceramics. The utility of sol-gel processing will now be discussed for different application areas; the categories adopted are arbitrary.

1.3.7.a Films and coatings

This category represents the most successful commercial application area of sol-gel technology. The dipping of a substrate into the desired sol permits the preparation of thin (< 1 μm) films; thicker films generally lead to cracking problems. Substrates with areas up to several square metres can be accommodated, as can awkward geometries which would be impossible to coat with other available techniques such as chemical vapour deposition (CVD).

One of the earliest commercial applications of the newly-emerging sol-gel technology was the coating of architectural glass. Single or multilayer films permit control of the reflectance, absorbance, transmittance, refractive index and colour of glasses. Refractive indices can be graded. Antireflective surfaces improve the efficiency of solar panels.

The close control over stoichiometry and the ability to achieve relatively flaw-free structures with sol-gel coating has led to advances in ferroelectric thin films for electronic, optoelectronic and optical memory products, electronic coatings (*e.g.* for photanodes) and high-temperature superconducting films. Other applications include abrasion- and wear-resistant coatings on polymers *e.g.* for opthalmic lenses, adhesion-promoting interlayers and passivation coatings to inhibit corrosion.

1.3.7.b Monoliths and powders

Hench's introduction of DCCAs [69] (see section 1.3.6) has enabled the preparation of glass components by casting followed by carefully-controlled ageing, drying and sintering. The possible crystallisation which would occur at the temperatures employed in melt-derived glasses are avoided at the low temperatures made possible by the high reactivity of the gels. This permits the fabrication of a very wide variety of glass compositions; James [73] provides references for over 40 binary, ternary and multicomponent glasses prepared by gel routes.

The principal uses for such glasses are in optical applications. Lenses may be made without melting or polishing. Surface finish and geometry may be retained even though the overall shrinkage of components may be very high. Graded refractive index glasses are prepared by permitting ionic exchange and/or diffusion in multicomponent gels. Sol-gel methods are competing with CVD methods for creating the cylindrical glass preforms from which optical fibres are drawn.

The high shrinkage of gels has prevented the preparation of dense, near-net-shape, monolithic components by sol-gel methods. However, the approach does lend itself to the preparation of ceramic powders which find widespread industrial application as the "raw" materials in conventional polycrystalline ceramic processing. The high uniformity of particle size and chemical composition achievable with sol-gel processing contrasts with the inherent variability of conventional, mineral-derived powders. Monosized, spherical powders are straightforward to shape and consolidate into green bodies, and their high reactivity permits low-temperature sintering (or HIPing *etc.*) into dense bodies.

Other industrial applications requiring tight control over composition include catalysts and pigments. Abrasives and fillers may be produced by harnessing the (usually detrimental) high shrinkage which occurs during the drying of gels; this is a lower-energy route to powder production than conventional comminution.

Colloidal suspensions are frequently useful industrial materials in their own right and are often manufactured by macromolecular routes. Iler [77] summarises application areas for colloidal silica and many of these exploit the purity of the silica which results from its chemical origins.

The excellent control over composition which is achievable by the use of sol-gel routes permits the preparation of stoichiometric mixed-oxide systems. Sol-gel processing has been used to prepare a wide variety of glass-ceramic materials which are of interest for their mechanical properties, *e.g.* anorthite [80], cordierite [81].

1.3.7.c Porous structures

The most prominent characteristics of a gel are its extremely high level of porosity and associated high surface area. Previous sections have described how pore sizes and size distributions in gels may be controlled via the chemistry and processing conditions of the sol-gel process, and it is well-established that such pore structures may be retained even after sintering. Sintered, porous gels are therefore natural candidates for filters, membranes and catalyst supports [82, 83], either as monoliths or as coatings on macroporous substrates. Note that such structures are often impossible to achieve with conventional ceramics processing. Other important application areas include sensors and the use of aerogels as thermal insulation materials.

Membranes (< 50 nm pore size), ultrafilters and microfilters (50 nm to 1 μm pore size) offer many advantages over the organic polymer structures which currently dominate many application areas: they have superior mechanical properties, they can be operated at higher temperatures, they are unaffected by common solvents and they are more resistant to damage by abrasion or by chemical attack. Pore sizes of the order of 1 nm are achievable in layered structures [75]. Sheppard [82] has summarised many potential and demonstrated applications in areas such as biotechnology (separation of enzymes, proteins, viruses), the food industry (brewing, by-product recovery) and environmental processing (cordierite substrates for

automotive catalytic converters, separating high-temperature gas mixtures, recycling of machining coolants, removal of metal oxides from polluted water systems).

1.3.7.d Fibres

The requirements of fibres for incorporation into ceramic-matrix composites were summarised in section 1.2.2.a: refractory, oxide, polycrystalline fibres exhibiting high strength, stiffness and chemical durability are desired. The preparation of glass and ceramic fibres from sols has been discussed in several reviews [*e.g.* see 84]. Continuous fibres for use as composite reinforcements may be drawn directly from viscous sols at room temperature and subsequently heat-treated to achieve densification and, where appropriate, controlled crystallisation. Table 1.5 summarises the compositions and basic mechanical properties of several commercially-available ceramic fibres manufactured by sol-gel routes. In particular, the Nextel ® (polycrystalline aluminoborosilicate) fibres manufactured by 3M have been considered for incorporation into ceramic-matrix composites. Experimental methods for producing mullite and mullite/zirconia fibres have been reported [85].

Several authors have described processing routes to glass and ceramic fibres which involve the unidirectional freezing of gels (*i.e.* following conventional gelation but prior to ageing and drying); fibres produced in this way include zirconia [86], silica [87] and alumina [88].

1.3.7.e Composite materials

Processing requirements for ceramic-matrix composites were reviewed in section 1.2.4. Sol-gel technology can contribute in three areas: (1) fabrication of matrix; (2) application of fibre coatings to modify the properties of fibre-matrix interface; (3) fabrication of fibre reinforcement (this has been discussed in the previous section).

The deposition of ceramic coatings on fibres may be achieved by passing continuous fibres or tows through a bath of sol, then drying and sintering the coating. Basic requirements are that the sol wets the fibres uniformly, that the fibres do not become damaged in any way, that the coatings are uniformly thick and non-porous, that bridges between fibres are not formed and

that the process can be scaled up to large throughputs. Different thickness coatings can be applied by repeated passing through the sol bath; this has the advantages that shrinkage cracking associated with thick (> 1 μm) coatings is avoided, and also that successive passes may "heal" the defects of previously-deposited layers. The approach has the potential to produce graded interlayer structures which could be used, for example, to bridge widely-differing thermal expansion coefficients.

Gulden *et al* [89] produced smooth, 100 nm-500 nm, coherent coatings of Y_2O_3 and Al_2O_3 on Nextel and Nicalon fibres by using a dip coating technique and calcination temperatures of 900 °C-1200 °C. Sol concentration could be adjusted to minimise the amount of bridging which occurred between fibres. Keeping fibres spread apart during coating was problematic, although the advantageous effect of the sols wicking into fibre tows and remaining there because of surface tension effects was reported. Hay and Hermes [90] applied Al_2O_3 coatings to SiC SCS-0, PRD-166 and FP fibres with a similar chemical sol technique. Coating thicknesses of between 50 nm and 750 nm were reported. The workers commented on the likelihood that fibres on the outsides of tows were coated satisfactorily but coating thicknesses on interior fibres were low (~50 nm) and less uniform. More recently,

A colloidal technique for producing Al_2O_3 coatings on SiC fibres was reported by Malghan *et al* [91]. Colloidal alumina particles carrying a strong negative charge were attracted to SiC fibres to which a strong positive charge had been imparted. Coating thicknesses from 50 nm to 50 μm were achieved, and some degree of control over coating characteristics was achieved by changing the chemistry of the colloidal sol and of the solution used to charge the fibre surface.

The prospect of fabricating ceramic- or glass-matrix composites by incorporating fibres into sols is attractive for the reasons outlined earlier: close control over matrix composition and phases, near-net-shape casting of components, flexibility and low processing temperatures. The general approach is either to infiltrate a fibrous preform with the sol or to pass

continuous fibres through the sol, induce gelation and then dry and densify following the principles outlined earlier [51]. Fitzer and Gadow [92] summarise several useful alkoxide chemistries for forming a variety of single and mixed-oxide matrices (*e.g.* various silica-based glasses, mullite, alumina) into which Nicalon, FP and carbon fibres have been incorporated. Lannutti and Clark [93] report on the preparation of fibre-reinforced Al_2O_3 composites and Hyde [94] describes the fabrication of a variety of carbon-fibre-reinforced silica shapes. Unfortunately, the same features of sol-gel processing which have precluded the wider adoption of the technique in the preparation of monoliths prevail in this instance, *i.e.* gross shrinkage and associated dimensional instability and cracking. Another problem is that even though conversion of the gel to a glass can be achieved at around 600 °C, a final hot-pressing step in the range 1250-1700 °C is required to consolidate the matrix and/or bring about matrix crystallisation [51].

Sol-gel techniques have been used to modify the slurry infiltration process outlined in section 1.2.4.b. Hegeler and Brückner [95] used an alkoxide sol as a carrier for glass powders (replacing the conventional water or alcohol) and succeeded in removing contamination introduced by organic binders. This modification to the slurry method has the additional advantage that the matrix composition may be adjusted by using mixed alkoxides [96]. Jamet *et al* [97] report that gel shrinkage may be reduced through the addition of solid particles into the sol; essentially, a small volume fraction of gel is used to bind together larger particles of the same or different material. Cornie *et al* [53], in their review of ceramic-matrix composite processing, make the point that the large matrix shrinkage which follows gelation may be exploited to attain higher fibre volume fractions once densification has been achieved.

1.4 FREEZE-GELATION

1.4.1 Introduction

A colloidal silica sol may be converted to a macroporous gel by rapidly cooling to subzero temperatures. The steps involved in this process, labelled ***freeze-gelation***, are represented schematically in figure 1.13. The ice crystals which form during freezing occupy slightly more volume than the parent water; the density of ice at 0 °C is 0.92 gcm^{-3} compared to liquid water's 1.00 gcm^{-3}, and this gives an expansion on freezing of ~ 8 volume%. Colloidal particles are consequently forced into close proximity in the channels between growing ice crystals, and readily aggregate. The structure of the aggregated colloidal particles is retained as gentle warming of the frozen gel thaws the ice crystals and subsequently expels free water. Very little change in overall dimensions occurs during freeze-gelation and subsequent thawing and drying; overall volume shrinkage levels are typically well below 1 %. The resulting green body is readily handled and machined. Residual porosity levels are usually in the range 0.4-0.6 (volume fraction), the pore structure in the dry gel corresponding to the pattern of ice crystal growth during the freeze-gelation step. The pores are large (*e.g.* up to ~ 50 μm) and open, presenting the possibility of achieving at least partial densification by gas- or liquid-phase infiltration.

Filler particles and short- and continuous-fibre reinforcements may be incorporated into the colloidal sol prior to freeze-gelation, offering a route to novel composite materials. A SERC ACME research project directed at evaluating how sol-gel technologies might be exploited in the fabrication of ceramic-matrix composites identified and subsequently focussed exclusively on the freeze-gelation approach. The objectives of this project are described in the following section. Parallel to this work was a PhD project [98,99], aspects of which are discussed in section 1.4.3, which investigated the physics of freeze-gelation and how the technique might be extended to colloid systems other than silica.

The ACME project established many "rules of thumb" in terms of materials and processing parameters [100-103]. These are reviewed in section 1.4.4 and form the ground rules upon which the filament winding route to continuous fibre-reinforced ceramic-matrix composites, explored in this thesis, is based.

1.4.2 Bath ACME project

The lack of broad success in exploiting sol-gel methods for the fabrication of glass- and ceramic-matrix composites has been discussed in previous sections (1.1.3.c and 1.3.7), and the technical problems which need to be overcome have been highlighted. A three year project at Bath University [103] was conceived to investigate how established composite-forming methods widely used in the polymer-matrix composites industry could be modified to accomodate sol-gel routes to ceramic-matrix composites. The analogy between the curing of thermoset resins and the gelation of sols (either colloidal or macromolecular) was believed to offer the prospect of using filament winding, pultrusion, resin-transfer moulding (RTM) and injection moulding to achieve a variety of complex, ceramic shapes containing either continuous or discontinuous fibres.

In contrast to the almost universal motivation for research into ceramic-matrix composites, the ACME project was not focussed on materials and components which can fulfil the demanding high-temperature, high-performance requirements for aerospace applications. Rather, the target applications were those where intermediate property levels would suffice, *e.g.* tubes, pipes, seals and diaphragms for the chemical industry. In addition to *useful* mechanical properties (especially toughness), such components require thermal stability and resistance to oxidation and chemical degradation, abrasion and wear at moderate temperatures (*e.g.* up to 500 °C). Low cost, low processing temperatures and flexibility in the range of shapes which could be produced were other criteria upon which the acceptance of any emergent techniques would depend. A secondary advantage of not aiming for

high-temperature aerospace applications is that a wider variety of fibres is available (many current fibres are degraded during manufacture or service at elevated temperatures). This may also lead to more consistent and predictable composite properties.

The key aims of the project were to:

- Produce fibre-reinforced ceramic components cheaply and to near-net-shape;
- Apply conventional composite-manufacturing technology to sol-gel-derived composites;
- Overcome the shrinkage problems associated with sol-gel processing;
- Identify useful fibre/matrix systems and;
- Construct a database of the relationships between measured properties, fibre and matrix types, and processing conditions.

Freeze-gelation of colloidal silica sols was identified at an early stage in the project as a method of producing near-net-shape silica-based bodies into which continuous or discontinuous fibres could be incorporated. The project aims were therefore refined when it was decided to concentrate exclusively on the freeze-gelation route.

1.4.3 The physics of freeze-gelation

In contrast to the enormous literature pertaining to conventional sol-gel science and technology, surprisingly little work has been published on sol-gel techniques which employ rapid freezing to cause gelation. An early patent [104] described how a colloidal silica sol which contained a large-particle-size filler could be poured into a mould, frozen and thawed to give a low-shrinkage, crack-free gel. Despite the apparent advantages of such an approach, no references to the subject could be found in the literature after this.

Laurie [98, 99] conducted an in-depth examination into the factors which control the freeze-gelation of colloidal silica sols. The examination of a series of unfilled and filled sols permitted the identification of materials and processing parameters which are critical to the efficacy of the freeze-gelation process. Briefly, these may be summarised thus:

colloidal silica sol

- must contain unaggregated silica particles
- minimum concentration is 20 wt%

filler particles

- should be inert
- particle size should be > 1 μm
- low-particle-size fillers promote large macropores in the dried gels
- unfilled gels exhibit very little shrinkage but have near-zero mechanical strength

freeze-gelation

- the entire structure should be frozen to (and held frozen at) -30 °C or below
- frozen gels should be thawed slowly

The expansion of of water on freezing is approximately 8 volume% (the density of the liquid is 1.00 kg m^{-3}, *cf* 0.92 kg m^{-3} for that of ice). The physical properties of water and ice are have been reviewed by Fletcher [105] and Franks [106]. During freeze-gelation, the nucleation and growth of ice crystals causes the liquid fraction of the colloidal silica sol to become more concentrated. Laurie proposes that unaggregated silica particles adopt a close-packed configuration between the growing ice crystals and that this structure is either retained or compressed by further growth. The forced, intimate contact of the silica particles provides an opportunity for interparticle bonds to form. These bonds result in a stable gel which undergoes minimal shrinkage (and cracking) when thawed and dried. Clearly, aggregated silica sols cannot form a close-packed structure and this is used by Laurie to explain why such sols will not freeze-gel but rather form a conventional gel which shrinks markedly during drying.

In broader terms, there are two principal requirements for a sol to be amenable to freeze-gelation: (i) that a close-packed structure be formed during the freeze-gelation step and (ii) that bonding occurs between the sol particles whilst the structure is frozen. Laurie

demonstrated successfully that these principles could be applied to non-silica systems by preparing small samples of zirconia gels by freeze-gelation.

1.4.4 Fabrication of ceramic-matrix composites by freeze-gelation

Figure 1.14 outlines how the freeze-gelation process may be employed in the fabrication of ceramic-matrix composite shapes. Throughout the ACME project, the principal shaping methods used for short-fibre- and continuous-fibre-reinforced materials were casting and filament winding respectively. Other possible techniques which were investigated during the early stages of the project include sol transfer moulding (an analogue of RTM used in manufacturing polymer-matrix composites) and hand layup.

Several variables which affect the processability, microstructures and properties of freeze-gelled composites may be identified. These may be classified as those associated with:

- composition (colloidal silica sol, matrix fillers and fibres);
- the shaping process and;
- processing parameters (gelation, sintering, infiltration and densification).

These are now discussed in turn. It will become apparent that changes in one or more of these variables may lead to beneficial and disadvantageous effects simultaneously. Moreover, parameters may be interdependent and possibly act synergistically. Optimisation of each matrix/filler/fibre system is therefore considered to be the most appropriate approach.

The casting route to short-fibre-reinforced composites was an effective, practicable method of screening different materials and processing variables. It frequently provided the background data and experience upon which the development of the filament winding route described in this thesis was built. The mechanical properties of such systems and their relation to microstructural features will be outlined in section 1.4.4.g.

1.4.4.a Colloidal silica sol

Investigations into the effects of colloidal particle diameter and weight fraction, which are considered to be the principal colloid variables, on the processability of freeze-gelled materials have permitted the identification of several rules of thumb. The minimum volume fraction of colloidal silica particles in the sol mixture which is necessary for freeze-gelation to occur is ~ 0.05. At such low volume fractions, the silica sol may be considered to act more as a processing aid, holding filler particles and short fibres together in the green state, than as a principal matrix component. Sols containing a high fraction of SiO_2 can accommodate relatively low amounts of filler and reinforcing fibres. Such sols also exhibit low initial gel viscosities and require lower volume fraction additions of filler particles or short fibres to retain the gel structure on drying. Not surprisingly, gels derived from sols which have small primary particle sizes are more reactive than those obtained from higher particle size sols and can generally be sintered at lower temperatures.

1.4.4.b Filler particles and short fibres

Filler particles are incorporated into freeze-gelled materials because (1) they are required for the freeze-gelation process to be successful in certain cases; (2) they provide a method of controlling the composition and mechanical properties of the composite matrix; and (3) the addition of short fibres offers the prospect of stiffening, strengthening and toughening the matrices (*i.e.* achieving a composite effect). The main variables which concern filler particles are type (*i.e.* chemistry), size and shape, and weight fraction, and these have been characterised and, to some extent, optimised for several systems.

The addition of filler particles to the sol leads to an increase in sol viscosity. Particles of small diameter have a greater effect than larger-diameter particles. A more marked increase in sol viscosity occurs when fibres are added and this has the effect of restricting the range of fibre lengths and fibre volume fractions which can be accommodated. Even when dispersants,

high-shear blenders and wetting agents are used, the highest fibre volume fraction which has been achieved is ~ 0.30. Care should also be taken to ensure that shear-blending does not cause fibre damage. "Clumping" of fibres is frequently encountered when fibre lengths exceed ~ 0.5 mm.

Shaping operations become difficult when the viscosity of the sol mixture becomes too high. Also, localised aggregation of the silica sol sometimes occurs, although it is not known whether this is due to steric effects (colloid particles being forced together by the high volumes of fillers and fibres) or to chemical destabilisation of the sol. Small filler particles are more stable in suspension than coarser ones, and would be expected to pass more freely between reinforcing fibres and be distributed more homogeneously in the final product. Very fine particles (*e.g.* fumed silica) exhibit a tendency to aggregate and are therefore difficult to disperse.

In contrast to these drawbacks, there are many advantages in maximising the volume fractions of filler particles and fibres in the sol mixture. Shrinkage levels are reduced to typically < 3 volume% and dimensional stability is correspondingly improved. Initial porosity levels are reduced, leading to enhanced final densities. The presence of even small quantities of fibres significantly ameliorates the strength and handleability of delicate shapes in the green state - the fibres effectively act as a processing aid in this case. Finally, increases in fibre and filler contents are generally reflected in the improved mechnical performance of the final components.

A wide variety of filler particles has been assessed. Some types (*e.g.* china clay) destabilise the silica sols and so are unsuitable. One can distinguish between ***reactive*** fillers, typically glasses or glass-ceramics which act as sintering aids, and ***non-reactive*** fillers, refractory ceramics *e.g.* silica, alumina. Reactive fillers were found to cause strong bonding between oxide fibres such as FP (alumina) and Nextel (mullite) and the sol-gel matrix, leading to weak, brittle composites.

By contrast, a lithium-alumino-silicate glass-ceramic filler was found to improve the interlaminar shear strength and flexural strength of unidirectional carbon-fibre-reinforced materials fabricated by hand layup. This is shown in the flexural stress/strain curves in figure 1.15; further data are summarised in table 1.6.

1.4.4.c Shaping

Casting provides a relatively quick and efficient way of screening different sol/filler/fibre combinations and examining the effects of different fabrication conditions. Metallic moulds are appropriate since they provide the necessary high heat-transfer rates. Gel strength is highest in its frozen state and at its minimum when wet (*i.e.* thawed but prior to drying), so demoulding is performed when frozen wherever practicable. The demoulding operation may be aided by incorporating draft angles in moulds and by the use of lubricating mould-release agents *e.g.* PTFE spray. Sharp changes in section and geometry are generally to be avoided since shrinkage cracking can occur in such areas, although the risk of this is minimised when short fibres are incorporated. Moulding becomes difficult when the addition of too much filler and fibre causes the viscosity of the sol mixture to become impracticably high.

1.4.4.d Gelation

Liquid nitrogen was found to be a suitably cheap, available and convenient refrigerant for inducing freeze-gelation of silica sols. The minimum freezing régime, determined empirically, is to cool rapidly to below -20 °C, hold for 20 min, demould, thaw to ambient temperature and dry. Rapid freezing also has the advantage of minimising the time available for fillers and fibres to settle. An increase in the period for which the gel is held frozen gives more opportunity for the colloidal silica particles to aggregate, and so enhances the stability of the gel.

If one recalls that the pores in green freeze-gelled samples are essentially those regions where ice crystals grew during the freeze-gelation process, then it could be predicted that the magnitude and direction of temperature gradients would control the final porosity patterns.

Work on cast systems has shown that two principal types of porosity exist: fine, equiaxed pores at the surface of samples give way to coarser, columnar porosity in the centre of samples in a direct analogy with the grain patterns observed in chill-cast metals; typical pore size ranges were 2-10 μm and 5-25 μm respectively. An important ramification of this is that even though thick sections can be successfully freeze-gelled (*e.g.* solid, cylindrical rods of diameter 150 mm have been cast), pore microstructure is non-uniform from sample edge to centre; in this respect, freeze-gelled materials may be considered to be functionally-graded structures.

1.4.4.e Sintering

The principal rôle of sintering is to achieve densification of the sol-gel-derived silica matrix. This may be assisted by fillers which act as sintering aids (*e.g.* glasses and glass-ceramics). As sintering temperature is raised, the porosity coarsens, and the possibility of chemical reactions between different components (particularly between fibres and matrix) increases. Differential thermal stresses may be important, particularly if these cannot be relieved as the sample cools. There also exists the possibility that the amorphous silica matrix may undergo crystallisation (once it is densified) and also that filler particles may undergo phase changes.

Experience with cast, short-fibre-reinforced composites has shown that compromises need to be reached between the conflicting requirements of a high sintering temperature for densification and a low sintering temperature to avoid undesirable chemical reactions, and also that each system needs to be evaluated individually. Appropriate sintering temperatures usually fall in the range 700-1300 °C. The economic advantage of sintering at low temperatures should also be considered.

The coarsening of inherent porosity which is encouraged at high sintering temperatures is believed to improve the efficiency of subsequent liquid-phase infiltration processes. A secondary, low-temperature sinter after liquid-phase infiltration (at ~ 500 °C) may be used to densify the infiltrant.

1.4.4.f Infiltration and densification

The coarse, open porosity in green, freeze-gelled materials occupies volume fractions typically in the range 0.40-0.60, and this presents the possibility of liquid- or gas-phase infiltration to try and attain a fully-dense matrix. Gas-phase routes were considered to be too expensive for consideration in a project directed at the fabrication of low-cost ceramic-matrix composites, and so attention was restricted to liquid-phase routes.

The most effective liquid-phase infiltrants were found to be colloidal sols having small particle sizes (*e.g.* 7 nm); figure 1.16 illustrates the gradual improvements in specimen density which were achieved as a Nextel fibre-reinforced, alumina-filled composite ring fabricated by filament winding was repeatedly infiltrated with both colloidal and macromolecular sols. Infiltration is aided by applying a small vacuum prior to infiltration and a small positive pressure after infiltration. Experience with short-fibre-reinforced systems suggests that, typically, 5-7 infiltrations are required to reach 80% of theoretical density. Infiltration whilst in the green state improves the machinability and handleability of green components, although the highest final densities are achieved when samples are infiltrated after the principal sintering.

1.4.4.g Properties of short fibre-reinforced composites

Table 1.7 presents basic mechanical property data for several short-fibre-reinforced composites prepared by casting. As would be expected, these data show a strong dependency on porosity. Figure 1.17(a) shows the variation of dynamic modulus with porosity volume fraction, and the data are satisfactorily described by an exponential decay law. Matrix composition exhibits no discernible influence on these data; the different symbols refer to different matrix compositions (not identified) and all lie on the same curve. A similar trend is seen (figure 1.17(b)) for the composite compression strength measured by loading small cubes of 10mm x 10mm x 10 mm. Residual porosity (volume fraction) of these materials is typically in the range 0.25-0.30 volume fraction.

Chapter 2

AIMS AND STRUCTURE OF THIS THESIS

The principal objective of the work described in this thesis was to exploit the freeze-gelation concept and develop a processing route to continuous-fibre-reinforced, silica-based composites. The work described here builds on the knowledge and experience gained during a previous project which investigated the effects of materials and fabrication parameters on the freeze-gelation of short-fibre-reinforced composite systems (this was reviewed in section 1.4.4). Throughout this work, an effort was made to understand the effects of processing parameters on the development of composite microstructures, and hence on mechanical performance.

For ease of assimilation, the work is divded into two chapters. Chapter 3 describes the development of a filament winding route to composites which comprised carbon fibres in a silica-based matrix. The effects of different matrix fillers and sintering temperatures on the development of composite microstructure were examined, and these conclusions then used to explain differences in mechanical (flexural) properties and fracture mechanisms.

Chapter 4 forms the majority of this thesis. The filament winding process was refined to overcome several of the inadequacies described in chapter 3, and employed successfully to prepare a series of composites with both filled and unfilled silica matrices and a range of fibre volume fractions. A lithium-aluminosilicate (β-spodumene) glass-ceramic filler was selected on the basis of its low thermal expansivity. Analysis of the composites' microstructures was followed by a comprehensive program of mechanical testing; this included flexural and tensile tests, toughness measurements, acoustic emission monitoring and fractography.

The objectives of this thesis are now defined more explicitly; they were to:

(a) Develop a filament winding / freeze-gelation route to silica-matrix composites;

(b) Determine the effects of:

i) Silica sol characteristics

- *particle size*

ii) Matrix filler

- *composition*
- *volume fraction incorporated*

iii) Processing parameters

- *sintering temperature*
- *liquid-phase infiltration conditions*

on

i) Processability

- *Ease and success of filament winding*

ii) Microstructure

- *Nanometre- and micrometre-scale porosity*
- *Crystallography of matrix phases*

iii) Mechanical performance

- *Flexural (including interlaminar shear and un-notched Charpy)*
- *Tensile (including transverse strain)*
- *Toughness (including work of fracture and notch-sensitivity)*
- *Damage mechanisms*

iv) Reproducibility of mechanical and microstructural properties

- *Batch-to-batch variability*
- *Consistency within a single batch*

Additionally, answers were sought to the following questions:

- Do the microstructural analysis data offer insights into the freeze-gelation process?
- Do conventional models of composite behaviour apply to freeze-gelled composites?
- Are freeze-gelled composites useful engineering materials?

Chapter 3

DEVELOPMENT OF A FILAMENT-WINDING ROUTE TO CARBON-FIBRE-REINFORCED, SiO_2-BASED COMPOSITES USING FREEZE-GELATION

3.1 INTRODUCTION AND OBJECTIVES

Section 1.4.4 reviewed the materials and fabrication parameters which affect the freeze-gelation of short-fibre-reinforced, ceramic-matrix composites. The principal goal of the work described in this chapter was to apply this knowledge and experience to the development of a filament winding/freeze-gelation route to continuous-fibre, unidirectional composites.

The colloidal silica sols employed in this study were from Monsanto's Ludox ® range (described earlier in table 1.4). HT50 contains 50% by weight of colloidal silica having a quoted particle size of 125 nm, although there is some evidence [108] that a range of particle sizes down to 50 nm is present. X30 sols contain 30 weight% of 25 nm particles. The appearances of these sols may be seen from figure 3.1.

Carbon fibres (Toray T300) were selected as the composite reinforcement on the basis of their (i) good mechanical properties and (ii) relatively low cost. Because carbon fibres exhibit a near-zero axial thermal expansion coefficient, conventional wisdom would dictate that suitable matrix materials should have a zero or negative thermal expansion coefficient in order to avoid the risk of generating tensile stresses and hence microcracking within the matrix (see section 1.2.2). However, since freeze-gelation produces highly porous materials which are subsequently infiltrated, the generation of cracks within a matrix of relatively high thermal expansion coefficient may assist the liquid-phase infiltration process. In this respect,

therefore, the choice of matrix fillers in freeze-gelled composites is not restricted by considerations of thermal expansion effects.

In the light of these comments and of the experience gained with short-fibre-reinforced composites (described in section 1.4.4), three different matrix filler systems were selected. These are summarised in table 3.1.

The matrix in composite samples designated 'HQ' consisted of HT50 silica sol to which had been added quartz filler particles. In the case of series 'XQ' samples, a mixture of quartz particles and amorphous silica particles of nominal mean particle size 2 μm were added to X30 silica sol; the intended function of this filler was to increase the yield of solid material on freeze-gelation. For the third series, 'HC', the HT50 sol was used with a mixture of amorphous silica and CMA6 glass-ceramic particles. The CMA6 glass-ceramic has a composition corresponding nominally to that of cordierite, $5SiO_2$-$2Al_2O_3$-2MgO, + CaO. The principal sintering temperature for these samples was varied between 500 °C and 1400 °C.

Briefly, these series of composites were designed to permit examination of the effects of matrix composition, colloidal silica particle size and sintering temperature on the following:

- Microstructure development
  - *Porosity patterns*
  - *Matrix densification and possible subsequent crystallisation*
  - *Fibre-matrix interfacial reactions*
- Mechanical properties
  - *Flexural response*
  - *SEM of fracture surfaces to investigate failure mechanisms*

3.2 EXPERIMENTAL METHODS

3.2.1 Fabrication of composite samples

The composites were prepared by the filament-winding route outlined in figure 3.2. Fibre tows (Toray T300) were passed through a desizing furnace at 750 °C and then through a bath containing an agitated mixture of colloidal silica and filler particles. A hollow, hexagonal mandrel of width 100 mm, constructed from 1 mm aluminium sheet, had been cleaned and sprayed with PTFE mould-release agent. The impregnated fibres were wound onto this mandrel until a sufficient composite thickness had been built up. The mandrel, sol bath and roller assemblies were installed on a lathe which had been modified appropriately. The tension on the fibre tows was controlled by adjusting the winding speed and the relative positions of the roller guides. A winding speed of 8 rpm was found to be satisfactory; this gave a tow width of ~ 1 mm and was fast enough to avoid premature drying/gelation of the colloidal silica sol.

When the winding operation was complete, the mandrel was removed, held vertically and liquid nitrogen poured into its hollow interior to cause freeze-gelation of the matrix. The assembly was kept frozen until the six composite plates were cut from the mandrel with a scalpel. The plates were then thawed at room temperature, gently dried at 60 °C and infiltrated three times with a 7 nm/30 wt% colloidal silica sol. At the beginning of each cycle the infiltration vessel was partially evacuated in order to remove at least some air from the porous plates and so ease the passage of the liquid infiltrant into the pores. The liquid infiltrant was introduced into the vessel and a positive pressure applied, once again in order to assist the efficiency of the infiltration process. The specimens were dried at room temperature after each infiltration.

After having been cut into strips of width 10 mm with a water-cooled diamond saw, the specimens were sintered in an argon atmosphere at 600 °C for 1 hour. Following subjection

to a further 5 infiltration cycles, batches of specimens were finally sintered in argon at temperatures of 600 °C, 750 °C, 900 °C, 1100 °C and 1400 °C. Table 3.2 summarises the gelation, infiltration and sintering conditions used for each matrix composition.

3.2.2 Microstructural analysis

3.2.2.a Microscopy

A low-feed-rate, water-cooled diamond saw was used to cut specimens for microstructural investigation following the plan shown in figure 3.3. Specimens for microscopy were sectioned according to the orientations described in figure 3.4 and subsequently mounted in a cold-curing epoxy resin ('Epofix', manufactured by Buehler). In order to assist the penetration of the mounting resin, the specimens were evacuated, infiltrated with resin and then cured for 18 hours at 50 °C under a slight positive pressure. The mounted samples were ground flat and planar on 240 grit silicon carbide paper, and polished with progressively finer oil-based diamond suspensions down to a nominal 0.05 μm finish. More details of the polishing routines developed are summarised in table 3.3. Particular care was taken to clean the samples ultrasonically between each stage to prevent coarse abrasives from damaging prepared surfaces during subsequent, finer polishing stages.

Optical microscopy was carried out in reflected light with Bright Field (BF), Nomarski Differential Interference Contrast (DIC) and Dark Field (DF) imaging modes on a Zeiss ICM 405 microscope. An image analysis system (Optimas 4.0) was used to quantify observed microstructural features, particularly porosity and fibre volume fraction (the principles of image analysis and the application of the technique to composite materials have been discussed elsewhere [*e.g.* see 109]). The samples were later sputtered with gold in an Edwards S105B sputter coater for between 3 and 8 minutes at $1.5 \cdot 10^{-5}$ bar for analysis by Scanning Electron Microscopy (SEM). A JEOL JSM 35C equipped with a LINK AN10000

energy-dispersive x-ray spectrometry (EDS) system and operating at 15 kV was used to examine these specimens. Where EDS was not required, a JEOL T330 was used.

Specimens for transmission electron microscopy (TEM) were prepared by carefully preparing thin (~ 1 mm) slices in orientation 'C' (figure 3.4) from which 3 mm discs could be cut with a hollow, diamond-tipped drill. The discs were then mechanically ground to a thickness of ~ 300 μm, ultrasonically cleaned, and dimpled to leave a central region 10-50 μm thick. The geometry of the dimpled specimens from which the thickness of the central region may be determined is described in figure 3.5. Thinning with argon ion bombardment was then carried out in a Gatan Duomill until specimen perforation occurred. TEM analysis was performed in a JEOL 2000FX operating at 200 kV. This instrument was also equipped with an EDS system.

Samples of desized T300 carbon fibre and small pieces of each composite were prepared for x-ray diffraction (XRD) analysis by grinding with a pestle and mortar. A Philips 1820 diffractometer employing a Cu Kα radiation source was used. Raw data (variation of intensity with diffraction angle) were imported into a PC spreadsheet package for manipulation and comparison with published patterns.

3.2.2.b Determination of density and porosity volume fraction

Composite density and porosity volume fraction were determined by a standard water-immersion technique [110]. Specimens measuring ~ 4 x 10 x 50 mm^3 were dried for 48 hours at 80 °C and weighed to give a dry mass, M_{dry}. The specimens were then saturated with water; a light vacuum was used to remove at least some air from the pores, the specimens were placed in a pressure vessel containing distilled water and a slight positive pressure applied to assist the penetration of the water into the pores. The water-saturated specimens were weighed whilst suspended in water ($M_{sat./water}$) and, after surface water

droplets had been wiped from their surfaces, whilst suspended in air ($M_{sat./air}$). Bulk density and apparent porosity volume fraction were then calculated from the relations:

Bulk density: $$\rho_{bulk} = \frac{M_{dry}}{M_{sat./air} - M_{sat./water}}$$ Equation 3.1

Porosity: $$V_{porosity} = \frac{M_{sat./air} - M_{dry}}{M_{sat./air} - M_{sat./water}} \cdot 100\%$$ Equation 3.2

Note that these porosity measurements accomodate only open pores which have been successfully infiltrated with water; the results are therefore lower-bound estimates of the true porosity.

Bulk density was also determined via basic volume and mass measurements. Specimens ~ 4 x 10 x 50 mm^3 were ground flat and square, measured using a micrometer and weighed.

3.2.2.c Determination of fibre volume fraction

Two approaches were employed. Image analysis was successful when the quality of microscopic images was such that fibres could be assigned exclusive greyscale ranges. However, it will be shown later that the highly-porous nature of the composites meant that fibres were frequently "obscured" by pores and could not, therefore, be polished or categorised reliably by their greyscale. Measurement of porosity content using image analysis was subject to similar problems.

Pyrolysis of the carbon fibres was considered to be a more reliable approach to obtaining V_f values. Specimens were weighed before and after heating in a furnace at 600 °C for 48 hours. Fibre volume fraction could then be determined from:

$$V_f = \frac{\Delta M \rho_{bulk}}{M_{initial} \rho_{fibre}}$$ Equation 3.3

where $M_{initial}$ is the original mass of the specimen, ΔM is the mass loss after pyrolysis, ρ_{fibre} is the fibre density and ρ_{bulk} is the bulk composite density. Microscopy of selected pyrolysed specimens confirmed that all the carbon fibres had been removed by oxidation.

3.2.2.d *Examination of filler particles*

SEM specimens were prepared by sprinkling a minute quantity of the filler particles over a planchette which had been coated with a carbon-based adhesive. Once the adhesive had dried, loose particles were shaken off and the specimens were gold-coated by sputtering. The specimens were placed in a low-vacuum chamber overnight in order to minimise the risk of particles becoming detached during analysis and contaminating the SEM chamber. SEM analysis was generally carried out at low (*e.g.* 7 kV) accelerating voltages in order to avoid charging effects.

Specimens were examined in the TEM while supported on carbon-coated copper grids. Thin films of carbon were deposited onto clean glass microscope slides by discharging a high voltage through a carbon filament in a vacuum unit. The carbon films were then transferred onto the surface of distilled water by gently floating the films off the glass slides. Fine (300 square mesh) copper grids could then be passed gently through the carbon films floating on the water's surface, and the carbon-coated copper grids then left to dry. Dilute supsensions of filler particles in distilled water were prepared by ultrasonic agitation, and small drops pipetted onto the carbon-coated copper grids and left to dry.

Filler particles in the as-received condition could be examined immediately by x-ray diffraction since they were already in powder form. Additionally, samples of the CMA6 glass-ceramic filler were cerammed at temperatures between 600 °C and 1400 °C (*i.e.* corresponding to the sintering temperatures of the composites), ground to a powder and analysed by XRD.

3.2.3 Mechanical property characterisation

Flexural (three-point bend) testing was performed on an Instron 1195 at a span of 80 mm (giving a span-to-depth ratio of between 25 and 35). All data were acquired by a digital data acquisition system for storage and subsequent analysis. Details of this system and of the software developed to analyse the data, including corrections for the compliance of the test machine, are discussed in more depth in section 4.2.3. The equations used to calculate stress and nominal strain at peak load, and elastic modulus are summarised thus:

Flexural strength: $$\sigma_{flex} = \frac{3F^{*}s}{2wt^{2}}$$ Equation 3.4

Strain at peak load: $$\varepsilon^{*} = \frac{6t\Delta^{*}}{s^{2}}$$ Equation 3.5

Elastic modulus: $$E = \left(\frac{F}{\Delta}\right)\frac{s^{3}}{4wt^{3}}$$ Equation 3.6

where F^{*} is the peak value of applied load, Δ^{*} is the mid-span displacement at peak load, w and t are specimen width and thickness respectively, and s is the loading span. The slope of the initial, linear region of each force-displacement curve, (F/Δ), was calculated by a linear regession method. Integrated force-displacement curves were divided by 2 x specimen cross-sectional area to give Work of Fracture (WOF)-type results. The methods used to analyse mechanical property data are described in more depth in section 4.2.3.v.

Fracture surfaces were examined in the SEM after having been coated with gold in a sputter coater. In order to minimise the risk of contaminating the SEM chamber and also to reduce the time taken for each specimen changeover, the porous specimens were kept under a high vacuum overnight before being introduced to the SEM.

Flexural test specimens were prepared also for optical microscopy and, later, gold-sputtering and examination in the SEM. The damaged regions of the specimens were mounted in Epofix blocks measuring ~ 80mm x 25mm x 30 mm, as shown in figure 3.6, by the routine described

in section 3.2.2.a. The specimens were examined in orientations 'b' and 'c' (in the notation of figure 3.4). The mounted specimens were held in a purpose-built jig and polished as described earlier. By grinding to different depths, both the exterior and interior regions of the specimens could be investigated.

Dynamic elastic moduli were determined by a time-of-flight method [111]. The ends of specimens were ground flat, and the time taken for a 150 kHz pulse to travel the length of each specimen was measured with an electronic detection system [112]. The shortest measured time was recorded. Petroleum jelly was used as the coupling agent between the specimens and the send/receive transducers. From the wave speeds, c, and the specimen densities, ρ_{bulk}, nominal values of longitudinal dynamic elastic modulus, E_{dyn}, were calculated from the relationship:

$$E_{dyn} = c^2 \rho_{bulk} \qquad \text{Equation 3.7}$$

3.3 RESULTS

3.3.1 Observations on fabrication

The preparation of an evenly dispersed colloidal silica sol/filler particle mixture required a mixing time in excess of five hours for each of the compositions considered. The sol mixtures were initially moderately fluid but their viscosities increased markedly with time. Also, larger filler particles showed a tendency to settle in the sol bath after several minutes.

The thixotropy of the sol mixtures adversely affected the filament winding process. The sol frequently formed a gelatinous film on the sol bath's rollers and caused the tension in the fibre tows to vary. The fibre tows broke several times during winding. The tension on the fibre tows had to be kept quite high to pull the tows through the viscous sol mixture, resulting in a lack of infiltration of the sol mixture into the fibre tows. The fibres were seen also to remain in their tows on the mandrel.

The composite samples were non-planar and of non-uniform thickness, as may be seen from figure 3.7. This rendered the specimens unsuitable for the determination of reliable mechanical property data, and tensile testing was certainly not a viable option. Three-point bend (flexure) testing was therefore used to characterise the mechanical responses of the specimens (in contrast to providing definitive property data), giving an indication of elastic modulus, of strength and of 'toughness'.

3.3.2 Microstructural analysis

The most prominent microstructural feature of all the composite samples investigated was a complex pattern of highly directional porosity which became less clearly defined as the sintering temperature was raised. Figures 3.8 to 3.10 present montages of optical micrographs which show the through-thickness microstructures of 'HC' series samples sintered at 750 °C, 900 °C and 1400 °C respectively. Similar features were observed in the

'HQ' and 'XQ' composite systems. The sample sintered at 750 °C shows several discrete layers across the width of a sample. Commencing from the surface where freeze gelation began (top of figure 3.8), one sees a fibre-free, dense layer at the outer surface, below which is a region of coarse, highly directional porosity. This porosity, of the order of ~ 30-60 μm in width, appears to follow the direction of heat flow during the freeze gelation process and resembles closely the columnar crystallisation patterns observed in chilled metallic ingots. This columnar porosity was observed in both planes perpendicular to the fibres (*i.e.* planes b and c in the notation of figure 3.4). There is then a reasonably well-densified region, and a region of fine, dendritic-like porosity in the centre where volume fractions of porosity of over 50% have been measured by image analysis.

Samples sintered beyond 750°C, figures 3.9 and 3.10, do not show this layered porosity to the same extent, although the directionality of the columnar-like porosity is still evident. As a general trend, an increase in sintering temperature led to a decrease in the overall degree of porosity and to a slightly enhanced degree of matrix densification near to the specimen surfaces, although no explicit relationship between degree of porosity and sintering temperature was established. The variations of bulk density and porosity volume fractions with matrix composition for the three composite systems considered are given in figure 3.11 and table 3.4.

Dark-field illumination in the optical microscope revealed the pores to have a crystalline texture, and more readily distinguished between the denser (darker) and more porous (lighter) regions of the specimens (*e.g.* figure 3.12). SEM analysis (figure 3.13) showed that the 'columnar' pores described above are in fact plates of porosity running in the direction of the specimen thickness (*i.e.* plane b, figure 3.4). The pore structures were frequently more complicated than the picture presented here. During SEM analysis the pores often charged up and 'glared', thus providing an effective means of viewing pore orientations and sizes as

shown in figure 3.14. The orientations of the pores were often variable, reflecting fluctuations in thermal gradients which influenced the growth of ice crsytals during freeze-gelation.

Fibre distribution was non-uniform in all samples. The variations seen between individual samples made it difficult to draw definite conclusions, but generally the fibres were better dispersed in the denser matrix regions, typically nearer to the edges of specimens (figure 3.15). Fibres were often seen bundled in their original tows, frequently on the plane adjacent to a particularly porous region. Measured fibre volume fraction was ~ 0.12 for all samples (table 3.4).

Liquid-phase infiltration of the residual porosity by a fine particle size colloidal silica sol was only partly successful. Figure 3.10 shows that the infiltrant reached a depth of ~ 500 μm, and SEM studies of the infiltrated regions of the composites revealed that the infiltrant had often shrunk during drying (figure 3.16) leading frequently to poor contact between fibres and infiltrant. TEM analysis indicated that the colloidal infiltrant particles were only partly fused with nanometre-scale, closed porosity appearing between the colloidal particles (figure 3.17).

Matrix cracks arising from residual stresses were observed at all sintering temperatures, and these tended to reach the specimen surface via dense matrix regions. Regularly-spaced transverse cracks were seen in dense, internal matrix layers (figures 3.18 and 3.19), although their presence was obscured frequently and interrupted by porosity. The spacing of these cracks in all three composite systems ranged from 1000 μm for samples sintered at 900 °C (figure 3.18) and below, to 200-400 μm for samples sintered at 1100 °C and above (figure 3.19). Matrix cracking around fibres was also seen in samples sintered at 1100 °C and 1400 °C; figure 3.20 shows typical cracking in a 'HQ' sample sintered at 1100 °C, the circumferential crack pattern being indicative of residual stresses arising from fibre/matrix thermal expansion mismatches.

These features were common to all the composite systems studied. The effects of matrix composition on the microstructure of each composite system will now be discussed in turn.

3.3.2.a 125 nm colloidal silica + amorphous silica/glass-ceramic fillers (Composite series 'HC')

XRD spectra from the ground powders of composites sintered at 750 °C, 1100 °C and 1400 °C are given in figure 3.21. Samples sintered between 600 °C and 900 °C appeared to be almost wholly amorphous, with no evidence of peaks attributable to crystalline material. Two crystalline phases were identified in samples sintered at 1100 °C and 1400 °C, namely anorthite ($CaO.Al_2O_3.2SiO_2$) and α-cristobalite (SiO_2). An increase in the sintering temperature from 1100 °C to 1400 °C led to a greater degree of crystallisation, indicated by the higher peaks, although the background trace indicates that the composite retained appreciable amounts of amorphous material.

SEM of polished samples revealed the multiphased nature of the composite matrix. Figure 3.22i is from a sample sintered at 900 °C. EDS indicated that the lighter particles (P1) and the sol-gel matrix consisted of silicon and oxygen (figure 3.22ii), whilst the darker particles (P2) contained silicon, oxygen, aluminum, magnesium, calcium and titanium (figure 3.22iii). After sintering at 1100 °C the large, interconnected porosity was still present, and many of the larger filler particles were cracked internally (figure 3.23).

Figure 3.24, a TEM micrograph from a sample sintered at 900 °C, shows a filler particle (labelled 'P') and a region of sol-gel-derived silica matrix ('M'). The sol-gel region consisted of agglomerated silica spheres up to 140 nm in diameter and many small pores of nanometre scale. Selected area diffraction (SAD) showed both phases to be amorphous and EDS indicated that silicon, oxygen, aluminium, magnesium, calcium and titanium were present in the filler and only silicon and oxygen in the sol-gel matrix. A second type of filler particle was found to be amorphous and to contain only silicon and oxygen.

After sintering at 1100 °C changes in the matrix were observed. SAD showed that the calcium- and magnesium-containing particles had become partially crystallised (figure 3.25),

to form a lath-like crystal phase. The sol-gel silica matrix and silica filler particles also appeared to have crystallised in some regions.

The interface between the carbon fibre and the surrounding matrix in the sample sintered at 1100 °C is shown in figure 3.26. Debonding was observed along the interface, indicating that the interfacial bond between the sol-gel region and the fibre was weak.

The as-received amorphous silica particles (figure 3.27) were approximately spherical and had sizes in the range 0.5-5 μm (estimated by SEM). The CMA6 filler particles were more irregularly shaped and had sizes up in the range 2-20 μm (figure 3.28). The fact that large CMA6 particles were not observed in the composites supports the observation that settling of the particles occurred in the sol bath during winding. XRD showed that as-received CMA6 particles were amorphous, and that the principal crystalline phase in CMA6 particles sintered at 1100 °C was cordierite (figure 3.29).

3.3.2.b 25 nm colloidal silica + amorphous silica/quartz fillers (Composite series 'XQ')

The XRD traces from powdered samples sintered at 750 °C and 1100 °C are given in figure 3.30. Samples sintered between 600 °C and 900 °C exhibited a series of crystalline peaks, identified as α-quartz, and some amorphous material. The composites sintered at 1100 °C and 1400 °C showed in addition a series of peaks which were identified as α-cristobalite, together with a corresponding reduction in the amorphous content and a decrease in the height of the quartz peaks.

SEM analysis revealed a non-uniform fibre distribution. In composites sintered between 600 °C and 900 °C, cracking in the sol-gel matrix and residual porosity were identified and filler particles were discernable (see figure 3.31, taken from a sample sintered at 900 °C). Sintering at 1100 °C changed the appearance of the microstructure (figure 3.32): filler particles were no longer distinguishable in the matrix, and the matrix itself was extensively

cracked in the fibre-free regions. Where fibre density was high, cracking was present but on a finer scale. EDS indicated the presence of silicon and oxygen in the matrix constituents.

TEM studies of the composite sintered at 900 °C showed that the originally spherical sol-gel silica particles began to form a fused network (figure 3.33). At lower magnifications (figure 3.34), quartz filler particles (Q) were seen, as well as regions where crystallisation of the matrix to α-cristobalite had commenced (C). This matrix crystallisation had proceeded to completion in the specimen sintered at 1100 °C, figure 3.35. In this micrograph a quartz filler particle (Q) is seen in a crystalline matrix (C). The filler particle exhibited strain bands and the matrix contained several twinned regions, both suggestive of residual strains within the material. The amorphous silica filler particles fused with the sol-gel silica matrix at sintering temperatures of 1100 °C and 1400 °C and are believed to have crystallised to α-cristobalite with the sol-gel silica matrix. Closed porosity of the order 0.1-2 μm in size was also visible in the matrix.

The as-received quartz filler particles were non-uniform in shape and particle sizes were in the approximate range 0.5-20 μm. As was the case with the CMA6 particles reported in the previous section, large quartz particles were not observed in the composites and are assumed to have settled out in the sol bath during winding.

3.3.2.c 125 nm colloidal silica + quartz filler (Composite series 'HQ')

Figure 3.36 presents XRD data for series 'HQ' samples sintered at 750 °C and 1100 °C. α-quartz was detected in all samples. Peaks attributable to α-cristobalite were detected in samples sintered at temperatures of 1100 °C and 1400 °C, although these were less intense than those recorded for the 'XQ' composites described earlier.

Microstructural details were very similar to those reported for the 'XQ' samples. Quartz filler particles were readily identified in samples sintered at 600 °C and 750 °C, but could be

distinguished only with difficulty when the sintering temperature reached 1100 °C. Nanometre-scale pores between colloidal silica particles were visible in the TEM (figure 3.37). Extensive matrix cracking was particularly prominent in fibre-free regions and in samples sintered at 1100 °C and 1400 °C. TEM analysis showed that the initially-amorphous sol-gel silica matrix crystallised to α-cristobalite at sintering temperatures of 1100 °C and 1400 °C.

3.3.3 Mechanical performance

Figures 3.38 to 3.40 summarise the flexural mechanical properties and dynamic moduli obtained for the HC, XQ and HQ composite samples, respectively. These show the variation of (a) flexural modulus, (b) dynamic modulus, (c) stress at proportional limit, (d) peak stress, (e) strain at peak stress and (f) work of fracture with sintering temperature. Error bars indicate 95% confidence levels; where no bars are shown, it may be assumed that the errors are of the same magnitude as the datum point markers. These data are also given in tables 3.5-3.7. Typical flexural force/displacement curves are presented in figures 3.41 (HC), 3.42 (XQ) and 3.43 (HQ). More detailed features of these mechanical test results are now discussed, followed by observations on the damage modes in these materials.

3.3.3.a 125 nm colloidal silica + amorphous silica/glass-ceramic fillers (Composite series 'HC')

Peak stress values were ~ 150 MPa for all sintering temperatures. The elastic modulus increased with sintering temperature, particularly beyond 900 °C, to reach a maximum value of 15 GPa (mechanical) or 20 GPa (dynamic). The difference between the dynamic moduli and the mechanically derived moduli became greater as sintering temperature was increased; the ratio between dynamic and flexural moduli, E_{dyn}:E_{mech}, was ~ 1.4. Work of fracture showed a sharp drop at a sintering temperature of 900 °C, falling from ~ 6 kJm^{-2} to ~ 2 kJm^{-2}.

This sudden reduction in toughness was reflected in the form of the force/displacement curves, figure 3.41.

3.3.3.b 25 nm colloidal silica + amorphous silica/quartz fillers (Composite series 'XQ')

Peak stress levels were ~ 200 MPa for samples sintered at 600 °C and 750 °C (figure 3.39) and decreased to ~ 100 MPa for samples sintered above 750 °C. The flexural modulus decreased gradually from ~ 18 GPa (600 °C sinter) to ~ 14 GPa for samples sintered at 1400 °C. Dynamic moduli were again consistently higher than the equivalent mechanical moduli, with E_{dyn}:E_{mech} varying between 1.2 and 1.4. With the exception of a possibly anomalous datum point at 750 °C, dynamic moduli decreased very gradually with increasing sintering temperature.

Work of fracture showed a very pronounced decrease beyond 750 °C, falling from ~ 8.5 kJm^{-2} to 1.5 kJm^{-2}. As with the HC composites, these trends were reflected in the form of the force/displacement curves (figure 3.42), and in the overall appearance of the fractured samples, *i.e.* minimal fibre pull-out for samples sintered at high temperatures and extensive fibre pull-out for samples sintered at lower temperatures.

3.3.3.c 125 nm colloidal silica + quartz filler (Composite series 'HQ')

Peak stress decreased from ~ 150 MPa to ~ 50 MPa as sintering temperature was increased from 600 °C to 1400 °C. Work of fracture decreased steadily as sintering temperature was increased, from 5.7 kJm^{-2} (600 °C) to 0.7 kJm^{-2} (1400 °C). This was also seen in the forms of the force/displacement curves (figure 3.43) and the fracture faces. Dynamic modulus values were again higher than the mechanical measurements; E_{dyn}:E_{mech} varied from 2.2 to 1.6 for samples sintered at 600 °C and 1400 °C respectively.

3.3.3.d Damage processes

The behaviour of the composite systems described in the previous sections was sufficiently similar that they will now be discussed together. The fracture behaviour of each composite depended on sintering temperature. Samples sintered below ~ 900 °C were 'tough' and samples sintered at higher temperatures exhibited brittle fracture. Several factors contributed to the difficulty in identifying and classifying the fracture mechanisms active in these samples. These include: complex porosity patterns and fibre distributions, non-uniformity of the test specimens, and the resultant complex stress states under flexure (which change in the course of a test), all of which vary between individual specimens. However, some features common to the damage behaviour of all the samples may be noted.

The transition from tough to brittle behaviour was reflected in the form of the force/displacement curves and in the macroscopic appearance of the fractured specimens. Figure 3.44, for example, shows the fracture surfaces of 'HC' samples. The sample sintered at 750 °C exhibited brush-like fibre (or bundle) pull-out which was visible to the naked eye, whilst the sample sintered at 1100 °C shows a brittle fracture surface.

This was seen in more detail in the SEM. Figure 3.45, from the tensile side of a 'HC' sample sintered at 750 °C, shows the form of fibre pull-out which was typical for samples sintered in the range 600 °C-900 °C. Large amounts of matrix debris adhered to the fibres, shown in more detail in figure 3.46. The fibres were frequently pulled out as a bundle rather than individually as a consequence of the poor dispersion of fibres during fabrication. This is illustrated in figure 3.47 for a 'HC' composite sintered at 750 °C.

Samples sintered at 1100 °C and 1400 °C, however, showed a typically brittle failure mode with no fibre pull-out (figure 3.48). SEM analysis also indicated that fibre-matrix bond strength was enhanced as sintering temperature was increased beyond 900 °C. Figure 3.49, from a sample sintered at 900 °C, shows an unbonded fibre/matrix interface where the relative cleanness of the fibre indicates little, if any, fibre/matrix adhesion. In contrast

figure 3.50, from a 'HC' sample sintered at 1400 °C, shows a fibre/matrix interface which is in the process of being debonded.

Extensive delamination was observed in tough samples. Cracks were often initiated perpendicularly to the fibres, apparently following the columnar porosity patterns described earlier. The first delaminations occurred typically within 1 mm of the specimen's tensile surface and often at the plane separating the dense and columnar porous strata. This crack deflection was often accompanied by fibre and/or ligament bridging; figure 3.51 is an example taken from a 'XQ' sample sintered at 750 °C. Tensile opening faces were accompanied by significant degrees of fibre pull-out. Delamination cracking coincided with the sudden load drops in the force/displacement curves, and the reloading moduli of the curves decreased with each major cracking/delamination event.

For samples sintered at 1100 °C and above, the primary crack initiated from the tensile face of the specimen and passed cleanly into the body of the specimen. Occasionally, limited delamination was observed well below the neutral plane of the specimen (*i.e.* in the compression region). Fibre-bridging and pullout across matrix cracks were not seen (figure 3.52).

These descriptions simplify what is evidently a very complex damage process and have not attempted to deal with the rôles of the different types of porosity in influencing crack growth. Indeed there were cases where the initiation and growth of matrix cracks could be attributed to or associated with porosity. Figure 3.53i, for example, illustrates the beginning of a pore link-up leading to fibre debonding (figure 3.53ii) and, ultimately, to the form of crack shown in figure 3.54. In other cases regions of porosity 'absorbed' or redirected cracks, making the analysis of fracture faces difficult.

3.4 DISCUSSION

3.4.1 Microstructural analysis

Composite samples were consistently non-planar and of non-uniform thickness. The change in tension experienced by the fibres when passing over the 'corners' of the mandrel caused the material in the centre of each face to be thicker than that at the corners, and each of the six plates to be bowed. This undesirable feature was unfortunately carried through to the final composites, as may be seen in figure 3.7.

Microscopy revealed that the carbon fibres remained in their original tows in all the composite systems, and the sol mixtures frequently did not penetrate to the centres of the fibre tows. This may be attributed to the high winding tension which was necessary to pull the fibres through the viscous colloidal sol/filler particle mixtures, and supports the tentative observation that poor fibre distribution appeared to be associated with matrix porosity in regions where matrix density was otherwise good.

The thixotropic behaviour of the sol mixtures indicates that partial aggregation (and possibly local gelation) of the colloidal silica particles may have occurred in the sol baths. One can envisage that the introduction of filler particles to a colloidal sol may force the colloidal particles closer together and so encourage their aggregation. Alternatively, chemical effects may locally disturb sol stability. The increase in sol viscosity caused by the introduction of filler particles may limit the volume fraction of filler particles achievable.

3.4.1.a Development of primary porosity

The freeze-gelation process gave rise to distinctive patterns of porosity within the composite samples. Several types of gross porosity were identifiable on a micrometre scale, and nanometre scale porosity was present between the colloidal particles of the silica sol-gel matrix. Whilst the details of these porosity patterns were obscured frequently by the effects of infiltration and subsequent sintering, it is apparent that the large uninfiltrated pores occupy the regions where ice crystals grew during the freeze-gelation step. In order to understand the

development of the complex porosity patterns in these materials, one therefore needs to consider the mechanisms of growth of the ice crystals during the freeze-gelation process and how these original pores are affected by the subsequent liquid phase infiltration and sintering steps. Background information on the freezing behaviour and crystallography of ice is available in many texts (*e.g.* see Fletcher [105] and Franks [106]).

The introduction of liquid nitrogen to the hollow mandrel generates a large temperature gradient through the wet composite plates. The manner in which water (from the colloidal silica sol) freezes to form ice crystals is considered to be analogous to the freezing behaviour of cast metallic structures (*e.g.* Fisher [117]). Figure 3.55 shows schematically how the original pore structure in freeze-gelled composites is believed to evolve.

A very thin, equiaxed layer of ice crystals is formed at the surface of the sample neighbouring the mandrel as many small crystals having random orientations are nucleated. Competition between the equiaxed crystals, all of which are trying to grow along crystallographically favoured directions, causes those growing in the direction of the heat flow to eliminate the others. The result is a well-defined region of columnar ice crystals which may extend to a depth of more than 2 mm into the sample and which dominates the morphology of the solid-liquid interface. As the ice growth front extends, the temperature at the head of this front increases and the temperature gradient therefore decreases. The ice crystals become less directional and this leads to an observed region of dendritic-like porosity in the composite matrix which extends to the other side of the sample.

The preceding paragraph presents an idealised description of how the pore structures in as-gelled materials are developed. In reality, the porosity patterns were not so clearly defined; the orientations of the columnar pores were often very variable, and the boundaries between the different types of porosity were hard to discern. The size, type and orientation of the ice crystals during freeze-gelation are evidently very sensitive to local thermal fluctuations, and may vary extensively within a single sample. It was seen in the SEM that the pores described

as 'columnar' appear as *plates* of porosity. These regions of the composites can, therefore, be considered alternatively as bundles of fibres held in position by thin, parallel sheets of matrix material. The porosity patterns were seen most easily in samples sintered at 900 °C and below. Figure 3.8, for example, shows a region of coarse (~ 30-50 μm), columnar porosity perpendicular to the fibres at the edges of the sample, followed by a reasonably well-densified layer and, in the centre of the specimen, an extensive network of open, dendritic porosity. As a general trend, specimens appeared to become better densified as sintering temperature was increased to 1100 °C and 1400 °C, although this was not reflected in porosity or density measurements. It is possible that, at high sintering temperatures, large pores grew at the expense of smaller pores (in a manner akin to Ostwald ripening) and so the efficiency of subsequent liquid-phase infiltration processes might be expected to be improved.

When colloidal silica sols are frozen, the ice crystals which form occupy more volume than the parent water and so the colloidal sol is concentrated in the regions between the ice crystals (this process has been described earlier in section 1.4). This concentration causes aggregation of and subsequent bonding between the colloidal silica particles and leads to a stable gel structure. The introduction of filler particles had no discernible effect on either ice crystal growth (and hence pore structures) or on the freeze-gelation process itself. Figure 3.56 shows schematically how filler particles are channelled into the regions between growing ice crystals and form an integral part of the aggregated silica particle network.

3.4.1.b Liquid-phase infiltration

Liquid-phase infiltration with a fine particle size (7 nm) colloidal silica sol was seen to be a partially successful means of densifying the porosity which results from freeze-gelation. During the liquid phase infiltration process, the coarse, directional pores in the composites provide little resistance to the infiltrant. The central region of fine, dendritic porosity, however, presents more of an obstacle and is only partly infiltrated. It seems likely that exterior pores become filled during the first infiltrations, and effective infiltration of the

central regions during subsequent infiltration cycles then becomes increasingly difficult. This is represented in figure 3.55b. Also, it is difficult to expel air completely from the central regions of the composites prior to infiltration.

Regions of infiltrant silica appeared cracked in the SEM. Shrinkage cracking of colloidal gels during drying is a recognised phenomenon (*e.g.* see section 1.3.6) and is difficult to avoid. An undesirable ramification of this shrinkage is that it locally reduces the degree of contact between the reinforcing fibres and the composite matrix; this slightly reduces the capacity for composite toughening by the mechanisms outlined in section 1.2.1. TEM analysis showed that the infiltrant particles did not densify completely but rather they formed an aggregated, semi-sintered solid gel (figure 3.17).

3.4.1.c Sintering and fine-scale porosity

The primary colloidal silica particles were shown by TEM to have completely fused in many areas. This is supported by the fact that the primary silica matrix crystallised (to α-cristobalite) in all samples sintered at temperatures of 1100 °C and above; the literature on 'conventional' sol-gel processing of ceramics indicates that crystallisation of sol-gel-derived ceramics must be preceded by complete fusing of the amorphous sol-gel particles. Laurie [98] reported that unfilled silica gels prepared by freeze-gelation crystallised to α-cristobalite when sintered at 1000 °C and above. The crystallisation behaviour of each composite system is discussed in more depth in the following sections.

The primary silica particles were incompletely fused in many regions, however, and remained amorphous. Nanometre-scale porosity was observed in the regions between these silica particles. Pores sizes were estimated (by TEM) to be up to ~ 10 nm for 125 nm colloidal particles (HT50 sol) and up to ~ 2 nm for 25 nm colloidal particles (X30 sol). No correlation was found between the degree of fusing and crystallisation of the primary silica particles and local microstructural conditions *e.g.* filler particle concentration.

In summary, two scales of porosity have been observed, both of which are directly attributable to the freeze-gelation process. The primary (micron scale) porosity patterns arose from the growth of ice crystals during freeze-gelation and were unaffected by the presence of fillers in the composite matrices. These pores were modified by subsequent liquid-phase infiltration and sintering. The size of the nanometre-scale pores between colloidal silica particles in unfused regions was a function of the particle size of the colloidal silica sol and, as above, was unaffected by the type of filler particles in the matrix.

The influence of filler type on matrix crystallography will now be discussed for each composite system in turn.

3.4.1.d 125 nm colloidal silica + amorphous silica/glass-ceramic fillers (Composite series 'HC')

Composite 'HC' samples remained amorphous when sintered at temperatures of 900 °C and below, with no evidence of crystallinity in either the sol-gel matrix or the silica and CMA6 filler particles. In contrast, composites sintered at 1100 °C and above contained two crystalline phases (α-cristobalite and anorthite). The α-cristobalite (SiO_2) phase is believed to have been formed by the crystallisation of both the silica filler particles and regions of fused colloidal silica during sintering. The amorphous material detected may be attributed partly to uncrystallised regions of the colloidal silica matrix. The colloidal silica was incompletely densified; TEM showed that the matrix comprised regions of discrete colloidal spheres even in samples sintered at 1100 °C.

EDS identified calcium, silicon, aluminium, magnesium, titanium and oxygen in the CMA6 filler particles in composite samples sintered in the range 600 °C to 900 °C. The anorthite ($CaO.Al_2O_3.2SiO_2$) which formed when the composites were sintered at 1100 °C and above was shown by EDS to comprise calcium, aluminium, silicon and oxygen. The remaining elements (magnesium and titanium) are, therefore, assumed to be present in the glassy phase found by SAD in the TEM. XRD showed that more anorthite was present in the sample

sintered at 1400 °C than in the sample sintered at 1100 °C, indicating that the CMA6 particles had not completely crystallised after sintering at 1100 °C.

The nominal composition of the CMA6 filler particles corresponded to that of cordierite ($2MgO.Al_2O_3.5SiO_2$) + CaO, and XRD confirmed that the principal crystalline phase in CMA6 particles sintered alone at 1100 °C was cordierite. It was therefore surprising that the CMA6 particles crystallised to anorthite in the composite samples. Thus, it is suggested that the environment of the CMA6 in the composites modified the expected crystallisation behaviour, although the exact details of how this occurred are not known.

Titanium is believed to have been introduced as TiO_2 into the CMA6 as a nucleating agent for crystallisation; this is a well-documented application of TiO_2 in glass-ceramics [29, 30].

3.4.1.e 25 nm colloidal silica + amorphous silica/quartz fillers (Composite series 'XQ')

Composite 'XQ' contained initially one crystalline phase, the α-quartz filler particles. Sintering at 900 °C caused the colloidal silica particles and the amorphous silica filler particles to fuse into a linked network and to begin crystallising to α-cristobalite. It was often impossible to distinguish what were originally the amorphous silica filler particles from the sol-gel silica matrix. The conversion of amorphous SiO_2 to α-cristobalite was almost complete in samples sintered at 1100 °C and above. The quartz filler particles remained as α-quartz; the reconstructive transformation of quartz to tridymite at 867 °C (section 1.2.2.b) is known to occur very slowly and then only if local conditions are favourable [32].

3.4.1.f 125 nm colloidal silica + quartz filler (Composite series 'HQ')

The crystallisation behaviour of 'HQ' composites was similar to that of the 'XQ' samples described in the previous section. XRD showed that the quartz filler particles remained as α-quartz at all sintering temperatures. In samples sintered at 1100 °C and above, the colloidal

silica matrix crystallised locally to α-cristobalite in those regions where the colloidal silica particles had fused sufficently; this crystallisation was more extensive than that observed in 'HC' samples sintered at identical temperatures.

The degree of crystallisation of colloidally derived silica to α-quartz at sintering temperatures of 1100 °C and 1400 °C was significantly lower in 'HC' samples than in either 'XQ' or 'HQ' samples. This is evidently associated with the presence of quartz filler particles; it is feasible that quartz can initiate matrix crystallisation in the 'XQ' and 'HQ' materials, whereas the CMA6 and amorphous silica fillers employed in 'HC' samples cannot.

3.4.1.g Residual stresses

The formation of α-cristobalite in samples sintered above 1100 °C has two important ramifications. Firstly, the 4 % volume change on transformation from the higher temperature β-cristobalite phase to α-cristobalite which occurs in the temperature range 200-270 °C [32] inevitably sets up strains in the matrix. Some of these strains can be relieved by twinning, but the majority are dissipated by extensive matrix cracking. This matrix cracking, which is easily seen in dense matrix regions, is effectively absorbed in more porous matrix areas by sub-critical microcracking. Secondly, the very large differences between the thermal expansion coefficients of colloidal silica, α-cristobalite and carbon fibres in the radial direction ($\sim 10^{-6}\,K^{-1}$, $27 \cdot 10^{-6}\,K^{-1}$ and $8 \cdot 10^{-6}\,K^{-1}$, respectively) may be expected to lead to "clamping" of the fibres by the matrix.

The difference in thermal expansion coefficients of fibres and matrix led to observable residual stresses in the composite samples, a result of cooling from elevated sintering temperatures to ambient conditions. If one uses the values of CTE and elastic moduli of fibres and matrix which are summarised in table 3.8, then equation 1.8 predicts *positive* residual stresses, varying from about 13 MPa to 30 MPa for sintering temperatures between 600 °C and 1400 °C. The tensile stresses thus generated within the matrix may be sufficient to cause

matrix cracking (as has been seen in dense matrix regions) or localised matrix cracks may be deflected and absorbed in regions of fine, dendritic porosity.

Transverse matrix cracking of the form predicted by Aveston, Cooper and Kelly (ACK) (see section 1.2.1) was observed in the dense matrix strata of all composites sintered at 1100 °C and above. These transverse cracks were generally quite regularly spaced, varying from about 1000 μm for samples sintered at temperatures up to 900 °C to around 250 μm for samples sintered at 1100 °C and above. ACK theory predicts that *saturation* matrix crack spacing, x, varies with interfacial shear strength, τ, as $x \propto \tau^{-1}$ [20]. This suggests that τ (1100 °C) is around 3-4 times greater than τ (900 °C), and this is qualitatively consistent with observed fibre pull-out lengths. This discussion assumes, of course, that the ACK model may be applied to freeze-gelled composites and that the levels of thermal residual stress which give rise to the matrix cracks are sufficent to cause saturation matrix cracking; this probably over simplifies the sutuation.

3.4.2 Mechanical properties

The pronounced non-planarity of the composites investigated in this study caused the samples to be unsuitable for tensile testing. Three-point bend testing was therefore used to characterise the mechanical responses of the samples, in contrast to providing definitive mechanical property data. It should be noted that the applicability of the formulae used to calculate flexural properties, particularly strength, is dubious since the development of damage in a specimen destroys the uniformity of the specimen 'beam' and renders invalid the beam theory upon which the calculations are based. However, it is generally accepted that before any significant deviation from linearity of the force-displacement curve occurs, the beam may be considered to be intact and standard beam-bending equations apply. Flexural modulus measurements may therefore be considered to be comparable with tensile moduli.

Integration of force-displacement curves yields the energy consumed during tests. Whilst these data cannot be related in a straightforward way to microstructural damage processes, the method is nevertheless useful for comparative studies and general characterisations as long as one remains aware of its limitations and accompanies numerical results with a microstructural evaluation of damage.

The mechanical responses of the three different composite systems considered in this chapter are sufficiently similar that they will be discussed together and exceptions to prevailing trends highlighted where necessary. Analysis of the stiffness and strength measurements will be followed by a discussion of observed microstructural damage mechanisms and how they relate to measured values of work of fracture.

3.4.2.a Strength and elastic modulus measurements

Mechanically-determined values of elastic modulus for all three composite systems lay in the range 10-20 GPa (tables 3.4 to 3.6). Dynamic moduli were in the range 12 to 20 GPa. Series 'HQ' and 'XQ' showed a very general decline in modulus as sintering temperature was increased, possibly indicative of degradation of the carbon fibres during sintering. The mechanical moduli of series 'HC' composites declined initially with increasing sintering temperature, but from 900 °C showed an upwards trend. This may be associated with the crystallisation of the glass-ceramic filler particles, although it should be borne in mind that the increases involved are quite small. Further, the experimental errors must be assumed to be relatively large because the 'ill-behaved' specimen geometries lead to uncertainties about the flexural calculations.

A simple rule-of-mixtures relation which ignores any contribution from the matrix predicts modulus values of about 28 GPa ($= V_f \cdot E_f = 0.12 \times 230$ GPa). This expected value is higher than all of the measured values, again supporting the proposal that fibre degradation is occurring during sintering. Selection of a value of matrix modulus, E_f, suitable for use in calculations is clearly problematic.

An approximate rule-of-mixtures prediction of strength, again a lower bound estimate which ignores the matrix contributions, is around 420 MPa ($= V_f \cdot \sigma_f = 0.12 \times 3.5$ GPa). This is more than twice the highest recorded value of flexural strength (see tables 3.4 to 3.6). It is highly likely that degradation of the carbon fibres during processing contributes to the difference between predicted and measured strengths. Tensile testing of both as-received and desized/handled T300 fibre bundles has shown that a drop in fibre strength of about 35% occurs as fibres are passed through the desizing furnace and winding apparatus (see figure 4.146 and table 4.38). This reduces the rule-of-mixtures prediction to ~ 275 MPa. Further degradation of the reinforcing fibres may be occurring during sintering, and this is supported also by the fact that composite strength declines with increasing sintering temperature.

It is widely accepted that there is a poor correlation between flexural and tensile data. This may be attributed, in part, to the different damage mechanisms which act during flexural and tensile testing and also to the different stressed volumes in flexural and tensile specimens. Even though the highest span-to-depth ratios possible were employed during mechanical testing, delaminations and coinciding load drops, indicative of shear failure, were clearly observed. The standard beam-bending equations used to calculate strengths were not, therefore, strictly applicable, and this introduces another source of error into the measured strength results.

Dynamic moduli were consistently higher than those obtained mechanically. Two features may be mentioned. Firstly, and perhaps most significantly, the application of beam-bending equations to calculate the elastic modulus of specimens which were non-planar and of non-uniform thickness is questionable. Secondly, the porosity in the materials could cause reflections of the ultrasonic pulses and hence disrupt the times of flight and calculated dynamic moduli. This point is explored in more depth in section 4.4.3.b. Thus, dynamic modulus values are useful in this instance as comparators rather than absolute measurements.

3.4.2.b *Toughness and fracture behaviour*

Despite the difficulties associated with toughness determination for ceramic-matrix composites, the experimental data demonstrate in a consistent, if qualitative, manner that a change from a tough to a more brittle mode of fracture is seen as the sintering temperature is increased. This transition from tough to brittle behaviour may be estimated from the mechanical test and microscopy results to occur at approximately 900 °C for all three composite systems. Since matrix composition had no discernible effect on damage behaviour, discussion will now be restricted to the effect of sintering temperature on mechanical properties and damage behaviour.

As sintering temperature is increased beyond ~ 900 °C, toughness (WOF) values fall rapidly, force-displacement curves show little or no post-peak load bearing ability, and primary crack growth occurs with minimal delamination, fibre-bridging and fibre pull-out. In the brittle region, fibre pull-out lengths were very low, typically ~ 25 μm compared to ~ several 100 μm seen for samples sintered at lower temperatures. SEM studies suggested that fibre-matrix bond strength increased as sintering temperature was increased (*e.g.* see figures 3.49 & 3.50) although it could not be determined whether the origin of such interactions was mechanical or chemical. Mechanical clamping of fibres by the matrix as a consequence of thermal expansion mismatches associated with α-cristobalite formation is expected. Degradation of fibres during winding and sintering would also have the effect of reducing fibre pull-out lengths and so encourage brittleness, particularly in samples sintered at high temperatures.

The accumulation of damage in flexural samples sintered in the range 600 °C-900 °C is believed to have occurred as follows. The initial damage is believed to take the form of matrix cracks which run through the tensile half of each specimen to the central plane, although the details of crack growth patterns were obscured invariably by porosity. In this central plane shear stresses are at their maximum, encouraging delamination. These delaminations are reflected in force-displacement traces as sudden drops in load, generally followed by

reloading with a lower modulus. Sliding between the separated laminae evidently requires energy to overcome frictional forces, and this contributes to work of fracture. Delaminations also occurred in the compressive half of the flexural specimens, although some compression damage may have occurred.

The sequence of delaminations and corresponding loads drops/reloads has been reported by other workers who have investigated the flexural behaviour of laminate structures with weak interlayers. Such studies have often been inspired by observations on Nature's composites such as shells which are strong and tough [118]. Clegg *et al*, for example, described how laminates of silicon carbide with graphite interlayers exhibited "graceful failure", with a work of fracture of 4.6 kJm^{-2} [119].

Damage behaviour frequently appeared to be strongly influenced by porosity patterns: columnar porosity seemed to provide preferred routes for tensile cracks into the centres of samples, and delaminations frequently occurred at the plane between the dense strata and the central layer of fine, dendritic porosity. The influence of porosity on cracking patterns and overall mechanical properties has not been fully assessed, and clearly this needs to be addressed in future work.

3.5 CONCLUSIONS

- The freeze-gelation of filled, colloidal silica sols was successfully incorporated into a filament winding process to prepare unidirectionally reinforced composites.
- The most prominent microstructural feature of such freeze-gelled composites was a complex pattern of porosity which replicates the ice crystals which grow during freeze-gelation. The shapes and sizes of different pore types (*i.e.* columnar, dendritic) can be explained by considering the mechanisms of ice-crystal growth during the freeze-gelation process. The pore structure was not affected by the presence of matrix fillers.
- Liquid-phase infiltration of porous, freeze-gelled structures with a fine-particle-size (7 nm) colloidal silica was successful to a maximum depth of ~ 1 mm. Initial infiltrations blocked pores near surfaces, thereby preventing subsequent infiltrations from penetrating the material. The infiltrant silica was generally poorly densified and subject to shrinkage.
- Overall porosity levels lay in the range 0.40 to 0.55 (volume fraction). The highest value of V_f achieved was 0.14.
- The degree of fusing and any subsequent crystallisation of the primary colloidal silica particles were determined by the presence of matrix fillers and sintering temperature:

  125 nm colloidal silica + amorphous silica/CMA6 glass-ceramic fillers (series 'HC')

  - Composite samples sintered between 600 °C and 900 °C remained amorphous. The colloidal silica particles were incompletely fused; fine-scale pores up to ~ 10 nm in size were observed between such particles.
  - The colloidal silica and the amorphous silica filler crystallised almost completely to α-cristobalite in samples sintered at 1100 °C and 1400 °C. Residual amorphous material in samples sintered at 1100 °C was attributed to the presence of localised regions of non-fused colloidal silica.

- The CMA6 glass-ceramic crystallised to anorthite in composite samples sintered at 1100 °C and 1400 °C. Pure CMA6 samples sintered at the same temperatures crystallised to cordierite.

25 nm colloidal silica + amorphous silica/quartz fillers (series 'XQ')

- The α-quartz filler particles underwent no phase changes when the composites were sintered at temperatures between 600 °C and 1400 °C.
- The colloidal silica was only partly fused in samples sintered at 600 °C and 750 °C. Residual pores between the colloidal particles measured ~ 2 nm.
- The colloidal silica and the amorphous silica filler began fusing and crystallising to α-cristobalite when the composite samples were sintered at 900 °C. This process was almost complete in samples sintered at 1100 °C.

125 nm colloidal silica + quartz filler (series 'HQ')

- The α-quartz filler particles underwent no phase changes when the composites were sintered at temperatures between 600 °C and 1400 °C.
- The colloidal silica was only partly fused in samples sintered at 600 °C and 750 °C. Residual pores between the colloidal particles measured ~ 10 nm.

- At sintering temperatures of 900 °C and above, the degree of fusing and crystallisation of the colloidal silica particles exceeded that observed in series 'XQ'.
- The highest measured values of flexural elastic modulus and flexural strength were 17.3 GPa and 200 MPa respectively. The fact that rule-of-mixtures-type predictions exceed measured values by a factor of ~ 2 was attributed in part to degradation of the carbon fibres during fabrication of the composite samples.
- Samples sintered in the range 600 °C to 900 °C failed by extensive delamination when tested under three-point flexure. Matrix composition did not appear to affect damage behaviour. Work of fracture values lay in the range ~ 3 kJm^{-2} to ~ 8.5 kJm^{-2}.

- The brittle nature of composite samples sintered at 1100 °C and 1400 °C was attributed to the formation of α-cristobalite. The high thermal expansion coefficient of this phase led to "clamping" of the carbon fibres by the matrix and hence brittle behaviour.
- Values of dynamic elastic modulus, E_{dyn}, exceeded flexural elastic moduli by typically 20-30 %. Possible reasons for this include (i) the non-planarity of the flexural test specimens mean that the beam-bending formulae on which calculations are based are incorrect; (ii) the abundance of interfaces within the specimens may disrupt the ultrasonic waves and lead to misleading measurements of time-of-flight.

Chapter 4

PROPERTIES OF COMPOSITES WITH UNFILLED SILICA AND ß-SPODUMENE / SiO_2 MATRICES

4.1 INTRODUCTION AND OBJECTIVES

The conclusions of chapter 3 suggest several aspects in which the filament winding process to freeze-gelled composites should be improved. Thus, two important goals of this chapter were to modify this fabrication route to achieve composites (i) which were planar and (ii) which incorporated a high volume fraction of fibres.

The selection of matrix fillers in the previous chapter followed the rationale that cracking arising from thermal expansion mismatches would not necessarily be problematic in a system which was already highly porous and which would be subject to liquid-phase infiltration. The results of chapter 3 illustrated that this reasoning was probably invalid. The materials investigated in this chapter employ a proprietary glass-ceramic filler system of nominally zero thermal expansion coefficient, designated NLAS. It will be shown that the principal crystalline phase of NLAS is β-spodumene. Such lithium aluminosilicate glass-ceramic systems and their relatives are frequently encountered in the literature as candidate matrix materials for high-temperature, high-performance ceramic-matrix composites. As was the case in the previous chapter, the principal matrix components were Monsanto's HT50 and X30 colloidal silica sols, and composite reinforcement was provided by Toray T300 carbon fibres.

During the early stages of the sol-gel project at Bath University, several unsuccessful attempts were made to prepare carbon fibre-reinforced silica composites with **no** matrix fillers. The lack of success was attributed in part to the low fibre volume fractions which

could be incorporated into the sol-gel silica matrix at that time. The modifications made to the filament winding route and the unquantifiable experience gained during the early part of this thesis permitted the fabrication of composites with unfilled matrices. Experimental data on such materials are presented in this chapter.

The ability to prepare planar composite samples enabled a more rigorous program of mechanical testing to be defined than was possible in the previous chapter. Tensile testing was carried out in both static and step-loading configurations, and transverse strains were measured. Tensile and flexural (three-point) tests were complemented by acoustic emission measurements in order to determine the onset of damage during testing and hopefully to identify different microstructural damage mechanisms during testing. Composite toughness was assessed by straightforward work of fracture (WOF) integration, un-notched Charpy impact and notched tensile and flexural testing. All mechanical tests were followed by fractographic examination by scanning electron microscopy.

The principal objectives of this study are to characterise the effects of matrix composition (NLAS filler content and colloidal silica sol particle size) and sintering temperature on the development of microstructure in the composites, and on mechanical performance. This will enable an optimised set of materials and processing conditions to be identified. Once a successful composite system has been defined, reproducibility and consistency of properties will be considered.

The properties of freeze-gelled ceramic-matrix composites will be examined with reference to information in the literature on other ceramic-matrix composite systems. Also, the degree to which freeze-gelled ceramic-matrix composites conform to 'standard' models of mechanical behaviour (such as those reviewed in section 1.2.1) will be considered.

4.2 EXPERIMENTAL METHODS

4.2.1 Fabrication of composite samples

The filament winding route described in section 3.2.1 and figure 3.2 was modified as shown in figure 4.1. Prior to the winding operation, square stainless steel plates of thickness 1 mm and side 100 mm were taped to the hexagonal mandrel and sprayed with a thin, even coating of PTFE mould-release agent. The fibre tows were desized and pulled through the sol + filler mixture and wound onto these plates. When a sufficient thickness had been built up, six further PTFE-coated plates were taped into position over the wet composites. The 'sandwiches' which resulted were gently cut free with a scalpel and stacked in a purpose-built aluminium box. A slight pressure was applied via a screw mechanism in an effort to keep the composites flat. Care was taken to ensure that the wet composites were not damaged at all and, particularly, that the fibres did not slip in the wet matrix.

Freeze-gelation of the composite matrix was effected by immersing the assembly into a bath of liquid nitrogen. After 12 hours, the composites were thawed at room temperature overnight. The six 'sandwiches' were then removed from the stack and the top steel plates were gently removed. The green composites were dried at room temperature whilst still supported on the lower steel plates; this was in order to reduce the likelihood of the composites warping during drying.

After having been infiltrated five times with 7 nm colloidal silica sol (Syton D30) and sintered at typically 750 °C (see below), the samples were reinfiltrated three times, cut into strips of width 10 mm and finally resintered at 500 °C. The infiltration conditions which were employed were the same as those employed in chapter 3 - refer to table 3.2. In order to assess whether specimen position (in the stack of six plates) during freeze-gelation influenced microstructural details (*e.g.* porosity) and hence mechanical properties, specimens from several batches were labelled according to the scheme shown in figure 4.2.

Matrix compositions and more details of fabrication conditions are summarised below within the scope of the objectives described in section 4.1:

Effect of matrix composition (i.e. NLAS content)

i. The nominal NLAS volume fraction (V_{NLAS}) in the composite matrix was varied between 0.02 and 0.40 in a series of 7 HT50-based composites.

ii. Two X30-based composites were prepared with a nominal V_{NLAS} value of 0.08 and 0.21.

These composites were sintered at 750 °C. Further details of matrix compositions may be found in tables 4.1 and 4.2. In systems with a high filler content it was necessary to use long (*e.g.* 6 hour) mixing times and to introduce a dispersing agent (Dispex A40). The properties of Dispex A40 are given in table 4.3.

Effect of sintering régime

i. HT50-derived composites with a V_{NLAS} value of 0.33 (designated HT50 / 0.33 V_{NLAS}) were sintered at temperatures of 500 °C, 630 °C, 750 °C and 850 °C.

ii. A batch of HT50 / 0.22 V_{NLAS} specimens were resintered at 750 °C for 30 minutes and 12 hours.

iii. A batch of composite specimens with a matrix comprising unfilled HT50 was sintered at temperatures of 500 °C, 750 °C and 850 °C.

In all cases, specimens within each experimental series were taken from the same winding and were randomly selected in order to reduce systematic errors.

Effect of infiltration régime

i. A batch of composite specimens with a matrix comprising unfilled HT50 was infiltrated a total of three, five and seven times. Following three initial infiltrations, samples were sintered at 750 °C and then batches infiltrated a further zero, two or four times.

Reproducibility of properties

i. A total of four batches of samples were prepared with a matrix composition HT50 / 0.22 V_{NLAS}

ii. A total of two batches of samples were prepared with a matrix comprising unfilled HT50

Properties of unreinforced matrix

Composite samples having matrix composition HT50 / 0.22 V_{NLAS} were heated at 450 °C in air for 72 hours in order to pyrolyse the carbon fibres.

4.2.2 Microstructural analysis

The details of specimen preparation for examination by optical microscopy, SEM, TEM and XRD are identical to those given in section 3.2.2. SEM analysis was performed with a digital system (JEOL JSM 6310) which was equipped with a LINK AN10000 EDS system and a back-scattered electron detector. Other items of analytical equipment were as described in section 3.2.2.a.

Density and porosity volume fraction values were determined by the water-immersion technique described in section 3.2.2.b. Image analysis of optical and digital SEM images was used to measure fibre volume fractions and to try to classify porosity distributions.

NLAS filler particles were cerammed at 750 °C for 12 hours, ground to a powder and examined by XRD and TEM according to the methods given in section 3.2.2. The densities of cerammed particles were determined by flotation in a mixture of bromoform (density 1.89 g/cm^3) and 1,2-dibromomethane (density 2.17 g/cm^3), and pycnometry.

4.2.3 Mechanical property characterisation

4.2.3.a Tensile tests

The geometry of the tensile specimens used during this study is shown in figure 4.3 (this follows the recommendations of Morell and McCartney [37]). Sample planarity was ensured by lightly grinding with 320 grit SiC paper on a purpose-built attachment which fitted a polishing machine. Aluminium end tabs having length 30 - 35 mm were cut from shot-blast, 1 mm thick sheet, thoroughly degreased and bonded to the unwaisted specimens with a high strength epoxy adhesive.

Foil resistance strain gauges and contact pads were bonded to the wide faces of the specimens using a cyanoacrylate adhesive. As a minimum configuration, pairs of gauges were bonded to opposite faces to detect the development of undesirable bending stresses; calculations were then performed on the means of these pairs. Gauges were amplified at different gains so that, for example, high-gain values were used for modulus measurement and limit of proportionality determination, and low-gain values were used to calculate overall works of fracture. Combined longitudinal/transverse (0°/90°) gauges were used extensively to measure transverse strain responses and hence determine values of Poisson's ratio. Specimens were loaded to failure at a strain rate of ~ 0.05%/min.

Acoustic emission (AE) activity during testing was measured with a 150 kHz piezoelectric transducer which was clamped to the specimen with rubber-faced grips and earthed to the test machine. Details of the combined acoustic emission and data acquisition system employed during this study are given in section 4.2.3.e.

Proportional limits were defined at (i) the point of deviation from linearity of the stress-strain curve and (ii) the onset of acoustic emission activity. These are explained more fully in section 4.2.3.e. Stresses and strains at these proportional limits are reported. Cumulative acoustic emission counts were normalised with respect to (i) specimen cross-sectional area and (ii) stressed volume (*i.e.* cross-sectional area multiplied by gauge length) and recorded at

(i) the proportional limits, (ii) the peak stress and (iii) the end of tests. Values of Poisson's ratio, $\nu = -\varepsilon_T/\varepsilon_L$, were calculated where possible from the linear regions of stress-strain curves.

Once tested, specimens were prepared for examination in the SEM according to the procedure outlined in section 3.2.3 (*i.e.* mounting in resin, polishing and gold-coating). Small pieces cut from tensile specimens were gold-coated and examined umounted in the SEM chamber. Some specimens were prepared when they had only been part-loaded (*e.g.* they were loaded to just past their limit of proportionality). Planes ***b*** and ***c*** in the notation of figure 3.4 (*i.e.* parallel to the direction of testing) were examined. The flexural and toughness test specimens described below were treated similarly.

4.2.3.b Flexural tests

Flexural (three-point bend) testing was carried out with a span-to-depth ratio of 25 - 35 (*i.e.* at a loading span of 80 mm). Details of calculations may be found in section 3.2.3. As was the case with the tensile tests, AE activity was detected using a transducer clamped to the specimen and its onset was used to determine a second type of proportional limit. AE counts were normalised with respect to specimen cross-sectional area.

Interlaminar shear strength (ILSS) was measured using the method recommended by CRAG for reinforced polymers [39]: three-point bend testing was carried out at a loading span of 30 mm (this corresponded to a span-to-depth ratio of ~5) and from the peak load (F^*) the ILSS was determined as:

$$\mathrm{ILSS} = \frac{3}{4}\frac{F^*}{wt} \qquad \text{Equation 4.1}$$

where w and t are the specimen width and thickness respectively.

4.2.3.c *'Toughness' measurement*

Stress-strain and force-displacement curves from tensile and flexural tests were integrated and normalised with respect to specimen cross-sectional area to give Work of Fracture (WOF) values. Integrated tensile data were also normalised with respect to cross-sectional area multiplied by gauge length to give an energy absorbed per unit volume. WOF values were calculated at (i) proportional limits, (ii) peak stress and (iii) end of test.

Charpy impact values were obtained on un-notched samples of length 50 mm. A 5 J capacity pendulum was used. Results are expressed as energy per specimen cross-sectional area and energy per stressed volume (*i.e.* cross-sectional area multiplied by bridge length).

The single-edge-notched beam (SENB) and double-edge-notched tensile configurations shown in figure 4.4 were used to measure values of nominal stress intensity factor, K^*. Notched tensile specimens were tabbed with aluminium as described earlier for normal tensile specimens. Two SENB specimen configurations were used in order to measure the crack growth resistance (i) through the specimen thickness and (ii) through the specimen width. SENB specimens were tested in three-point flexure at a span of 80 mm. In all specimens, notches were machined with a 400 μm blade having a 120° cutting angle. The ratio of notch depth, a, to specimen width, w, designated $\theta = a/w$, was maintained between 0.48 and 0.52. The specimens were loaded at a rate of 0.5 mm/min and the peak recorded loads used to determine values of K^* from the relationship:

$$K^* = \frac{F^* \Theta}{b\sqrt{w}} \qquad \text{Equation 4.2}$$

where F^* is the peak recorded load, b is the specimen thickness, w is the specimen width and Θ is geometry factor given by [120]:

$$\Theta = \frac{\sqrt{\frac{\pi\theta}{2}}}{1-\theta}\left[1.122 - 0.561\theta - 0.205\theta^2 + 0.471\theta^3 + 0.190\theta^4\right] \qquad \text{Equation 4.3}$$

for the double-edge-notched tension specimens and [120]:

$$\Theta = \frac{3\frac{s}{w}\sqrt{\theta}}{2(1+2\theta)(1-\theta)^{3/2}}\left[1.99-\theta(1-\theta)\{2.15-3.93\theta+2.7\theta^2\}\right] \qquad \text{Equation 4.4}$$

for the SENB configuration.

Peak recorded loads from the tensile tests were used also to calculate values of notched stress.

4.2.3.d *Ultrasonic time-of-flight measurements*

The time taken for a 150 kHz pulse to travel the length of each specimen was measured by the method described in section 3.2.3.

4.2.3.e *Marandy data acquisition system and treatment of data*

Figure 4.5 shows schematically the Marandy MR1004 data acquisition system employed during this work. It comprises three main elements: acoustic emission signal processing unit; strain gauge amplifiers; and analogue to digital (A/D) converters.

Acoustic emission (stress-wave) signals are detected by a piezoelectric transducer with a resonant frequency of 150 kHz, and passed to the Marandy processing unit via a 60 dB amplifier. The Marandy has a detection threshold of 10 mV (80 dB with respect to 1 μV at the transducer) and an overall dynamic range of 60 dB [121]. Each event is sorted by amplitude into one of 25 bins (channels 0 to 25) of 2.4 dB class interval. Events of greater than 60 dB are counted in an overflow bin (channel 25). The instrument threshold can be raised to reject background noise. During this study a 20 minute dummy run was carried out prior to each day's testing to establish the background noise level and necessary threshold. All the data reported in this thesis have been corrected to a standard threshold of channel 4.

AE data are stored in fast memory buffers and spooled to the controlling personal computer's hard disk in a space-efficient binary format. Time and A/D data from up to 8 inputs are recorded simultaneously. Each A/D unit has an input range of 0-10 V with a resolution of

4.88 mV. When in use, the outputs from strain gauge amplifiers were fed into the A/D converters. Conditioned load cell outputs from an Instron 1195 were also fed into the Marandy A/D system.

In order to deal with the large amounts of data generated during this thesis and to automate repetitive tasks which are susceptible to errors, a series of macro programs was developed for Microsoft's Excel 4 spreadsheet. This enabled a predetermined series of tasks to be automated for each test type, and typically involved:

1) Calling an external program to convert each binary Marandy file to ASCII;
2) Importing the ASCII file into Excel;
3) Stripping out redundant data (*e.g.* the lead-in to tests);
4) Converting parametric voltages to loads, strains *etc.* and time stamps to displacements;
5) Calculating stresses from load values (this involved using specimen dimensions looked up from a central database);
6) Generating graphs in a standard format;
7) Integrating force-displacement (f-d) curves to calculate works of fracture;
8) Differentiating (f-d) curves to calculate elastic moduli and elastic limits (see below);
9) Storing calculated results in a central database.

In the case of flexural tests, a routine was written to correct automatically each f-d data pair to accommodate the test machine deflection. For each loading configuration a steel bar (thickness 40 mm) was loaded up to the load cell's capacity and a machine stiffness calculated from the resulting force-displacement curve. At any measured load during subsequent tests, the machine deflection could then be subtracted from the recorded deflection to leave a "true" specimen deflection. In practice, this correction had a negligible effect on calculated results.

Figure 4.6 shows schematically the method by which elastic modulus and limits of proportionality were determined. Secant moduli were calculated with reference to a nominal

zero point. Tangent moduli were calculated by performing a linear regression on small portions of the stress-strain curve. When these values corresponded well with elastic modulus values calculated by linear regression, this was taken to indicate that a reliable value of elastic modulus had been determined. Deviation from proportionality in the stress-strain curve was taken to be the point where the measured strain was at least 2% greater than that predicted by the elastic modulus. Although this was an arbitrary criterion, it is argued that it was a systematic method of determining elastic limits and, moreover, it was amenable to automatic calculation.

The onset of acoustic emission activity was used to determine a second type of elastic limit. The point at which this elastic limit was reached was defined to be when the cumulative AE counts exceeded 0.5% of the number of the counts at the peak load.

4.2.3.f Bundle strength of T300 carbon fibres

Cardboard tabs having dimension 25 mm x 40 mm were carefully bonded to 120 mm lengths of T300-carbon-fibre tows to give tensile bundle strength specimens with gauge length 80 mm. The fibre tows were tested in two conditions: (i) as-received and (ii) after the fibres had been desized at 750 °C and wrapped around the mandrel which had been used to form the composites. The objective of the latter was to introduce the same degree of damage into the fibres as would be introduced during fabrication of the composites.

4.3 RESULTS

4.3.1 Observations on fabrication

In order to produce well-dispersed, stable sol/filler mixtures it was necessary to (i) mix under high-shear conditions for several hours and (ii) employ a dispersing agent (Dispex A40) to prevent the filler particles from settling out in the sol bath. Where it was necessary, about 0.5 – 2 wt% Dispex was typically used. The viscosities of the mixtures, and the associated difficulties in impregnating the carbon fibre tows and winding the tows onto the mandrel, increased with increasing filler content. In contrast, matrix precursors containing little (*e.g.* 10 wt%) or no filler were easy to mix and were stable. Their low viscosities enabled fibre tows to be easily impregnated and wound.

The tension on the fibre tows was kept as high as possible in an effort to produce composites with a high fibre volume fraction, although this had to be balanced against the possibility of fibre tow breakages and lack of infiltration of the tows. The technique of sandwiching the impregnated, wound fibre tows between steel sheets successfully produced composite plates which were flat and planar, typically to within 1 mm from end to end.

Great care had to be taken when handling the wet 'sandwiches' (*i.e.* prior to freeze-gelation) to avoid the impregnated fibre tows sliding over one another. The plate shown in figure 4.7 did slide slightly before freeze-gelation and resulted in fibre misalignment and cracks in the final test specimens (figure 4.8). Cutting the plates into test strips with a water-cooled diamond-tipped saw presented no problems, although the cut edges on samples with little or no matrix filler showed a tendency to be 'fluffy', as may be seen in figure 4.9. In some samples which contained no matrix filler, cracking between fibre bundles could be seen with the naked eye (figure 4.10).

4.3.2 Microstructural analysis

4.3.2.a Porosity and fibre distributions

Measured density, porosity and fibre volume fraction data for composite samples are summarised in the following tables:

• *Samples with NLAS-filled HT50 matrices*	Table 4.4
• *Samples with NLAS-filled X30 matrices*	Table 4.5
• *Samples with unfilled HT50 matrices*	Tables 4.6 & 4.7
• *Reproducibility of samples with HT50 / 0.22* V_{NLAS} *matrices*	Table 4.8
• *Resintering samples with HT50 / 0.22* V_{NLAS} *matrices*	Table 4.9
• *Samples with HT50 / 0.33* V_{NLAS} *matrices, sintered at 500 °C - 850 °C*	Table 4.10

Values of theoretical (*i.e.* fully dense) composite bulk density, ρ_{th}, given in tables 4.4 to 4.9 were calculated from the relationship:

$$\rho_{th} = \frac{V_f \cdot \rho_f + V_s \cdot \rho_s + V_{NLAS} \cdot \rho_{NLAS}}{V_f + V_s + V_{NLAS}} \qquad \text{Equation 4.5}$$

where V and ρ represent volume fraction and density respectively and the subscripts f, s and NLAS correspond to the carbon fibres, colloidal silica sol and NLAS filler particles respectively. In addition to the directly measured values of total composite porosity volume fraction, measured values of bulk density, ρ_{meas}, and ρ_{th} were used to calculate porosity volume fraction from the relationship:

$$V_{porosity} = 100 - \left(\frac{\rho_{meas}}{\rho_{th}} \cdot 100 \right) \qquad \text{Equation 4.6}$$

Total porosity volume fractions measured by water-displacement varied between 0.23 and 0.43 in NLAS-filled systems. These values generally correspond well to those calculated from density measurements. Figures 4.11 and 4.12 summarise the variations in density and measured porosity with matrix composition for all samples sintered at 750 °C. Fibre volume

fractions (V_f) varied from 0.46 to 0.09 as the filler volume fraction (V_{NLAS}) in HT50-derived matrices was varied from 0 to 0.40; figure 4.13 shows the variation of V_f with matrix composition. The problems associated with measuring V_f are discussed below.

As was the case with the materials described in the previous chapter, distinctive patterns of coarse, columnar, highly-directional porosity were obvious artefacts of the freeze-gelation process; figure 4.14 is typical of the patterns seen. Such pore structures were independent of matrix composition. Variations in the orientation of columnar pores, *e.g.* as seen in figure 4.15, may be attributed to thermal fluctuations which affected the growth of ice crystals during freeze-gelation.

Pore structure was not always clearly defined. Figure 4.16 presents a pair of through-section optical micrographs taken from the same specimen. Whilst one picture clearly shows columnar pores running from one face to the other, the second shows a region of extensive, shapeless porosity within the centre of the specimen which leads into columnar pores closer to the specimen edges. The layered structure reported in the previous chapter was only rarely observed.

Although fibres often remained closely associated with their original tows, figure 4.17 shows that the fibres were quite evenly separated by matrix material. In this example, which is taken from a dense matrix region, three fibre bundles can be discerned. Within each fibre bundle, fibre volume fractions were locally high, *e.g.* up to $V_f = 0.55$ measured by image analysis. Several samples appeared to indicate that matrix density was higher within fibre tows than between the tows (*e.g.* figure 4.18). Individual tows were observed also when samples were viewed in planes parallel to the fibre direction; figure 4.19 shows matrix-rich regions between each wound layer, and each wound tow has a slightly different orientation. Whilst image analysis was an appropriate tool for measuring fibre volume fractions in regions of composites with high matrix density, figure 4.20 shows the difficulty in applying the technique in porous regions; the fibres in the pores were chipped and damaged during

polishing, and it was, therefore, impossible to establish accurate thresholds (*i.e.* of fibre brightness versus matrix brightness) and take measurements. Fibre pyrolysis was considered to be a more reliable method of measuring overall fibre volume fraction values.

Microscopy and density measurements indicated that the degree of matrix porosity was most pronounced in systems with low filler contents (and consequently high fibre volume fractions). As was the case with the materials described in chapter 3, regions of intermediate levels of porosity appeared as fibres held by thin (10 - 50 μm), parallel plates of matrix at ~ 50 μm intervals (see figure 4.21). Figure 4.22, an SEM micrograph of an unfilled composite, shows how highly porous regions appear as fibres connected by ~ 10 μm threads of matrix material. At the extreme, some fibres seemed to be (locally) in contact with no matrix material at all, *e.g.* see figure 4.23.

In addition to the coarse pore sructures described above (to be referred to as primary porosity), SEM occasionally revealed the existence of a second, much finer network of pores, generally in samples containing little or no matrix filler; this will be referred to as secondary porosity. Figure 4.24, an example taken from a HT50 / 0.09 V_{NLAS} system, has a mottled appearance in some regions of matrix due to fine, directional pores. EDS detected only silicon and oxygen in these regions, confirming the absence of NLAS filler. Evidence of fine-scale porosity between individual colloidal silica particles was provided by TEM. Figure 4.25 shows a region of HT50-derived matrix in which the colloidal silica particles have only partly sintered together, leaving an apparently open pore pattern; again, EDS detected only silicon and oxygen, and electron diffraction showed that this region was amorphous.

In section 4.2.1 the possibility was raised that specimen position in the stack of plates during freeze-gelation would lead to local variations in the growth behaviour of ice crystals and hence to possible variations in density and microstructure in the final composites. Figure 4.26 summarises the variations in density and porosity with specimen position for composite samples with an unfilled HT50 – derived matrix. The x and y axes correspond to plate

number (1 – 6) and specimen number (1 – 10) respectively (refer to figure 4.2), and measured values of density and porosity appear on the z axes. No systematic variations were observed in any of the eight series of specimens examined in this way. The time-of-flight elastic modulus values (E_{dyn}) which are also shown in figure 4.26 will be described in section 4.3.3.

4.3.2.b Observations on the liquid-phase infiltration process

Figure 4.27, a through-section montage of optical micrographs, shows that liquid-phase infiltration with a 7 nm colloidal silica was effective to a depth of up to ~ 1 mm from the sample surface. Table 4.7 shows that in the case of a composite with unfilled HT50 matrix, there was no difference in density or porosity for samples which had been subjected to 3, 5, or 7 liquid-phase infiltration cycles. Within infiltrated regions, there was invariably evidence that the infiltrant had contracted and cracked (*e.g.* see figures 4.28 and 4.29) and this led to a lack of integrity between the infiltrant and fibres (figure 4.30).

Examination in the TEM showed that the 7 nm colloidal silica particles in the infiltrant sol had barely fused together and that the silica remained amorphous. It may be seen from figure 4.31 that cracking occurred between small regions of infiltrant, and that there was a lack of integrity between the infiltrant and the neighbouring matrix material.

4.3.2.c Properties of NLAS filler

As-received NLAS resembled a floury powder. Sintering at 500 °C did not change this appearance, but samples sintered at 750 °C had flowed to form a very hard mass. The density of the sintered material was measured to be 2.43 g cm^{-3}. XRD indicated that the as-received NLAS was amorphous and that the sample sintered at 750 °C had crystallised to form a phase identified as β-spodumene (figure 4.32). A sample of NLAS was analysed by differential scanning calorimetry over the temperature range 20 °C to 800 °C (figure 4.33) and exotherms were detected at 590 °C and 665 °C.

Examination of the sintered material in the TEM revealed crystallites embedded in a glassy matrix (figure 4.34). Electron diffraction of such an area gave a ring pattern which was consistent with β-spodumene. EDS detected the presence of silicon, aluminium and oxygen as principal elements (figure 4.35) and a series of minor elements. Note that the copper peaks seen in figure 4.35b are attributable to the copper grid on which these powdered samples were supported.

4.3.2.d Effect of matrix composition on microstructure development

Investigation by differential interference contrast (DIC) and dark field modes in the optical microscope revealed two types of matrix appearance in samples containing intermediate levels of matrix filler. Figures 4.36 and 4.37 present optical, DIC micrographs of samples with matrix compositions HT50 / 0.19 V_{NLAS} and HT50 / 0.22 V_{NLAS} respectively. Regions of bright, apparently crystalline material formed abrupt boundaries with regions of low, uniform brightness. No relationships could be found between the presence of porosity, degree of infiltration or specimen position and whether the matrix appeared bright or dull. In samples which contained a high matrix filler content, the bright appearance was dominant; figure 4.38 gives a typical example. In all cases, great care had to be taken to distinguish between bright images formed by the dense matrix and misleading reflections from pores which also appeared bright under DIC conditions.

In order to assess whether there were compositional differences between the two types of matrix, a series of microindents were used to provide reference points to enable the appropriate regions to be identified in the SEM for analysis by EDS. By using the ratio of silicon : aluminium peak heights to semi-quantitatively describe the amount of NLAS filler material present in a specified region, it was shown that the bright regions contained appreciably more filler than did the dull regions.

XRD showed that composites with unfilled HT50 matrices remained amorphous to 750 °C (figure 4.39). α-cristobalite was detected in samples sintered beyond this temperature. The two broad peaks in figure 4.39 may be attributed to the carbon fibres, as may be seen from figure 4.40.

Figure 4.41 presents typical XRD responses of composites which contained NLAS matrix fillers. Two series of peaks were identified as β-spodumene and α-quartz. The β-spodumene peak is evidently attributable to the NLAS filler, and its height varied with the amount of filler in the composite. The α-quartz peak height increased rapidly as NLAS was introduced to the composite matrix. There was a corresponding reduction in the amount of amorphous material detected (*e.g.* compare the spectra from samples with V_{NLAS} values of 0.02 and 0.19). As expected, β-spodumene content increased with increasing NLAS content.

The variations of the principal XRD peak heights of α-quartz and β-spodumene with matrix composition (V_{NLAS}) for all samples sintered at 750 °C are given in figure 4.42. It may be seen that the amount of quartz detected increased rapidly from zero (for unfilled composites) as NLAS filler is introduced to the composite matrix. NLAS-filled samples which were sintered at different temperatures indicated that quartz formation had commenced at temperatures as low as 630 °C (figure 4.43). Resintering under standard conditions (*i.e.* 750 °C) for different periods had no effect on the amount of β-spodumene detected, but caused appreciable increases in the α-quartz content (figure 4.44).

NLAS particles were easily identified by SEM in samples sintered at 500 °C, as may be seen from figures 4.46 and 4.47. The particles were evenly distributed throughout samples and their distribution appeared to be unaffected by the primary matrix porosity; for example, figure 4.48 shows particles located within the strips of matrix which separated the coarse, columnar pores. The particles were less easily discerned in samples sintered at 630 °C (figure 4.49) and it was generally impossible to identify individual filler particles in

samples sintered at 750 °C; in this latter case, the composite matrix appeared homogeneous (figure 4.50).

The nature of the matrix phases was examined more deeply in the TEM. Regions which contained no NLAS filler (as indicated by EDS) were invariably shown by electron diffraction to be amorphous. Also, the colloidal particles were only partly fused in some filler-less regions, as was the case in figure 4.51. In contrast, regions which did contain NLAS particles were denser (individual colloidal silica particles were rarely discernible) and electron diffraction indicated a high degree of crystallinity (figure 4.52). Within such filler-rich regions, β-spodumene crystals between 1 nm and 200 nm were distinctive (figure 4.53). Regions of colloidal silica which adjoined filler-rich areas were frequently completely fused and either completely or semi-crystallised to α-quartz. Non-fused colloidal silica was never found to have crystallised.

4.3.3 Mechanical performance

This section presents the results of an extensive program of mechanical testing and complementary fractography. After numerical results have been presented in tabular form, further details of mechanical performance will be explored under headings relating to details of the composites' matrix compositions and fabrication conditions. These subsections will include graphical representations of selected data, example stress-strain curves and fractography results.

Mechanical property measurements are summarised in the following tables and are grouped according to the composites samples' matrix compositions and fabrication conditions:

Samples with NLAS-filled HT50 & X30 matrices (effect of matrix composition)

- *Dynamic (time-of-flight) elastic modulus* Tables 4.11 & 4.12

- *Flexural (three-point bend) (mechanical)* Tables 4.13 & 4.14
- *Flexural (three-point bend) (acoustic emission)* Tables 4.15 & 4.16
- *Tensile (mechanical)* Tables 4.17 & 4.18
- *Tensile (acoustic emission)* Tables 4.19 & 4.20
- *Interlaminar shear strength* Tables 4.21 & 4.22
- *Un-notched Charpy impact* Tables 4.23 & 4.24
- K_{1q} *- single edge notched beam configuration* Table 4.25
- K_{1q} *- notched tension configuration* Table 4.26

Samples with unfilled HT50 matrices (effect of sintering temperature)

- *Flexural (three-point bend) (mechanical and acoustic emission)* Table 4.27
- *Tensile (mechanical and acoustic emission)* Table 4.28
- *Dynamic (time-of-flight) elastic modulus, ILSS, Charpy* Table 4.29

Batch to batch reproducibility of samples with HT50 / 0.22 V_{NLAS} matrix

- *Flexural (three-point bend) (mechanical and acoustic emission)* Table 4.30
- *Tensile (mechanical and acoustic emission)* Table 4.31
- *Dynamic (time-of-flight) elastic modulus, ILSS, Charpy* Table 4.32

Effect of sintering temperature on samples with HT50 / 0.33 V_{NLAS} matrix

- *Flexural (three-point bend) (mechanical and acoustic emission)* Table 4.10
- *Dynamic (time-of-flight) elastic modulus, ILSS, Charpy* Table 4.10

Effect of resintering on samples with HT50 / 0.22 V_{NLAS} matrix

- *Flexural (three-point bend) (mechanical and acoustic emission)* Table 4.33

- *Dynamic (time-of-flight) elastic modulus, ILSS, Charpy* Table 4.34

4.3.3.a *Effect of matrix composition on the flexural properties of composites with NLAS-filled HT50 and X30 matrices*

This section presents results for samples which were sintered at a primary temperature of 750 °C and which were subject to a total of 7 liquid-phase infiltration cycles. The mechanical properties of samples fabricated under different conditions are described in section 4.3.3.d.

Figures 4.54 and 4.55 show the effect of nominal NLAS content in the composite matrix (V_{NLAS}) on flexural elastic modulus and flexural peak stress. The datum points corresponding to composites with unfilled HT50 matrices, *i.e.* $V_{NLAS} = 0$, are taken from samples which were fabricated under the same conditions as the NLAS-filled materials, *i.e.* sintered at 750 °C and infiltrated seven times. This convention will be used also in subsequent sections.

Elastic moduli decreased with increasing V_{NLAS}, from ~ 90 GPa for composites with no NLAS to 23 GPa for composites with $V_{NLAS} = 0.4$. Both HT50- and X30-derived composites appeared to fit this apparently exponential decay. In contrast, the highest value of flexural strength (350 MPa) was measured in a composite of matrix composition HT50 / 0.19 V_{NLAS}, although the flexural strength of an X30-derived material having a similar NLAS volume fraction was significantly lower at ~ 100 MPa. Interlaminar shear strength varied with V_{NLAS} in a similar way to flexural strength (figure 4.56).

Figure 4.57 summarises the variations in work of fracture to peak load (WOF_{peak}) and to end of test (WOF_{end}) with matrix composition. WOF_{peak} increases with increasing V_{NLAS} to a maximum of ~ 7 kJm^{-2} at $V_{NLAS} = 0.27$, and WOF_{end} similarly increases but reaches a peak value of ~ 16 kJm^{-2} at $V_{NLAS} = 0.08$. Once again, samples having matrix composition X30 / 0.21 V_{NLAS} fell outside of this trend. Total acoustic emission counts at peak load and end of test are shown in figure 4.58. Whilst the variation of peak load counts with V_{NLAS}

appears to have no pattern, counts at end of test decrease with increasing V_{NLAS}; both X30- and HT50-derived materials fitted this trend.

Composite samples which had a matrix composition in the approximate range HT50 / 0.19 - 0.22 V_{NLAS} were essentially brittle and exhibited the form of force-displacement curve shown in figure 4.59. The onset of acoustic emission activity, shown by the red line, coincided approximately with the mechanically-determined proportional limit in most cases, and AE counts accumulated apparently exponentially after this. The lower part of figure 4.59 shows acoustic emission amplitude distribution histograms obtained at four points on the force-displacement curve: 'a' and 'b' correspond to proportional limits determined mechanically and using acoustic emission data respectively, 'c' is a point at a higher load and 'd' gives the final distribution, *i.e.* at failure. The distribution is seen to shift to higher channels (*i.e.* higher energy events) with increasing applied load.

In contrast, the force-displacement curve shown in figure 4.60 for a sample with matrix HT50 / 0.09 V_{NLAS} shows a series of load drops followed by reloads. Whilst the initial AE amplitude distribution (point 'a') has the familar exponential form, additional activity centred around channels 12/13 is seen in distributions at higher applied loads (points 'b' - 'd'). This effect was even more pronounced for samples with unfilled HT50 matrices (see figure 4.61), and samples with matrix composition X30 / 0.08 V_{NLAS} exhibited similar behaviour.

Three principal failure modes were observed: (i) partial delamination on the tensile side of specimens localised around the loading point, (ii) extensive delamination throughout the whole specimen and (iii) brittle. These are summarised schematically in figure 4.62 and examples are shown in figures 4.63 to 4.69. It proved to be impossible to categorise samples' failure behaviour rigourously; the variability in behaviour of nominally identical samples will be explored in more depth in section 4.2.3.d. In spite of these difficulties, several trends may be reported.

HT50-derived samples which contained more than ~ 0.22 V_{NLAS} were generally, although not exclusively, brittle; specimens fractured into two matching pieces, although the growing crack often meandered as may be seen in figure 4.63.

Samples whose matrix compositions fell outside of this range failed primarily by delamination. Extensive delamination such as that shown in figure 4.64 was seen in samples which contained no matrix filler and samples of matrix composition HT50 / 0.02 V_{NLAS} and X30 / 0.08 V_{NLAS}. In such cases, delaminations occurred at regular planes right down to the compressive face of the test specimen and damage appeared to be spread evenly throughout the specimen volume. In some cases, compressive damage such as that shown in figures 4.65 and 4.66 was evident.

Partial delamination was localised around the centres of specimens and was generally, although not exclusively, restricted to the upper two thirds of the specimens (*i.e.* on the tensile side). Figures 4.67 and 4.68 demonstrate how this frequently gave rise to interlocking of either clumps of material or to apparent bridging of fibres (figure 4.69). Compression damage was rarely evident in such samples.

Interlaminar shear strength specimens generally followed these same trends. Figure 4.70(i) shows the brittle fracture seen in composites which contained more than ~ 0.19 V_{NLAS}, and samples with either no matrix filler or low V_{NLAS} (*i.e.* 0.02) showed the extensive delamination seen in figure 4.70(ii). Both HT50- and X30-derived materials which contained 0.08 V_{NLAS} occasionally showed kinking as may be seen in figure 4.70(iii).

SEM analysis of fracture surfaces provided more details of damage behaviour, although the descriptions that follow were subject to the same difficulties in categorising behaviour that were described above. The high levels of porosity in many of the samples precluded effective examination in the SEM because of charging problems; this was particularly the case in composites with either unfilled matrices or which contained only small (0.02 V_{NLAS}) filler

contents. Mounting followed by metallographic polishing and examination by optical microscopy was generally unsuccessful.

As might be expected, the damage in samples which failed in a brittle manner was located almost exclusively in one fracture plane. Figure 4.71 demonstrates the absence of any signs of toughening (*e.g.* fibre pullout *etc.*) in such samples.

Samples which failed by delamination, such as that shown in figure 4.64 earlier, generally divided into discrete laminae. Figures 4.72 and 4.73 present typical views of such laminae; the orientation of these pictures is 'c' in the notation introduced in figure 3.4. Within the lamina shown in figure 4.72, which is evidently from a region of coarse, columnar porosity, the fibres apparently hold perpendicular plates of undamaged solid material in place. Such plates or clumps of material were frequently observed to have become detached from the fibres and fractured at random points; where the matrix was well bonded locally to the fibres then fibre fracture and pullout processes were observed (figure 4.74). Where fibre-matrix bond strength was lower matrix clumps were seen to 'float' within the arrays of parallel fibres (figure 4.75). These processes occurred in both porous and more dense regions of specimens. Apparently tensile damage of an individual lamina may be seen in figure 4.76. In this example, there is only limited evidence of effective crack-bridging or fibre pullout. However, these processes are present unambiguously in figure 4.77.

Figures 4.78 and 4.79 demonstrate how delamination (shear) cracking was unaffected by the presence of either matrix porosity or infiltrated matrix pores. The intersection of delamination cracks, such as that shown in figure 4.80, was similarly unaffected. Attempts to employ EPMA to seek correlations between matrix cracking patterns and local matrix composition (*i.e.* NLAS filler content) were unsuccessful. However, optical microscopy in DSC mode suggested that boundaries between dull and apparently crystalline regions might provide preferential cracking paths (figure 4.81). There is evidence also that matrix-rich regions of

X30-derived materials were quite often not effectively consolidated, and this seemed to encourage matrix cracks to branch and meander (figure 4.82).

Laminae which had become debonded often slid over one another (in the notation of figure 3.4, the sliding occurred in plane 'c'). Figure 4.83 shows the intersection of two such sliding planes. Whilst no correlation could be found between matrix composition and the amount of matrix material which adhered to fibres in the fractured specimens, some fibres were evidently better coated with and better bonded to their matrix than others (*e.g.* figure 4.84). Strong fibre-matrix bonding caused localised matrix tearing in delamination (shear) planes (figures 4.83 to 4.87) and, where interlaminar sliding occurred, caused more widespread matrix damage as clumps of matrix were sheared between intact planes moving in opposite directions (figure 4.87). Figure 4.88, an optical micrograph, demonstrates that fibres which bridged delamination planes often kinked before fracture. In samples which exhibited compression damage, such fibre kinking was frequently much more pronounced (figure 4.89).

4.3.3.b Effect of matrix composition on the tensile properties of composites with NLAS-filled HT50 and X30 matrices

As was the case in section 4.3.3.a, this section presents results for samples which were sintered at 750 °C and infiltrated 7 times. Values of tensile elastic modulus and strength both show an apparently exponential decrease with increasing matrix filler content V_{NLAS} (figures 4.90 and 4.91). A similar trend is shown by stress at proportional limit (figure 4.92), strain at proportional limit was around 0.15% for all values of V_{NLAS} (figure 4.93). Strain at peak stress was in the range 0.35% to 0.40% for most matrix compositions (figure 4.94). Calculated values of Poisson's ratio, shown in figure 4.95, lay in the range 0.15 to 0.25 and did not vary systematically with V_{NLAS}.

Work of fracture decreased with increasing filler content from a maximum value of ~ 60 kJm^{-2} for composites with unfilled matrices (figure 4.96). Acoustic emission counts at peak load show a general decrease with increasing V_{NLAS} although these data were subject to considerable scatter (refer to figure 4.97 and tables 4.19 and 4.20).

Figures 4.98, 4.99 and 4.100 present typical stress-strain curves of samples with HT50-derived matrices containing 0.02, 0.09 and 0.27 V_{NLAS} respectively. Cumulative acoustic emission counts are superposed over the stress-strain curves in the central parts of these figures. Although the AE data exhibited considerable scatter, the trend which emerged showed that AE activity commenced at lower applied strains in samples with low V_{NLAS} than was the case in samples with higher matrix filler contents. Further, AE counts tended to accumulate gradually in samples with low matrix filler content, whereas samples with higher V_{NLAS} often showed a rapid increase in AE activity at a point which corresponded approximately with the proportional limit of the stress-strain curves; compare, for example, figures 4.98 and 4.100.

The top parts of figures 4.98 and 4.100 illustrate the means by which elastic moduli were determined; instananeous secant and tangent moduli are plotted against each strain datum, and the final moduli, determined by least-squares regression, are shown also. Two sets of nominally identical samples were tested both at Bath University and at the National Physical Laboratory's Materials Metrology department. The results of these tests, presented in table 4.35, confirm the quality of the tensile data obtained at Bath; in particular, determinations of elastic moduli matched well.

The lower curves in figures 4.98 to 4.100 show the variations of transverse strain and instananeous Poisson's ratio with longitudinal strain. Although transverse response was "well-behaved" in some cases (*e.g.* figure 4.100) it was frequently difficult to determine reliable values of Poisson's ratio (figure 4.99).

The technique of pairing strain gauges on opposites faces of test specimens proved to be successful. A typical pair of gauge outputs is shown in figure 4.101. The outputs coincide over the region used for elastic modulus determination although beyond this they differ slightly. Means of such paired outputs were used for all calculations.

The evolution of acoustic emission amplitude distributions with increasing applied load is shown in figures 4.102 and 4.103 for two composite specimens with unfilled HT50 matrices. In each case 'a' and 'b' correspond to proportional limits (determined from the stress-strain data and from the onset of acoustic emission activity respectively), 'c' is a point at a higher applied load, and 'd' gives the final distribution, *i.e.* at failure. The amplitude distribution histograms shown in figure 4.102 show the familiar exponential-shaped curves at all points. In contrast, the histograms 'c' and 'd' in figure 4.103 show many more events after channel 10; moreover, the specimen from which these data were acquired exhibited extensive lateral splitting and delamination prior to failure (further details of damage modes in all specimens are given below).

Overall, the trend was for samples with V_{NLAS} greater than about 0.22 to exhibit the exponential AE amplitude distributions such as those seen in figure 4.102. Samples with lower values of V_{NLAS} more frequently followed the form of figure 4.103, *i.e.* essentially exponential but with markedly more high energy events when the specimens were loaded beyond their proportional limits.

X30- and HT50-derived samples which contained more than ~ 0.22 V_{NLAS} were generally brittle. Specimens either fractured cleanly along a single plane in the centre of the gauge or, as is shown in figure 4.104, exhibited a crenellated fracture pattern. The tendency of brittle specimens to fail outside of their gauge lengths was overcome principally by careful specimen preparation. Samples with lower matrix filler contents exhibited the tougher, more fibrous failure mode exemplified in figure 4.105, and samples with very low NLAS filler contents (*i.e.* samples with matrix compositions HT50 / 0.02 V_{NLAS} and unfilled HT50) failed by

extensive delamination and longitudinal splitting (figure 4.106). These latter samples were not amenable to examination in the SEM.

Tensile fracture surfaces showed very little evidence of fibre pullout and their general appearance was essentially that shown earlier in figure 4.71. Damage appeared to be restricted to the fracture planes - analysis both of specimens which had been part-loaded and specimens which had been loaded to failure did not reveal any evidence of damage having occurred away from the final fracture plane. In particular, transverse matrix cracking was seen only very rarely. SEM revealed that some interlaminar cracking had occurred even in brittle specimens; an example is given in figure 4.107.

Evidence of regularly spaced, transverse matrix cracking was absent also in tensile specimens which failed in a tougher manner (*i.e.* samples with matrix compositions in the range HT50 / V_{NLAS} < 0.22). However, damage in such specimens was not restricted to a single fracture plane; rather, clumps of intact composite material were distributed evenly throughout gauge lengths. Such clumps varied in size from ~50 μm to ~500 μm and were interconnected by either (i) regions of matrix bridging and fibre pullout or (ii) delamination planes. The details of the processes which had occurred between the intact clumps were obscured frequently by debris.

Figure 4.108 shows a typical view of the fibre pullout which occurred when such clumps separated in a tensile mode. This appearance is similar to that seen at exterior surfaces (figure 4.109). Figures 4.110 and 4.111 demonstrate that intact clumps of material separated by sliding (*i.e.* shear). Within intact clumps, there was occasional evidence of fibre fracture *etc.*, exemplified by figure 4.112. No correlations were found between (i) local matrix porosity content, (ii) local matrix composition (*i.e.* local NLAS filler content) or (iii) degree of infiltration and the details of the fracture process, although delamination cracks tended to prefer fibre-free planes.

4.3.3.c *Effect of matrix composition on the toughness of composites with NLAS-filled HT50 and X30 matrices*

To recapitulate, three approaches were used to measure composite "toughness":

(i) Integration of flexural and tensile force-displacement curves;

(ii) Un-notched Charpy impact tests;

(iii) K^* determination.

Variation of WOF with matrix composition were presented earlier in figures 4.57 and 4.96 for flexural and tensile data respectively. Figure 4.113 shows the variation of energy absorbed during Charpy impact tests with matrix composition. Specimens which contained more than ~ 0.19 V_{NLAS} absorbed relatively little energy (10-20 kJm^{-2}) and failed in a brittle manner (figure 4.114). In contrast, specimens with a lower matrix filler content had higher values of impact toughness (values over 60 kJm^{-2} were recorded) and failed by extensive delamination and lateral splitting (figure 4.115).

Values of K^* (nominally mode I) determined from single-edge-notched beam (SENB) and notched tensile tests are summarised in tables 4.25 and 4.26 respectively. Values of K^* were calculated from peak loads and from limits of proportionality; the latter were determined from force-displacement curves and from acoustic emission data. Constraints on material availability meant that such toughness testing was performed on a limited number of materials compositions only; figure 4.116 shows the variation of K^* with matrix composition for those compositions which were tested.

Notched tension specimens which contained more than ~ 0.20 V_{NLAS} gave measured toughness values, K^*, of between ~3 and 5 $MPa{\cdot}m^{1/2}$; these values corresponded well with those obtained from the SENB tests. Even though such specimens were invariably brittle (figure 4.117) they still showed an occasional tendency to shear (figure 4.118). Figure 4.119 gives a typical force-displacement curve; note that acoustic emission activity is quite low. SENB samples which contained more than ~ 0.20 V_{NLAS} failed in either a completely brittle

manner or, equally frequently, they failed by tearing at the crack tip. Figure 4.120 shows a typical specimen which failed by tearing.

Measured K^* values of samples which contained less than ~ 0.20 V_{NLAS} were much higher (up to ~ 45 MPa·$m^{1/2}$ - refer to tables 4.25 and 4.26). Figure 4.121 demonstrates how notched tensile specimens with matrix composition HT50 / 0.02 V_{NLAS} failed by delamination, the delaminating planes emanating from the tip of the preintroduced cracks. Such specimens generated a lot of acoustic emission activity, typically up to ~100k counts at peak load *cf* 10k counts for the brittle specimens described in the previous paragraph (see figure 4.122).

SENB specimens which contained either no NLAS filler or 0.02 V_{NLAS} failed by extensive delamination (figure 4.123), occasionally accompanied by compression damage (figure 4.124). SENB specimens with matrix compositions X30 / 0.08 V_{NLAS} and HT50 / 0.09 V_{NLAS} exhibited the fibrous, tensile fracture mode shown in figures 4.125 and 4.126. The acoustic emission amplitude distribution histograms in such samples often exhibited a secondary peak (figure 4.127).

4.3.3.d Effect of sintering temperature

Figure 4.128 summarises the variations of microstructural and flexural properties with sintering temperature for samples having matrix composition HT50 / 0.33 V_{NLAS}. Marked increases in density were seen as sintering temperature was increased from 500 °C to 750 °C, and porosity decreased from ~ 35 vol% to ~ 32 vol% as sintering temperature was increased from 500 °C to 630 °C. Whilst samples sintered at 500 °C were shown by XRD to be amorphous, samples sintered at 630 °C and above contained α-quartz and β-spodumene (figure 4.129); the intensities of these latter peaks increased as sintering temperature was raised. Neither optical microscopy nor SEM detected any differences in pore structure in samples sintered at different temperatures. However, when viewed in optical DIC samples sintered at 630 °C and above exhibited the apparently crystalline appearance described in

section 4.3.3.a (*e.g.* see figure 4.36); in contrast, samples sintered at 500 °C were uniformly dull.

Whilst elastic moduli (mechanical and dynamic) remained unaffected by sintering temperature, flexural strength and flexural work of fracture decreased and ILSS increased as sintering temperature was raised. Flexural specimens which were sintered at 500 °C failed by delamination and were essentially tough; the form of their force-displacement curves and details of their failure modes were broadly similar to those described in section 4.3.3.a for samples which contained less than ~ 0.20 V_{NLAS} and which were sintered at 750 °C. In contrast, flexural specimens which were sintered at 750 °C and 850 °C were brittle.

The density and porosity of HT50 / 0.22 V_{NLAS} samples remained unchanged when the samples were resintered at 750 °C for ½ hour and 12 hours (figure 4.130). XRD revealed that resintering did not affect β-spodumene content, although slightly more α-quartz was detected in resintered samples (figure 4.131). Flexural strength, WOF and ILSS decreased when resintered, whilst flexural and dynamic moduli remained constant (figure 4.130).

XRD showed that HT50-derived composites which contained no NLAS filler remained amorphous when sintered at 500 °C and 750 °C, but a small amount of α-cristobalite was detected in samples which had been sintered at 850 °C (figure 4.132). Although no differences in microstructures could be discerned by either optical or electron microscopy for these composites, measured porosity levels did decrease as sintering temperature was raised (figure 4.133).

Mechanical property data are tabulated in tables 4.27 to 4.29. Figures 4.134 and 4.135 summarise the variations of flexural and tensile properties with sintering temperature for the unfilled HT50 composites. Additionally, figure 4.133 presents dynamic modulus and Charpy impact energies. Measured elastic moduli did not change with sintering temperature; dynamic, flexural and tensile moduli were approximately 47 GPa, 96 GPa and 125 GPa respectively.

Flexural strength, WOF, and ILSS increased when sintering temperature was raised above 500 °C. Tensile strength, WOF, and ε_{max} showed peaks at a sintering temperature of 750 °C; Charpy impact energies exhibited this trend also. In all cases, the mechanical test specimens failed by extensive delamination as described in sections 4.3.3.a and 4.3.3.b for unfilled, HT50-derived composites. SEM of fracture surfaces sintered at different temperatures failed to reveal any differences in fracture mechanisms.

4.3.3.e Reproducibility of properties

The development of new materials and fabrication technologies must necessarily include consideration of consistency and reproducibility of properties. Two aspects concerning the reproducibility of composite materials fabricated by freeze-gelation were explored: (i) batch to batch variability of nominally identical composite samples and (ii) spread of properties within a single batch of material. A batch refers to the six plates of ten specimens obtained from a single winding.

In order to assess batch to batch variability, two windings of composites with unfilled HT50 matrix and four windings of composites with matrix composition HT50 / 0.22 V_{NLAS} were fabricated. The matrix composition of the latter materials was selected because the experimental data available at the time of fabrication indicated that this composition offered a good combination of mechanical properties and processability. Composites with unfilled HT50 matrices offered very high V_f and therefore high strength and stiffness.

Microstructural parameters, flexural properties and tensile properties of these materials are presented in figures 4.136 to 4.141. The data are presented in bar chart form to aid their assimilation. The unfilled materials showed no differences in microstructure or flexural properties, although the batch 2 samples were slightly weaker in tension than the first batch. Batches 2,3 and 4 of the HT50 / 0.22 V_{NLAS} samples were fabricated 12 months after batch 1, and the accumulation of processing experience over this period was reflected in the increased

V_f and hence slightly increased elastic moduli of these later materials (figures 4.139 to 4.141 and tables 4.30 to 4.32). No large differences in flexural and tensile strengths and works of fracture *etc.* were observed, although interestingly the ILSS of batch 1 was more than twice that of batches 2, 3 and 4.

In order to assess the consistency of properties within a single batch of material, a series of flexural tests were performed on HT50 / 0.22 V_{NLAS} composite specimens taken from a single winding. All the failure modes described in section 4.3.3.a were encountered; of the 38 specimens tested, 16 failed by partial delamination (mode 1), 17 failed by extensive delamination (mode 2) and 5 were brittle (mode 3). No relation could be found between failure mode and position in the 'sandwich' during freeze-gelation (figure 4.142). The forms of the force-displacement curves, acoustic emission responses and details of fracture surfaces in the SEM were as described in section 4.3.3.a for these three modes. Flexural properties categorised by failure mode (1, 2 or 3) are given in table 4.36. It may be seen that whilst there are no differences between elastic modulus values, specimens which failed in mode 2 (partial delamination and some compression damage) exhibited the highest values of strength and work of fracture. Specimens which failed in mode 3 were weakest. It is interesting to note that specimens of high strength and toughness generated considerably more acoustic emission than weaker, more brittle specimens. Note also that the "double hump" acoustic emission amplitude distribution pattern described in section 4.3.3.a (*e.g.* see figure 4.61) was frequently observed in specimens which failed in mode 2 and occasionally in specimens which failed in mode 1.

The strength properties of ceramic-matrix composites are described frequently by statistical models based on weakest-link theory, most commonly that due to Weibull [*e.g.* see 1]. The flexural data described above were used to investigate whether the mechanical properties of freeze-gelled composites could be adequately described by a 2-parameter model which relates failure probability, P_f, to applied stress, σ, thus:

$$P_f = 1 - \exp\left[-\left(\frac{\sigma}{\sigma_0}\right)^m\right]$$ Equation 4.7

where σ_0 is a normalising parameter, which has no physical significance, and m is the Weibull modulus, a measure of sample variability. Equation 4.7 may be rearranged to give the linear relation:

$$\ln\left[\ln\left(\frac{1}{1-P_f}\right)\right] = m\ln(\sigma) - m\ln(\sigma_0)$$ Equation 4.8

Values of P_f may be calculated using the probability estimator

$$P_f = \frac{i - \frac{1}{2}}{N}$$ Equation 4.9

where *i* is the rank number of N datum points [124, 125]. Figure 4.143 gives the Weibull plot for the flexural strength data presented earlier (matrix composition HT50 / 0.22 V_{NLAS}, batch 3). Different markers were used to identify the different failure modes. Linear regression through all points gave m = 2.7 and σ_0 = 258 MPa.

4.3.3.f Flexural properties of unreinforced matrix

Unreinforced matrix specimens with nominal composition HT50 / 0.22 V_{NLAS} were prepared by heating specimens of the corresponding carbon-fibre-reinforced composite in air at 450 °C for 72 hours. Microscopy showed that this approach succeeded in pyrolysing all of the carbon fibres to leave a highly porous body (figure 4.144). XRD of a ground sample confirmed that the crystallographic composition did not differ significantly from that of the composite matrix.

Microstructural and flexural properties of the unreinforced matrix sample are summarised in table 4.37. Strength and stiffness were 2.77 MPa and 3.08 GPa respectively. The flexural force-displacement curves exhibited marked non-linearity (figure 4.145).

4.3.3.g *Bundle strength of T300 carbon fibres*

Tensile specimens of T300 bundles were tested in two conditions: (i) as-received and (ii) after the fibres had been desized at 750 °C and wrapped around the mandrel which had been used to form the composites. The bundle breaking loads, summarised in table 4.38 and figure 4.146, dropped from 112.1 N for the as-received specimens to 73.7 N for the desized/handled specimens; this represents a decrease of 34%. Thus, the manufacturer's quoted fibre strength of 3600 MPa may be corrected to 2375 MPa to give an approximate value of fibre strength in the composite studied.

4.4 DISCUSSION

4.4.1 Fabrication of composite samples

In response to the conclusions of chapter 3 concerning the limitations of the processing route, the fabrication method was modified in several ways in order to prepare the composite samples studied in this chapter. Most importantly, the method of sandwiching impregnated fibre tows between stainless steel sheets and freeze-gelling whilst under a slight pressure resulted in planar composites with uniform thickness and relatively high fibre volume fractions.

The improvements to the fabrication route and the experience gained permitted the fabrication of HT50- and X30-derived samples which contained no matrix fillers. The viscosity of the sol mixtures increased significantly as the amount of filler particles was increased, and this decreased the fibre volume fraction which could be achieved. Although individual fibre tows were discernible in the final composites (*e.g.* see figure 4.17) it appeared that all fibres were adequately coated by the sol mixture during winding.

4.4.2 Development of microstructure

4.4.2.a Porosity

In the previous chapter, the patterns of coarse, highly directional porosity were attributed to the freeze-gelation process - the pores effectively replicate the ice-crystals which grew during freeze-gelation. The materials studied in this chapter exhibited a similar pore structure, but the 'layered' effect observed in the previous chapter was not seen (*e.g.* compare figures 3.8 and 4.14). This is believed to be because of the difference in freeze-gelation conditions - the samples in the previous chapter were effectively frozen from one face only whereas the samples fabricated in this chapter were stacked and immersed in refrigerant. Porosity content and structure were unaffected by the position in this stack (section 4.3.3.e).

The partial fusing of primary colloidal silica again gave rise to a second much finer scale of porosity (*e.g.* see figures 4.24 & 4.25). This effect was particularly pronounced in samples fabricated from a small-particle-size (X30), colloidal silica sol (figure 4.82). In HT50-derived samples, however, it appeared that the presence of NLAS filler particles acted as a sintering aid (this is discussed below).

Poor fusing and significant shrinkage cracking were observed in regions which had been infiltrated with a small-particle-size (D30) colloidal silica sol. Liquid-phase infiltration was effective to a maximum depth of ~ ½ mm; as was the case with the materials analysed in the previous chapter, it is believed that exterior pores become filled during the initial infiltration cycles and this prevents infiltrant from penetrating the central regions during subsequent infiltration cycles (see section 3.4.1.b).

4.4.2.b Matrix crystallography

Two features of the matrix crystallography were considered: (i) the crystallisation of the NLAS filler particles and (ii) the densification and subsequent crystallisation of the (originally amorphous) colloidal silica. XRD analysis showed that composite samples which contained no NLAS filler remained amorphous when sintered at temperatures up to 750 °C, and that samples sintered at 850 °C contained a very small amount of α-cristobalite (figure 4.39); this latter phase is evidently a crystallisation product of the densified silica.

Studies of sintered, ground powders of NLAS showed that the crystallisation product of this filler was β-spodumene, $Li_2O \cdot Al_2O_3 \cdot 4SiO_2$ (figures 4.32, 4.34). The introduction of even small amounts of NLAS filler gave rise to strong α-quartz lines in the composites' XRD spectra (figure 4.41). Resintering had no effect on the β-spodumene XRD peak heights, but led to increases in α-quartz content (figure 4.44).

These results suggest that the presence of β-spodumene somehow aided the densification and subsequent, incomplete crystallisation of amorphous, colloidally derived silica to α-quartz. In spite of the difficulties experienced in preparing adequate TEM specimens, this proposal is supported by TEM evidence obtained from the analysis of NLAS-filled specimens:

(i) Regions which locally contained no NLAS filler tended to be amorphous and the colloidal silica particles remained partly discrete (figure 4.51) and

(ii) Regions which contained NLAS showed strong crystallinity (revealed by ED) and colloidal particles appeared to be almost completely fused (figure 4.53). Moreover, the colloidal silica particles in adjoining regions (which contained no filler) had also fused and apparently crystallised.

These conclusions correspond with optical microscopy results (figures 4.36, 4.37). Bright, apparently crystalline regions were shown by EDS (SEM) to have a high NLAS content and dull, apparently amorphous regions were shown to contain little NLAS. Composite samples which contained very high NLAS contents or which had been resintered contained more bright than dull regions (some were uniformly bright). No correlations were found between matrix appearance and porosity levels, specimen position, infiltration conditions *etc.* The boundaries between the bright and dull regions were clearly defined, and appeared to provide a preferential cracking path in mechanical test specimens (figure 4.81).

Whilst the NLAS filler particles remained discrete (and amorphous) in composite samples sintered at 500 °C, the matrix in samples sintered at 750 °C appeared homogeneous and the NLAS had evidently flowed and crystallised. The distribution of filler particles throughout the composite samples was uniform and appeared to be unaffected by local microstructural features such as fibre volume fraction or porosity. Filler particles were observed within the threads of material between plate-like pores, and evidently did not affect the freeze-gelation process (see figures 3.56 and 4.48).

4.4.3 Mechanical properties

A complex interplay between several, non-independent materials parameters makes it difficult to provide a comprehensive analysis of the mechanical performance of the composite samples described in the preceding sections. As the volume fraction of glass-ceramic filler in the matrix slurry (V_{NLAS}) was increased:

- the fibre volume fraction in the composite decreased;
- the matrix volume fraction showed a corresponding increase;
- the overall degree of composite porosity increased;
- the properties of the matrix changed (*e.g.* owing to crystallisation of sol-gel-derived silica).

Thus, in this section, an effort is made to identify the important factors which affect the composites' mechanical properties.

4.4.3.a Elastic behaviour

Figure 4.147 compares flexural, tensile and ultrasonic (time-of-flight) elastic moduli with theoretical values which were calculated by using a modified rule-of-mixtures relationship:

$$E_c = E_f V_f + (1 - V_f) E_m \qquad \text{Equation 4.10}$$

where the subscripts f and m have their usual significance. The matrix elastic modulus (E_m) was calculated by using a silica/NLAS mixtures relationship modified by an exponential term to accommodate matrix porosity:

$$E_m = \left[V_{NLAS} E_{NLAS} + (1 - V_{NLAS}) E_{silica} \right] \exp(-\alpha p) \qquad \text{Equation 4.11}$$

where E_{silica} and E_{NLAS} represent the elastic moduli of fully dense amorphous silica (= 72 GPa) and NLAS (=86 GPa [23]) respectively, p represents porosity volume fraction and α is a constant. Although simplistic, the utility of equation 4.11 has been demonstrated previously;

the elastic modulus of pyrolysed HT50 / 0.22 V_{NLAS} samples, described in section 4.3.3.f, is adequately described by equation 4.11 when $\alpha = 5$ (see figure 4.148).

Linear regression through the three sets of data points in figure 4.147 show that the measured tensile, flexural and dynamic moduli attained, respectively, 97%, 73% and 33% of the predicted modulus. Thus, the tensile data matched the predictions reasonably well. The fact that the flexural moduli were consistently lower than the the tensile moduli may be attributed in part to the questionable assumption that the composite specimens behaved as linear, elastic beams when tested in flexure, *i.e.* the beam-bending equations used to calculate materials parameters from force-displacement data do not apply exactly.

4.4.3.b Comparison of dynamic and mechanical elastic moduli

It is confusing that the dynamic modulus measurements on the composite samples described in chapter 3 were slightly greater than the mechanically determined (flexural) moduli, whereas the dynamic moduli measured in this chapter were consistently lower than flexural or tensile moduli (section 4.4.3.a). As the reasons why this should be the case are not properly understood, the following discussion is speculative.

The wavelengths, λ, of the ultrasonic waves which passed through the specimens may be calculated from the relationship $c = \lambda f$. The frequency, f, of the longitudinal ultrasonic waves used was 150 kHz and measured wave velocities, c, ranged from ~ 2500 ms^{-1} to ~ 6000 ms^{-1} (table 4.11), indicating that λ would be expected to vary between 16 mm and 40 mm. Since this wavelength is of the order of the specimen dimensions, it was not considered appropriate to apply correction factors which accommodate Poisson contraction effects in those cases where the ultrasonic waves pass through 'bulk' rather than 'rod' specimens.

The point was made in chapter 3 that the abundance of interfaces in freeze-gelled composites (particularly those associated with porosity) could retard the passage of the ultrasonic waves and so lead to increased times of flight. The corresponding decreases in wave velocity would

in turn lead to lower values of dynamic modulus. Whilst such an explanation would explain why the dynamic moduli of the composites investigated in this chapter were exceeded by the mechanically determined moduli (*i.e.* flexural and tensile), it still leaves the question of why the dynamic moduli of the composites examined in chapter 3 were greater than the flexural moduli. The structures of the composites investigated in chapter 3 and in this chapter were essentially similar with the notable exception that the composites described in chapter 3 were very non-planar. Feasible consequences of this are that (i) the beam-bending equations used to calculate flexural modulus gave false values and (ii) that the ultrasonic waves travelled through the specimens in an unpredictable manner.

4.4.3.c Flexural, tensile and interlaminar shear strength

Predictions of composite strength need to consider the series of failure processes which lead to fracture. Section 1.2.1 reviewed a simplistic model of tensile strength in which matrix fracture results in the applied load being borne exclusively by the reinforcing fibres. The composite failure stress (σ_c) may then be given to a first approximation by equation 1.6.

Figure 4.149 presents a comparison of predicted versus measured tensile strengths based on assumed fibre strengths of 2375 MPa and 3600 MPa for handled and virgin fibres respectively (see section 4.3.3.g). The predicted strength values shown in figure 4.149 generally exceeded the measured values; the fitted line through the data (solid line) is consistent with an apparent fibre strength of 1760 MPa. Although equation 1.6 suffers from several limitations (*e.g.* it ignores contributions to strength from the matrix and the statistical nature of fibre fracture) the data illustrate that one reason why the potential tensile strengths of the composites are not being realised is that the fibres become damaged during processing.

The complexity of the relationships between tensile and flexural strengths was reviewed in section 1.2.3.a. It should be emphasised that the term "flexural strength" should more properly be interpreted as "nominal peak flexural stress" for samples which failed in modes

other than pure tension, because of the uncertainty in applying beam-bending equations derived for linear, elastic materials.

Figure 4.150 demonstrates the poor overall correlation between measured tensile and flexural strength values for all the composites considered in this chapter (*i.e.* HT50- and X30-derived, unfilled and NLAS-filled matrices). However, figure 4.150 does reveal a linear relationship between flexural and tensile strengths for brittle samples, *i.e.* those which failed in tension (mode I) when tested in tension and flexure. Linear regression of these data indicates that flexural strengths exceeded tensile strengths by ~100%. This may be explained by considering the relative stressed volumes in the two types of test specimen; the higher stressed volume in the tensile specimen means that there is a higher probability, at a given applied load, of finding a flaw of critical size which will lead to fracture in such a brittle material.

The remaining data in figure 4.150 (*i.e.* those which failed by complete or partial delamination when tested in flexure) exhibit relatively little variation in flexural strength as tensile strength increases. The apparently linear relationship between tensile strength and fibre volume fraction shown in figure 4.149 suggests that the composite tensile strengths were principally controlled by the reinforcing fibres.

However, the fact that the majority of composite samples failed by delamination when tested in flexure (see section 4.3.3.a) suggests that flexural strength was dominated by the matrix. Since flexural strengths increased only slightly with increasing interlaminar shear strength (figure 4.151), it is feasible that the high levels of matrix porosity effectively masked any differences in matrix properties (samples which contained more than ~ 0.22 V_{NLAS} failed in a brittle, tensile mode in both flexure and short beam shear (ILSS) configurations, and these data are excluded from figure 4.151). The dependence of flexural strength on matrix porosity was discussed by Sambell *et al* [8] in a paper describing work carried out on unidirectional, carbon-fibre-reinforced borosilicate glass. These workers reported that the flexural strength

of samples which contained ~35 vol% matrix porosity was ~30% that of the near-fully dense material (see also the review by Phillips [9]).

The variation of interlaminar shear strength with matrix composition described in figure 4.56 will be a function of matrix volume fraction, porosity and composition:

◊ *Matrix volume fraction*

The rapid decrease in fibre volume fraction as V_{NLAS} increases (figure 4.13) implies that matrix volume fraction increases as V_{NLAS} is increased, thereby providing more opportunity for matrix-dominated fracture mechanisms (such as interlaminar shear) to occur.

◊ *Porosity*

Total porosity volume fraction shows a minimum at $V_{NLAS} \sim 0.19$ (figure 4.12); this matrix composition corresponds approximately with that which gave rise to the highest measured values of ILSS. It is well-known in the field of polymer-matrix composites that ILSS decreases as matrix porosity increases [*e.g.* see 126]. Data from experiments performed on freeze-gelled composites sintered at different temperatures support the proposition that ILSS is influenced by matrix porosity; increases in ILSS and decreases in porosity as sintering temperature was increased over the range 500 °C to 850 °C were observed in both unfilled and highly-filled composites (section 4.3.3.d).

Similarly, values of ILSS reported for other ceramic-matrix composite systems are generally higher than those measured for freeze-gelled composites. For example, Sambell *et al* [8] reported an ILSS of 48 MPa for a unidirectional carbon-fibre-reinforced soda glass composite prepared by hot pressing; this compares with 5 - 10 MPa for freeze-gelled, carbon fibre/unfilled silica composites which had a similar fibre volume fraction. This difference may also be attributed to the high levels of matrix porosity in freeze-gelled systems.

◊ *Matrix composition and crystallography*

The mechanical properties of glass-ceramics, including shear strength and mode II toughness, are expected to be superior to those of amorphous silica or quartz. Also, it has been

demonstrated that the NLAS filler acts as a sintering aid (reducing fine-scale matrix porosity) and encourages the amorphous silica matrix to crystallise to quartz, thereby changing the mechanical properties of the matrix.

4.4.3.d Damage mechanisms and toughness measurements

The two principal aspects of toughness which need to be considered during the materials development process are (i) the total amount of energy required to cause complete specimen/component failure (however failure is defined) and (ii) the sensitivity of strength to the presence of flaws such as cracks. The emphasis during this study was on whether freeze-gelled composites offered a practicable degree of damage tolerance and energy consumption during failure. Thus, WOF and Charpy impact measurements were employed in order to provide a straightforward, comparative measure of failure energy, and notched beam and notched tension geometries were designed to assess notch sensitivity. The measurement of more rigorously defined fracture parameters (*e.g.* strain energy release rates, stress intensity factors) would be required at a later stage (*e.g.* when gathering data for design purposes) and did not fall within the scope of this project.

Figure 4.93 demonstrated that for all matrix compositions (and hence all values of V_f) the onset of tensile damage, as indicated by the deviation from linearity of the stress-strain curve and from acoustic emission data, occurred at a mean measured strain of ~ 0.15%. The values of stress at proportional limit (figure 4.92) reduced to this same mean measured strain when divided by measured tensile modulus. Note also that the mean first-damage strain of 0.15% is an order of magnitude lower than the quoted failure strain of the T300 carbon fibres (1.5%, see table 1.1).

These data imply that the first damage in the composites occurred within the matrix, an observation that accords with the generally accepted picture of the mechanical behaviour of ceramic-matrix composites. However, the matrix cracking strain did not increase with fibre

volume fraction; this is contrary to the models of mechanical behaviour of ceramic-matrix composites reviewed in section 1.2.1. Further, the matrix failure strain appeared not to vary with matrix composition or degree of matrix crystallisation. It is feasible that the initial damage in freeze-gelled ceramic-matrix composites is associated with the growth of pre-existing matrix pores rather than the widespread generation of transverse matrix cracks of the type described by Aveston *et al* (section 1.2.1). Indeed, it was perhaps surprising that no evidence of transverse matrix cracking could be found; one should recall that the formation of regularly spaced matrix cracks in some samples described in chapter 3 was attributed to the generation of high residual stresses associated with the formation of α-cristobalite. It is possible also that the extensive matrix porosity obscured any transverse matrix cracks which did form.

A conceivable explanation for the brittle nature, in tension and in flexure, of HT50-derived composites which contained more than $\sim 0.22\ V_{NLAS}$ is that these materials contained insufficient fibres for specimen integrity to be maintained once the matrix failure strain had been reached, *i.e.* the critical fibre volume fraction described in section 1.2.1 was not reached. Thus, when matrix cracking (of whatever form) commenced, there were insufficient fibres to accommodate the additional load which was carried by the matrix prior to cracking. In such materials, the localised nature of damage and the lack of fibre-associated, energy-consuming mechanisms both contributed to the low works of fracture in tension and flexure. These samples were notch-sensitive, *e.g.* the unnotched and notched tensile strengths of samples with matrix composition HT50 / $0.22\ V_{NLAS}$ were 101 MPa and 48 MPa respectively (see table 4.39). There was no evidence that the brittle response of these samples was associated with any fibre-matrix interactions (whether chemical or mechanical); areas of apparent good and poor contact between fibres and matrix were observed in highly filled and unfilled composites alike. Note that the K^* values presented in tables 4.25 and 4.26 could, in the cases of the linearly brittle samples HT50 / $0.22\ V_{NLAS}$ and X30 / $0.21\ V_{NLAS}$, be referred to as K_1^*.

The results presented in section 4.3.3.b described how composite samples which contained less than ~ 0.22 V_{NLAS} matrix filler (and consequently more than ~ 0.15 V_f) exhibited an essentially tough failure mode. Although the classical matrix cracking/fibre-matrix debonding/fibre-bridging/fibre fracture and pullout sequence (*i.e.* the conventional picture of unidirectionally reinforced ceramic-matrix composites) was not observed, fractographic analysis of the 'tough' flexural and tensile specimens provided direct evidence that several energy-absorbing, fibre-associated toughening mechanisms were active in these materials: fibre-bridging across matrix cracks, filament-bridging across delamination planes and fibre pullout. Such processes contributed to the relatively high works of fracture (up to ~ 20 kJm^{-2} in flexure and ~ 60 kJm^{-2} in tension). These materials were less notch-sensitive, *e.g.* the unnotched and notched tensile strengths of samples with matrix composition HT50 / 0.09 V_{NLAS} were 333 MPa and 278 MPa respectively (table 4.39). The delocalisation of damage accumulation in such specimens may account for the lack of registration between different strain gauge outputs which was sometimes seen as tests progressed (*e.g.* figure 4.101) and may also explain the occasional unpredictability of transverse strain (and hence Poisson's ratio) measurements (figures 4.98, 4.99). The process zones in such materials were so large that the concept of a stress intensity factor was probably invalid; K^* values were useful comparators.

The strong influence of fibre content on measured toughness is illustrated by figure 4.152. Tensile and flexural WOF values and un-notched Charpy impact energies increased with fibre volume fraction. Whilst flexural WOF and Charpy data were in reasonable agreement, they were generally exceeded by tensile works of fracture.

4.4.3.e Acoustic emission

Throughout this work, one application of acoustic emission monitoring was to determine the onset of damage in mechanical test specimens (flexural and tensile). The good correlation

between AE-determined 'proportional limits' and true proportional limits determined from mechanical response curves is illustrated in figures 4.153 & 4.154 for flexural and tensile data respectively. These data suggest that little damage occurred within the specimens prior to the onset of widescale damage. This is perhaps surprising in view of the high porosities of the samples; for example, other authors have attributed acoustic emission activity prior to matrix cracking in SiC/glass-ceramic composites to subcritical crack growth emanating from matrix porosity [47]. One reasonable interpretation is that the abundance of defects in these materials caused damage to initiate earlier than would have been the case had the matrices been fully dense, and that this damage was detected by AE and reflected in the mechanical response of the specimens immediately.

Acoustic emission data and measured works of fracture from flexural tests showed no correlation (figure 4.155), reflecting the variety of different failure modes which were encountered in flexural samples. However, the relationship between tensile work of fracture was reasonably clearly defined (figure 4.156).

The development of acoustic emission amplitude distribution histograms as mechanical tests progressed gave an insight into the evolution of damage in different samples. Flexural samples which failed by gross delamination (mode II in the notation of figure 4.62) typically exhibited a bimodal AE distribution histogram in the later stages of each test (*e.g.* see figure 4.61). The secondary peaks coincided with the development of extensive interactions between neighbouring laminae and the high amplitudes and relatively high energies (indicated by channel number) indicate that such interactions were quite energetic; the frictional sliding of adjoining laminae would indeed be expected to require energy and thereby contribute to the composite's toughness.

The occurrence of such bimodal AE distribution histograms in other test configurations suggested that similar delamination events were occurring. The very slight second peak in the histograms of tensile samples with unfilled HT50 matrix (*e.g.* figure 4.103) may be attributed

to the delamination cracking detected by SEM analysis. More obviously, histograms from notched tensile samples (*e.g.* figure 4.127) showed very pronounced peaks when these samples failed by delamination (figure 4.121).

4.4.3.f Effectiveness of the materials studied as composite materials

A key element of this investigation was the development and refinement of a fabrication process for ceramic-matrix composites which employed freeze-gelation. Thus, it was pertinent to assess the factors which influenced the variability of materials properties (i) between different batches and (ii) within a single batch. These results were presented in section 4.3.3.e.

A total of six batches with two different matrix compositions (unfilled and HT50 / 0.22 V_{NLAS}) confirmed that the filament winding/freeze-gelation process was capable of producing composite plates of consistent quality. The superior performances of batches 2 - 4 of the filled samples over that of batch 1 (*e.g.* see figures 4.139 - 4.131) may be attributed to the experience gained and the process refinements which were made between fabricating batch 1 and fabricating batches 2 - 4. The matrix composition HT50 / 0.22 V_{NLAS} was selected on the basis of the information available at the time; composites with this composition appeared to offer the best combination of processability, fibre volume fraction and mechanical properties. With the advantage of hindsight, it would perhaps have been more valuable to have performed this exercise with composites which exhibited higher toughness, *e.g.* those with matrix composition HT50 / 0.09 V_{NLAS}.

Section 4.3.3.e also presented results on the variability of microstructural and mechanical properties of specimens from a single batch. This was in order to investigate the possibility that such variations could be related to the porosity of individual specimens and, moreover, that porosity varied systematically with specimen position during freeze-gelation (see also

figure 4.26). No such relationships could be found. Also, the fact that specimens from a single batch exhibited tough and brittle responses contributed to a low measured Weibull modulus (m = 2.7), although the applicability of such weakest-link statistics to non-brittle materials is questionable.

Previous work with unreinforced, silica-based systems prepared by freeze-gelation indicates that flexural strength and toughness (work of fracture) typically lie within the ranges 1 - 30 MPa and 0.1 - 1 Jm^{-2} respectively. Comparison of these data with the highest recorded values of tensile strength and work of fracture of the composites studied (> 600 MPa and > 55 kJm^{-2} respectively) confirms the effectiveness of the composites fabricated. This may be seen more readily from a comparison of the tensile stress-strain curves of the unreinforced matrix, T300 carbon fibres and a typical freeze-gelled composite (figure 4.157).

Table 4.40 summarises the mechanical properties of the most effective materials developed during this project. These properties compare well with similar composite systems which have been reported in the literature. In their early work, Sambell *et al* [8] described how unidirectional, carbon-fibre-reinforced silica and LAS glass-ceramic composites (prepared by hot-pressing) had flexural strengths of 570 MPa and 680 MPa respectively, and flexural works of fracture of 4.3 kJm^{-2} and 3.0 kJm^{-2} respectively. More recently, flexural strengths of up to 645 MPa have been reported for carbon-fibre-reinforced LAS composites prepared by a slurry/hot-pressing route [127]. The most likely reason why these materials exhibited higher flexural strengths than the freeze-gelled composites (up to 244 MPa) is that hot-pressing achieved a low matrix porosity (total reported porosity was ~ 2 vol%). It is believed that the high degree of matrix consolidation achieved by hot-pressing accounted also for the reported interlaminar shear strength value of nearly 50 MPa in Sambell's composites, *cf* up to 36 MPa for the freeze-gelled composites. This supports the idea expressed earlier that matrix porosity reduces interlaminar shear strength in freeze-gelled composites.

In order to place the properties of freeze-gelled composites into context, it is useful to compare their properties with those of other ceramic-matrix composites. In terms of product maturity and commercial exploitation, one of the more successful ceramic-matrix composite systems is the family of silicon-carbide-reinforced glass-ceramics (*e.g.* SiC/LAS). As described in section 1.2.4.b, these are produced by slurry infiltration of fibres to produce tapes which are subsequently stacked and hot-pressed in shaped moulds. Typical properties of SiC/LAS and carbon/SiO_2 (fabricated by freeze-gelation) are summarised in table 4.41; the SiC/LAS composites outperform the carbon/SiO_2 materials in terms of mechanical properties and maximum use temperature.

However, it should be borne in mind that the principal objective of this project was to exploit the freeze-gelation concept to fabricate *low-cost* ceramic-matrix composites which exhibit reasonable mechanical properties at slightly elevated temperatures. As mentioned in section 1.4.2, this contrasts with the incentive behind the development of the SiC/LAS composites (*i.e.* excellent high- temperature mechanical performance). Thus, table 4.41 also presents estimated price data for the two composite systems. In the case of the freeze-gelled materials, the cost of £25/kg was calculated from the prices of carbon fibres and colloidal silica (~ £40/kg and ~ £5.50/kg respectively). A figure of £2500/kg is a reasonable estimate for the SiC/LAS system (acquiring reliable information proved to be difficult - Bader [26] recently estimated that the price of continuous SiC-reinforced ceramic-matrix composite components was of the order of £5000/kg).

Although these data are only estimates and therefore subject to possible variation, they do indicate that the freeze-gelled composites are two orders of magnitude cheaper than the SiC/glass-ceramic composites. These raw cost figures have also been used in table 4.41 to calculate cost : strength ratios (by dividing price per unit weight by flexural strength) of £2.00/MPa for the SiC/LAS system and £0.1/MPa for the freeze-gelled composites. On this basis, the freeze-gelled composites are likely to be approximately twenty times more cost-

effective than the SiC-based materials produced by hot-pressing (provided that appropriate design requirements are satisfied).

4.5 CONCLUSIONS

- The filament winding/freeze-gelation process developed in Chapter 3 was modified to permit the fabrication of planar specimens with uniform thickness. This was achieved by sandwiching impregnated fibre tows between stainless steel sheets prior to freeze-gelation.
- A series of carbon-fibre-reinforced, SiO_2/NLAS (β-spodumene) composites was prepared. The volume fraction of NLAS matrix filler introduced was varied between 0.02 and 0.40. Also, carbon fibre/SiO_2 (HT50) composites were prepared which contained no matrix filler.
- Total porosity volume fraction was in the range 0.23 to 0.43. Values of V_f ranged between 0.09 and 0.46.
- It is believed that the porosity patterns in the composites replicated the ice crystals which grew during freeze-gelation. These patterns were unaffected by the presence of matrix fillers or by position in the 'sandwich stack' during freeze-gelation.
- The fact that freeze-gelation was carried out by completely immersing specimens in refrigerant (as opposed to freezing from one side only as was the case with the samples described in chapter 3) is believed to account for the uniformity of pore structure throughout specimen thickness; the layered pore structures described in chapter 3 were not prominent in the samples considered in this chapter.
- As the NLAS content in the matrix slurry was increased:
  - the fibre volume fraction in the composite decreased;
  - the matrix volume fraction showed a corresponding increase;
  - the overall degree of composite porosity increased.
- HT50-derived matrices which contained no fillers remained essentially amorphous when sintered at temperatures up to 750 °C.

- The NLAS glass-ceramic filler particles were amorphous in the as-received condition and contained large amounts of β-spodumene when sintered above 630 °C.
- The presence of even small quantities of NLAS filler particles in the composite matrix aided the densification of the amorphous, colloidal silica particles and their subsequent (incomplete) crystallisation to α-quartz when sintered at 630 °C and above. Whilst individual filler particles were easily discernible in composites sintered at 500 °C, the matrix appeared homogeneous in composites sintered at 630 °C and above.
- No evidence of any interfacial reactions could be found. The efficiency with which the fibres were coated by the matrix did not appear to be related to matrix composition.
- The highest recorded value of tensile elastic modulus was 130 GPa. Measured tensile and flexural moduli were 97% and 73% respectively of the values predicted by a simple rule of mixtures.
- Composites which contained large amounts of NLAS filler ($V_{NLAS} \sim 0.22$ and above) were brittle in both tension and flexure. This may be attributed partly to the low fibre volume fractions in these samples, a consequence of the difficulty in pulling the fibre tows through the viscous, highly filled slurry prior to filament winding.
- Composites which contained less NLAS filler (up to $\sim 0.19\ V_{NLAS}$) or no filler at all exhibited a tough, fibrous fracture mode in tension and failed in flexure by extensive or partial delamination.
- The optimum matrix composition for a useful balance of mechanical properties is HT50 / 0.05 - 0.10 V_{NLAS}. The optimum sintering temperature is 750 °C.
- Non-linearity in tensile stress-strain data occurred at a strain of ~ 0.15% for composites of all matrix compositions and was attributed to the initiation of matrix damage, most probably associated with the growth of pre-existing matrix pores. Transverse matrix cracking (*i.e.* of the type described by Aveston *et al*) was not observed in any case,

although it is feasible that any such cracking might be modified and/or obscured by porosity.

- Maximum recorded values of tensile and flexural strength were 630 MPa and 250 MPa respectively.
- Tensile strength was fibre-dominated – a linear relationship was found between tensile strength and fibre volume fraction which indicated that effective fibre strength was ~ 1760 MPa *cf* the manufacturer's value of 3600 MPa. The suggestion that the fibres are degraded during processing was confirmed by fibre bundle tests; the breaking load of handled fibres was 34% lower than 'as-received' fibres.
- Flexural strength appeared to be matrix-dominated.
- Measured values of interlaminar shear strength were low (5 - 36 MPa) compared with data reported for similar ceramic-matrix composite systems. This was attributed principally to the high levels of matrix porosity.
- Measured values of Poisson's ratio lay in the range 0.08 - 0.24.
- Maximum recorded values of work of fracture were 60 kJm^{-2} and 20 kJm^{-2} for the tensile and flexural data respectively.
- The tough composite samples (*i.e.* those which contained up to ~ 0.19 V_{NLAS}) exhibited several, desirable, energy-consuming mechanisms which contributed to work of fracture: fibre-bridging across matrix cracks, filament bridging across delamination planes and fibre pullout. The strong dependence of these processes on fibre content was reflected in the strong correlations between fibre volume fraction and works of fracture.
- Notched tension and single-edge-notched-beam tests indicated that the tough samples were not sensitive to the presence of notches. The brittle samples were notch-sensitive.
- Values of dynamic elastic modulus were consistently lower than mechanically determined moduli. It is feasible that the abundance of scattering centres in the

composite samples (*e.g.* interfaces associated with the extensive matrix porosity) could lead to low measured times of flight and hence low values of dynamic modulus.

- The reasons why the dynamic moduli of the composite samples studied in chapter 3 exceeded the fllexural moduli are not completely understood. It is possible that this result may be attributed in part to the lack of validity of the beam-bending equations used to determine the flexural moduli of the non-planar specimens.
- The reproducibility of the composites has been assessed in terms of:
  - batch - to - batch variability of mechanical and microstructural properties;
  - variability of mechanical and microstructural properties within a single batch.
- The utility of acoustic emission measurements during mechanical testing was demonstrated. In particular:
  - A good correlation was obtained between proportional limits obtained from the acoustic emission data and those determined from the force-displacement curves;
  - A second, high-energy peak in some amplitude distribution histograms was attributed to the sliding of laminae in specimens which had delaminated;
- A reasonable correlation was obtained between acoustic emission counts and tensile work of fracture.

- The composite samples described in this chapter demonstrate the viability of freeze-gelation as a fabrication route to useful ceramic-matrix composites. The objectives outlined in chapter 2 (and, more generally, in section 1.4.2) have been successfully fulfilled.

Chapter 5

FUTURE WORK

Whilst the work described in this thesis has illustrated the viability of the freeze-gelation concept for fabricating low-cost, unidirectionally reinforced ceramic-matrix composites which exhibit a useful combination of mechanical properties, there clearly remains substantial scope for further research. A sensible next phase would be to devise projects which centre around the development of components; this would serve not only to demonstrate the technology, but would also necessitate improvements in (for example) fabrication methods, understanding of the materials science and composites science of freeze-gelled materials, design rules, environmental resistance (*e.g.* thermal shock, mechanical fatigue), and joining methods. However, care should be taken to ensure that future research does not contradict the low-cost ethos of the freeze-gelation approach.

In view of the poor oxidation resistance of carbon fibres beyond ~ 450 °C, the incorporation of fibres more appropriate to high temperature applications into freeze-gelled composites should be explored, *e.g.* oxide ceramic fibres. Also, the applicability of freeze-gelation techniques to the preparation of composites with different matrices should be investigated, *e.g.* zirconia, alumina – the feasibility of freeze-gelling such non-silica, oxide systems on a small scale has been demonstrated previously [98]. The possibility of optimising particular fibre/matrix combinations by controlling the characteristics of the fibre-matrix interface is also an important area for future study – coating the fibres by sol-gel methods prior to their incorporation into the composite matrix is an obvious route to pursue.

The filament winding method used to manufacture the materials explored in this thesis is limited in the range of component geometries and fibre layups which can be achieved. Sol-transfer moulding (the direct analogue of resin-transfer moulding used in the field of

polymer-matrix composites) has the potential for producing three-dimensional shapes with complex reinforcement architectures.

The extensive porosity which is a key microstructural feature of freeze-gelled composites will inevitably be expensive to remove completely, and should probably be accepted as an intrinsic feature of such materials. The porosity may offer advantages in terms of developing joining technologies, or in applications areas such as high-temperature filtration. It is clear that conventional models of mechanical behaviour (particularly fracture behaviour) of brittle-matrix composites cannot be applied to freeze-gelled materials and that this is attributable in part to the high levels of porosity. Thus, alternative models of mechanical performance need to be developed.

REFERENCES CITED

1 Kelly, A. and Macmillan, N.H. "Strong Solids" (Oxford University Press, 1986).

2 Brandt, A.M., "Cement-Based Composites; Materials, Mechanical Properties and Performance" (E & FN Spon, London, 1995).

3 Bentur, A. and Mindess, S., "Fibre Reinforced Cementitious Composites" (Elsevier, Barking, UK, 1990).

4 Phillips, D.C., Composites Science and Technology, **40**, 1991, pp. 1-17.

5 Rühle, M. and Evans, A.G., Progress in Materials Science, **33**, 1989, pp. 85-167.

6 Wiederhorn, S.M., Annual Review of Materials Science, **14**, 1984, pp. 373-403.

7 Faber, K.T., Ceramic Engineering and Science Proceeedings, **5**, 1984, pp. 408-439.

8 Sambell, R.A., Briggs, A., Phillips, D.C. and Bowen, D.H., Journal of Materials Science, **7**, 1972, pp. 676-681.

9 Phillips, D.C., In: "Handbook of Composites, Volume 4 - Fabrication of Composites", Eds. Kelly, A. and Mileiko (Elsevier Science Publishers, London, 1983), pp. 373-428.

10 Marshall, D.B. and Cox, B.N., Acta Metallurgica, **35** (11), 1987, pp. 2607-2619.

11 Jansson, S. and Leckie, F.A., Acta Metallurgica et Materialia, **40** (11), 1992, pp. 2967-2978.

12 Aveston, J. and Kelly, A., Journal of Materials Science, **8**, 1973, pp. 352-362.

13 Partridge, P.G. and Ward-Close, C.M., International Materials Reviews, **31** (1), 1993, pp. 1-24.

14 Yurgatis, S.W., MacGibbon, B.S. and Mulvaney, P., Journal of Materials Science, **27**, 1992, pp. 6679-6686.

15 Dharani, L.R. and Tang, H., Journal of Composite Materials, **23** (4), 1989, pp. 308-325.

16 Mah, T., Mendiratta, M.G., Katz, A.P. and Mazdiyazni, K.S., Ceramic Bulletin (American Ceramic Society), **66** (2), 1987, pp. 304-308.

17 Marshall, D.B. and Ritter, J.E., Ceramic Bulletin (American Ceramic Society), **66** (2), 1987, pp. 309-317.

18 Davidge, R.W., In: "Application of Fracture Mechanics to Composite Materials", Ed. Friedrich, K., Elsevier, Oxford, 1989, pp. 547-569.

19 Sakai, M., Journal of the Ceramic Society of Japan, **99** (10), 1991, pp. 983-992.

20 Aveston, J., Cooper, G.A. and Kelly, A., In "The Properties Of Fibre Composites" (IPC Science and Technology Press, Guildford, 1971), pp. 15-26.

21 Budiansky, B., Hutchinson, J.W. and Evans, A.G., Journal of the Mechanics and Physics of Solids, **34** (2), 1986, pp. 167-189.

22 McCartney, L.N., Proceedings of the Royal Society of London, A409, 1987, pp. 329-350.

23 Prewo, K.M., Journal of Materials Science, **21**, 1986, pp. 3590-3596.

24 Cooke, T.F., Journal of the American Ceramic Society, **74** (12), 1991, pp. 2959-2978.

25 Bunsell, A.R. (Ed.), "Fibre Reinforcements for Composite Materials" (Elsevier, Oxford, 1988).

26 Bader, M.G., Materials World, January 1993, pp. 22-26.

27 Mah, T., Mendiratta, A.P., Katz, A.P., Ruh, R. and Mazdiyazni, K.S., Journal of the American Ceramic Society, **68** (1), 1985, pp. C27-C30.

28 Davidge, R.W., Composites, **18** (2), 1987, pp. 92-98.

29 McMillan, P.W., "Glass Ceramics 2nd Edition" (Academic Press, London, 1979).

30 Strnad, Z., "Glass-Ceramic Materials" (Elsevier, Oxford, 1986).

31 Rawson, H., "Inorganic Glass-Forming Systems" (Academic Press Ltd., London, 1967).

32 Kingery, W.D., Bowen, H.K. and Uhlmann, D.R., "Introduction to Ceramics, 2nd Edition" (John Wiley and Sons, Chichester, 1976).

33 Phillips, D.C., Sambell, R.A.J. and Bowen, D.H., Journal of Materials Science, **7**, 1972, pp. 1454-1464.

34 Cao, H.C., Bischoff, E., Sbaizero, O., Rühle, M., Evans, A.G., Marshall, D.B. and Brennan, J.J., Journal of the American Ceramic Society, **73** (6), 1990, pp. 1691-1699.

35 Evans, A.G., Zok, F.W. and Davis, J., Composites Science and Technology, **42**, 1991, pp. 3-24.

36 Cooper, R.F. and Chyung, K., Journal of Materials Science, **22**, 1987, pp. 3148-3160.

37 Morrell, R. and McCartney, L.N., British Ceramic Transactions, **92** (1), 1993, pp. 1-7.

38 Davidge, R.W. and Davies, J.J., International Journal of High Technology Ceramics, **4**, 1988, pp. 341-358.

39 Curtis, P.T., "CRAG Test Methods for the Measurement of the Engineering Properties of Fibre Reinforced Plastics", Royal Aircraft Establishment Report No. 85099, 1985.

40 Sbaizero, O. and Evans, A.G., Journal of the American Ceramic Society, **69** (6), 1986, pp. 481-486.

41 Morrell, R., Presentation at : "Mechanical Testing and Standards for Ceramics", Institution of Mechanical Engineers, London, 11 June 1993.

42 Harris, B., Dorey, S.E. and Cooke, R.G., Composites Science and Technology, **31**, 1988, pp. 121-141.

43 ASTM E1316, "Terminology for Nondestructive Examination", 1992.

44 Scott, I.G., "Basic Acoustic Emission" (Gordon and Breach Science Publishers, London, 1991).

45 Kline, R.A., In "Manual on Experimental Methods for Mechanical Testing of Composites", Editors: Pendleton, R.L. and Tuttle, M.L., Elsevier Applied Science Publishers, London, 1989, pp. 105-113.

46 Bunsell, A.R., and Harris, B., Composites, **5**, 1974, p. 157.

47 Harris, B., Habib, F.A. and Cooke, R.G., Proceedings of the Royal Society of London, **A437**, 1992, pp. 109-131.

48 Faudree, M., Baer, E., Hiltner, A.and Collister, J., Journal of Composite Materials, **22** (12), 1988, pp. 1170-1195.

49 Barré, S. and Benzeggagh, M.L., Composites, **52**, 1994, pp. 369-376.

50 Guild, F.J., Phillips, M.G. and Harris, B., In: "Conference Proceedings of the First International Symposium on Acoustic Emission from Reinforced Composites, San Francisco, USA, 1983" (The Society of the Plastics Industry, 1983).

51 Strife, J.R., Brennan, J.J., and Prewo, K.M., Ceramic Engineering and Science Proceedings, **11** (7), 1990, pp. 871-919.

52 Lange, F.F., Lam, D.C., Sudre, O., Flinn, B.D., Folsom, C., Velamakanni, B.V., Zok, F.W. and Evans, A.G., Materials Science and Engineering, **A144**, 1991, pp. 143-152.

53 Cornie, J.A., Chiang, Y.M., Uhlmann, D.R., Mortensen, A. and Collins, J.M. Ceramic Bulletin (American Ceramic Society), **65** (2), 1986, pp. 293-304.

54 Sheppard, L.M., Ceramic Bulletin (American Ceramic Society), **69** (4), 1990, pp. 666-673.

55 Prewo, K.M. and Brennan, J.J., Journal of Materials Science, **15**, 1980, pp. 463-468.

56 Prewo, K.M. and Brennan, J.J., Journal of Materials Science, **17**, 1982, pp. 1201-1206.

57 Brennan, J.J. and Prewo, K.M., Journal of Materials Science, **17**, 1982, pp. 2371-2383.

58 Hegeler, H. and Brückner, R., Journal of Materials Science, **24**, 1989, pp. 1191-94.

59 Guo, J.K., Mao, Z.Q., Bao, C.D., Wang, R.H. and Yan, D.S, Journal of Materials Science, **17**, 1982, pp. 3611-16.

60 Newkirk, M.S., Lesher, H.D., White, D.R., Kennedy, C.R., Urquhart, A.W. and Clarr, T.D., Ceramic Engineering Science and Proceedings, **8** (7/8), 1987, pp. 879-885.

61 Khatri, S.C. and Koczak, M.J., Ceramic Engineering Science and Proceedings, **13** (7/8), 1992, pp. 485-494.

62 Schioler, L.J. and Stiglich, J.J., American Ceramic Society Bulletin, **65** (2), 1986, pp. 289-292.

63 Fitzer, E. and Gadow, R., American Ceramic Society Bulletin, **65** (2), 1986, pp. 326-335.

64 Naslain, R. and Langlais, F., in: "Tailoring Multiphase and Composite Ceramics", Materials Science Research, Vol. 20, Plenum Press, New York, 1985, pp. 145-164.

65 Caputo, A.J., Lackey, W.J., and Stinton, D.P., Ceramic Engineering and Science Proceedings, **6**, 1985, pp. 694-706.

66 Stinton, D.P., Caputo, A.J. and R.A. Lowden, American Ceramic Society Bulletin, **65** (2), 1986, pp. 347-350.

67 Shaw, D.J., "Introduction to Colloid and Surface Chemistry, 3rd Edition" (Butterworths, London, 1980)

68 Colomban, Ph., Ceramics International, **15**, 1989, pp. 23-50.

69 Hench, L.L. and West, J.K., Chemistry Review, **90**, 1990, pp. 33-72.

70 Mackenzie, J.D., Journal of Non-Crystalline Solids, **100**, 1988, pp. 162-168.

71 Wilson, G. and Patel, A. Materials Science and Technology, **9**, 1993, pp. 937-944.

72 Schmidt, H., Journal of Non-Crystalline Solids, **100**, 1988, pp. 51-64.

73 James, P.F., Journal of Non-Crystalline Solids, **100**, 1988, pp. 93-114.

74 Scherer, G.W., Journal of Non-Crystalline Solids, **100**, 1988, pp. 77-91.

75 Brinker, C.J. and Scherer, G.W., "Sol-Gel Science" (Academic Press Inc., London, 1990).

76 Segal, D., "Chemical Synthesis of Advanced Ceramic Materials", (Cambridge University Press, 1991).

77 Iler, R.K., "The Chemistry of Silica", (Wiley, New York, 1979).

78 Stöber. W., Fink, A., and Bohn, E., Journal of Colloid and Interface Science, **26**, 1968.

79 Cooper, R.G., "Winning at New Products, 2nd Edition", (Addison Wesley, Wokingham, England, 1993).

80 Sales, M., and Alarcon, J., Journal of Materials Science, **29**, 1994, pp. 5253-5157.

81 Nogami, M., Ogawa, S. and Nagasaka, K., Journal of Materials Science, **24**, 1989, pp. 4339-4342

82 Sheppard, L.M., "Porous Ceramics: Processing and Applications" (in: Porous Materials, Ceramic Transactions Volume 31, Editors: Ishizaki, K., Sheppard L.M., Okada, S., Hamasaki, T. and Huybrechts, B., The American Ceramic Society, 1993, pp. 3-23).

83 Xu, Q. and Anderson, M.A., Journal of the American Ceramic Society, **76** (8), 1993, pp. 2093-2097

84 Bunsell, A.R., Simon, G., Abe, Y. and Akiyama, M., In: "Fibre Reinforcements for Composite Materials", Ed. Bunsell, A.R., Elsevier, Oxford, 1988, pp. 427-478.

85 Venkatachari, K.R., Moeti, L.T., Scakd, M.D. and Simmons, J.S., Ceramic Engineering Science and Proceedings, **11** (9/10), 1990, pp. 1512-1525.

86 Kokubo, T., Teranishi, Y., Maki , T.and Sakka, S., Journal of Materials Science, **23**, 1988, pp. 1126-1130.

87 Mahler, W. and Bechtold, M.F., Nature, **285** (1), 1980, pp. 27-28.

88 Maki, T. and Sakka, S., Journal of Non-Crystalline Solids, **82**, 1986, pp. 239-245.

89 Gulden, T.D., Hazelbeck, D.A., Norton, K.P and Streckert, H.H., Ceramic Engineering Science and Proceedings, **11** (9/10), 1990, pp. 1539-1553.

90 Hay, R.S. and Hermes, E.E., Ceramic Engineering Science and Proceedings, **11** (9/10), 1990, pp. 1526-1538.

91 Malghan, S.G., Minor, D.B., Wang, P.S. and Ostertag, C.P., Ceramic Engineering Science and Proceedings, **11** (9/10), 1990, pp. 1674-1684.

92 Fitzer, E. and Gadow, R., in: "Tailoring Composite and Multiphase Ceramics", Materials Science Research, **20**, Plenum Press, New York, 1985, pp. 571-608.

93 Lannutti, J.J. and Clark, D.E., Materials Research Society Symposium, **72**, 1984, pp. 369-374.

94 Hyde, A.R., Materials And Design, **10** (1), 1989, pp. 29-35.

95 Hegeler, H. and Bruckner, R., Journal of Materials Science, **24**, 1989, pp. 1191-1194.

96 Pannhorst, W., Spallek, M., Bruckner, R., Hegeler, H., Reuch, C., Grathwohl, G., Meier, B. and Spelmann, D., Ceramic Engineering and Science Proceedings, **11** (7), 1990, pp. 947-963.

97 Jamet, J., Spann, J.R., Rice, R.W., Lewis, D. and Coblenz, W.S., Ceramic Engineering and Science Proceedings, **5** (7-8), 1984, pp. 677-694.

98 Laurie, J., "Freeze Casting - A Modified Sol-Gel Process", PhD Thesis, University of Bath, 1994.

99 Laurie, J., Bagnall, C.M., Harris, B., Jones, R.W., Russell-Floyd, R., Wang, T.W. and Hammett, F.W., Journal of Non-Crystalline Solids, **147** (8), 1992, pp. 320-325.

100 Russell-Floyd, R., Harris, B., Jones, R.W., Cooke, R.G., Wang, T.W., Laurie, J. and Hammett, F.W., In: "Proceedings Fifth European Conference on Composite Materials (ECCM 5); Developments in the Science and Technology of Composite Materials, Bordeaux, April 1992", Eds. Bunsell, A.R., Jamet, J.F. and Massiah, A., (EACM Bordeaux), 1992, pp. 685-690.

101 Russell-Floyd, R., Harris, B., Jones, R.W., Cooke, R.G., Wang, T.W., Laurie, J. and Hammett, F.W., British Ceramic Transactions, **92**, 1993, pp. 8-12.

102 Russell-Floyd, R., Harris, B., Cooke, R.G., Laurie, J., Hammett, F.W., Jones, R.W. and Wang, T.W., Journal of the American Ceramic Society, **76** (10), 1993, pp. 2635-2643.

103 Harris, B., Cooke, R.G., Hammett, F.W., Russell-Floyd, R., Jones, R.W. and Wang, T.W., "Sol-Gel Processing of Fibre-Reinforced Ceramic Shapes; Final Report on (SERC) ACME Program GR/F/99588", November 1993.

104 American Cast Iron Pipe Company, German Patent No. 1,917,142, 1968.

105 Fletcher, N.H., "The Chemical Physics of Ice" (Cambridge University Press, 1972).

106 Franks, F., "Water [volumes 1 and 3]" (Plenum Press, New York, 1991).

107 Manufacturer's data, Monsanto Limited.

108 Laurie, J., Private communication, 1992.

109 Guild, F.J. and Summerscales, J., Composites, **24** (5), 1993, pp. 83-393.

110 BS EN 632, Part 2, "Advanced Technical Ceramics (Monolithic Ceramics, General and Textural Properties) – Determination of Density and Porosity", 1993.

111 BS1881, Part 203, "Recommendations for non-destructive methods of test for concrete. Measurement of the velocity of ultrasonic pulses in concrete", 1986.

112 "PUNDIT (Portable Ultrasonic Non-destructive Digital Indicating Tester)", CNS Electronics Ltd., London.

113 Joint Committee on Powder Diffraction Standards, International Centre for Diffraction Data : anorthite ($CaO.Al_2O_3.2SiO_2$), 41-1486.

114 Joint Committee on Powder Diffraction Standards, International Centre for Diffraction Data : α-cristobalite (SiO_2), 39-1425.

115 Joint Committee on Powder Diffraction Standards, International Centre for Diffraction Data : cordierite ($5SiO_2.2Al_2O_3.2MgO$), 12-303.

116 Joint Committee on Powder Diffraction Standards, International Centre for Diffraction Data : α-quartz (SiO_2), 33-1161.

117 Kurz, W. and Fisher, D.J., "Fundamentals of Solidification" (Trans Tech Publications, Switzerland, 1989).

118 Nicholson, P.S., Canadian Ceramics Quarterly, February 1995.

119 Clegg, W.J., Kendall, K., Alford, N.McN., Button, T.W. and Birchall, J.D., Nature, **347**, 1990, pp. 455-457.

120 Anderson, T.L., "Fracture Mechanics: Fundamentals and Applications" (CRC Press, Boston, 1991).

121 Bowman, S., Private communication, 1993.

122 Allied Colloids Limited, Coatings and Specialities Divison, Bradford, England, "DISPEX Pigment Dispersants for Aqueous Systems", Technical and Processing Data TPD 6022.

123 Joint Committee on Powder Diffraction Standards, International Centre for Diffraction Data : β-spodumene ($Li_2O.Al_2O_3.4SiO_2$), 35-797.

124 Dortmans, L. and De With, G., Journal of the American Ceramic Society, **74** (9), 1991, pp. 2293-2294.

125 Lamon, J., Journal of the American Ceramic Society, **71** (2), 1988, pp. 106-112.

126 Bowles, K.J. and Frimpong, S., Journal of Composite Materials, **26** (10), 1992, pp. 1487-1509.

127 Zhien, L., Jianjun, Y., Zhiyun, X., Journal of Materials Science, **30**, 1995, pp. 399-404.

TABLES

Fibre	Type	Diameter (μm)	Density (g/cm^3)	Tensile strength (GPa)	Tensile Modulus (GPa)	Failure strain (%)	CTE (10^{-6} K^{-1})
Saffil†	Al_2O_3	3	3.3	1.5	300	1.5	8
Nicalon‡	SiC, O	15	2.6	2.8	200	1.5	3.1
Tyranno*	SiC	8.5	2.4	3.2	176	1.5	3.1
SCS8§	SiC mono.	140	3.0	3.4	430	0.8	
T300¶	C (PAN)	7	1.8	3.5	230	1.5	0 (axial) 8 (radial)

Table 1.1 Properties of fibres suitable for incorporation into ceramic-matrix composites. † ICI, ‡ Nippon Carbon Co., * Ube, § Textron, ¶ Toray Industries Inc.

Matrix type	Major crystalline phase	Young's modulus (GPa)	Tensile strength (MPa)	Density (g/cm^3)	CTE (10^{-6} K^{-1})	Max. temp (°C)
Glass-ceramics						
Lithium aluminosilicate	β-spodumene	100	100-150	2.0	1.5	1000
Magnesium aluminosilicate	cordierite	120	110-170	2.7	2.5-5.5	1200
Ceramics						
MgO		210-300	97-130	3.6	13.8	
Al_2O_3		360-400	250-300	3.9	8.5	
Si_3N_4		310	410	3.2	2.2-2.9	
Glasses						
Borosilicate		60	100	2.3	3.5	600
Soda-lime		60	100	2.5	8.9	1150

Table 1.2 Properties of glasses, ceramics and glass-ceramics suitable for use as matrix materials in ceramic-matrix composites. See text for references.

Process	Matrices	Typical porosity†
Hot-pressing	SiC, Si_3N_4	<2
Sintering	Glasses and glass-ceramics	<2
Viscous phase consolidation	Carbides, nitrides, oxides, borides	<2
Sol-gel	Oxides	20-30
Polymer pyrolysis	Carbides and nitrides of Si	15-30
Gas-metal reaction	Al_2O_3, AlN, ZrN, TiN	<5
Melt infiltration	Si/SiC	<2
Gas phase reactions (CVD, CVI)	Carbides, nitrides, oxides, borides	15-30

Table 1.3 Summary of possible matrix processing methods for ceramic-matrix composites. † Volume% residual porosity.

Designation	Mean particle diameter (nm)	Weight% SiO_2	Density (g/cm^3)	pH	Viscosity (cP)
D30	7	30	1.20	10.1	7
X30	25	30	1.20	9.9	6
HT50	125	50	1.39	10.2	9

Table 1.4 Properties of Monsanto Syton® colloidal silica sols [107].

Fibre	Producer	Composition	Tensile strength (GPa)	Tensile Modulus (GPa)	Density (g/cm^3)
Nextel 312	3M	Al_2O_3, SiO_2, B_2O_3	1.75	154	2.70
Nextel 440	3M	Al_2O_3, SiO_2, B_2O_3	2.10	189	3.05
Nextel 480	3M	Al_2O_3, SiO_2, B_2O_3	2.28	224	3.05
PRD 166	du Pont	Al_2O_3, ZrO_2	2.1	385	4.2
FP	du Pont	α-Al_2O_3	1.4	385	3.9
	Sumitomo	Al_2O_3, SiO_2	~2.2	~230	3.2

Table 1.5 Properties of commercially-available ceramic fibres manufactured via sol-gel processing (see text for references).

Sample	Density (g/cm^3)	Flexural strength (MPa)	Strain at peak load (%)	Dynamic modulus (GPa)
Without added filler particles	1.6 (0.02)	118 (17)	0.4 (0.05)	40 (4)
With added glass-ceramic filler†	1.7 (0.01)	212 (10)	0.7 (0.15)	43 (5)

Table 1.6 Effect of glass-ceramic matrix filler particles on the mechanical properties of freeze-gelled, unidirectional carbon-fibre-reinforced ceramic-matrix composites made by hand layup. Figures in parentheses are standard deviations. († cordierite, $5SiO_2 \cdot 2Al_2O_3 \cdot 2MgO$, + CaO).

Fibre	Principal filler powder	V_f	Density (g/cm^3)	Flexural strength (MPa)	Dynamic modulus (GPa)	Work of fracture (J/m^2)	Processing temperature (°C)
Saffil	Mullite	0.10	1.88	46	30	230	1050
Saffil	SiO_2 & ZrO_2	0.08	2.38	32	29	150	1150
Saffil	Al_2O_3 & glass-ceramic	0.10	2.06	25	53	160	1300
Carbon	Glass-ceramic	0.20	1.74	18	15	250	900†

Table 1.7 Mechanical properties of short fibre-reinforced composites prepared by casting and freeze-gelation. († sintered in vacuo).

HC	HQ	XQ
50 % HT50	50% HT50	48 % X30
25 % dried, amorphous SiO_2	50 % dried quartz	14 % dried, amorphous SiO_2
25 % CMA6 glass-ceramic †		38 % dried quartz

Table 3.1 Matrix compositions of composite samples 'HC', 'HQ' and 'XQ' (weight %). Details of the colloidal silica sols are given in table 1.4.

† The composition of CMA6 glass-ceramic corresponds nominally to cordierite ($5SiO_2 \cdot 2Al_2O_3 \cdot 2MgO$) + CaO.

	Sample		
	HC	HQ	XQ
Freeze-gelation			
Time held frozen	24 hours	24 hours	18 hours
Thawing time at room temperature	24 hours	24 hours	30 hours
Drying time at 60 °C	48 hours	72 hours	72 hours
1st infiltrations			
Infiltrant sol †	D30	D30	D30
Number of infiltrations	3	3	3
Infiltration pressure	1 MPa	1 MPa	1 MPa
Infiltration time	6 hours	6 hours	6 hours
1st sintering			
Sintering temperature (in Argon)	600 °C	600 °C	600 °C
Dwell time	6 hours	6 hours	6 hours
2nd infiltrations			
Number of infiltrations	5	5	5
(0ther conditions as for 1st infiltration)			
2nd sintering			
Sintering temperature (1)	600 °C	600 °C	600 °C
Sintering temperature (2)	750 °C	750 °C	750 °C
Sintering temperature (3)	900 °C	900 °C	900 °C
Sintering temperature (4)	1100 °C	1100 °C	1100 °C
Sintering temperature (5)	1400 °C	1400 °C	1400 °C
Dwell time	60 minutes	60 minutes	60 minutes

Table 3.2 Gelation, infiltration and sintering conditions used to prepare composite samples 'HC', 'HQ' and 'XQ'. Matrix compositions are given in table 3.1. Each composite system was divided into 5 samples which were sintered at different primary temperatures. †Refer to table 1.4 for details of infiltrant sol.

Stage	Surface	Agent
i Planar grinding	SiC paper (240 grit)	—
ii Sample integrity	PerfTex	9 μm oil/based diamond
	TexMet	1 μm oil/based diamond
iii Polishing	Chemomet	0.06 μm SiO_2 ***or***
		0.06 μm SiO_2 / Al_2O_3

Table 3.3 Summary of the method developed to prepare composite samples for optical microscopy.

(i) Series HC	Sintering temperature (°C)				
	600	750	900	1100	1400
Density, ρ (g cm^{-3})	1.36 *0.04*	1.33 *0.02*	1.33 *0.02*	1.43 *0.02*	1.42 *0.02*
Porosity	0.47 *0.02*	0.44 *0.02*	0.45 *0.03*	0.51 *0.04*	0.47 *0.02*
Fibre volume fraction, V_f	0.13	0.13	0.14	0.12	0.12

(ii) Series XQ	Sintering temperature (°C)				
	600	750	900	1100	1400
Density, ρ (g cm^{-3})	1.39 *0.03*	1.40 *0.04*	1.41 *0.05*	1.41 *0.05*	1.41 *0.04*
Porosity	0.48 *0.02*	0.43 *0.04*	0.52 *0.03*	0.46 *0.04*	0.47 *0.04*
Fibre volume fraction, V_f	0.12	0.12	0.12	0.12	0.11

(iii) Series HQ	Sintering temperature (°C)				
	600	750	900	1100	1400
Density, ρ (g cm^{-3})	1.51 *0.03*	1.45 *0.04*	1.54 *0.02*	1.44 *0.11*	1.50 *0.03*
Porosity	0.46 *0.04*	0.42 *0.04*	0.45 *0.02*	0.47 *0.02*	0.47 *0.04*
Fibre volume fraction, V_f	0.12	0.13	0.12	0.11	0.12

Table 3.4 Density, porosity and fibre volume fraction data for composite series 'HC', 'HQ' and 'XQ'. Figures in italics are standard deviations.

	Sintering temperature (°C)				
	600	750	900	1100	1400
Mechanical modulus, E (GPa)	12.4	10.6	11.3	12	13
	1.9	*1.3*	*1.8*	*1.2*	*1.3*
Dynamic modulus, Edyn (GPa)	16.3	16.6	16.3	17.4	18.7
	1.1	*1.2*	*1.1*	*1.0*	*0.6*
Stress at proportional limit, σ_{prop} (MPa)	80	70	51	82	68
	22	*14*	*10*	*16*	*24*
Peak stress, σ_{max} (MPa)	140	124	113	124	141
	38	*10*	*36*	*17*	*6*
Failure strain, ε_{fail} (%)	1.21	1.21	1.13	1.14	1.15
	0.17	*0.04*	*0.19*	*0.09*	*0.10*
'Work of Fracture' (kJ m^{-2})	5.86	4.47	4.72	2.65	2.72
	1.7	*1.1*	*1.1*	*0.6*	*0.2*
Number of specimens tested	6	5	5	5	5

Table 3.5 Flexural mechanical properties of 'HC' series composites sintered at temperatures between 600 °C and 1400 °C. Figures in italics are standard deviations.

	Sintering temperature (°C)				
	600	750	900	1100	1400
Mechanical modulus, E (GPa)	17.3	16.4	14.7	13.2	14.2
	1.0	*3.0*	*2.2*	*2.0*	*1.7*
Dynamic modulus, E_{dyn} (GPa)	20.6	23.7	18.5	19.7	19.5
	2.1	*1.9*	*0.6*	*1.0*	*1.6*
Stress at proportional limit, σ_{prop} (MPa)	124	98	114	70	93
	76	*13*	*32*	*8*	*24*
Peak stress, σ_{max} (MPa)	200	189	117	72	93
	60	*15*	*33*	*9*	*24*
Failure strain, ε_{fail} (%)	1.16	1.21	0.91	0.56	0.66
	0.36	*0.11*	*0.24*	*0.08*	*0.15*
'Work of Fracture' (kJ m^{-2})	8.65	8.09	2.99	0.7	1.06
	3.2	*0.6*	*0.8*	*0.1*	*0.5*
Number of specimens tested	6	5	5	5	5

Table 3.6 Flexural mechanical properties of 'XQ' series composites sintered at temperatures between 600 °C and 1400 °C. Figures in italics are standard deviations.

	Sintering temperature (°C)				
	600	750	900	1100	1400
Mechanical modulus, E (GPa)	9.3	13.7	10.6	8.9	9.4
	2.5	*4.1*	*1.4*	*2.4*	*1.4*
Dynamic modulus, E_{dyn} (GPa)	20.3	17.5	17	14.6	15.4
	0.4	*1.8*	*0.7*	*2.6*	*1.2*
Stress at proportional limit, σ_{prop} (MPa)	74	25	70	55	33
	29	*5*	*16*	*12*	*9*
Peak stress, σ_{max} (MPa)	124	64	91	71	54
	30	*20*	*22*	*10*	*12*
Failure strain, ε_{fail} (%)	1.65	2.42	0.95	0.91	0.62
	0.31	*0.34*	*0.14*	*0.25*	*0.16*
'Work of Fracture' (kJ m^{-2})	5.7	4.1	3.13	1.19	0.67
	1.6	*0.8*	*0.8*	*0.2*	*0.3*
Number of specimens tested	6	4	5	4	5

Table 3.7 Flexural mechanical properties of 'HQ' series composites sintered at temperatures between 600 °C and 1400 °C. Figures in italics are standard deviations.

Matrix Young's modulus, E_m	75 GPa
Fibre Young's modulus, E_f	230 GPa
Matrix axial CTE, α_m	10^{-6} K^{-1}
Fibre axial CTE, α_f	0
Mean fibre volume fraction, V_f	0.12

Table 3.8 Materials parameters used to estimate thermal residual stresses in composite samples 'HC', 'XQ' and 'HQ'.

	Sample designation						
	HN6	HN8	HN2	HN7	HN3	HN4	HN5
HT50 sol (wt %)	98.2	90.9	80.0	77.5	71.5	65.2	58.6
NLAS filler (wt %)	1.8	9.1	20.0	22.5	28.5	34.8	41.4

Table 4.1 Compositions of the sol + filler slurries used to fabricate composites with HT50 / NLAS matrices (series HN).

	Sample designation	
	XN3	XN2
X30 sol (wt %)	80.0	77.4
NLAS filler (wt %)	20.0	22.6

Table 4.2 Compositions of the sol + filler slurries used to fabricate composites with X30 / NLAS matrices (series XN).

Nature	Low-molecular-weight, anionic, water-soluble polymer system intended for use as a dispersion agent where high mineral loadings in aqueous systems are required
Type	NH_4^+ stabilised polycarboxylic acid
Appearance	Straw-coloured liquid
pH	8.0
Solid content (wt%)	40
Density (kg m^{-3})	1.16

Table 4.3 Properties of Dispex A40 dispersion agent manufactured by Allied Colloids [122].

	Sample						
	HN6	HN8	HN2	HN7	HN3	HN4	HN5
Nominal NLAS volume fraction							
... in sol mixture	0.01	0.05	0.13	0.14	0.19	0.23	0.29
... in composite matrix	0.02	0.09	0.19	0.22	0.27	0.33	0.40
Measured V_f							
... by pyrolysis	0.46	0.43	0.21	0.18	0.15	0.12	0.09
... by image analysis	0.37	0.44	0.22	0.15	0.12	0.08	0.07
Composite bulk density (g/cm^3)							
Theoretical	2.06	2.06	2.19	2.22	2.24	2.27	2.29
Measured	1.29 *0.07*	1.61 *0.03*	1.76 *0.04*	1.72 *0.04*	1.76 *0.04*	1.71 *0.06*	1.59 *0.05*
Composite porosity (vol. fraction)							
Measured	0.43 *0.013*	0.27 *0.017*	0.23 *0.011*	0.24 *0.014*	0.30 *0.017*	0.33 *0.020*	0.39 *0.021*
Calculated from bulk density	0.44	0.32	0.22	0.23	0.26	0.27	0.30
Mean specimen thickness (mm)	3.3	4.1	1.8	5.1	2.5	4.1	4.9

Table 4.4 Microstructural parameters of composites with HT50 / NLAS matrices (series HN). The data are means of at least 10 measurements. Figures in italics are standard deviations.

	Sample	
	XN3	XN2
Nominal NLAS volume fraction		
... in sol mixture	0.05	0.13
... in composite matrix	0.08	0.21
Measured V_f		
... by pyrolysis	0.44	0.18
... by image analysis	0.39	0.10
Composite bulk density (g/cm^3)		
Theoretical	2.05	2.21
Measured	1.68 *0.03*	1.71 *0.05*
Composite porosity (vol. fraction)		
Measured	0.23 *0.013*	0.27 *0.014*
Calculated from bulk density	0.29	0.25
Mean specimen thickness (mm)	4.3	5.6

Table 4.5 Microstructural parameters of composites with X30 / NLAS matrices (series XN). The data are means of at least 10 measurements. Figures in italics are standard deviations.

	Sintering temperature (°C)		
	500	750	850
Measured V_f			
... by pyrolysis	0.50	0.49	0.46
... by image analysis	0.48	0.48	0.48
Composite bulk density (g/cm^3)			
Theoretical	2.03	2.03	2.03
Measured	1.41 *0.05*	1.45 *0.03*	1.44 *0.02*
Composite porosity (volume%)			
Measured	34 *2.6*	30 *2.8*	28 *1.2*
Calculated from bulk density	30	28	29
Mean specimen thickness (mm)	2.7	2.7	2.7

Table 4.6 Effect of sintering temperature on the microstructural parameters of composites with unfilled HT50 matrices (sample reference: H_5). The data are means of at least 10 measurements. Figures in italics are standard deviations.

	Number of infiltrations		
	3	5	7
Measured V_f			
... by pyrolysis	0.47	0.48	0.50
... by image analysis	0.47	0.48	0.47
Composite bulk density (g/cm^3)			
Theoretical	2.03	2.03	2.02
Measured	1.40 *0.02*	1.41 *0.02*	1.41 *0.02*
Composite porosity (volume%)			
Measured	34 *2.0*	33 *1.6*	33 *1.4*
Calculated from bulk density	31	31	30
Mean specimen thickness (mm)	3.2	3.2	3.2

Table 4.7 Effect of infiltration régime on the microstructural parameters of composites with unfilled HT50 matrices (sample reference: H_6). The data are means of at least 10 measurements. Figures in italics are standard deviations.

	Batch number			
	1	2	3	4
Nominal NLAS volume fraction				
... in sol mixture	0.14	0.14	0.14	0.14
... in composite matrix	0.22	0.22	0.22	0.22
Measured V_f				
... by pyrolysis	0.18	0.30	0.33	0.28
... by image analysis	0.15	0.26	0.39	0.38
Composite bulk density (g/cm^3)				
Theoretical	2.22	2.16	2.11	2.13
Measured	1.72 *0.04*	1.61 *0.06*	1.65 *0.09*	1.71 *0.05*
Composite porosity (volume%)				
Measured	24 *1.4*	24 *1.2*	25 *2.6*	26 *1.9*
Calculated from bulk density	23	25	22	19
Mean specimen thickness (mm)	5.1	4.8	4.0	3.3

Table 4.8 Reproducibility of microstructural parameters of composites with HT50 / 0.22 V_{NLAS} matrix (series HN). The data are means of at least 10 measurements. Figures in italics are standard deviations.

	Resinter time (hours)		
	0	½	12
V_f measured by pyrolysis	0.38	0.38	0.38
Composite bulk density (g/cm^3)			
Theoretical	2.10	2.10	2.10
Measured	1.71 *0.05*	1.67 *0.04*	1.68 *0.03*
Composite porosity (volume%)			
Measured	25.7 *1.9*	22.3 *1.6*	23.0 *1.7*
Calculated from bulk density	18.7	20.6	20.1
Mean specimen thickness (mm)	3.3	3.3	3.3

Table 4.9 Effect of resintering on the microstructural properties of composites with HT50 / 0.22 V_{NLAS} matrix (sample reference: HN11). Samples were tested in the as-received condition and after resintering at 750 °C for ½ hour and 12 hours. The data are means of at least 18 measurements. Figures in italics are standard deviations.

	Sintering temperature (°C)			
	500	630	750	850
Microstructural parameters				
Density (g/cm^3)	1.55 *0.08*	1.62 *0.06*	1.71 *0.06*	1.73 *0.03*
Measured porosity (volume%)	35 *2.3*	32 *1.3*	33 *2.0*	32 *1.4*
Measured fibre volume fraction	0.12	0.12	0.12	0.12
Elastic modulus (GPa)				
Dynamic	14.4 *1.2*	13.6 *1.0*	12.0 *0.4*	11.8 *0.2*
Flexural	36.8 *2.0*	37.4 *2.7*	35.5 *1.6*	34.6 *0.6*
Strength (MPa)				
Flexural strength (MPa)	361 *96*	301 *30*	278 *16*	245 *15*
ILSS (MPa)	19.1 *2.9*	22.7 *2.1*	20.7 *2.1*	23.7 *3.9*
Flexural work of fracture (kJm^{-2})				
to peak load	11.4 *3.0*	7.8 *2.2*	6.6 *2.5*	5.6 *1.9*
to end of test	11.6 *2.0*	7.9 *2.7*	6.7 *1.6*	5.7 *0.6*

Table 4.10 Effect of sintering temperature on the basic microstructural and mechanical properties of composites with HT50 / 0.33 V_{NLAS} matrix. The data are means of at least 8 measurements. Figures in italics are standard deviations.

	V_{NLAS} in composite matrix						
	0.02	0.09	0.19	0.22	0.27	0.33	0.40
Wave velocity (ms^{-1})	5855 *1862*	4431 *1223*	2899 *657*	2905 *791*	2538 *794*	2652 *1263*	2562 *502*
Dynamic modulus (GPa)	44.2 *4.5*	31.6 *2.4*	14.8 *0.8*	14.5 *1.1*	11.3 *1.1*	12.0 *2.7*	10.4 *0.4*

Table 4.11 Measured wave velocities and dynamic (time-of-flight) elastic moduli of composites with HT50 / NLAS matrices (series HN). The data are means of at least 10 measurements. Figures in italics are standard deviations.

	V_{NLAS} in composite matrix	
	0.08	0.21
Wave velocity (ms^{-1})	4253 *1089*	2577 *763*
Dynamic modulus (GPa)	29.1 *1.9*	12.0 *1.0*

Table 4.12 Measured wave velocities and dynamic (time-of-flight) elastic moduli of composites with X30 / NLAS matrices (series XN). The data are means of at least 10 measurements. Figures in italics are standard deviations.

	V_{NLAS} in composite matrix						
	0.02	0.09	0.19	0.22	0.27	0.33	0.40
Elastic modulus (GPa)	84 *14*	71 *3*	41 *1*	34 *3*	38 *4*	35 *2*	23 *3*
Stress (MPa)							
at prop. limit (from mech data)	232 *60*	274 *69*	119 *26*	251 *106*	94 *15*		58 *21*
at prop. limit (from AE data)	227 *70*	253 *73*	120 *26*	196 *141*	49 *34*		50 *9*
at peak load	286 *71*	329 *71*	362 *83*	285 *118*	334 *53*	278 *52*	87 *23*
Strain (%)							
at prop. limit (from mech data)	0.27 *0.04*	0.34 *0.09*	0.29 *0.06*	0.75 *0.30*	0.25 *0.05*		0.24 *0.06*
at prop. limit (from AE data)	0.27 *0.06*	0.34 *0.10*	0.29 *0.06*	0.57 *0.40*	0.12 *0.09*		0.22 *0.01*
at peak load	0.27 *0.11*	0.53 *0.11*	0.86 *0.18*	0.56 *0.34*	0.95 *0.14*		0.42 *0.12*
Work of fracture (kJm^{-2})							
to prop. limit (from mech data)	1.2 *0.7*	2.5 *1.2*	0.8 *0.3*	3.9 *2.2*	0.6 *0.2*		0.3 *0.2*
to prop. limit (from AE data)	1.2 *0.8*	2.3 *1.4*	0.6 *0.4*	2.4 *2.8*	0.2 *0.2*		0.2 *0.1*
to peak load	1.6 *0.9*	3.9 *2.0*	5.5 *1.1*	5.3 *2.3*	7.1 *1.8*	6.7 *2.5*	0.9 *0.5*
to end of test	4.8 *3.2*	17.0 *4.8*	7.0 *2.9*	6.4 *2.6*	7.3 *1.5*	6.7 *1.6*	1.8 *0.6*

Table 4.13 Flexural mechanical properties of composites with HT50 / NLAS matrices (series HN). The data are means of at least 10 measurements. Figures in italics are standard deviations.

	V_{NLAS} in composite matrix	
	0.08	0.21
Elastic modulus (GPa)	66 *7*	31 *4*
Stress (MPa)		
at prop. limit (from mech data)	187 *90*	104 *20*
at prop. limit (from AE data)	177 *101*	26 *12*
at peak load	249 *81*	101 *14*
Strain (%)		
at prop. limit (from mech data)	0.28 *0.12*	0.34 *0.05*
at prop. limit (from AE data)	0.26 *0.14*	0.09 *0.04*
at peak load	0.84 *0.38*	0.38 *0.04*
Work of fracture (kJm^{-2})		
to prop. limit (from mech data)	1.3 *1.2*	0.7 *0.2*
to prop. limit (from AE data)	1.3 *0.8*	0.1 *0.0*
to peak load	2.3 *1.2*	0.9 *0.2*
to end of test	16.0 *4.8*	1.0 *0.3*

Figure 4.14 Flexural mechanical properties of composites with X30 / NLAS matrices (series XN). The data are means of at least 10 measurements. Figures in italics are standard deviations.

	V_{NLAS} in composite matrix						
	0.02	0.09	0.19	0.22	0.27	0.33	0.40
AE counts (counts/mm^2)							
at prop. limit (from mech data)	24 *13*	7 *5*	1 *1*	22 *11*	4 *4*		3 *2*
at prop. limit (from AE data)	17 *8*	3 *3*	0 *0*	9 *7*	0 *0*		2 *1*
at peak load	57 *47*	25 *21*	75 *39*	51 *38*	141 *94*		23 *24*
at end of test	2570 *1621*	697 *579*	92 *33*	158 *97*	184 *89*		123 *125*

Table 4.15 Acoustic emission data acquired during flexural testing of composites with HT50 / NLAS matrices (series HN). The data are means of at least 10 measurements. Figures in italics are standard deviations.

	V_{NLAS} in composite matrix	
	0.08	0.21
AE counts (counts/mm^2)		
at prop. limit (from mech data)	13 *10*	26 *13*
at prop. limit (from AE data)	8 *0*	1 *0*
at peak load	27 *17*	27 *13*
at end of test	339 *181*	30 *13*

Table 4.16 Acoustic emission data acquired during flexural testing of composites with X30 / NLAS matrices (series XN). The data are means of at least 10 measurements. Figures in italics are standard deviations.

	V_{NLAS} in composite matrix					
	0.02	0.09	0.19	0.22	0.27	0.40
Elastic modulus (GPa)	105 *10*	92 *8*	40 *9*	45 *6*	36 *3*	28 *1*
Stress (MPa)						
at prop. limit (from mech data)	270 *96*	109 *30*	41 *16*	35 *15*	55 *23*	39 *8*
at prop. limit (from AE data)	234 *85*	133 *26*	49 *16*	32 *11*	85 *23*	35 *9*
at peak load	378 *48*	333 *72*	148 *46*	101 *28*	169 *15*	64 *16*
Strain (%)						
at prop. limit (from mech data)	0.27 *0.10*	0.11 *0.05*	0.11 *0.05*	0.08 *0.04*	0.14 *0.06*	0.14 *0.03*
at prop. limit (from AE data)	0.23 *0.01*	0.14 *0.02*	0.14 *0.03*	0.07 *0.03*	0.23 *0.07*	0.12 *0.03*
at peak load	0.42 *0.10*	0.43 *0.10*	0.34 *0.10*	0.23 *0.07*	0.37 *0.01*	0.32 *0.08*
Work of fracture (i) (kJm^{-2})						
to prop. limit (from mech data)	8.0	2.2	0.5	0.3	0.8	0.6
to prop. limit (from AE data)	6.9	1.5	0.7	0.3	1.5	0.5
to end of test	16.4 *5.8*	19.4 *8.2*	6.1 *3.0*	2.0 *1.7*	4.4 *0.3*	2.2 *1.4*
Work of fracture (ii) (kJm^{-3})						
to prop. limit (from mech data)	406	85	27	18	49	29
to prop. limit (from AE data)	7	66	38	15	95	24
to end of test	842 *290*	762 *325*	318 *160*	130 *69*	272 *18*	100 *65*
Poisson's ratio	0.17 *0.04*	0.15 *0.07*	0.13 *0.06*	0.11 *0.03*	0.24 *0.09*	0.17 *0.06*

Table 4.17 Tensile properties of composites with HT50 / NLAS matrices (series HN). The data are means of at least 18 measurements. Figures in italics are standard deviations. Fracture energies are normalised with respect to (i) specimen cross-sectional area and (ii) stressed volume.

	V_{NLAS} in composite matrix	
	0.08	0.21
Elastic modulus (GPa)	96 *27*	45 *5*
Stress (MPa)		
at prop. limit (from mech data)	157 *80*	25 *1*
at prop. limit (from AE data)	131 *48*	41 *8*
at peak load	356 *55*	53 *8*
Strain (%)		
at prop. limit (from mech data)	0.16 *0.06*	0.06 *0.01*
at prop. limit (from AE data)	0.14 *0.02*	0.09 *0.01*
at peak load	0.37 *0.04*	0.13 *0.03*
Work of fracture (i) (kJm^{-2})		
to prop. limit (from mech data)	3.2	0.2
to prop. limit (from AE data)	2.4	0.6
to end of test	19.9 *4.9*	1.1 *0.1*
Work of fracture (ii) (kJm^{-3})		
to prop. limit (from mech data)	126	8
to prop. limit (from AE data)	95	25
to end of test	789 *214*	49 *3*
Poisson's ratio	0.12 *0.03*	0.08 *0.02*

Table 4.18 Tensile properties of composites with X30 / NLAS matrices (series XN). The data are means of at least 18 measurements. Figures in italics are standard deviations. Fracture energies are normalised with respect to (i) specimen cross-sectional area and (ii) stressed volume.

	V_{NLAS} in composite matrix					
	0.02	0.09	0.19	0.22	0.27	0.40
(i) (counts/mm^2)						
at prop. limit (from mech data)	353	4	5	8	9	33
at prop. limit (from AE data)	2	5	4	3	11	7
at end of test	489	547	143	37	292	171
(ii) (100 x counts/mm^3)						
at prop. limit (from mech data)	1799	14	24	37	59	155
at prop. limit (from AE data)	12	19	23	13	71	30
at end of test	2514	2195	760	176	1827	775

Table 4.19 Acoustic emission data acquired during tensile testing of composites with HT50 / NLAS matrices (series HN). The data are means of at least 18 measurements. The data are normalised with respect to (i) specimen cross-sectional area and (ii) stressed volume.

	V_{NLAS} in composite matrix	
	0.08	0.21
(i) (counts/mm^2)		
at prop. limit (from mech data)	345	0
at prop. limit (from AE data)	66	2
at end of test	2543	34
(ii) (100 x counts/mm^3)		
at prop. limit (from mech data)	1374	1
at prop. limit (from AE data)	259	8
at end of test	9962	150

Table 4.20 Acoustic emission data acquired during tensile testing of composites with X30 / NLAS matrices (series XN). The data are means of at least 18 measurements. The data are normalised with respect to (i) specimen cross-sectional area and (ii) stressed volume.

	V_{NLAS} in composite matrix						
	0.02	0.09	0.19	0.22	0.27	0.33	0.40
Interlaminar shear strength (MPa)	7 *1*	13 *3*	31 *3*	26 *2*	36 *3*	21 *2*	11 *3*

Table 4.21 Interlaminar shear strength values of composites with HT50 / NLAS matrices (series HN). The data are means of at least 10 measurements. Figures in italics are standard deviations.

	V_{NLAS} in composite matrix	
	0.08	0.21
Interlaminar shear strength (MPa)	10 *2*	5 *2*

Table 4.22 Interlaminar shear strength values of composites with X30 / NLAS matrices (series XN). The data are means of at least 10 measurements. Figures in italics are standard deviations.

	V_{NLAS} in composite matrix						
	0.02	0.09	0.19	0.22	0.27	0.33	0.40
Energy/cross-sectional area (kJ/m^2)	35 *5*	56 *7*	20 *3*	7 *5*	17 *2*	7 *3*	8 *3*
Energy/bridged volume (kJ/m^3)	865 *123*	1411 *178*	510 *78*	170 *116*	421 *52*	175 *71*	212 *84*

Table 4.23 Un-notched Charpy impact strength values of composites with HT50 / NLAS matrices (series HN). The data are means of at least 10 measurements. Figures in italics are standard deviations.

	V_{NLAS} in composite matrix	
	0.08	0.21
Energy/cross-sectional area (kJ/m^2)	44 *3*	3 *1*
Energy/bridged volume (kJ/m^3)	1091 *72*	67 *24*

Table 4.24 Un-notched Charpy impact strength values of composites with X30 / NLAS matrices (series XN). The data are means of at least 10 measurements. Figures in italics are standard deviations.

	Sample					
Sol	X30	X30	X30	HT50	HT50	HT50
V_{NLAS}	0.08	0.08	0.21	0.09	0.09	0.27
Crack configuration	a	b	a	a	b	a
Mean a/w	0.48	0.48	0.50	0.49	0.49	0.50
Number of specimens	10	12	8	11	11	6
K^* (MPa $m^{1/2}$)						
at prop. limit (from mech. data)	3.70	3.13	2.56	4.05	2.73	0.68
	0.58	*0.67*	*0.60*	*0.82*	*0.93*	*0.32*
at prop. limit (from AE data)	3.50	2.84	2.44	3.17	2.67	1.52
	1.48	*0.88*	*0.31*	*1.01*	*0.98*	*0.12*
at peak load	12.13	12.61	5.07	15.12	13.50	4.22
	2.14	*4.11*	*0.75*	*3.35*	*3.74*	*0.97*

Table 4.25 K^* values obtained from notched three point bend tests. The crack configurations 'a' and 'b' are explained in figure 4.4. Figures in italics represent standard deviations.

	Sample				
Sol	X30	X30	HT50	HT50	HT50
V_{NLAS}	0.08	0.21	0.02	0.09	0.22
Mean a/w	0.50	0.52	0.51	0.49	0.51
Number of specimens	6	9	17	6	8
K^* (MPa $m^{1/2}$)					
at prop. limit (from mech. data)	7.92	1.52	9.60	12.78	2.72
	2.78	*0.88*	*2.60*	*3.27*	*0.87*
at prop. limit (from AE data)	8.45	1.31	9.95	10.54	3.09
	2.12	*0.56*	*5.05*	*2.85*	*0.77*
at peak load	26.15	3.46	44.40	28.45	4.55
	4.55	*1.01*	*4.79*	*5.52*	*1.28*

Table 4.26 K^* values obtained from notched tensile tests. Figures in italics represent standard deviations.

	Sintering temperature (°C)		
	500	750	850
Elastic modulus (GPa)	100 *8*	94 *23*	97 *7*
Peak stress (MPa)	176 *22*	244 *38*	228 *53*
Strain at peak (%)	0.38 *0.22*	0.23 *0.11*	0.39 *0.23*
Work of fracture (kJm^{-2})			
to peak load	0.9 *0.1*	1.5 *0.3*	1.3 *0.6*
to end of test	8.5 *2.1*	9.0 *1.3*	12.0 *1.9*
AE ($counts/mm^2$)			
to peak load	66 *16*	74 *10*	81 *17*
to end of test	1353 *204*	1180 *353*	1796 *287*

Table 4.27 Effect of sintering temperature on the flexural properties of composites with unfilled HT50 matrices (sample reference: H_5). The data are means of at least 10 measurements. Figures in italics represent standard deviations.

	Sintering temperature		
	500	750	850
Elastic modulus (GPa)	126 *8*	121 *7*	130 *9*
Stress (MPa)			
at prop. limit (from mech data)	197 *11*	218 *18*	133 *25*
at prop. limit (from AE data)	132 *35*	128 *16*	101 *18*
at peak load	568 *15*	629 *27*	486 *25*
Strain (%)			
at prop. limit (from mech data)	0.16 *0.01*	0.18 *0.02*	0.10 *0.02*
at prop. limit (from AE data)	0.11 *0.03*	0.11 *0.02*	0.07 *0.01*
at peak load	0.56 *0.03*	0.68 *0.03*	0.62 *0.02*
Work of fracture (i) (kJm^{-2})			
to prop. limit (from mech data)	4.4	4.1	1.8
to prop. limit (from AE data)	2.1	1.5	1.0
to end of test	44.9 *2.7*	58.1 *4.9*	38.6 *8.6*
Work of fracture (ii) (kJm^{-3})			
to prop. limit (from mech data)	164	180	72
to prop. limit (from AE data)	76	67	39
to end of test	1687 *86*	2528 *184*	1507 *307*
Poisson's ratio	0.16	0.13	0.12

Table 4.28 Effect of sintering temperature on the tensile properties of composites with unfilled HT50 matrices (sample reference: H_5). The data are means of at least 10 measurements. Figures in italics are standard deviations. Fracture energies are normalised with respect to (i) specimen cross-sectional area and (ii) stressed volume.

	Sintering temperature (°C)		
	500	750	850
Dynamic modulus tests			
Wave velocity (ms^{-1})	5898 *1157*	5662 *1147*	5673 *1483*
Modulus (GPa)	49.1 *1.9*	46.5 *3.5*	46.3 *3.2*
Un-notched Charpy impact values			
Energy/cross-sectional area (kJ/m^2)	20.5 *1.3*	38.1 *5.0*	27.6 *6.1*
Energy/bridged volume (kJ/m^3)	513 *34*	952 *125*	690 *153*
ILSS (MPa)	4.5 *0.3*	6.7 *0.6*	7.4 *1.0*

Table 4.29 Effect of sintering temperature on dynamic moduli, Charpy impact toughnesses and interlaminar shear strengths of composites with unfilled HT50 matrices (sample reference: H_5). The data are means of at least 10 measurements. Figures in italics represent standard deviations.

	Batch number			
	1	2	3	4
Elastic modulus (GPa)	34 *3*	65 *3*	55 *5*	66 *4*
Stress at peak load (MPa)	285 *118*	214 *33*	229 *100*	252 *70*
Strain at peak load (%)	0.56 *0.34*	0.41 *0.05*	0.43 *0.21*	0.45 *0.07*
WOF to peak load (kJm^{-2})	5.3 *2.3*	1.8 *0.7*	2.7 *1.8*	2.4 *1.3*
WOF to end of test (kJm^{-2})	6.4 *2.6*	5.9 *2.5*	7.1 *3.1*	4.9 *3.1*
AE to peak load (counts/mm^2)	51	14	34	40
AE to end of test (counts/mm^2)	158	406	480	543

Table 4.30 Reproducibility of flexural mechanical properties of composites with HT50 / 0.22 V_{NLAS} matrix (series HN). The data are means of at least 10 measurements. Figures in italics are standard deviations.

	Batch number		
	1	3	4
Elastic modulus (GPa)	45 *6*	61 *5*	68 *7*
Stress (MPa)			
at prop. limit (from mech data)	35 *15*	58 *10*	61 *13*
at prop. limit (from AE data)	32 *11*	56 *8*	64 *16*
at peak load	101 *28*	142 *18*	166 *25*
Strain (%)			
at prop. limit (from mech data)	0.08 *0.04*	0.10 *0.02*	0.09 *0.02*
at prop. limit (from AE data)	0.07 *0.03*	0.09 *0.01*	0.10 *0.03*
at peak load	0.23 *0.07*	0.24 *0.03*	0.28 *0.10*
Work of fracture (i) (kJm^{-2})			
to prop. limit (from mech data)	0.3	0.5	0.7
to prop. limit (from AE data)	0.3	0.5	0.5
to end of test	2.0 *1.7*	4.2 *0.9*	6.4 *2.6*
Work of fracture (ii) (kJm^{-3})			
to prop. limit (from mech data)	18	34	30
to prop. limit (from AE data)	15	36	22
to end of test	130 *69*	474 *183*	263 *92*
Poisson's ratio	0.11 *0.03*	0.09 *0.03*	0.07 *0.02*

Table 4.31 Reproducibility of tensile properties of composites with HT50 / 0.22 V_{NLAS} matrix. The data are means of at least 10 measurements. Figures in italics are standard deviations.

	Batch number			
	1	2	3	4
Dynamic modulus tests				
Wave velocity (ms^{-1})	2905 *791*	3692 *969*	3722 *1203*	3546 *917*
Modulus (GPa)	14.5 *1.1*	21.9 *1.5*	22.9 *2.4*	21.5 *1.4*
Un-notched Charpy impact values				
Energy/cross-sectional area (kJ/m^2)	6.8 *4.6*	18.9 *13.5*	12.6 *5.7*	9.7 *5.0*
Energy/bridged volume (kJ/m^3)	170 *116*	472 *337*	315 *142*	243 *126*
ILSS (MPa)	26.4 *2.0*	11.3 *6.2*	10.0 *1.6*	8.6 *5.5*

Table 4.32 Reproducibility of dynamic moduli, Charpy impact toughnesses and interlaminar shear strengths of composites with HT50 / 0.22 V_{NLAS} matrix. The data are means of at least 10 measurements. Figures in italics are standard deviations.

	Resinter time (hours)		
	0	½	12
Elastic modulus (GPa)	66 *4*	52 *2*	59 *5*
Peak stress (MPa)	252 *70*	123 *22*	96 *12*
Strain at peak (%)	0.45 *0.07*	0.30 *0.02*	0.16 *0.05*
Work of fracture (kJm^{-2})			
to peak load	2.4 *1.3*	0.7 *0.2*	0.4 *0.2*
to end of test	4.9 *3.1*	0.9 *0.4*	0.5 *0.3*
AE ($counts/mm^2$)			
to peak load	40 *17*	82 *76*	44 *39*
to end of test	543 *284*	265 *241*	139 *76*

Table 4.33 Effect of resintering on the flexural properties of composites with HT50 / 0.22 V_{NLAS} matrix (sample reference: HN11). Samples were tested in the as-received condition and after resintering at 750 °C for ½ hour and 12 hours. The data are means of at least 10 measurements. Figures in italics represent standard deviations.

	Resinter time (hours)		
	0	½	12
Dynamic modulus tests			
Wave velocity (ms^{-1})	3546 *917*	3727 *1067*	4147 *1247*
Modulus (GPa)	21.5 *1.4*	23.2 *1.9*	28.9 *2.6*
Un-notched Charpy impact values			
Energy/cross-sectional area (kJ/m^2)	9.7 *5.0*		1.4 *0.6*
Energy/bridged volume (kJ/m^3)	243 *126*	187 *54*	35 *15*
ILSS (MPa)	8.6 *5.5*	6.9 *3.2*	2.7 *1.1*

Table 4.34 Effect of resintering on dynamic moduli, Charpy impact toughnesses and interlaminar shear strengths of composites with HT50 / 0.22 V_{NLAS} matrix (sample reference: HN11). Samples were tested in the as-received condition and after resintering at 750 °C for ½ hour and 12 hours. The data are means of at least 8 measurements. Figures in italics represent standard deviations.

	V_{NLAS} = 0.19		V_{NLAS} = 0.27	
	Bath	NPL	Bath	NPL
Elastic modulus (GPa)	40.0 *8.6*	41.2 *5.0*	35.9 *3.4*	38.1 *3.1*
Stress at proportional limit (MPa)	40.9 *16.5*	15.5 *4.5*	54.6 *22.9*	24.0 *12.1*
Peak stress (MPa)	148 *46*	146 *33*	169 *15*	135 *15*
Peak strain (%)	0.34 *0.10*	0.42 *0.11*	0.37 *0.01*	0.45 *0.06*

Table 4.35 Comparison of tensile data obtained at Bath University and the National Physical Laboratory. The matrices of the composite samples comprised HT50 and two different volume fractions of NLAS filler. The data are the means of at least 8 measurements. Figures in italics are standard deviations.

	Failure mode		
	1	2	3
Peak stress (MPa)	**185** *55*	**299** *100*	**132** *12*
Flexural modulus (GPa)	56 *6*	54 *4*	54 *5*
Nominal strain at peak load (%)	0.35 *0.11*	0.56 *0.24*	0.24 *0.02*
WOF to end of test (kJ/m^2)	3.2 *1.9*	13.2 *7.6*	0.8 *0.1*
AE counts to end of test	388	685	77
Number of specimens	16	17	5

Table 4.36 Flexural mechanical properties of a single batch of composite samples with matrix composition HT50 / 0.22 V_{NLAS}. The results are categorised by failure mode; modes 1, 2, and 3 correspond to failure by partial delamination, extensive delamination and brittle fracture respectively (see figure 4.62). Figures in italics are standard deviations.

Microstructural properties	
Bulk density (g/cm^3)	1.06 *0.09*
Measured porosity (volume %)	57 *8*
Flexural properties	
Elastic modulus (GPa)	3.08 *1.03*
Peak stress (MPa)	2.77 *0.70*
Strain at peak (%)	0.09 *0.02*
WOF to peak stress (J/m^2)	7.5 *2.3*
WOF to end of test (J/m^2)	10.8 *6.3*
AE at peak stress ($counts/mm^2$)	57 *9*
AE at end of test ($counts/mm^2$)	117 *71*
Dynamic modulus (GPa)	4.09 *0.81*

Table 4.37 Microstructural and flexural properties of pyrolysed composite samples with HT50 / 0.22 V_{NLAS} matrix. The carbon fibres in the composites were completely removed by heating the samples in air at 450 °C for 72 hours. The data are means of at least 10 measurements. Figures in italics represent standard deviations.

	Fibre condition	
	as-received	desized/handled
Breaking load (N)	112 *18.5*	74 *22.1*
Nominal fibre strength (MPa)	3600	2375

Table 4.38 Bundle breaking loads and nominal breaking stresses of T300 carbon fibre tows (i) in the as-received condition and (ii) after having been desized at 750 °C, and wound dry onto the composite-forming mandrel in order to emulate the damage the fibres would acquire during composite forming.

The 'as-received' fibre strength figure is taken from manufacturer's data sheet; this figure was multiplied by a factor of 74/112 to give a nominal value of fibre strength in the 'handled' condition.

		Sample				
	Sol V_{NLAS}	X30 0.08	X30 0.21	HT50 0.02	HT50 0.09	HT50 0.22
Un-notched		356	53	378	333	101
Notched (nominal)		308	37	467	278	48

Table 4.39 Comparison of un-notched and notched tensile strengths. The notched data were obtained from the peak loads obtained during notched tension (K^* measurement) divided by apparent specimen cross-sectional area.

Tensile properties	
Stiffness (GPa)	130
Strength (MPa)	630
Failure strain (%)	0.70
Work of fracture (kJm^{-2})	60
Flexural properties	
Stiffness (GPa)	100
Strength (MPa)	250
Work of fracture (kJm^{-2})	20

Table 4.40 Summary of the best properties obtained with freeze-gelled composites.

	SiC/glass-ceramic	Carbon/silica
Components		
Fibre	SiC (Nicalon)	carbon (T300 PAN)
Matrix	LAS glass-ceramic	amorphous silica
Fabrication		
Main process steps	slurry infiltrate fibres + hot-press	freeze-gelation + low-temp sinter
Maximum process temperature (°C)	> 1000	750
Typical properties[§]		
Density (kg/m^3)		2.0
Flexural stiffness (GPa)	120	100
Flexural strength (MPa)	1250	250
Flexural WOF (kJm^{-2})	50	10
Max. use temperature (°C)	> 1000	450
Cost information		
Estimated material price (£/kg)[†]	2500	25
Cost : strength ratio (£/kg/MPa)	2	0.1

Table 4.41 Comparison of processing conditions, typical flexural properties and cost information of (i) freeze-gelled composites and (ii) SiC/LAS composites.

† see text

§ Reviews of the mechanical properties of SiC/glass-ceramic composites have been published by several authors *e.g.* see [9].

FIGURES

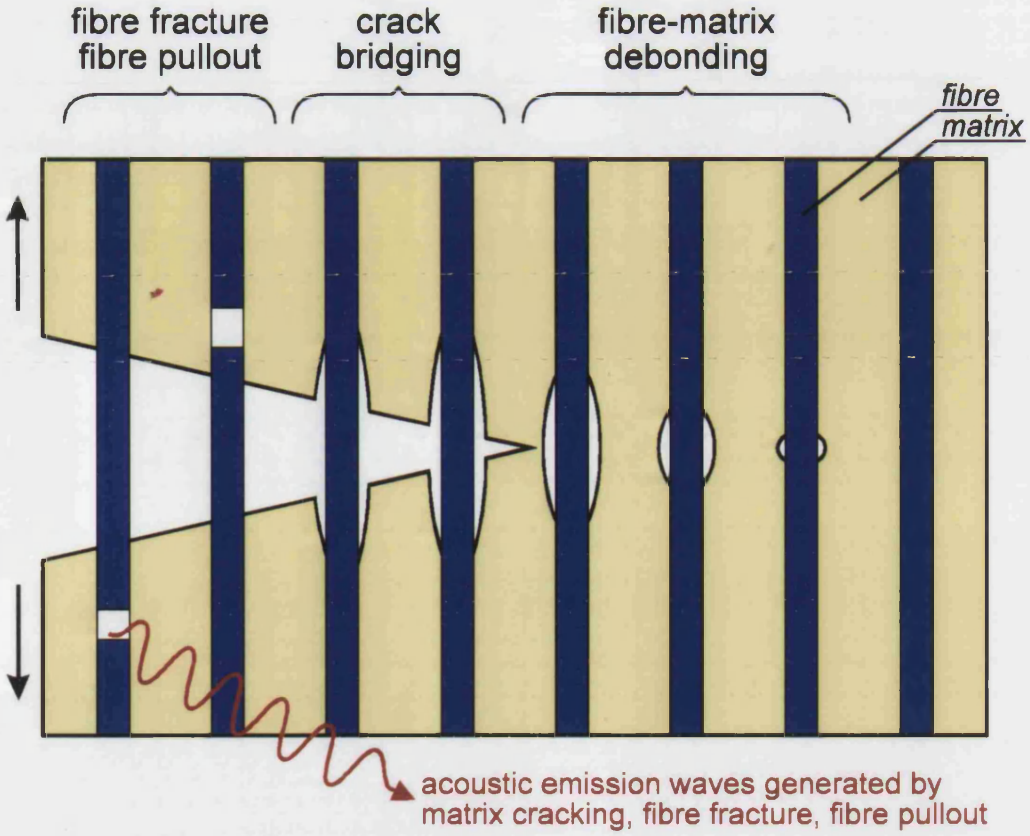

Figure 1.1 Schematic representation of damage mechanisms reported for ceramic-matrix composites.

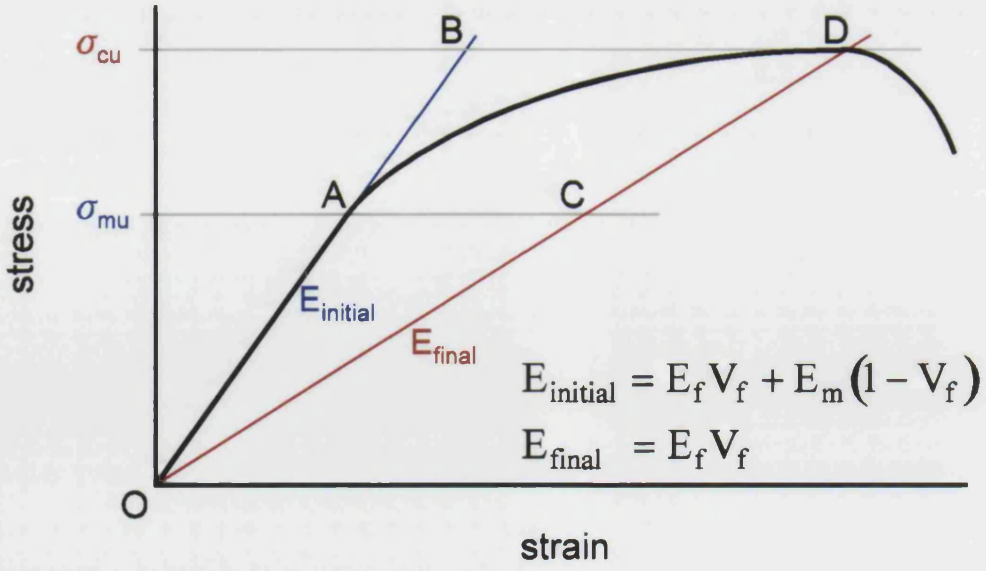

Figure 1.2 Idealised stress–strain curve for a unidirectional, ceramic-matrix composite tested in tension in the fibre direction.

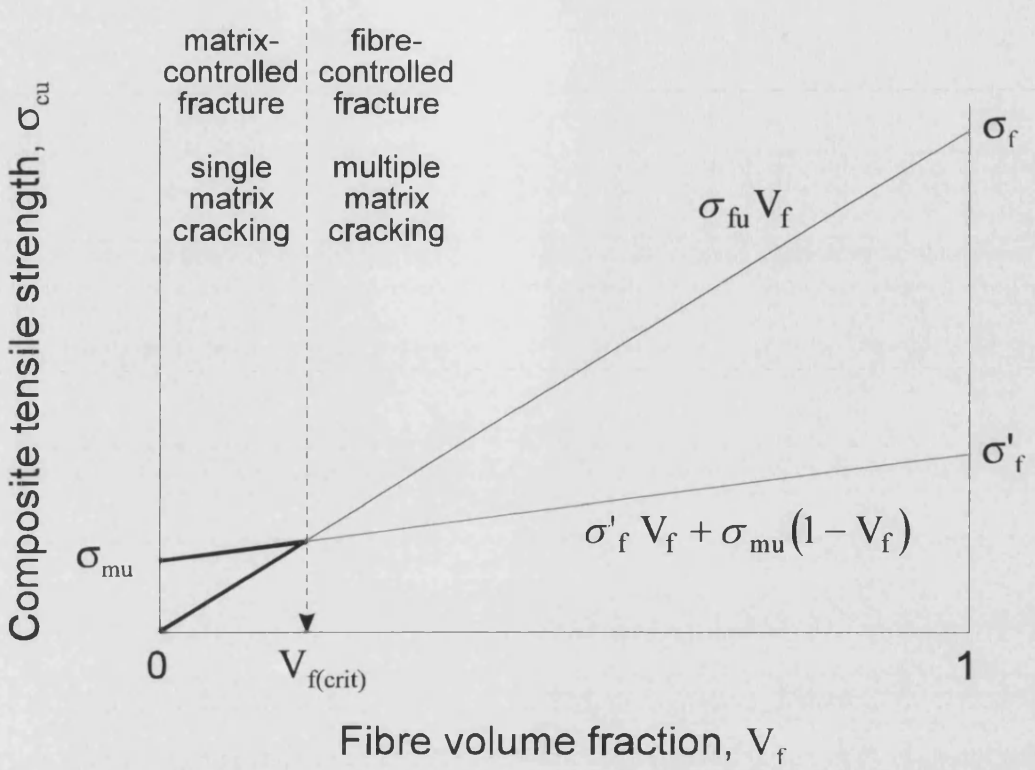

Figure 1.3 Predicted variation of composite strength with fibre volume fraction (V_f) for the case of a composite where the fibres have a larger ultimate strain than the matrix ($\varepsilon_{fu} > \varepsilon_{mu}$) and the fibres are stiffer than the matrix ($E_f > E_m$). After Kelly & MacMillan [1].

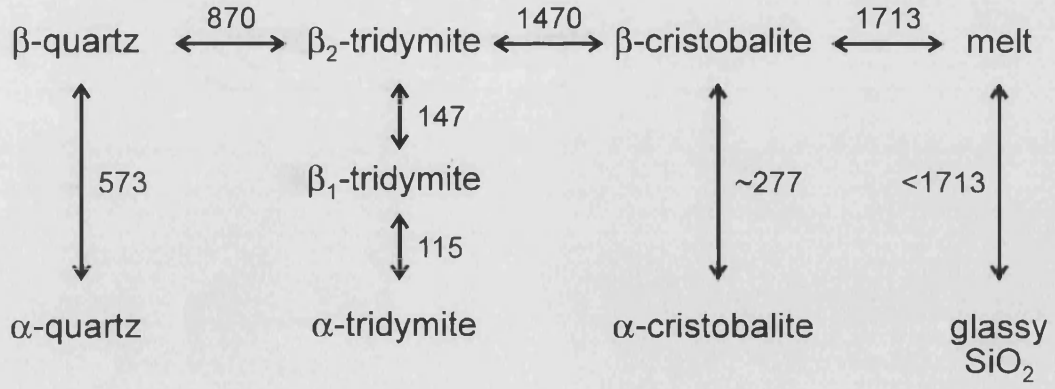

Figure 1.4 Summary of the transitions which occur between the crystalline forms of silica, SiO_2. The figures are transition temperatures (°C). After Kingery *et al* [32].

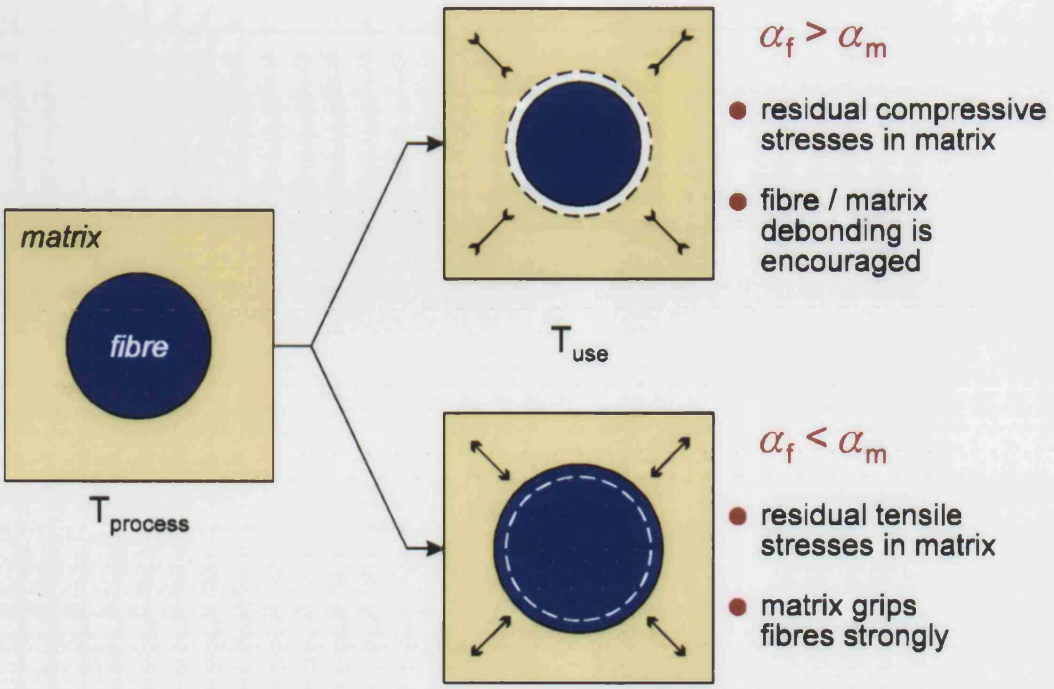

Figure 1.5 Development of residual stresses due to the different thermal expansion coefficients of fibres and matrix. Radial effects are shown, similar arguments apply to axial stresses.

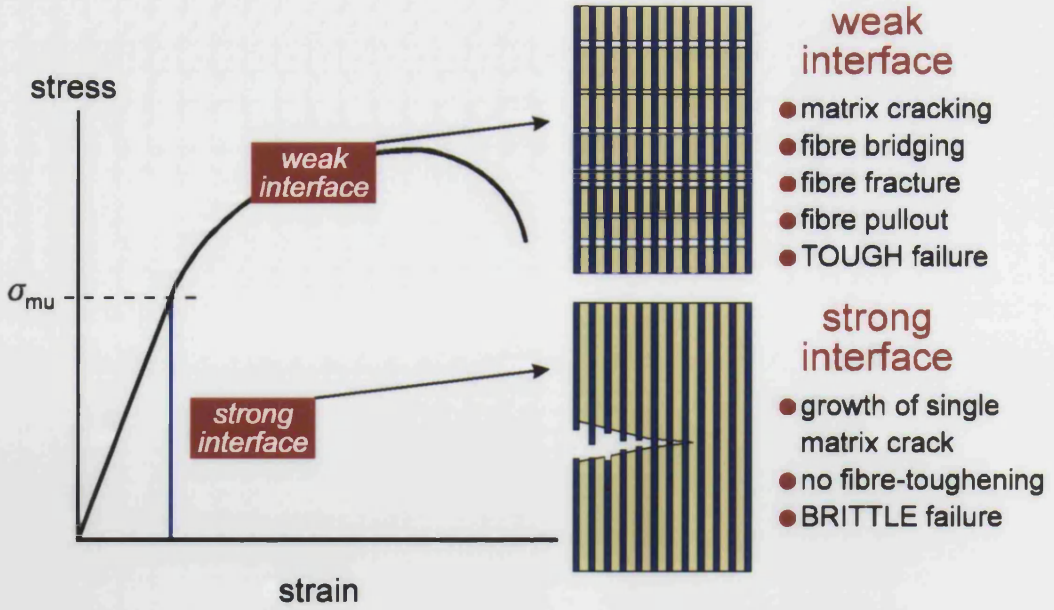

Figure 1.6 Effect of fibre / matrix interface on the fracture mode of unidirectionally reinforced, ceramic-matrix composites tested in tension along the fibre axis. A weak interface permits the toughening processes summarised in figure 1.1 to occur, whilst too strong an interface leads to a brittle composite.

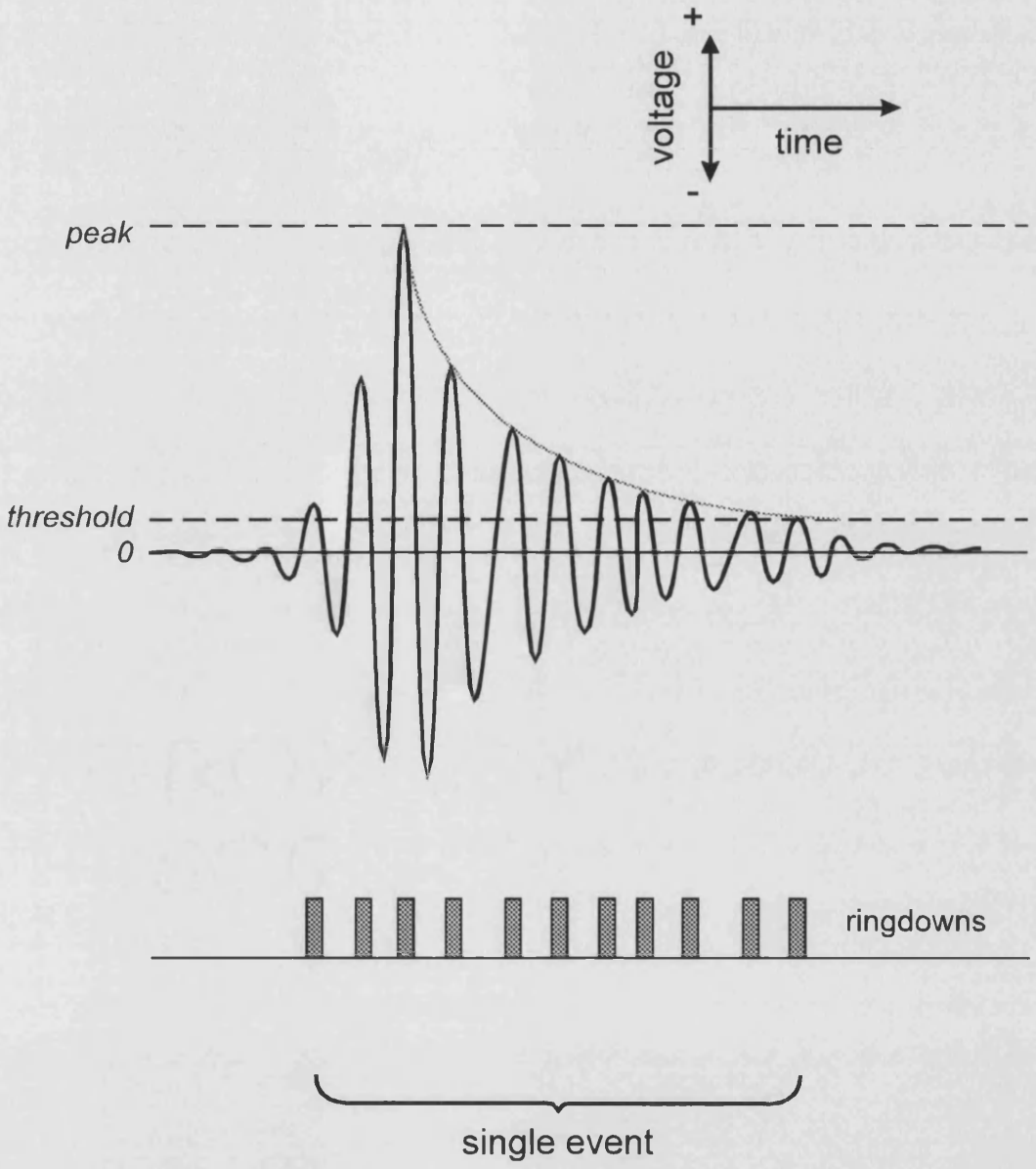

Figure 1.7 Definition of parameters employed in acoustic emission analysis. The idealised voltage - time signal shown is attributable to a single event, which may alternatively be considered as a series of excursions over a defined voltage threshold ('ringdowns').

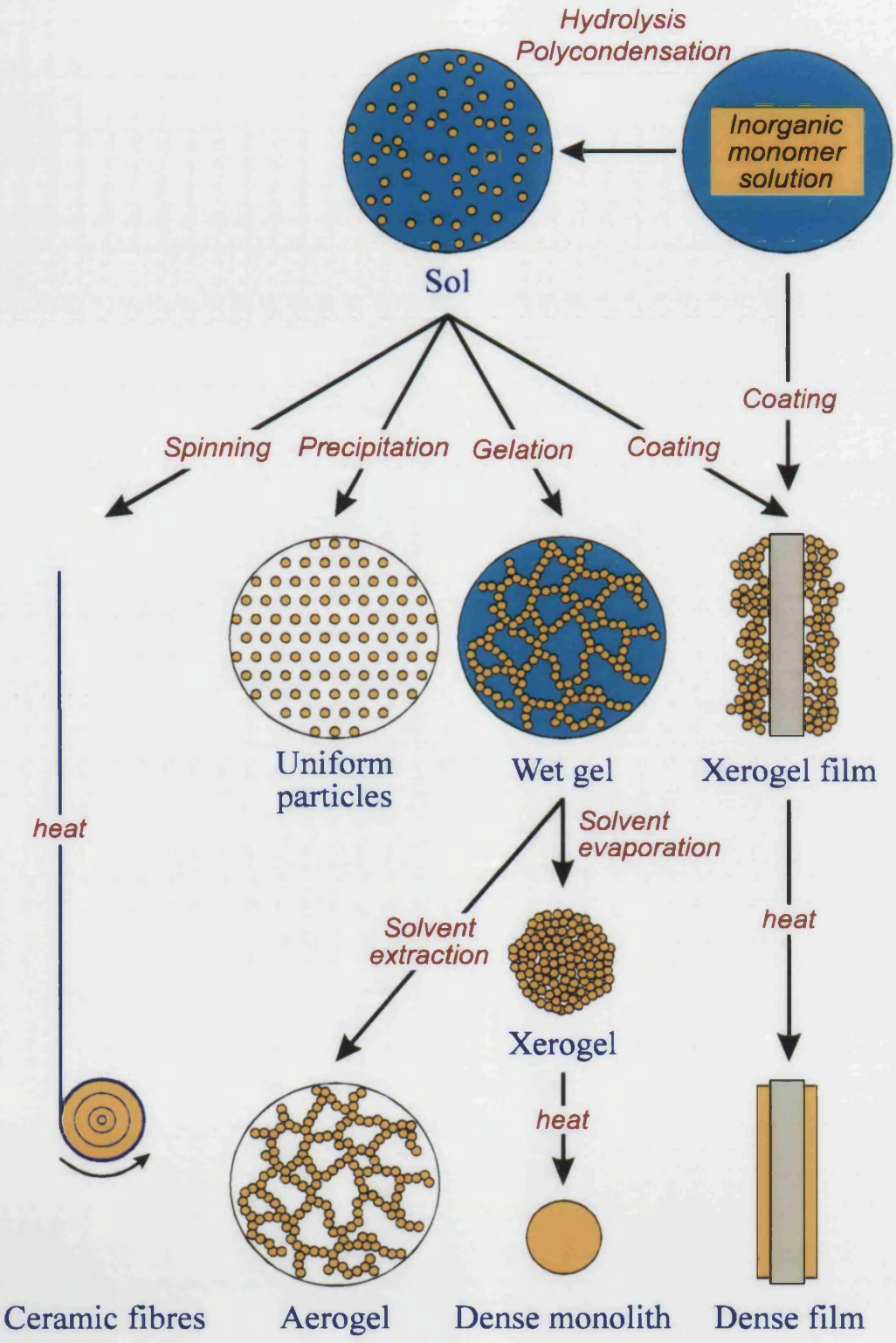

Figure 1.8 Schematic representation of the steps involved in conventional sol-gel processing.

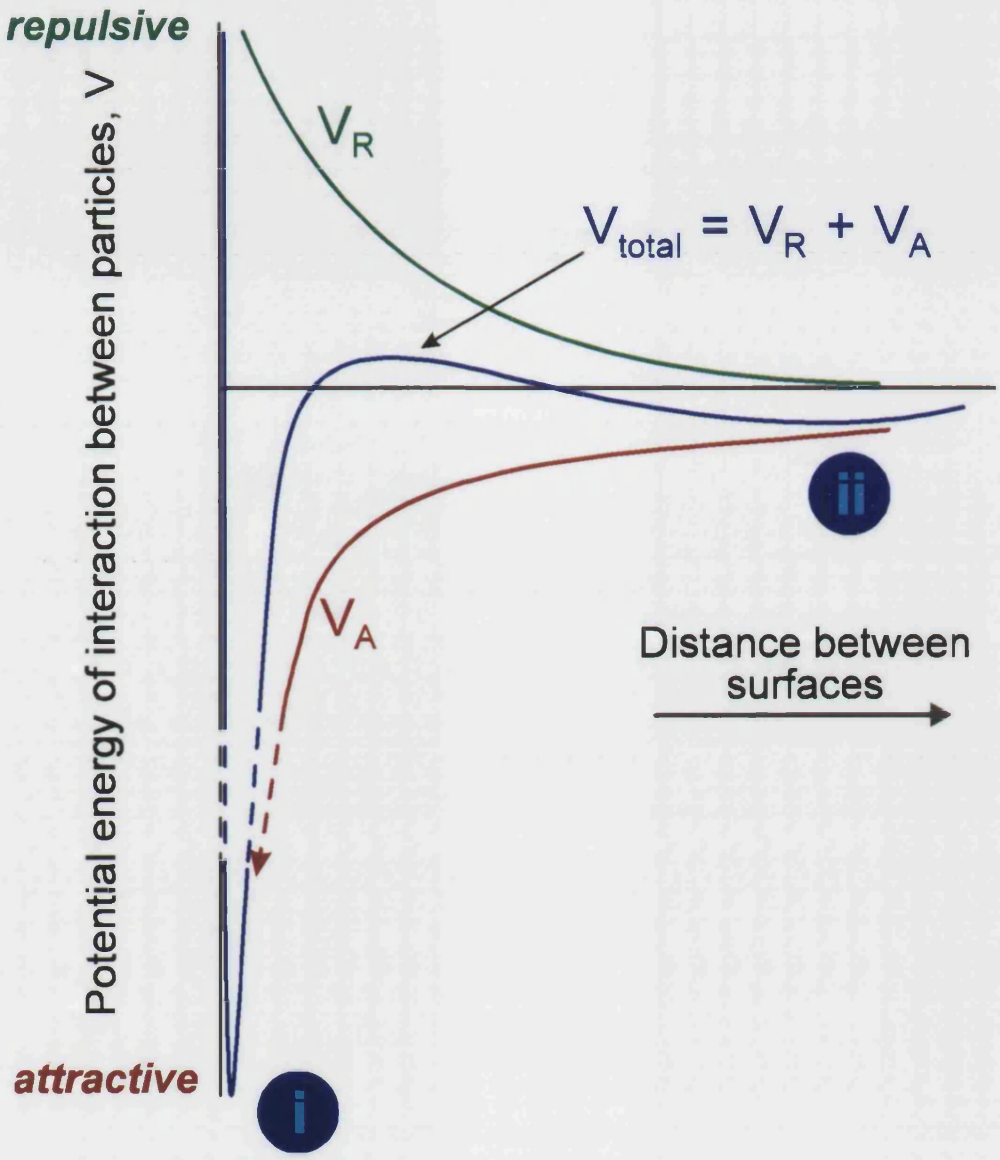

Figure 1.9 Schematic variation of total potential energy, V_{total}, with interparticle separation according to the DLVO theory. V_A and V_R represent attractive and repulsive potentials respectively. (i) indicates the primary minimum and (ii) indicates the secondary minumum in potential energy. After Shaw [67]).

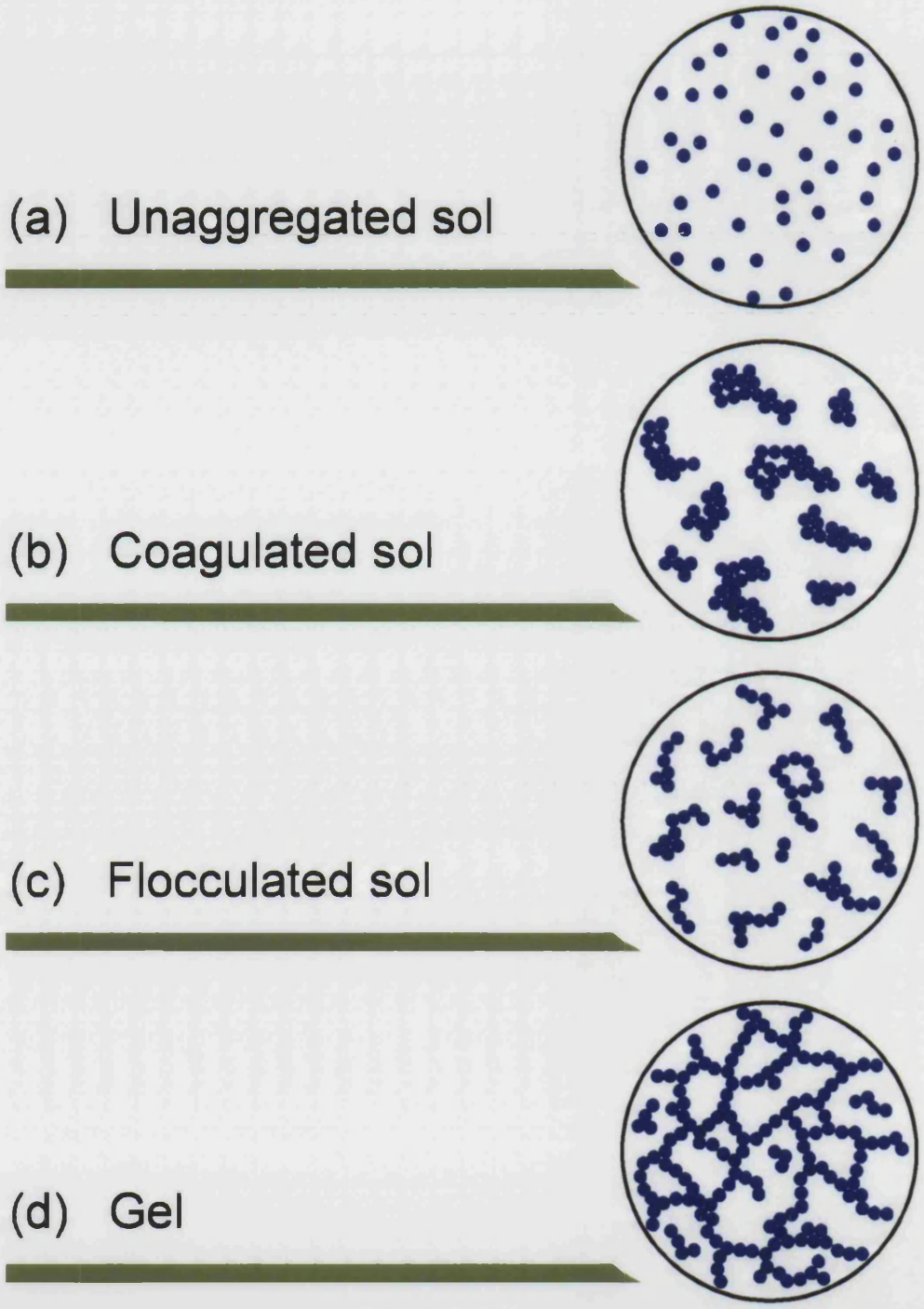

Figure 1.10 Schematic representation of the structures an unaggregated sol (a) may adopt when caused to aggregate: flocculated (b), coagulated (c) or gelled (d).
Note that flocculation and gelation are generally considered to be reversible processes.

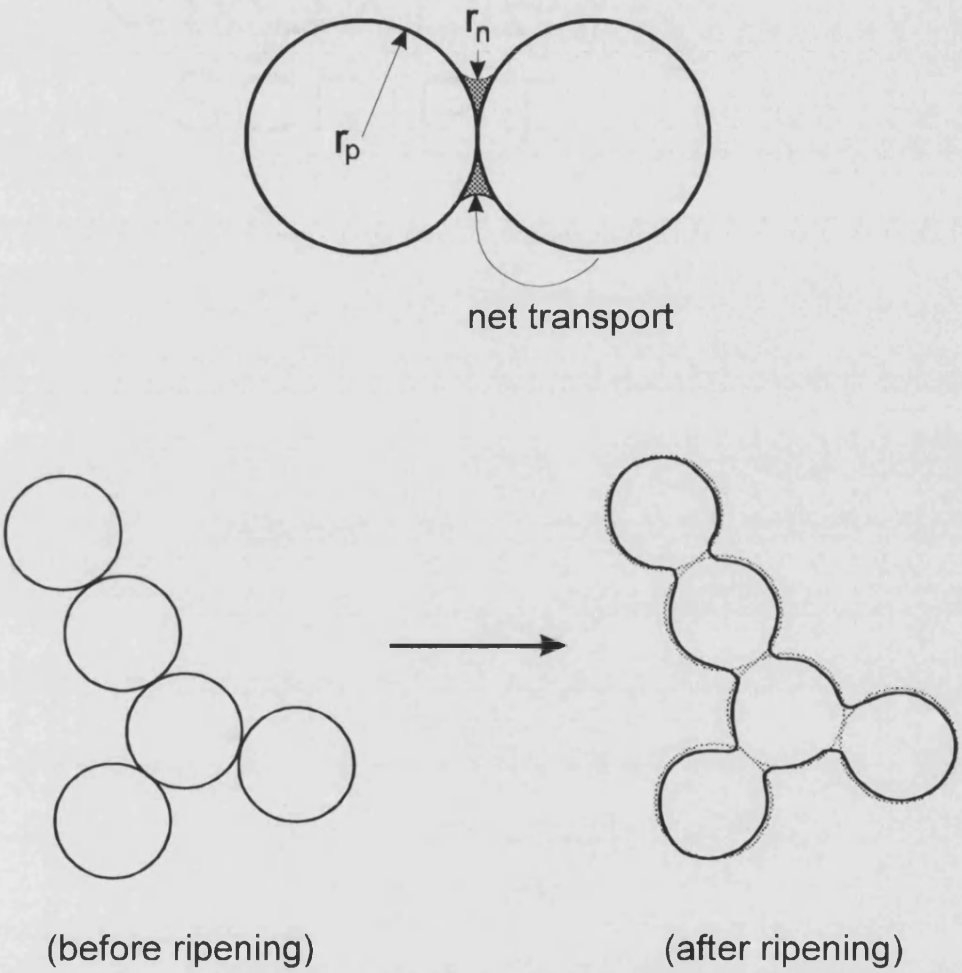

Figure 1.11 (*TOP*) Ostwald ripening involves material dissolving from surfaces with positive curvature and depositing in regions of negative curvature. The radius of the neck, r_n, is negative and that of each solid particle, r_p, is positive, with the consequence that the neck "grows" (shaded region).

(*BOTTOM*) The strength and stiffness of a gel will increase as a result of Ostwald ripening depositing material at the necks between particles.

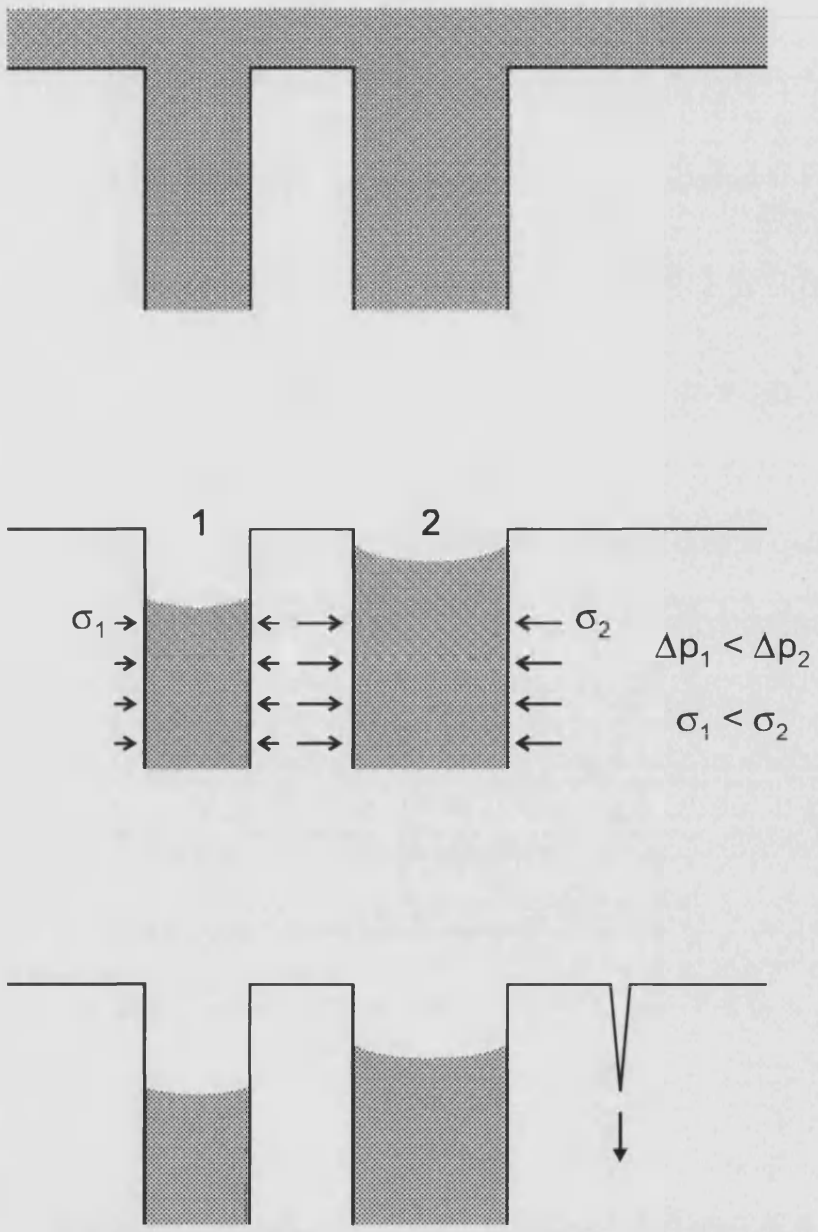

Figure 1.12 The differential pressures between pores of different sizes will lead to differential stresses during drying which may be sufficient to generate cracks as water is expelled from a wet gel.

(*TOP*) Wet gel.

(*MIDDLE*) Larger pores empty first, and stresses develop in the solid walls of material.

(*BOTTOM*) Cracking occurs.

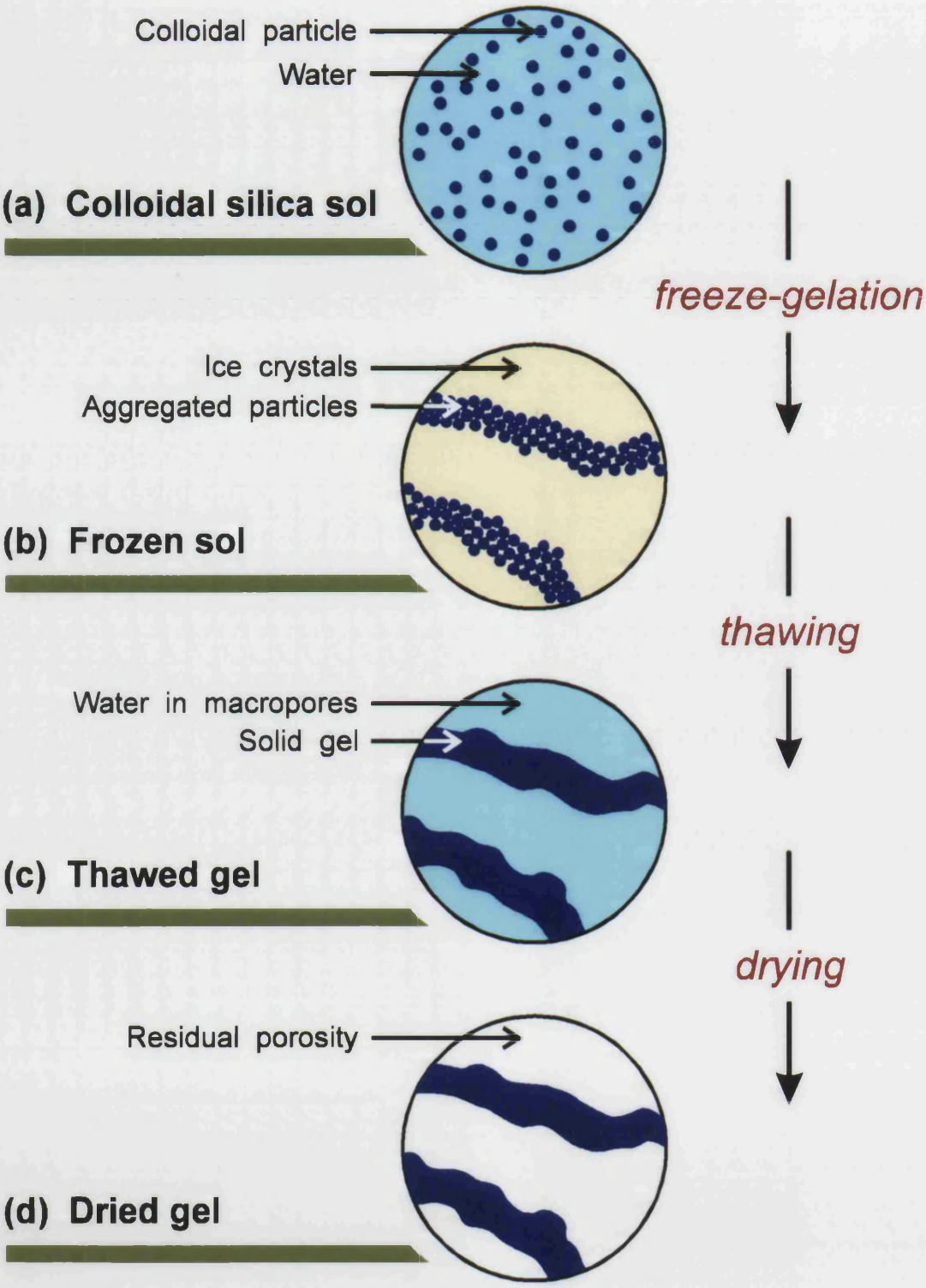

Figure 1.13 Schematic representation of the freeze-gelation process.

When a colloidal silica sol (a) is rapidly frozen, aggregation of silica particles occurs in the regions between growing ice crystals (b). The macroporous silica structure is retained as the gel is thawed (c) and dried (d).

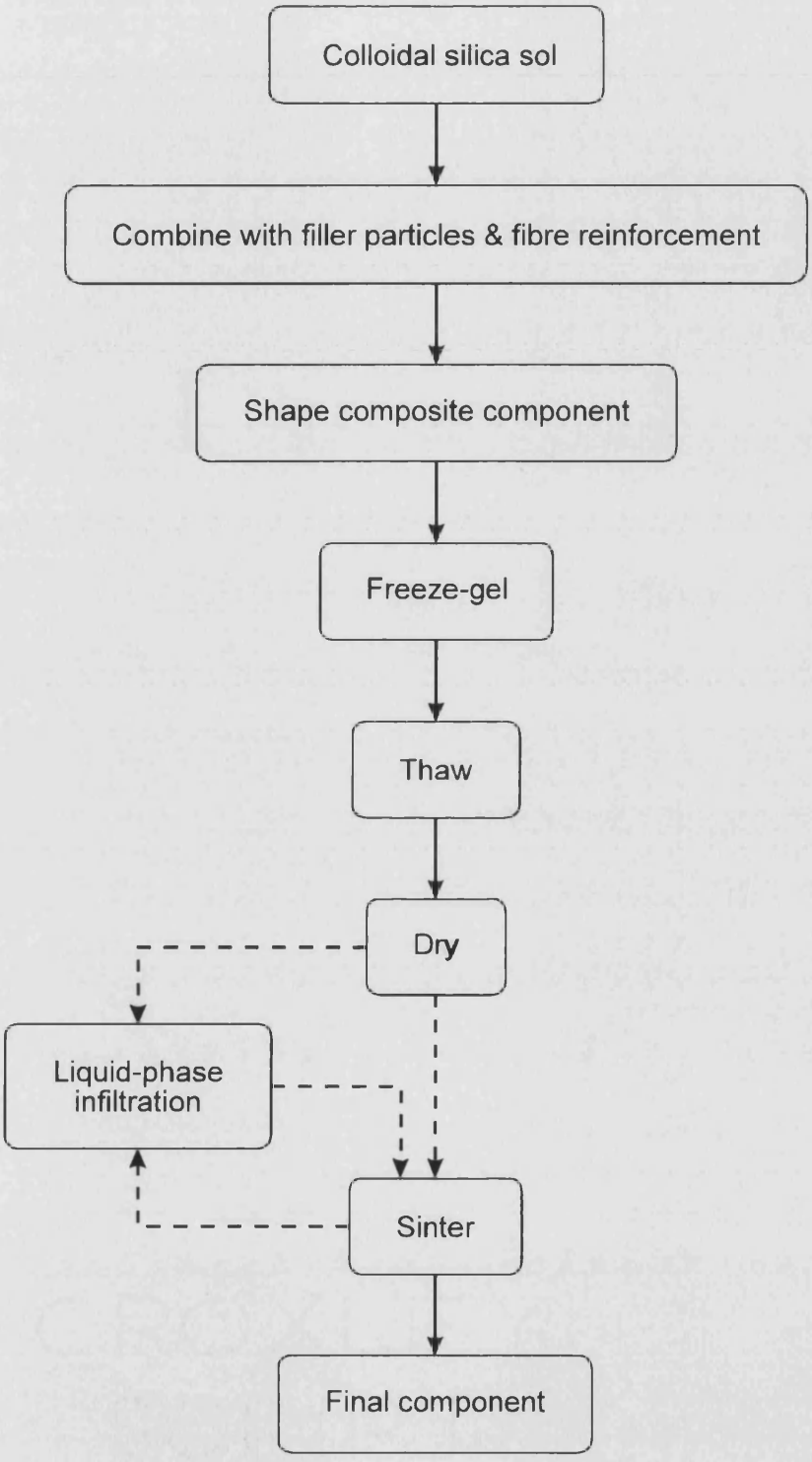

Figure 1.14 Flow diagram showing the operations involved in producing ceramic-matrix composite components by the freeze-gelation route.
Liquid-phase infiltration cycles may follow either drying or sintering. Additional, low-temperature sintering steps may be incorporated to densify the infiltrant.

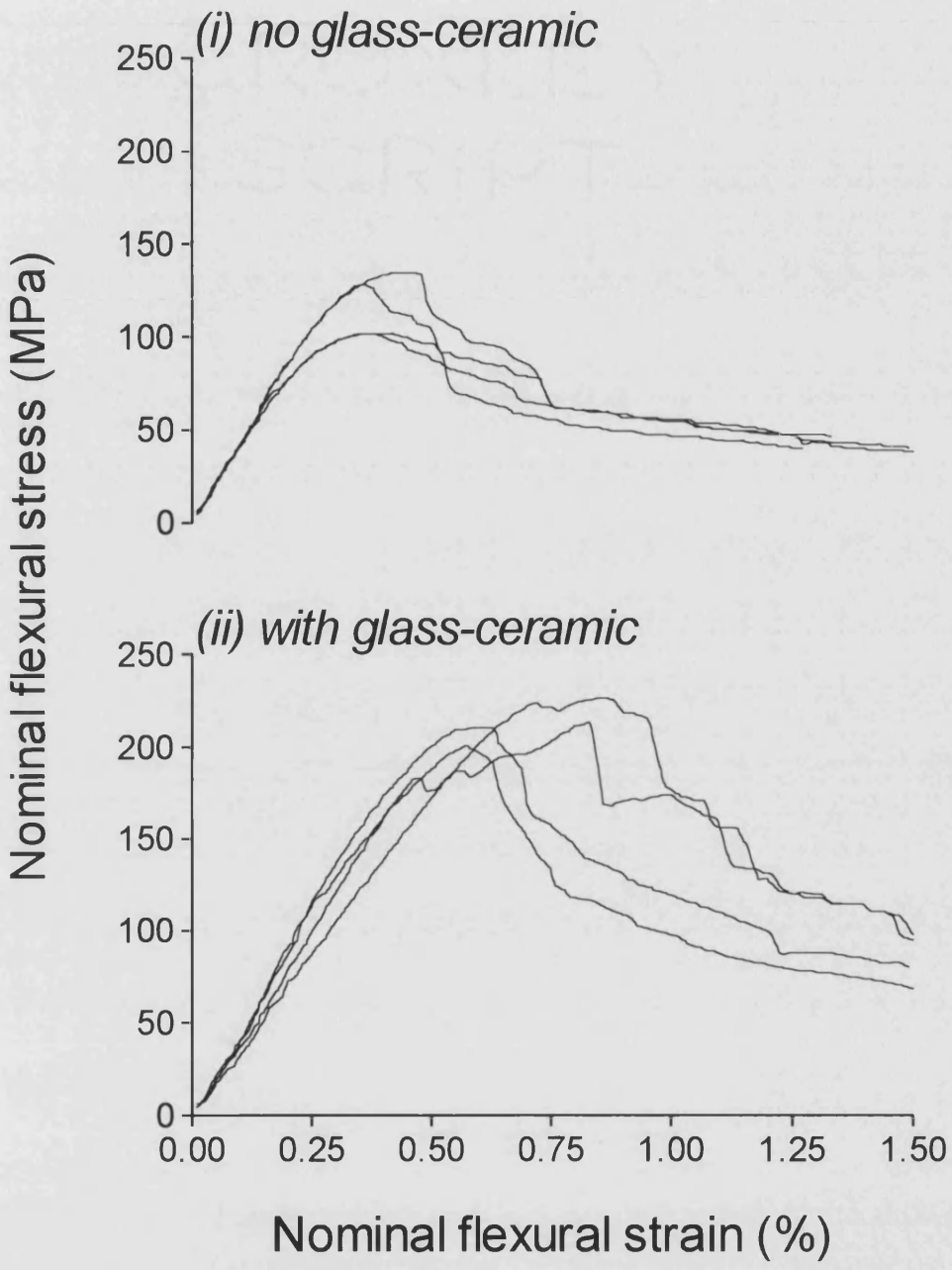

Figure 1.15 Effect of matrix filler on flexural stress/strain curves of unidirectional, carbon fibre-reinforced silica fabricated by hand layup and freeze-gelation [102].

(a) no matrix filler;

(b) glass-ceramic (lithium alumino-silicate) filler.

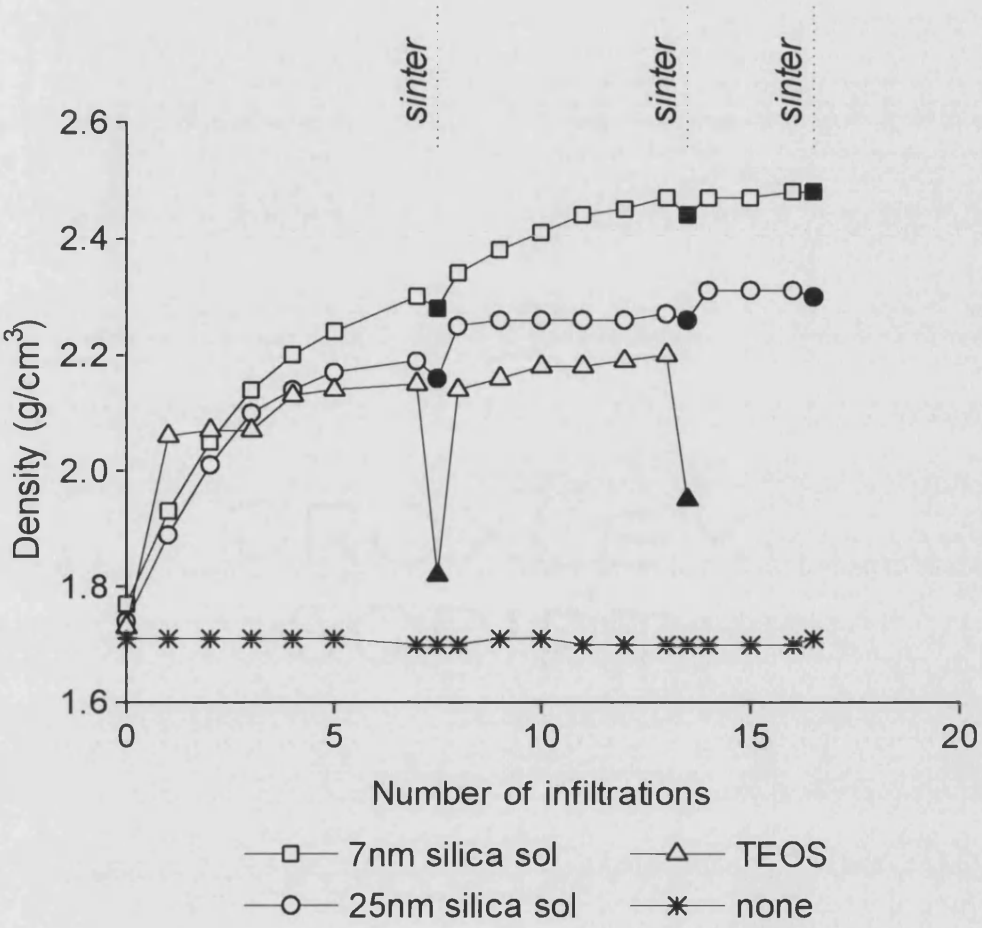

Figure 1.16 Variation of density of a Nextel (mullite) fibre-reinforced ceramic-matrix composite with repeated vacuum-assisted, liquid-phase infiltrations in various media. The composite rings were prepared by filament winding and freeze-gelation. The specimens were sintered after 7, 13 and 16 infiltration cycles (solid symbols).

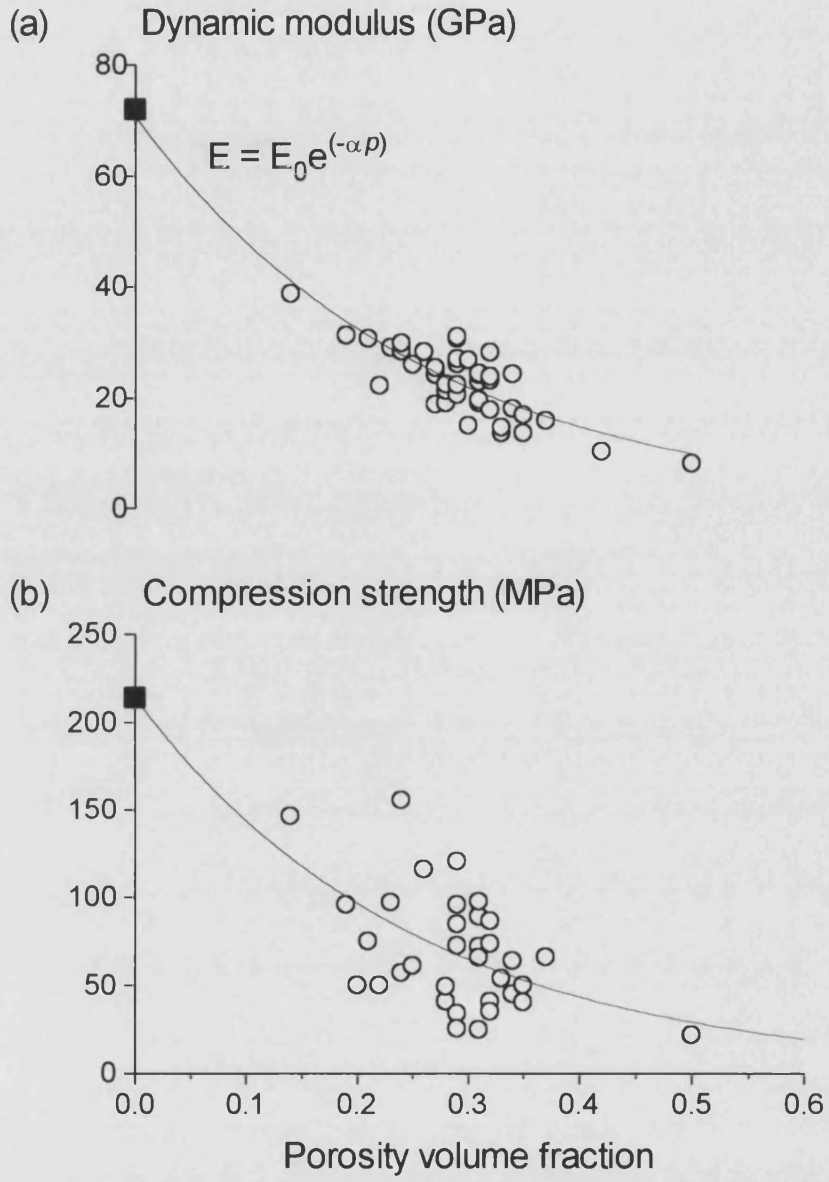

Figure 1.17 Variation of (a) dynamic elastic modulus and (b) compression strength with porosity in Saffil (short-fibre)-reinforced cast composites. The data were obtained from composites with several matrix compostions. The modulus data are satisfactorily described by an exponential decay function with $E_0 = 72$ GPa and $\alpha = 4$ [102].

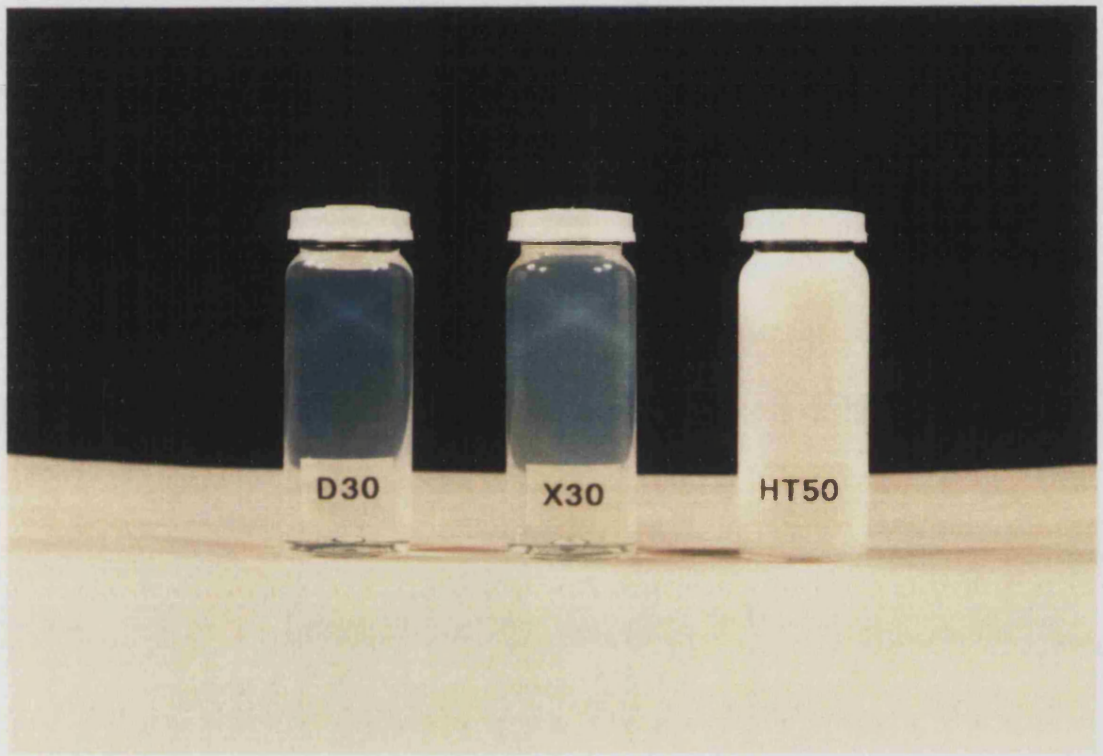

Figure 3.1 Appearance of Monsanto's Syton ® colloidal silica sols.

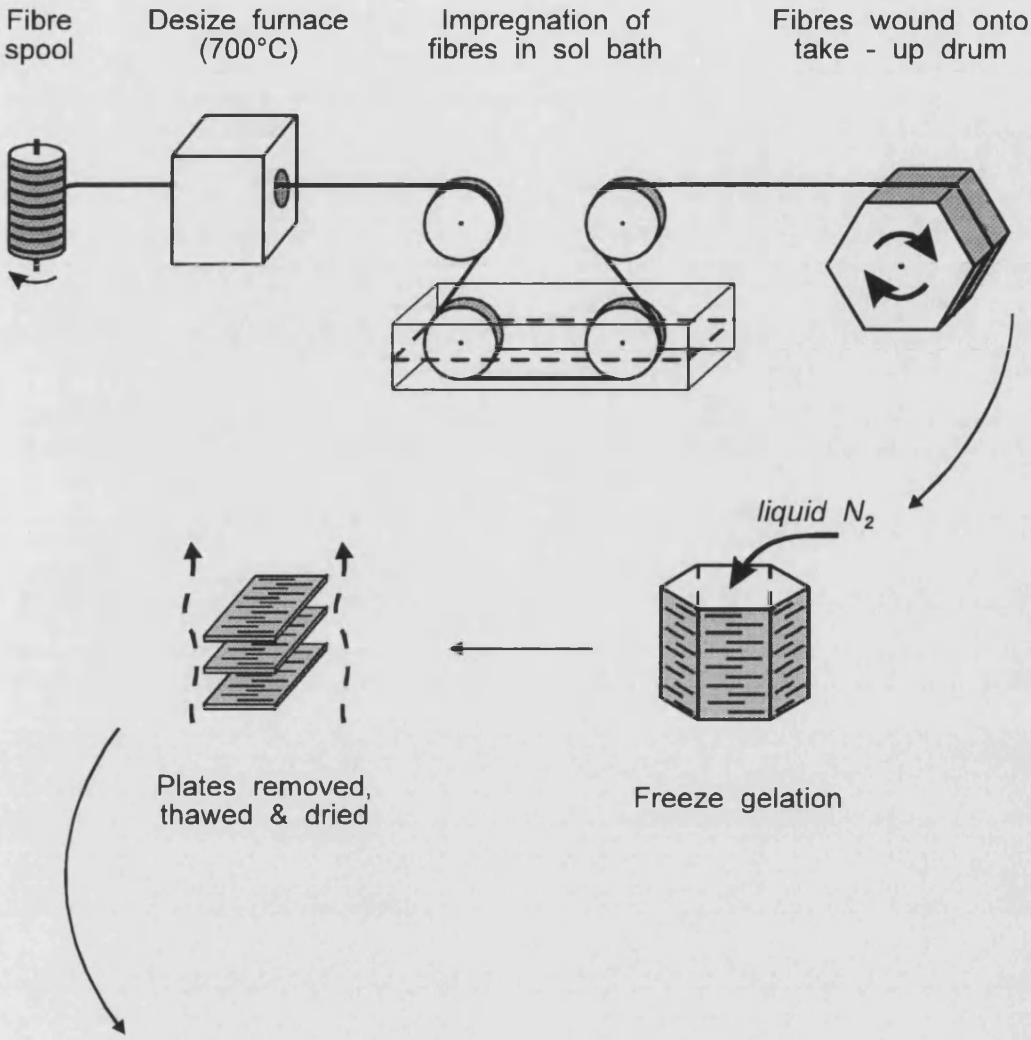

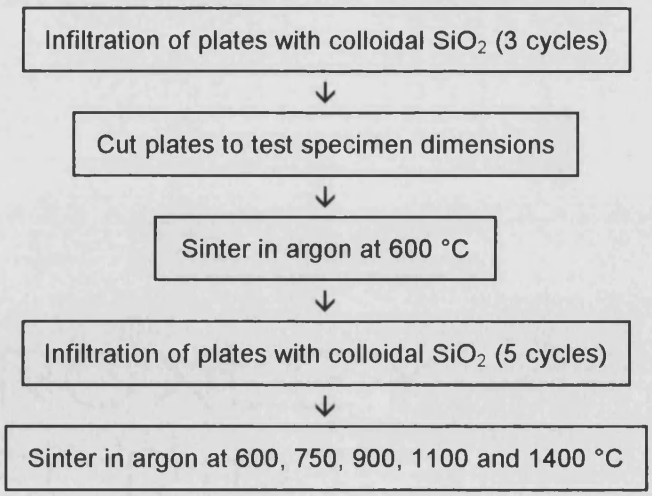

Figure 3.2 Schematic representation of the filament winding/freeze-gelation processing route used to fabricate composite samples designated 'HC', 'XQ' and 'HQ'.

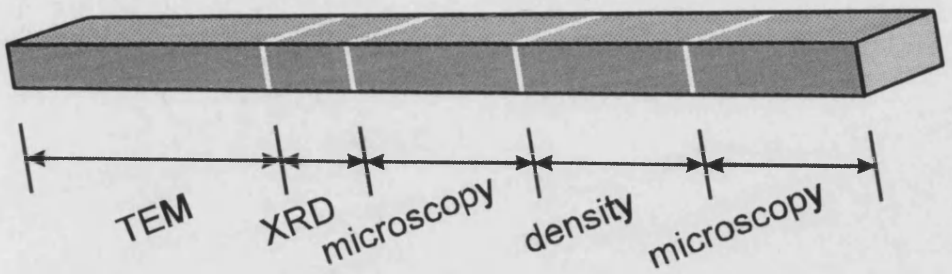

Figure 3.3 Cutting plan for microstructural characterisation of samples.

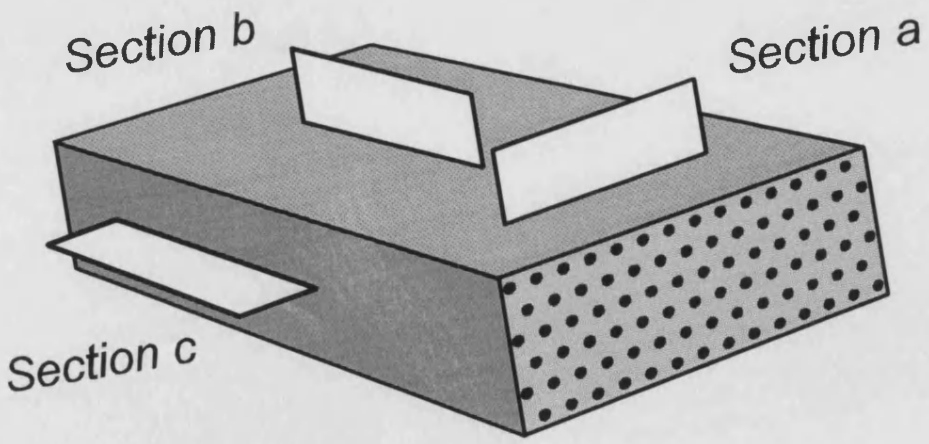

Figure 3.4 Definition of sections used in microscopy.

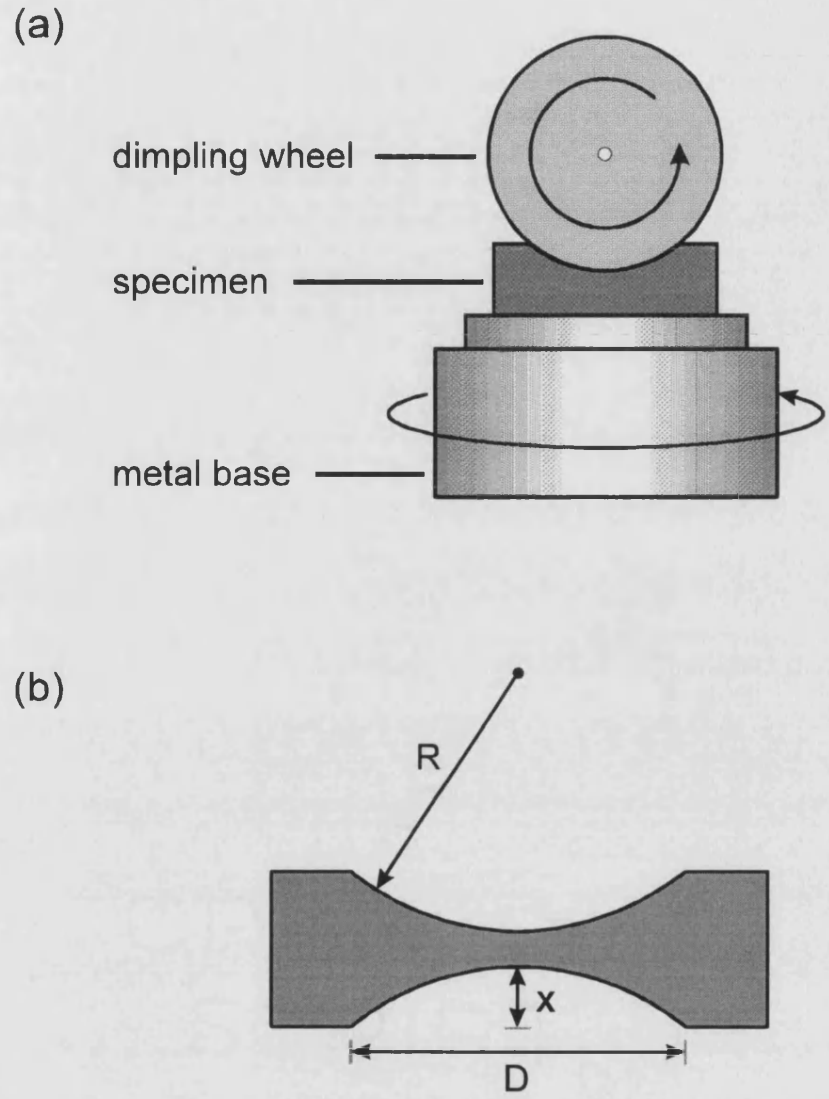

D dimple diameter
x dimple depth
R wheel diameter

$$x = R - \sqrt{R^2 - \left(\frac{D}{2}\right)^2}$$

Figure 3.5 (a) Geometry of dimpling operation.

(b) Calculation of specimen thickness from diameter of dimpled area.

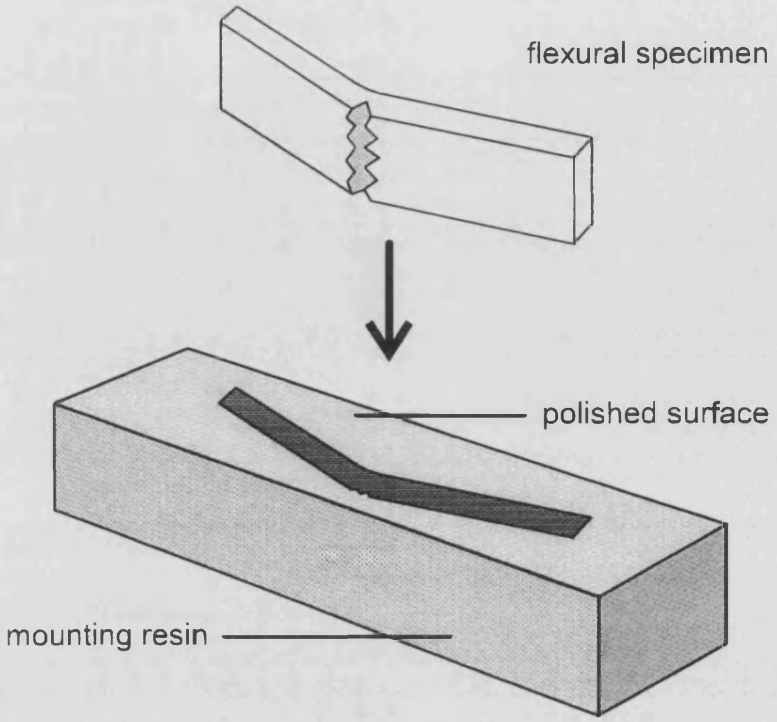

Figure 3.6 Flexural test specimens were prepared for optical microscopy and SEM by mounting in resin and polishing.

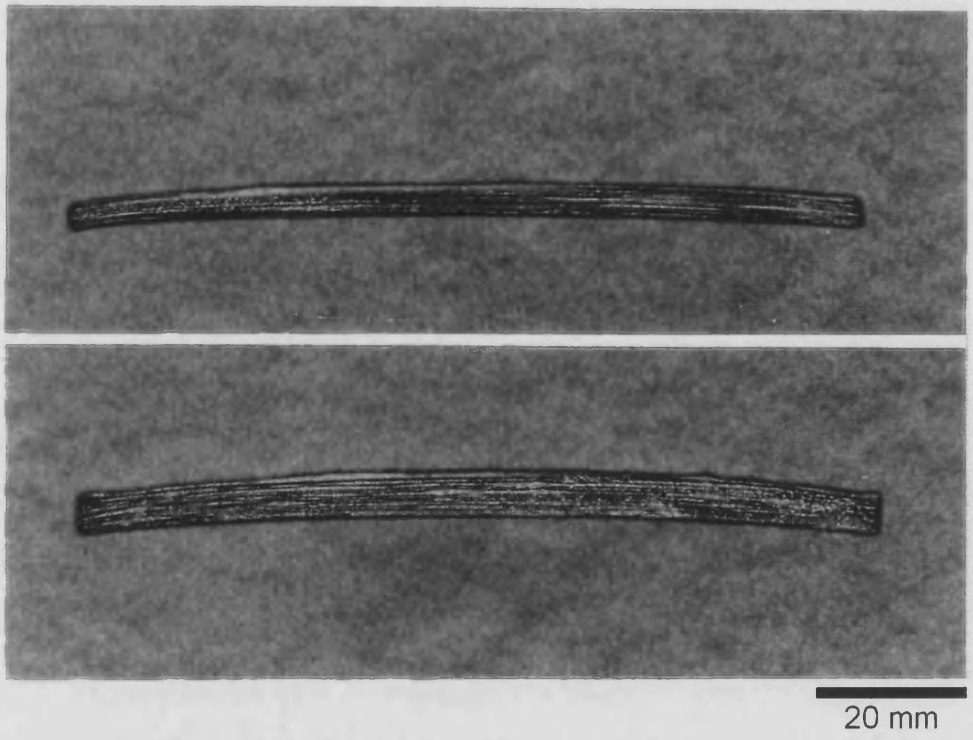

Figure 3.7 Typical appearance of as-received composite samples.

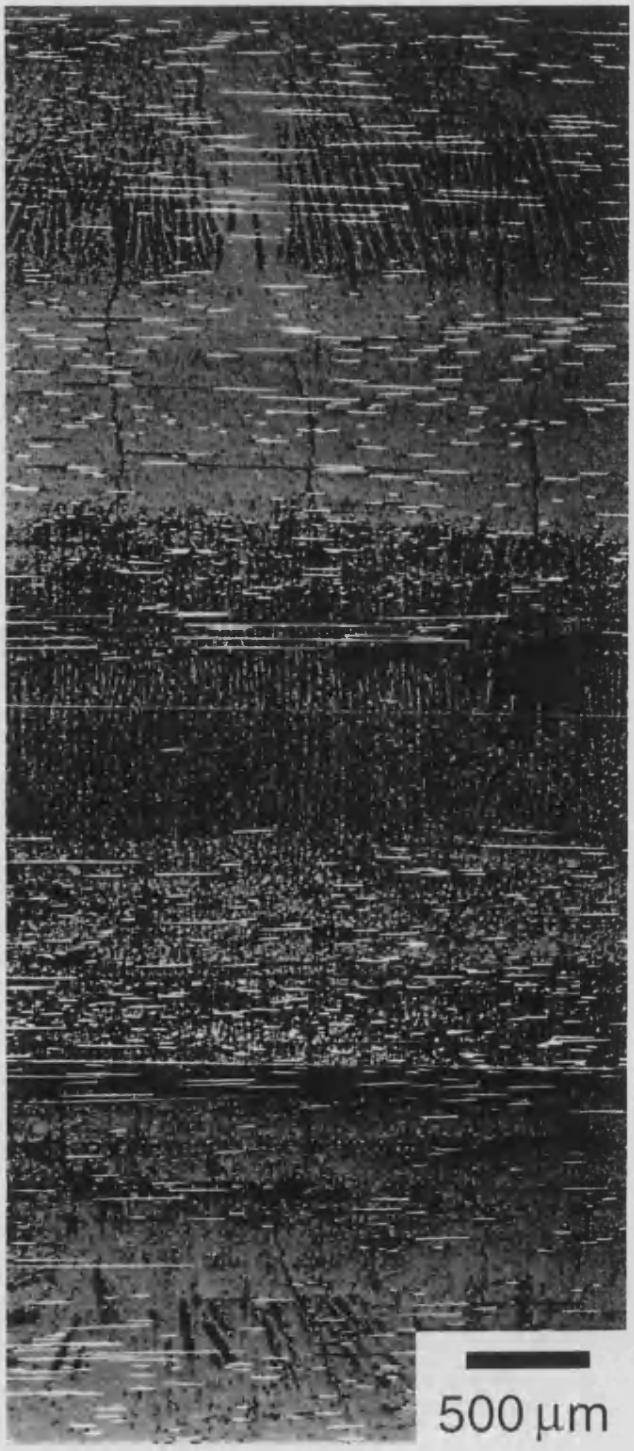

Figure 3.8 Optical micrograph of sample 'HC' sintered at 750 °C. Freeze-gelation began at the top of this picture. The specimen is oriented in plane b (figure 3.4).

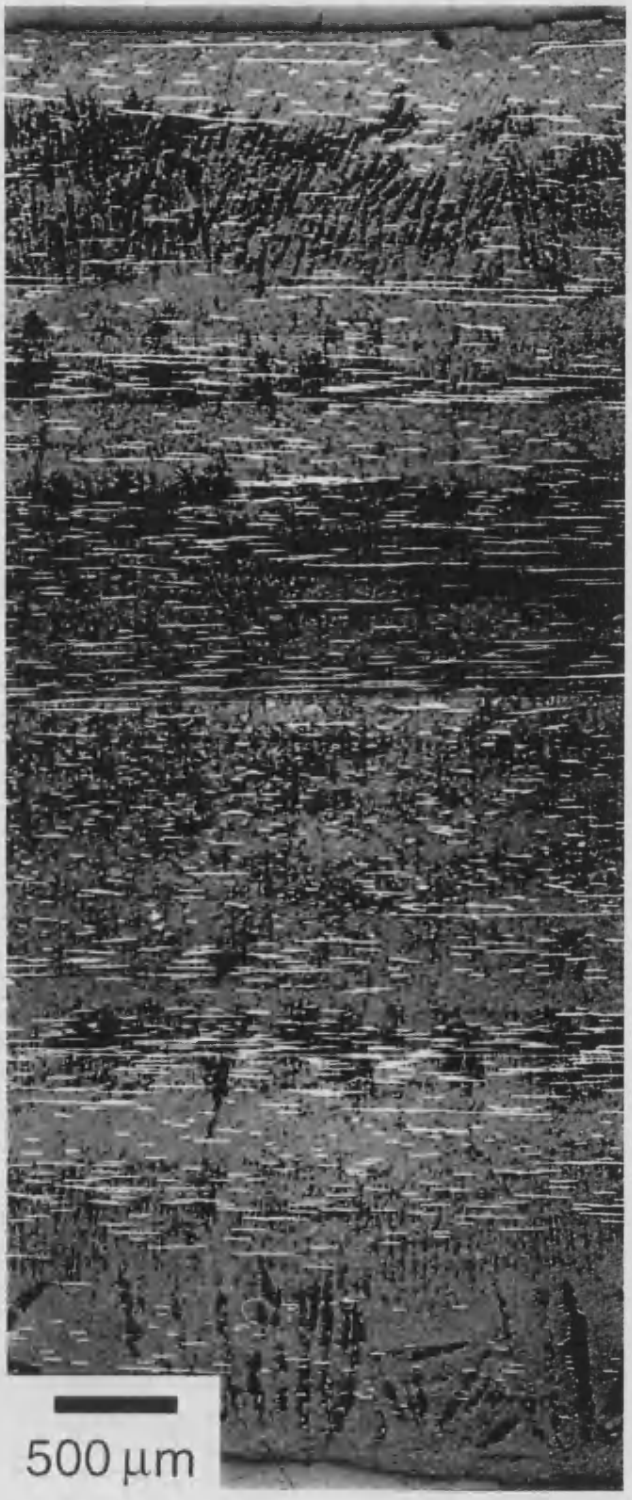

Figure 3.9 Optical micrograph of sample 'HC' sintered at 900 °C. Freeze-gelation began at the top of this picture. The specimen is oriented in plane b (figure 3.4).

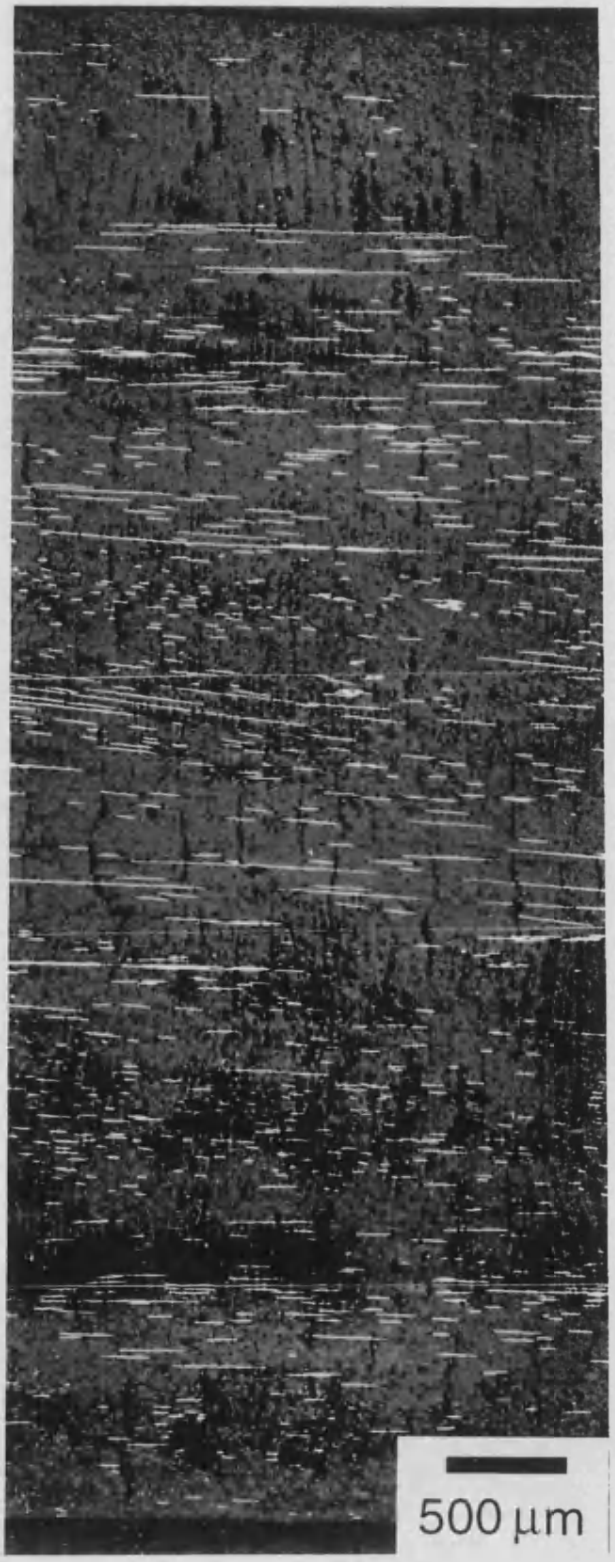

Figure 3.10 Optical micrograph of sample 'HC' sintered at 1100 °C. Freeze-gelation began at the top of this picture. The specimen is oriented in plane b (fig. 3.4).

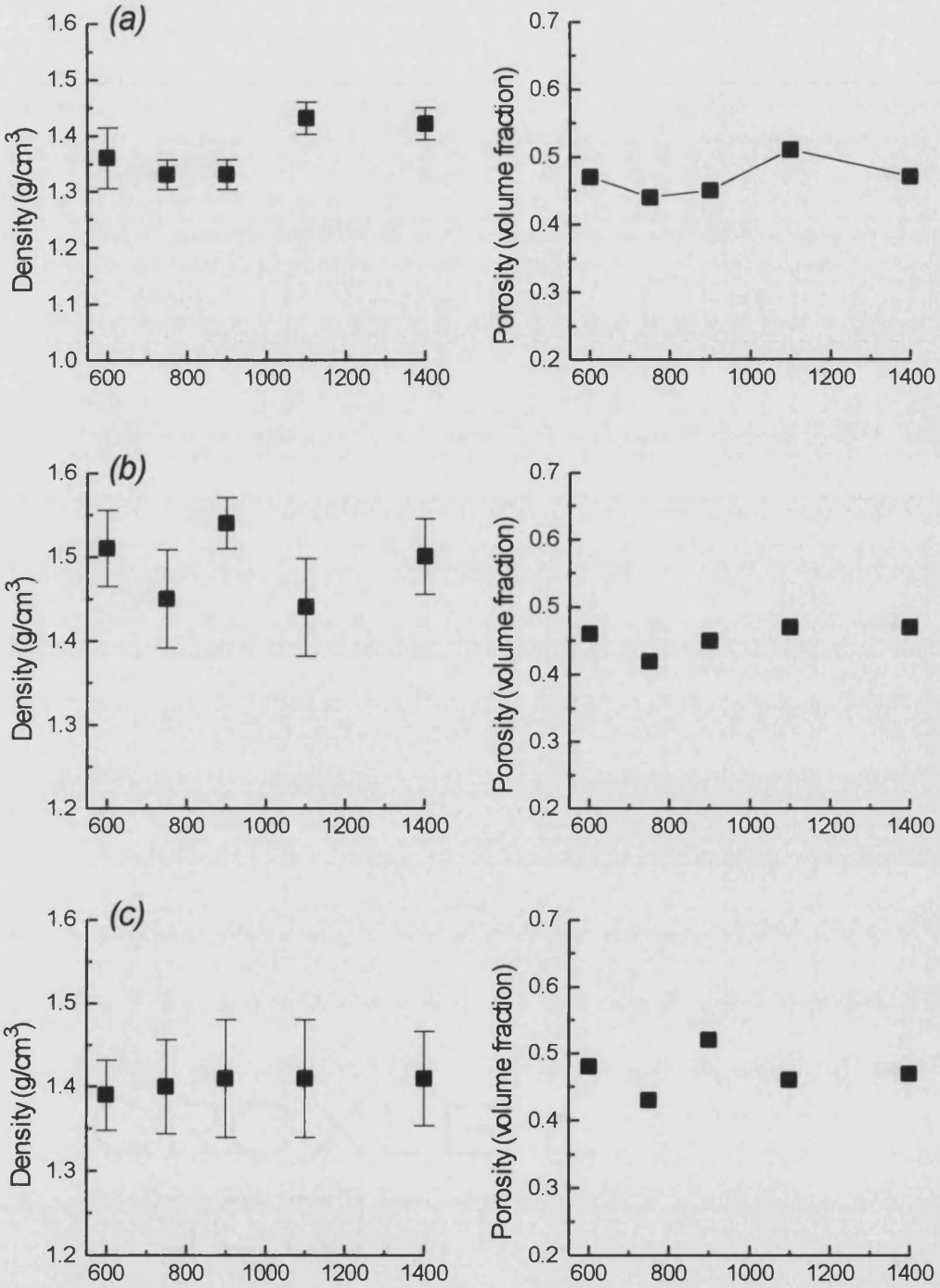

Figure 3.11 Variation of density and porosity volume fraction with sintering temperature for (a) 'HC' samples; (b) 'HQ' samples; (c) 'XQ' samples.
Error bars indicate standard deviations.

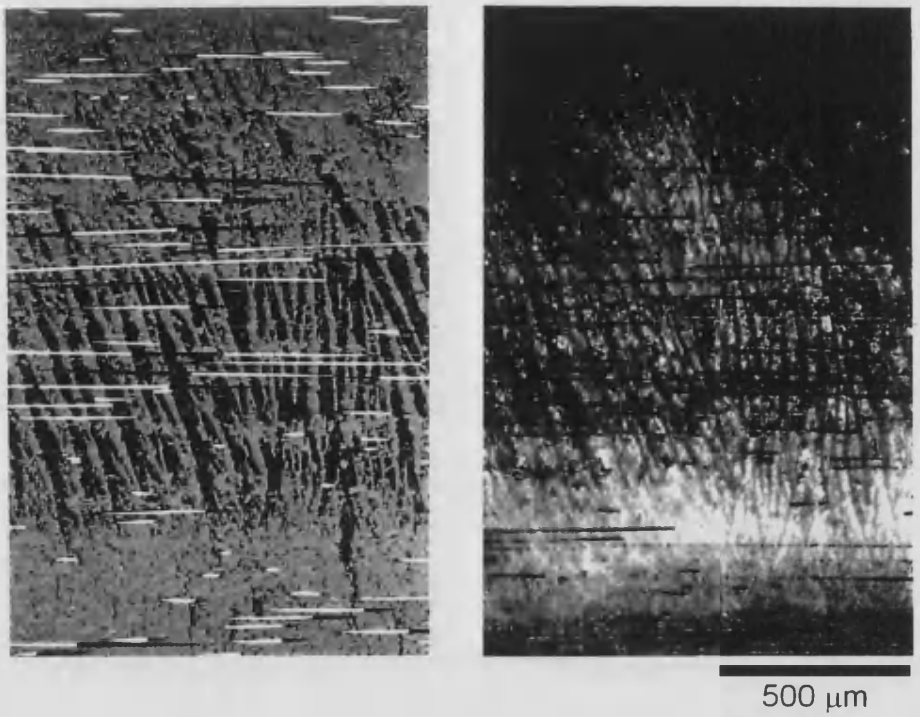

Figure 3.12 'Columnar' pore structure observed by (left) bright field and (right) dark field microscopy.

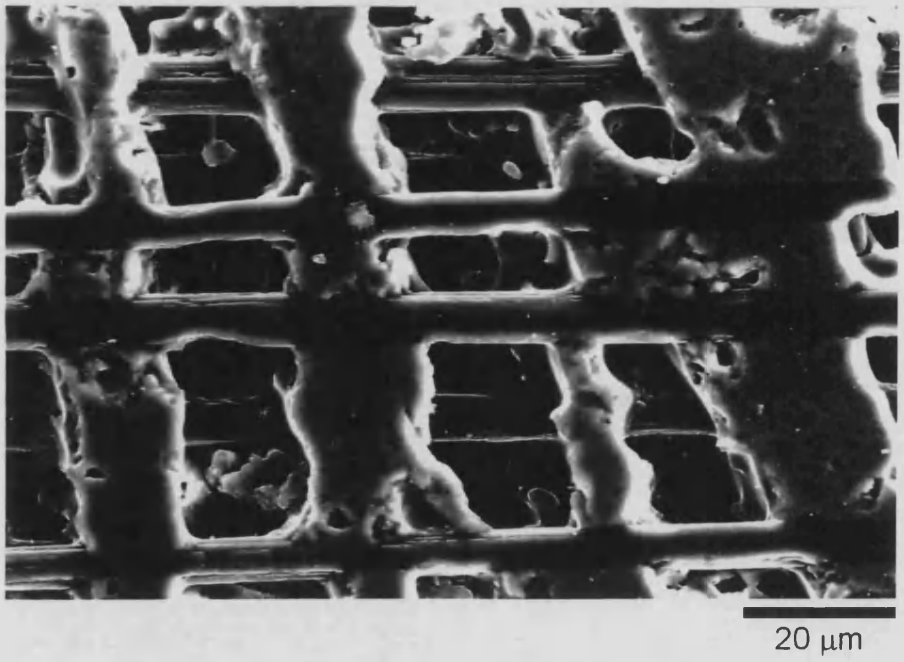

Figure 3.13 SEM micrograph demonstrating the plate-like nature of the 'columnar' pores observed in the central regions of the composites.
Sample: 'HQ' sintered at 750 °C, sectioned in plane b (figure 3.4).

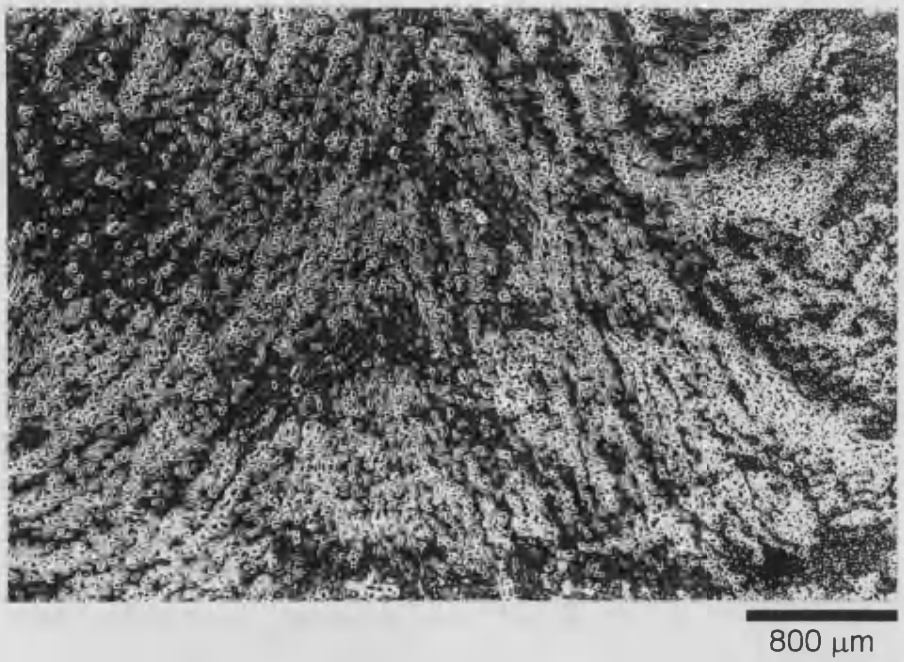

Figure 3.14 Patterns of porosity are effectively revealed in the SEM when charge accumulates in pores and appears bright against the background. The variable orientation in porosity is attributed to the thermal fluctuations affecting ice-crystal growth during freeze-gelation.
Sample: 'HC' sintered at 900 °C, sectioned in plane a (figure 3.4).

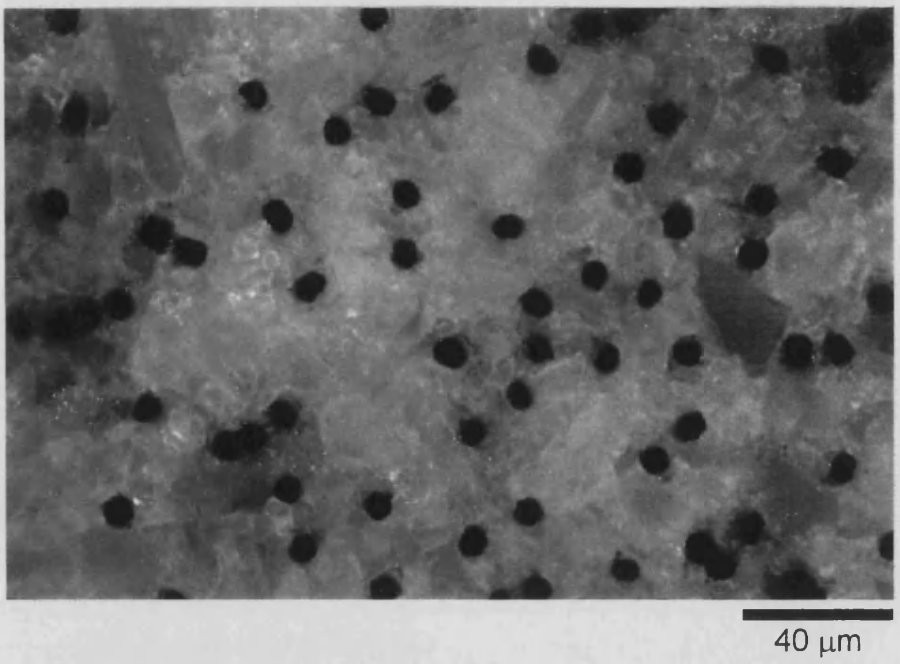

Figure 3.15 Optical micrograph showing good fibre distribution in dense matrix regions.
Sample: 'HC' sintered at 900 °C, sectioned in plane a (figure 3.4).

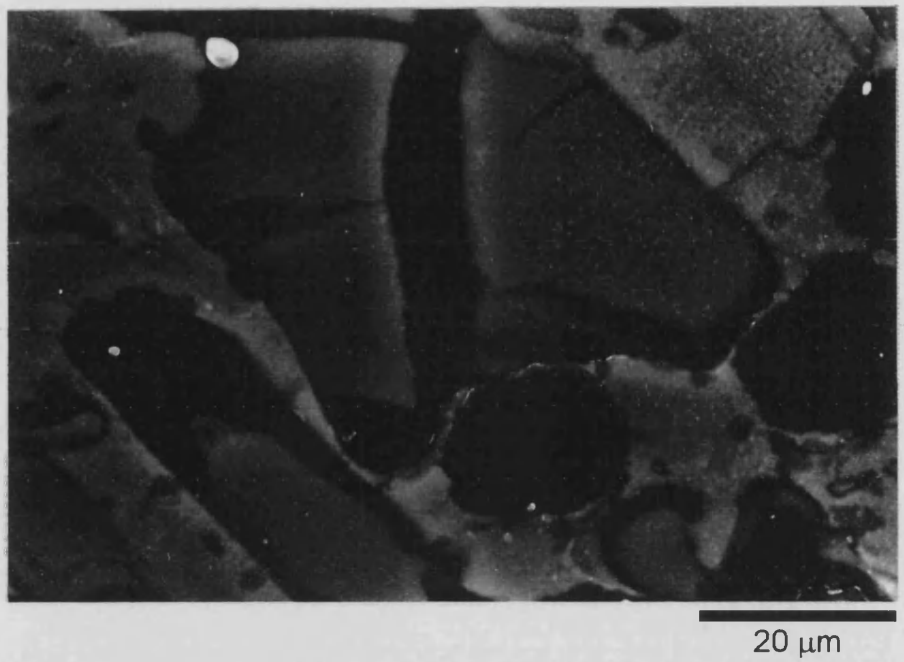

Figures 3.16 SEM micrograph showing how the fine-particle-size colloidal silica infiltrant shrinks and cracks during drying.
Sample: 'HQ' sintered at 750 °C, sectioned in plane a (figure 3.4).

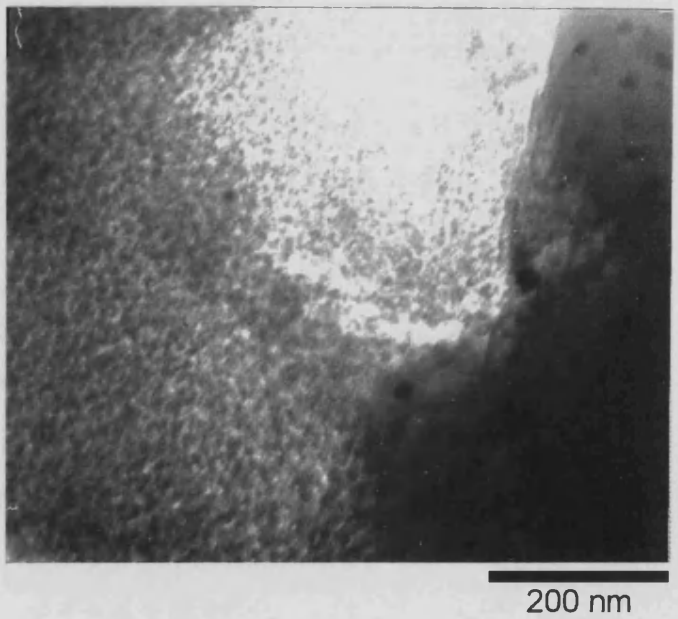

Figure 3.17 TEM micrograph of a region of 7 nm colloidal silica infiltrant (Syton X30). Shrinkage cracks are clearly seen, and the limited degree of fusing between colloidal silica particles leads to nanometre-scale porosity between those particles. Sample: 'XQ' sintered at 750 °C, sectioned in plane c (figure 3.4).

3.18

3.19

Figures 3.18 and 3.19

Optical micrographs showing transverse matrix cracking in dense matrix strata. These 'HQ' composite samples were sintered at 750 °C (figure 3.18) and at 1400 °C (figure 3.19) and were sectioned in plane b (figure 3.4).

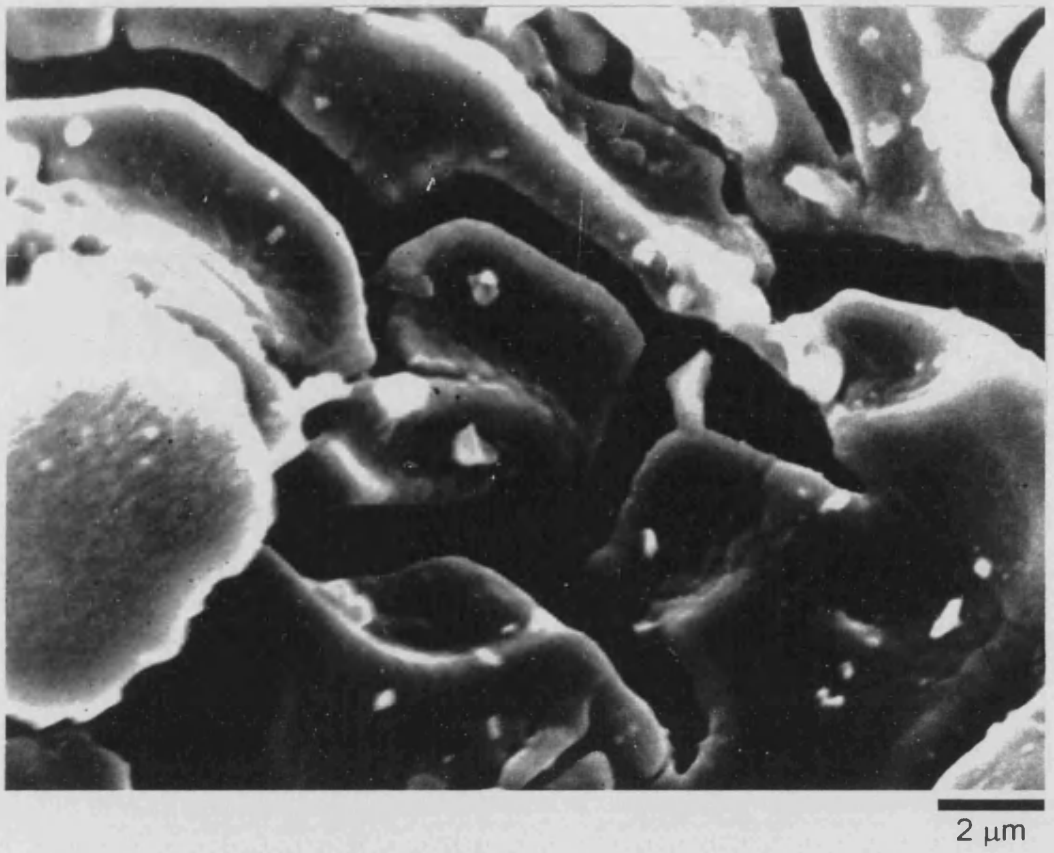

Figure 3.20 Circumferential and radial matrix cracks around fibres arising from residual thermal stresses. This was seen most clearly in fracture surfaces.
Sample: Series 'HC' composite sintered at 1100 °C.

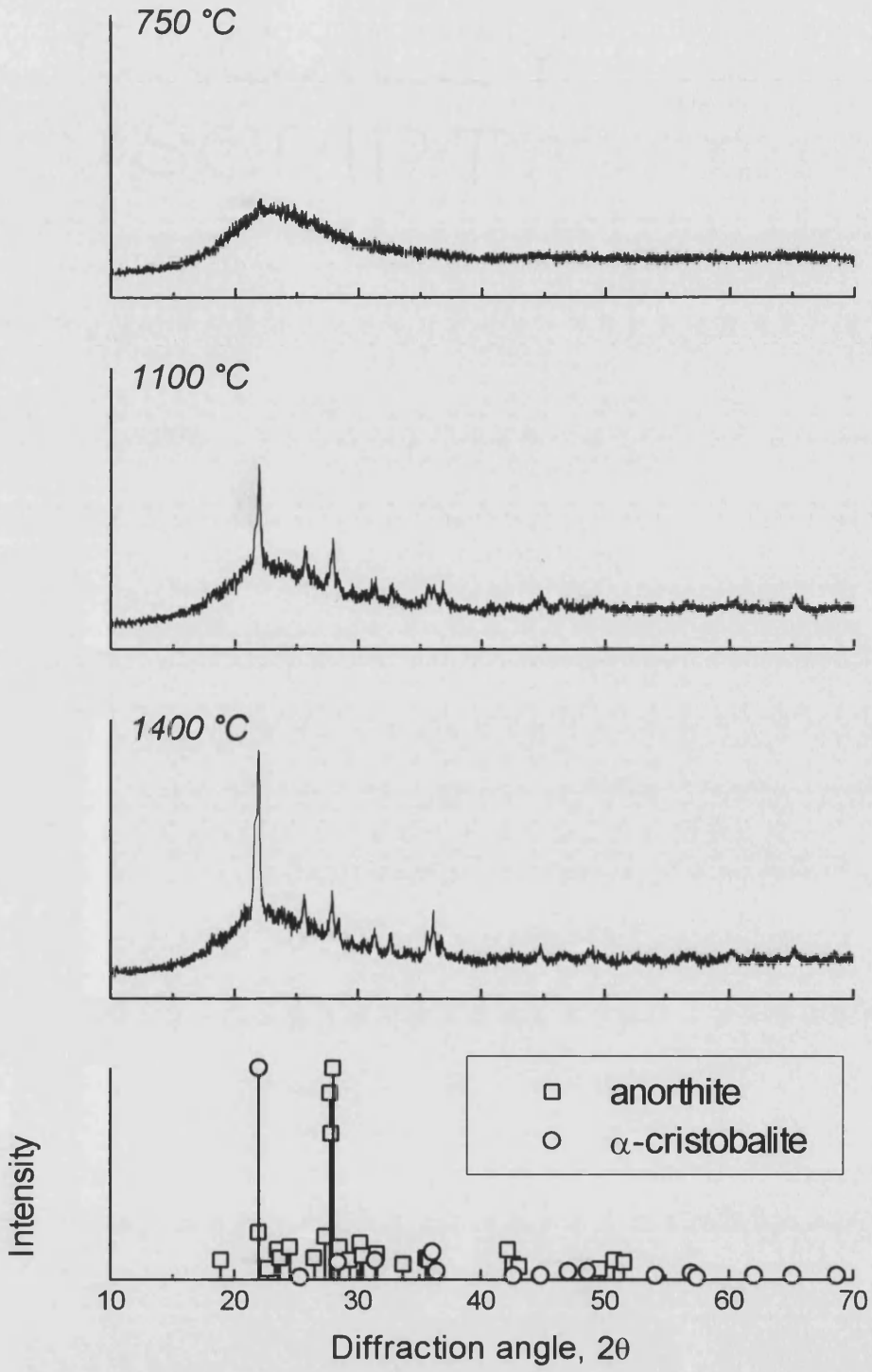

Figure 3.21 XRD curves for 'HC' specimens sintered at 750 °C, 1100 °C & 1400 °C. All data are plotted to the same ordinate scale. The standard patterns for anorthite [113] and α-cristobalite [114] (lower graph) are both normalised with respect to the height of their principal peak.

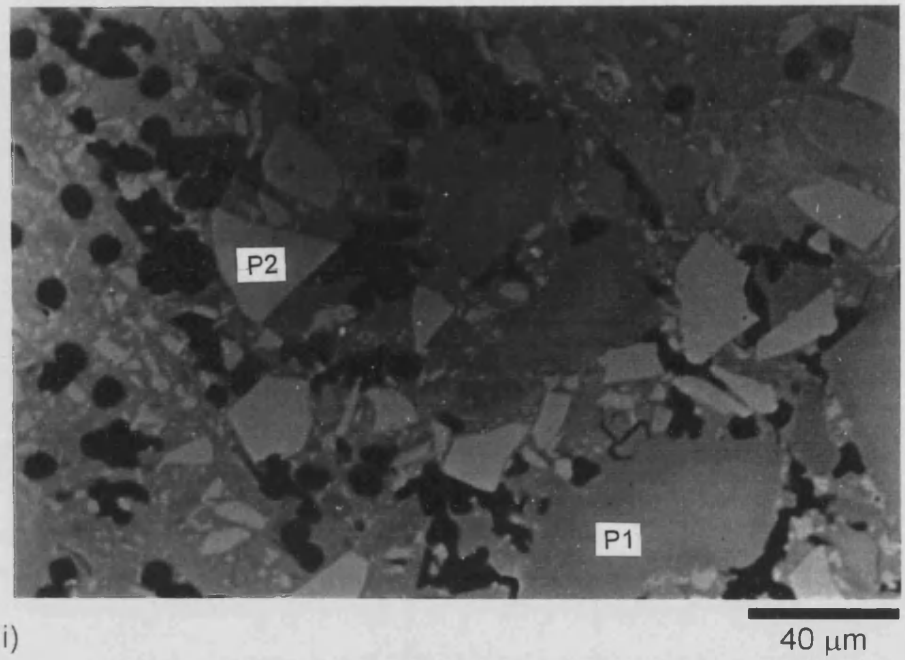

i)

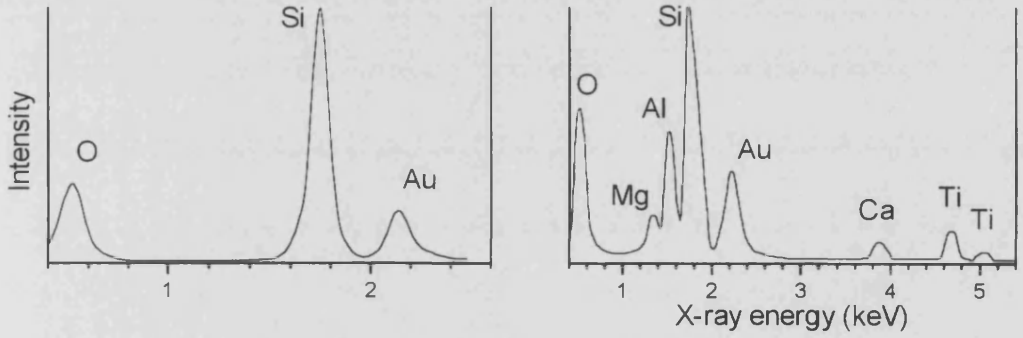

(ii) P1

(iii) P2

Figure 3.22 (i) SEM micrograph of sample 'HC' sintered at 900 °C. The compositions of the light filler particles (P1) and the darker particles (P2) are given in the EDS traces (ii) and (iii) respectively.

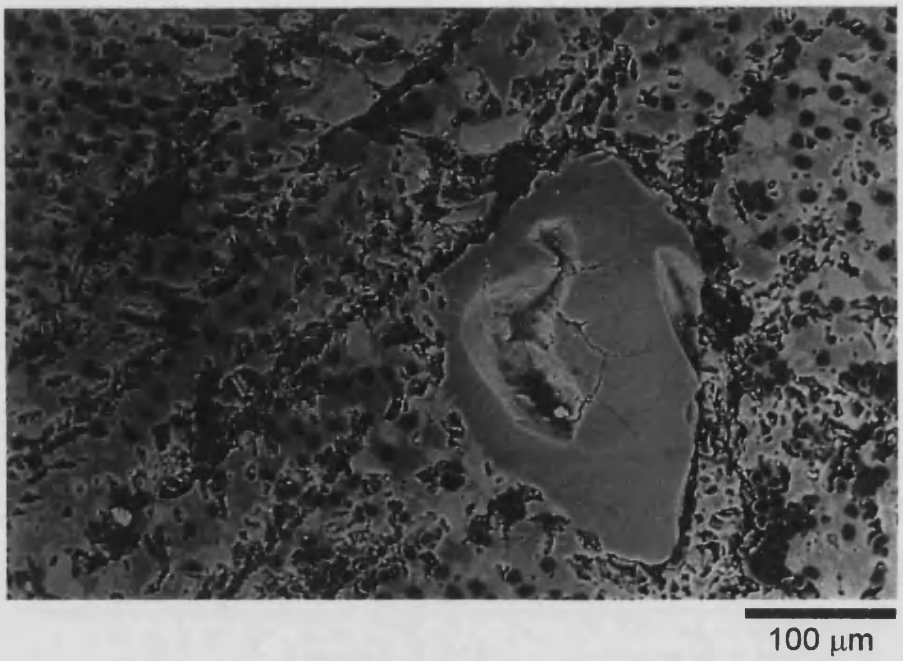

Figure 3.23 SEM micrograph of sample 'HC' sintered at 1100 °C revealing internal cracking of a filler particle.

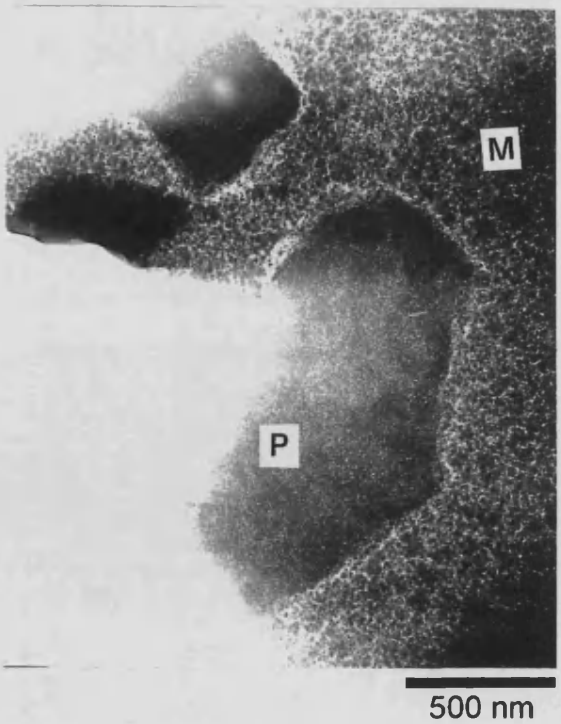

Figure 3.24 TEM micrograph of sample 'HC' sintered at 900 °C showing CMA6 filler particle (P) and sol-gel-derived silica matrix (M).

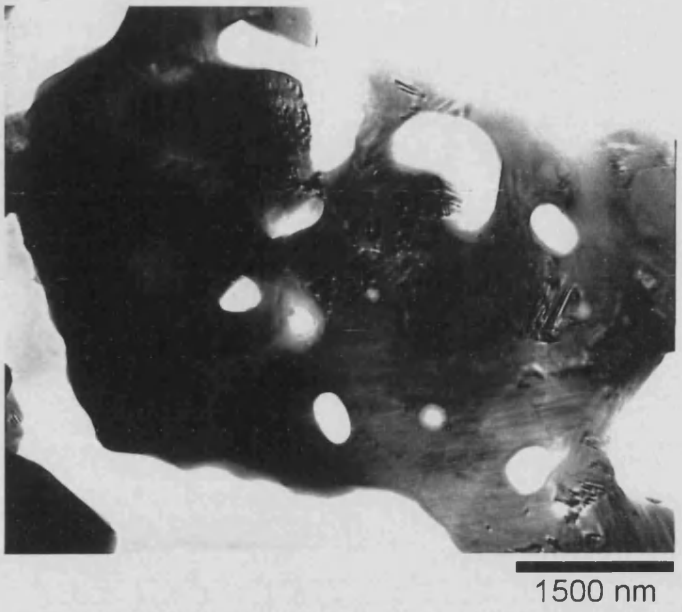

Figure 3.25 TEM micrograph of sample 'HC' sintered at 1100 °C showing a partially-crystallised CMA6 filler particle.

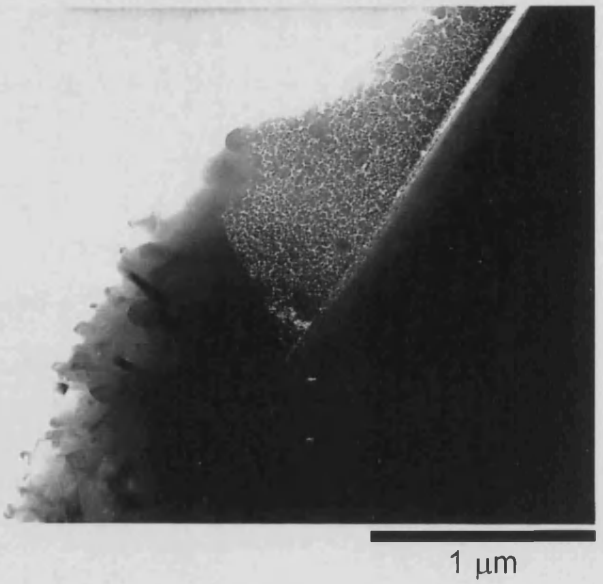

Figure 3.26 TEM micrograph showing lack of intimate contact between fibre and sol-gel silica matrix in a 'HC' sample sintered at 1100 °C.

Figure 3.27 SEM micrograph of as-received amorphous silica filler particles employed in composite series 'HC' and 'XQ'.

Figure 3.28 SEM micrograph of as-received CMA6 filler particles employed in composite series 'HC'.

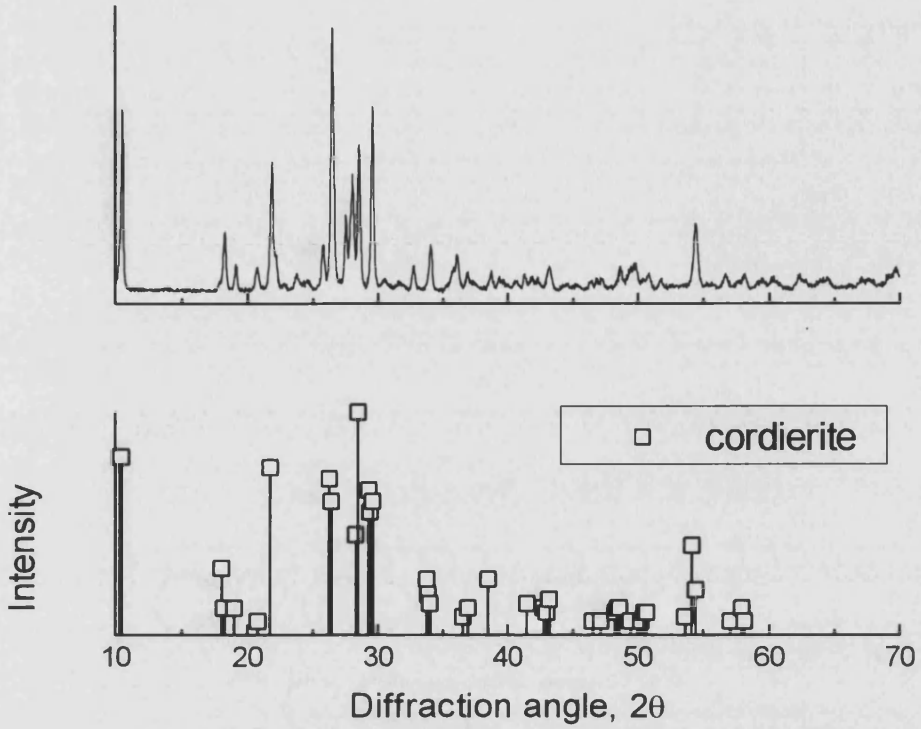

Figure 3.29 XRD spectrum from 'as-received' CMA6 filler particles sintered at 1100 °C. The standard pattern for cordierite ($2MgO.Al_2O_3.5SiO_2$) [115] (lower graph) is normalised with respect to the height of the principal peak.

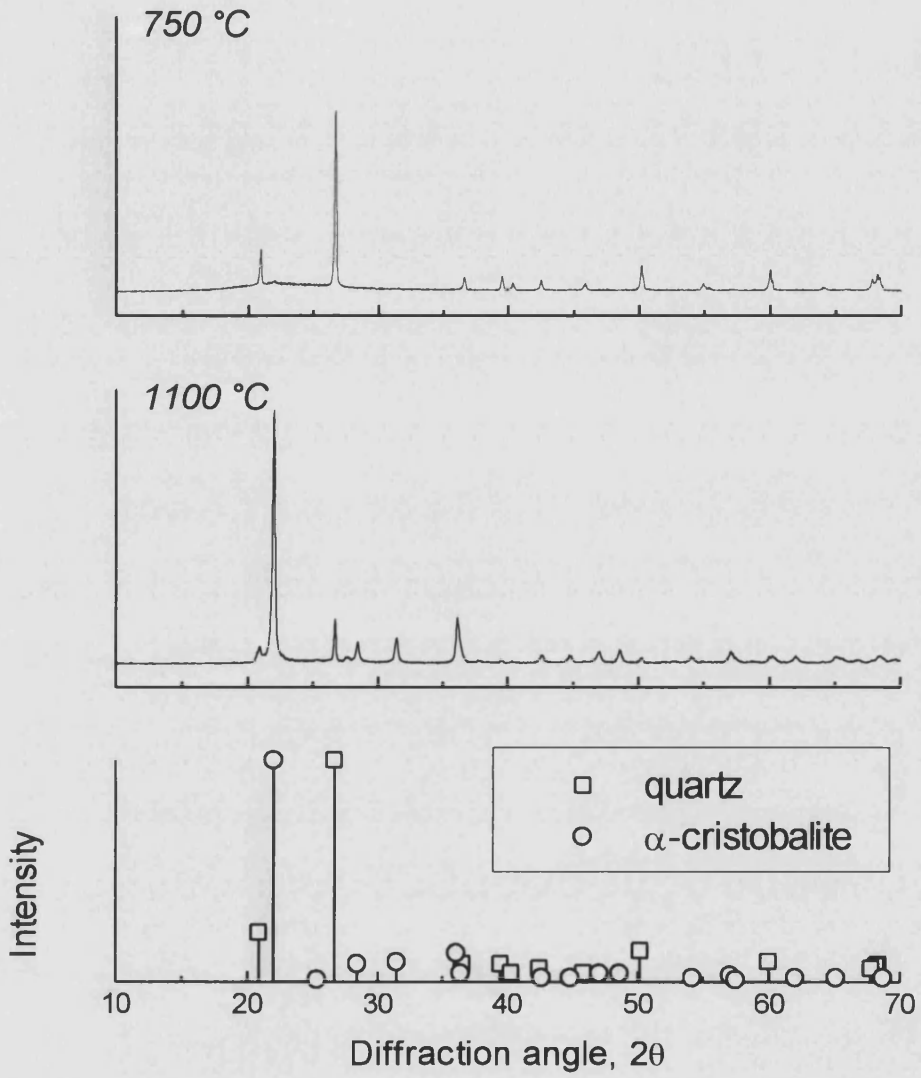

Figure 3.30 XRD curves for 'XQ' specimens sintered at 750 °C and 1100 °C. All data are plotted to the same ordinate scale. The standard patterns for quartz [116] and α-cristobalite [114] (lower graph) are both normalised with respect to the height of their principal peak.

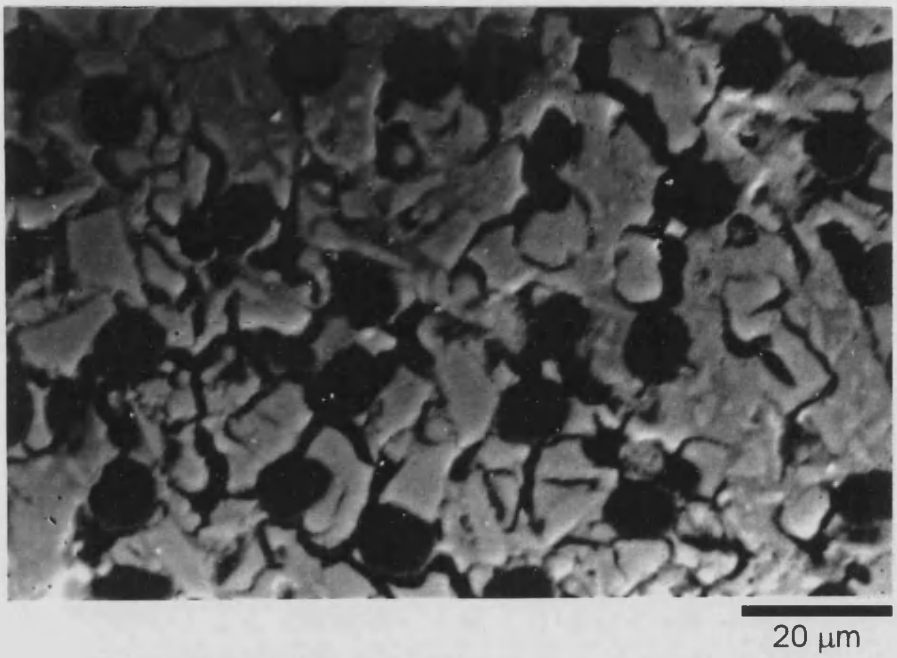

Figure 3.31 SEM micrograph of sample 'XQ' following sintering at 900 °C.

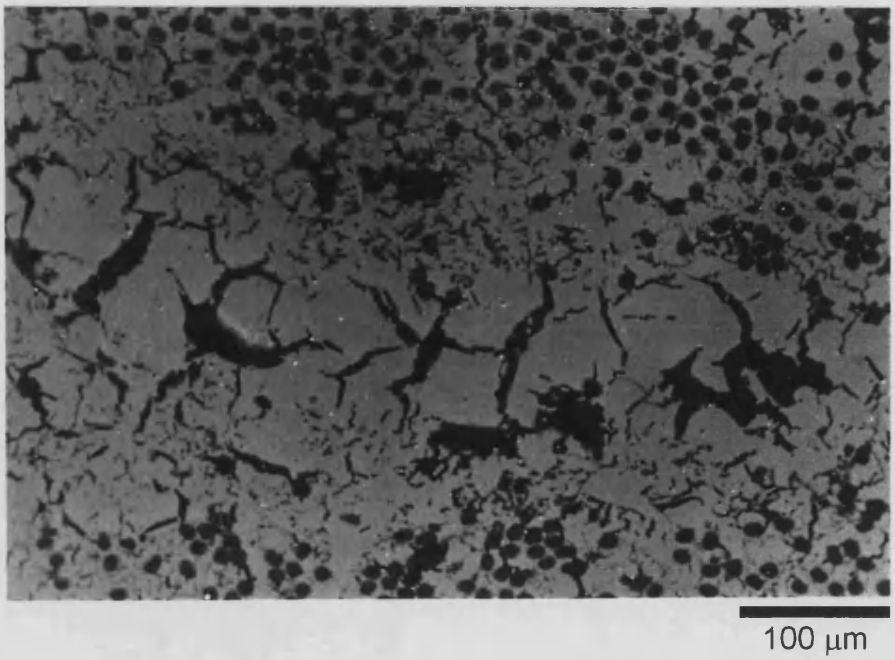

Figure 3.32 SEM micrograph of sample 'XQ' following sintering at 1100 °C.

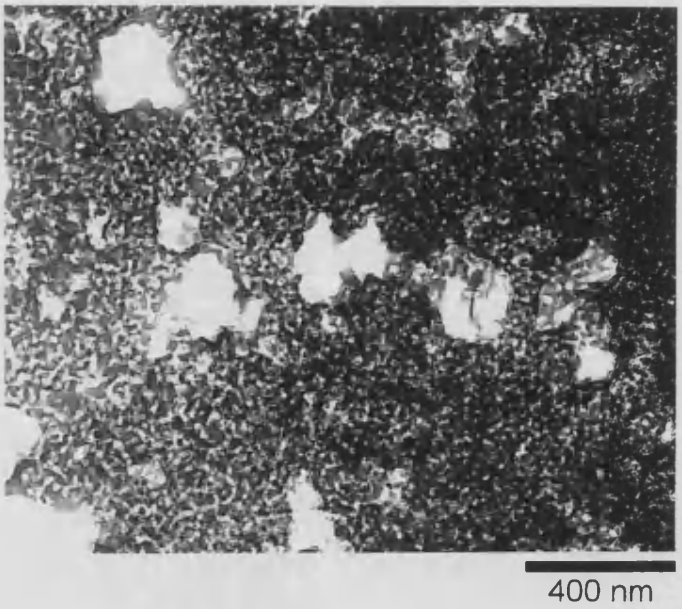

Figure 3.33 TEM micrograph of sample 'XQ' following sintering at 900 °C showing limited fusing of colloidal silica particles.

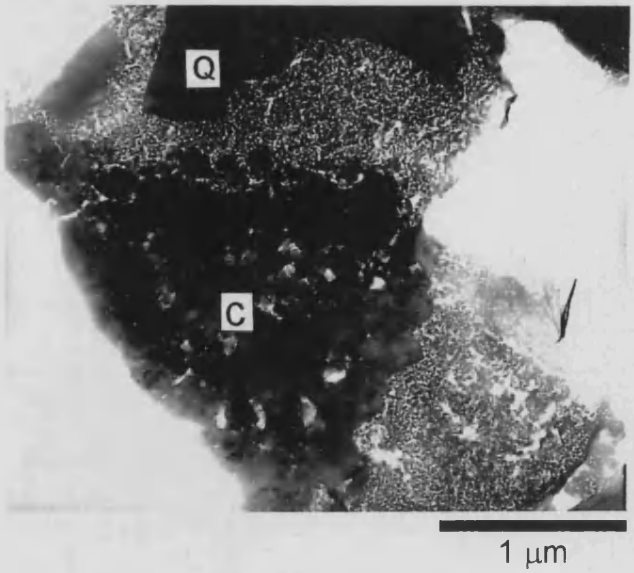

Figure 3.34 TEM micrograph of sample 'XQ' following sintering at 900 °C showing partial crystallisation of densified sol-gel matrix (C) in regions adjoining quartz filler particles (Q).

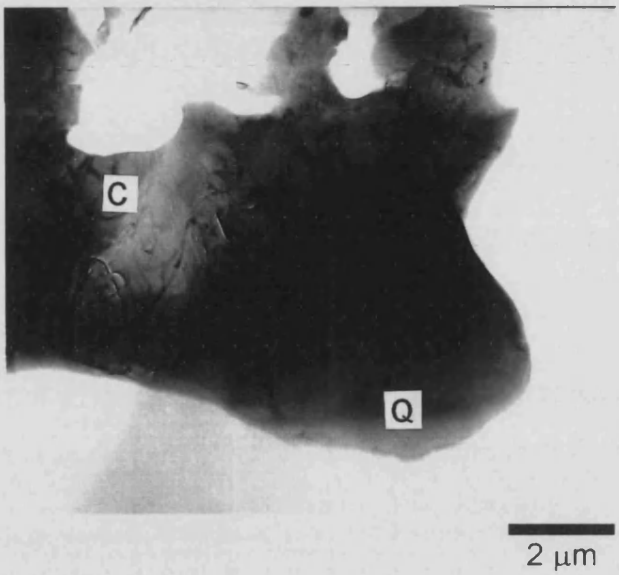

Figure 3.35 TEM micrograph of sample 'XQ' following sintering at 1100 °C showing that the sol-gel silica has completely crystallised (C) in regions adjoining quartz filler particles (Q).

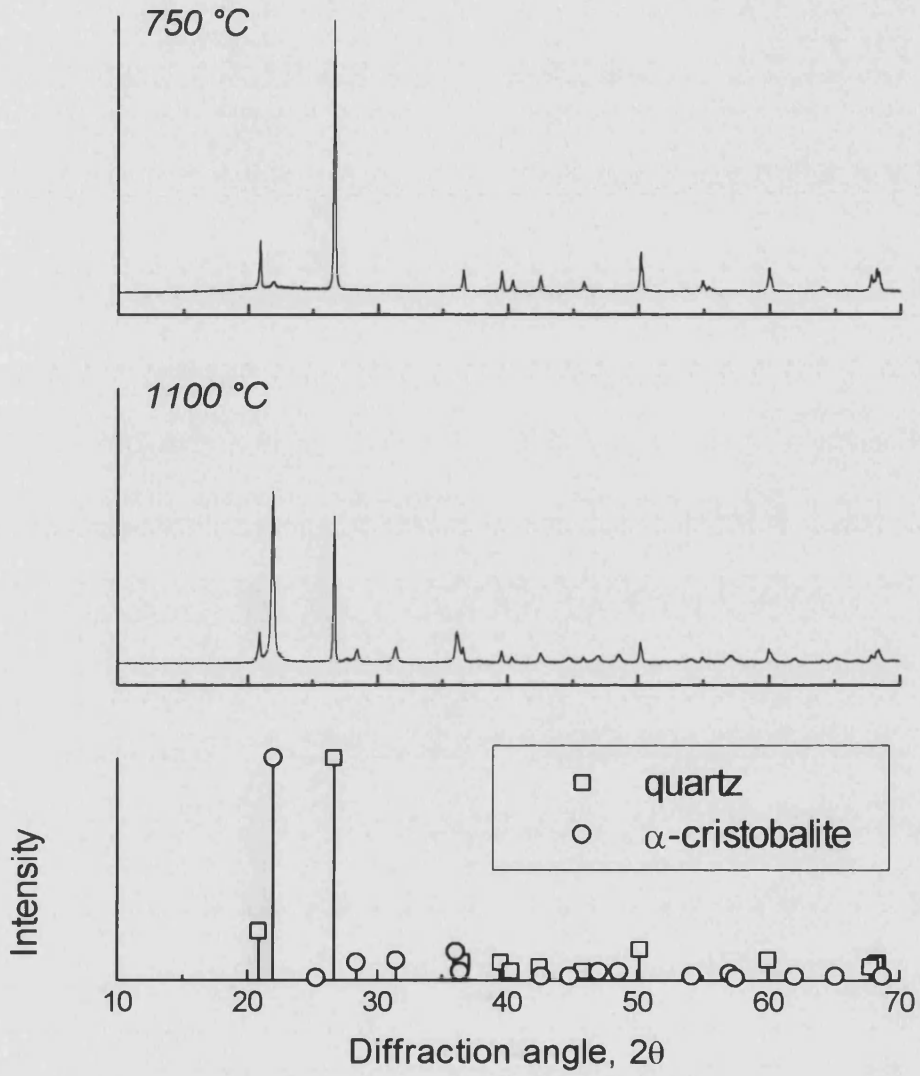

Figure 3.36 XRD curves for 'HQ' specimens sintered at 750 °C and 1100 °C. Data are plotted to the same ordinate scale. The standard patterns for quartz [116] and α-cristobalite [114] (lower graph) are both normalised with respect to the height of their principal peak.

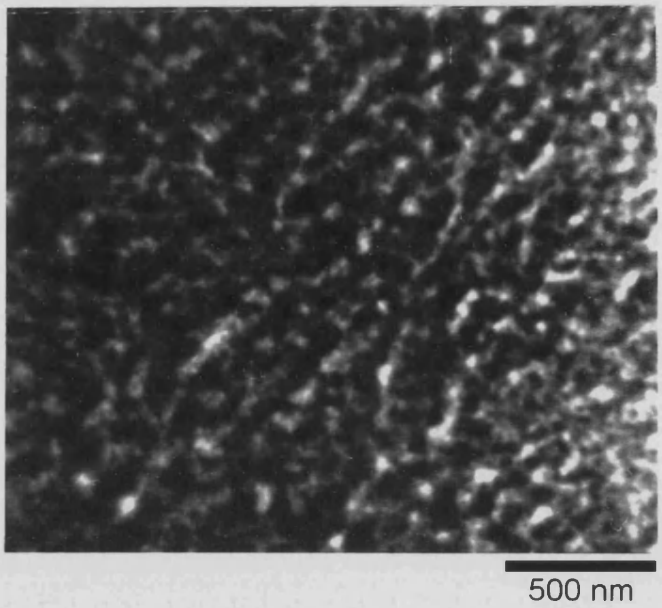

Figure 3.37 TEM micrograph of sample 'HQ' sintered at 1100 °C showing partial fusing of colloidal silica particles and residual nanometre-scale porosity.

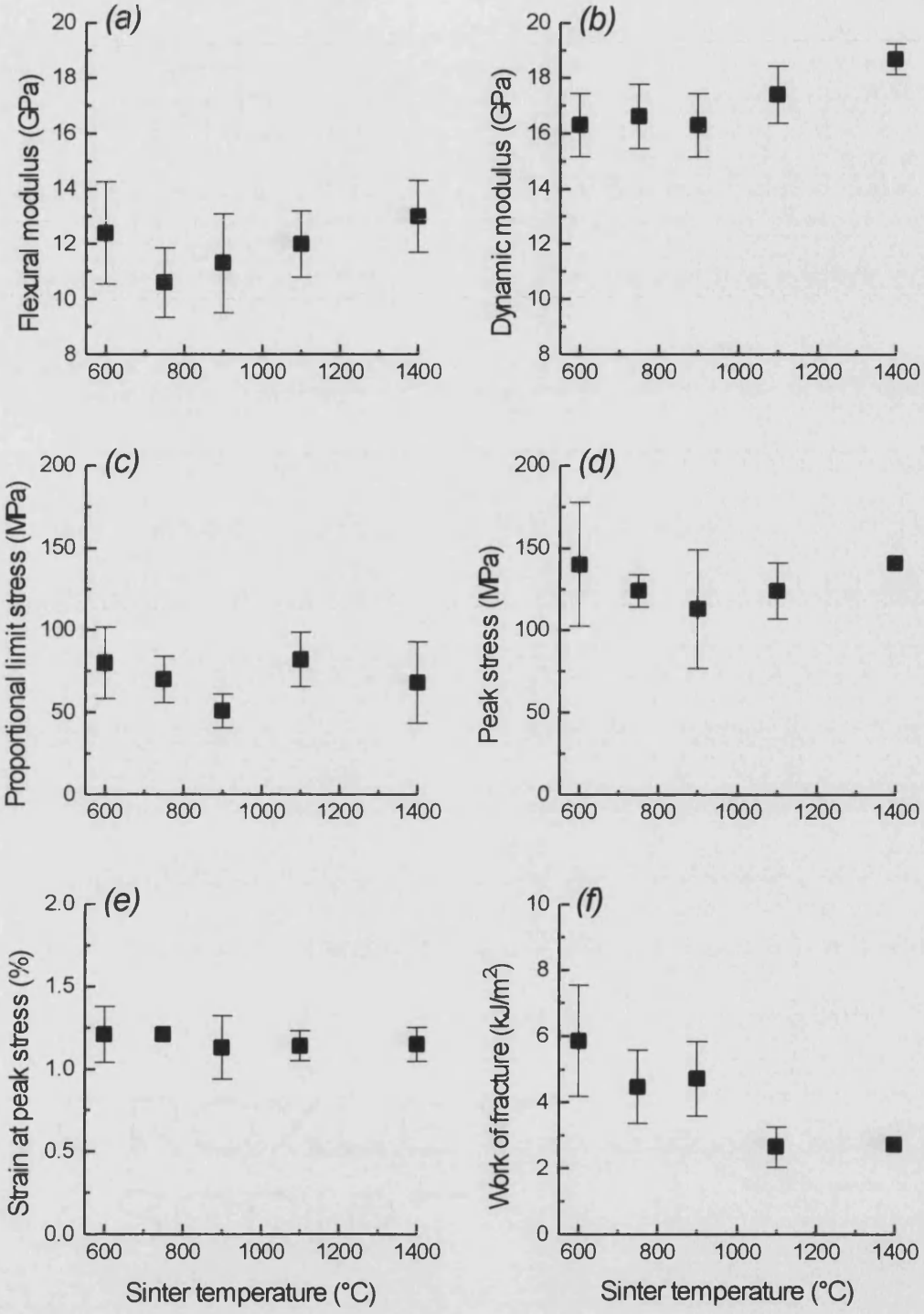

Figure 3.38 Variation of flexural properties with sintering temperature for 'HC' samples.
(a) Flexural modulus; (b) Dynamic modulus; (c) Stress at proportional limit;
(d) Peak stress; (e) Strain at peak stress; (f) Work of fracture.
Error bars indicate standard deviations.

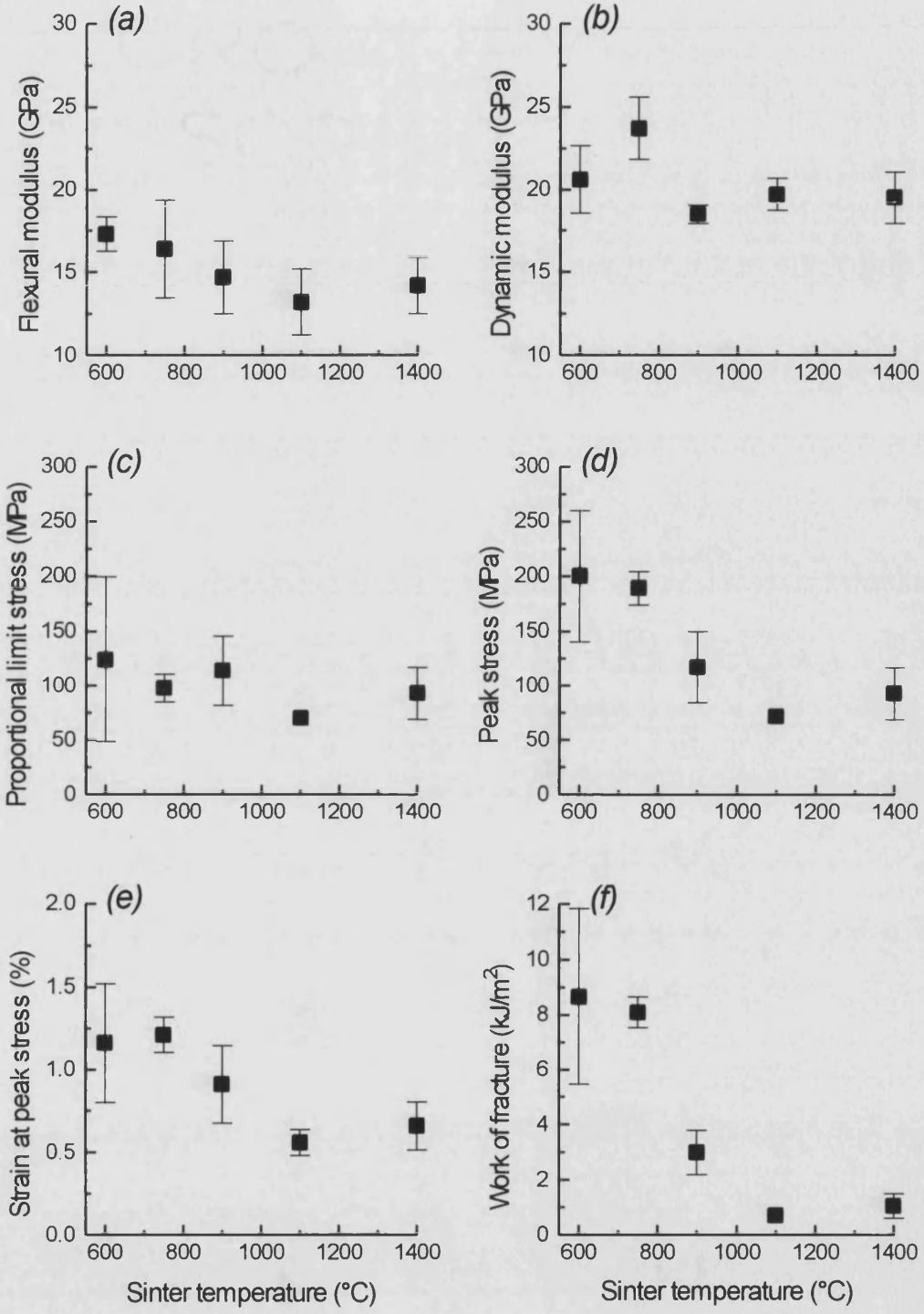

Figure 3.39 Variation of flexural properties with sintering temperature for 'XQ' samples.
(a) Flexural modulus; (b) Dynamic modulus; (c) Stress at proportional limit;
(d) Peak stress; (e) Strain at peak stress; (f) Work of fracture.
Error bars indicate standard deviations.

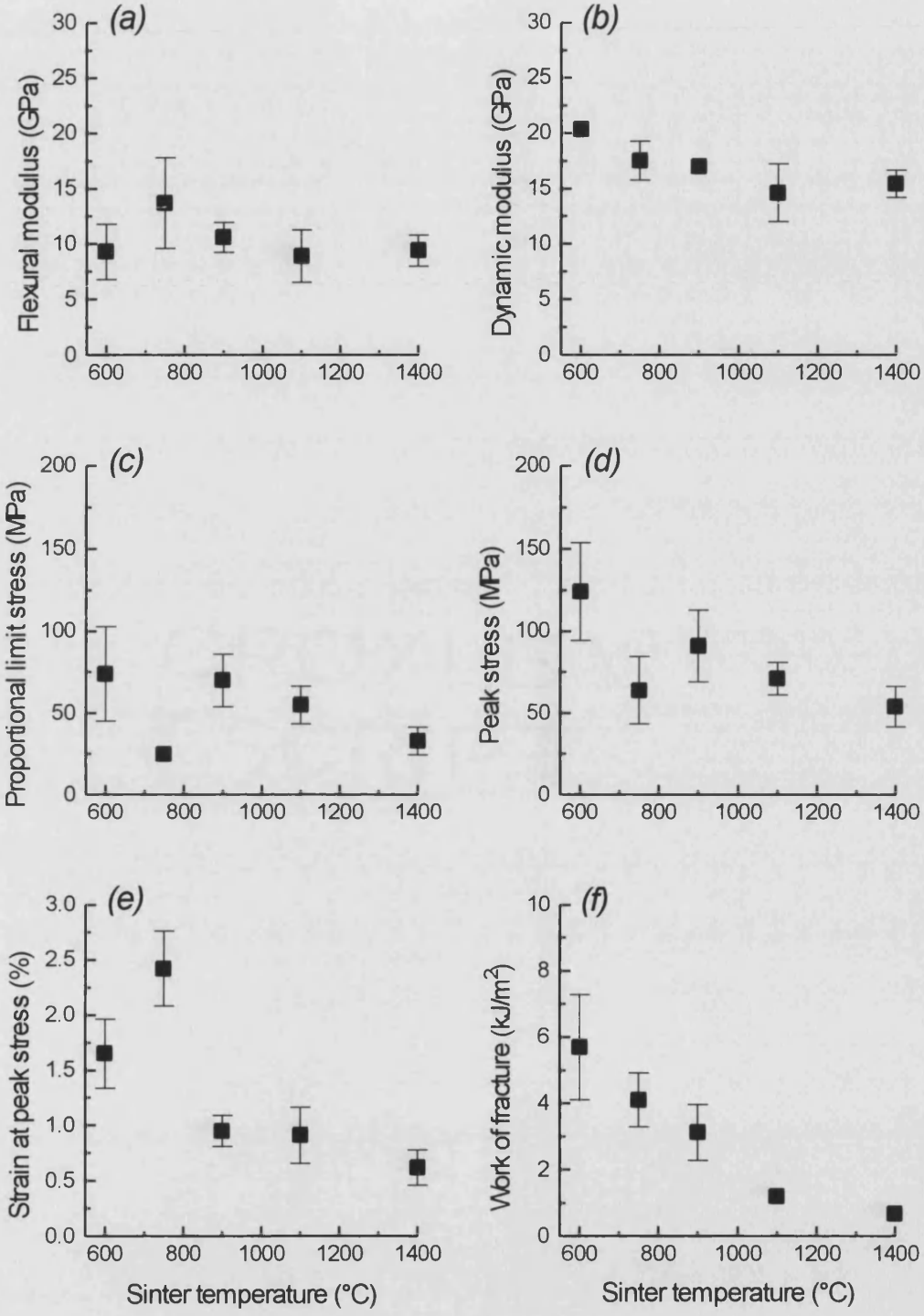

Figure 3.40 Variation of flexural properties with sintering temperature for 'HQ' samples. (a) Flexural modulus; (b) Dynamic modulus; (c) Stress at proportional limit; (d) Peak stress; (e) Strain at peak stress; (f) Work of fracture. Error bars indicate standard deviations.

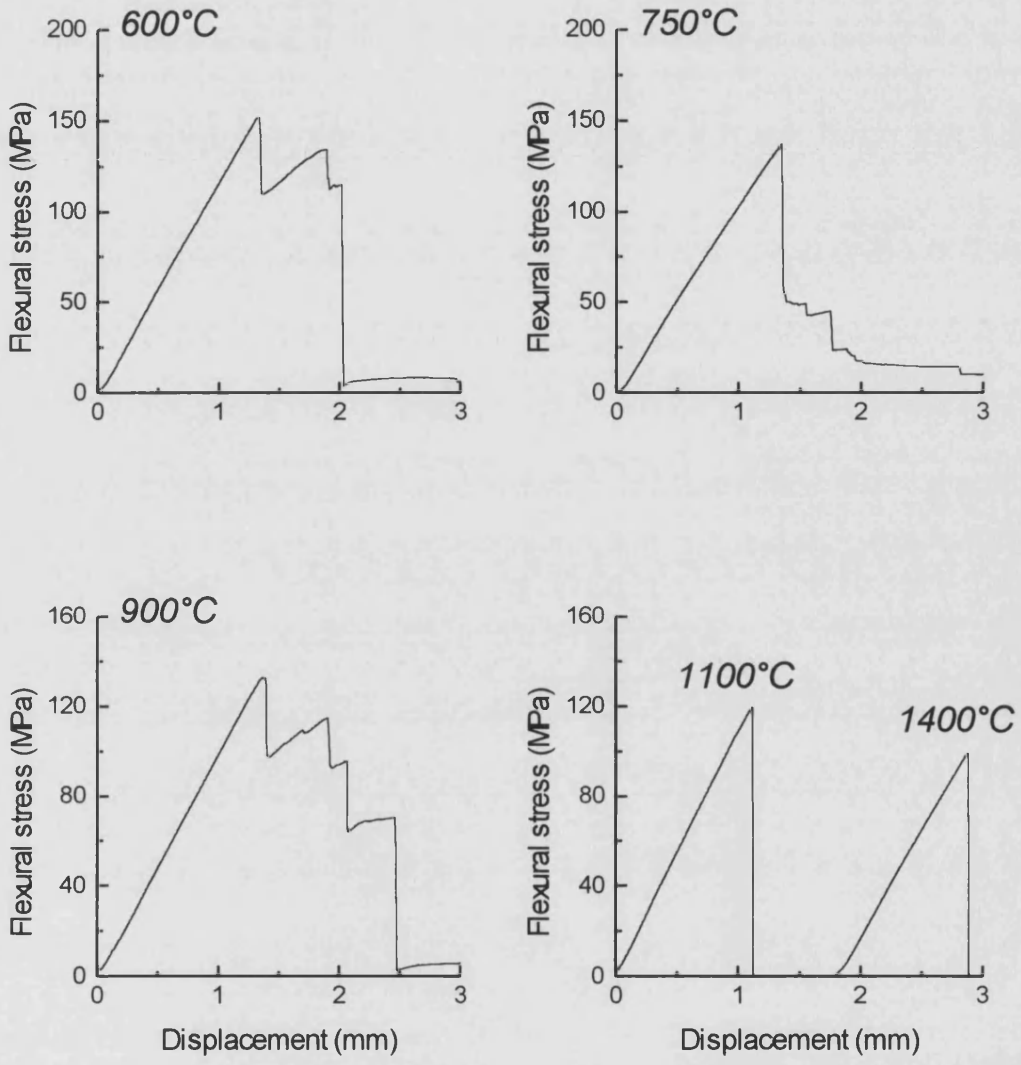

Figure 3.41 Example force-displacement curves for 'HC' series samples sintered at different temperatures.

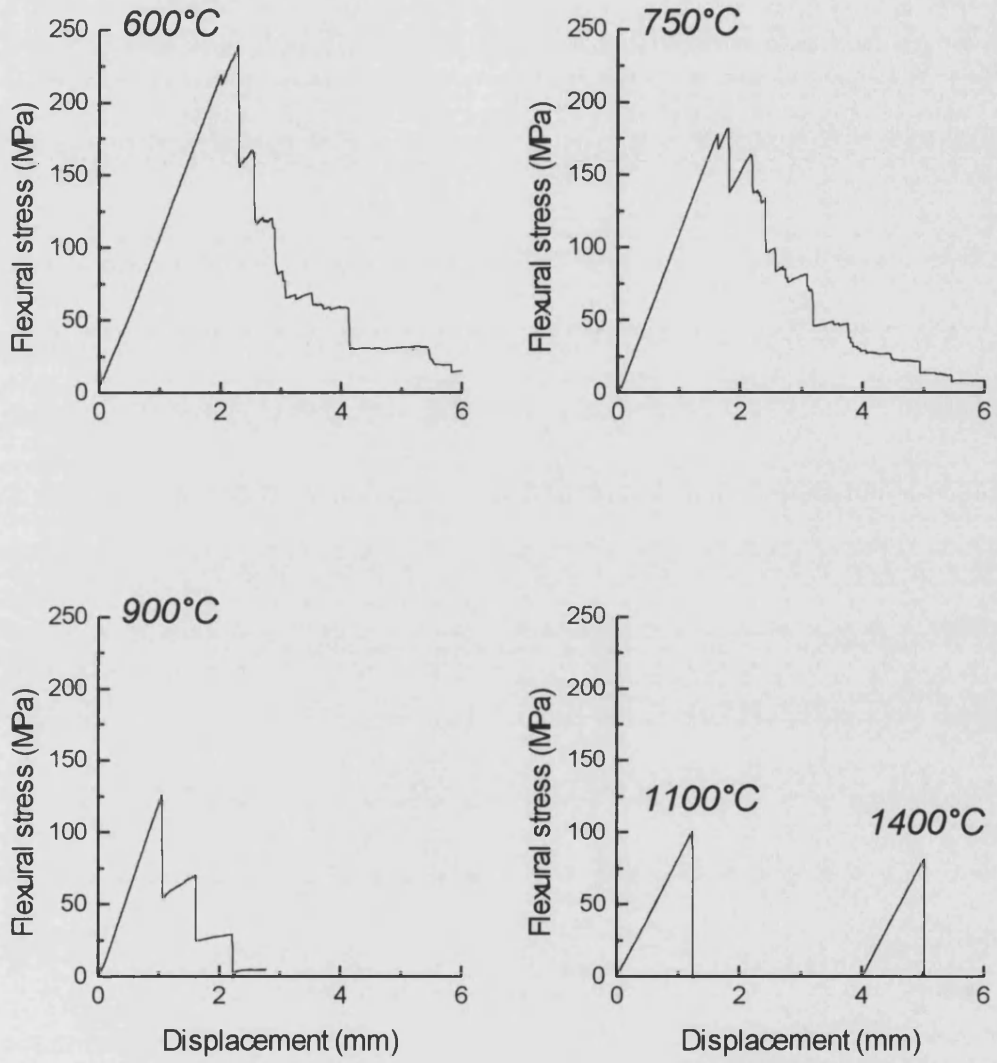

Figure 3.42 Example force-displacement curves for 'XQ' series samples sintered at different temperatures.

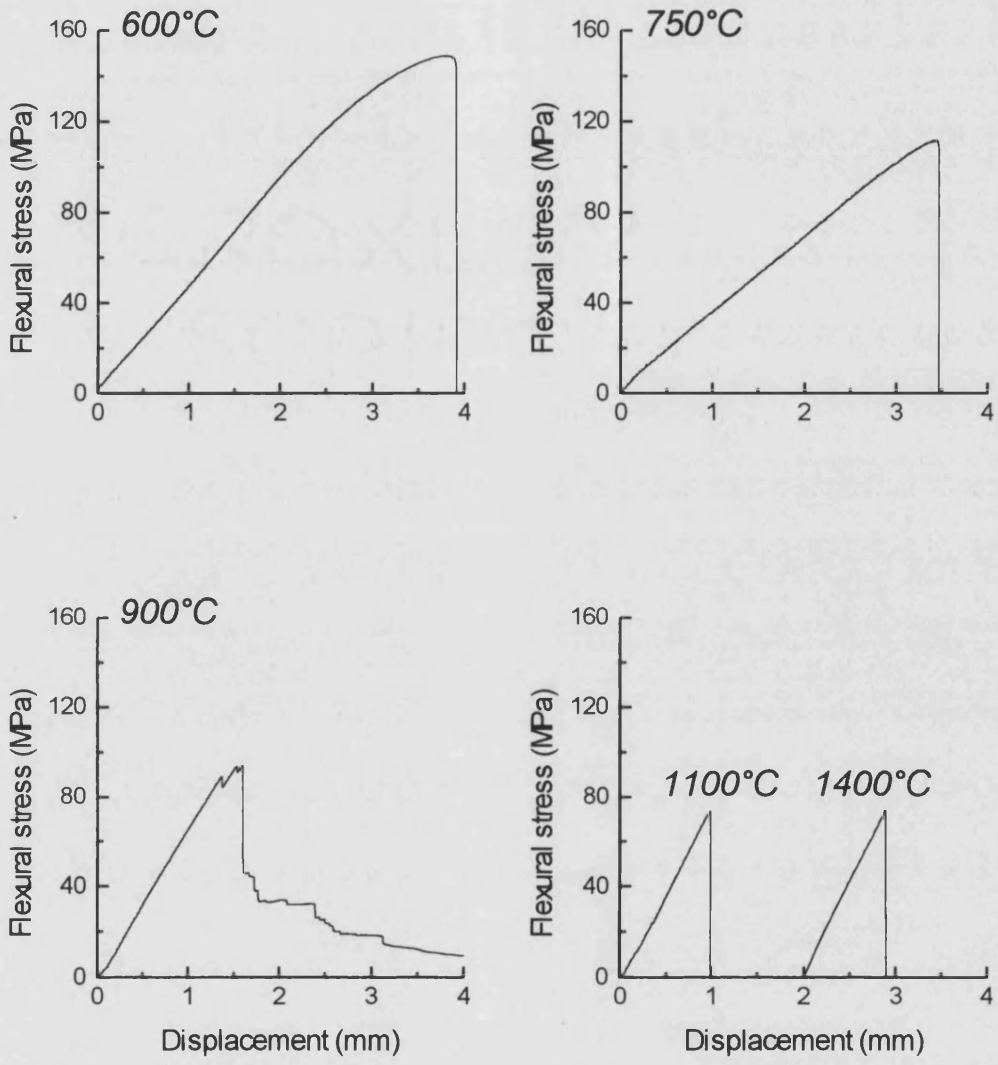

Figure 3.43 Example force-displacement curves for 'HQ' series samples sintered at different temperatures.

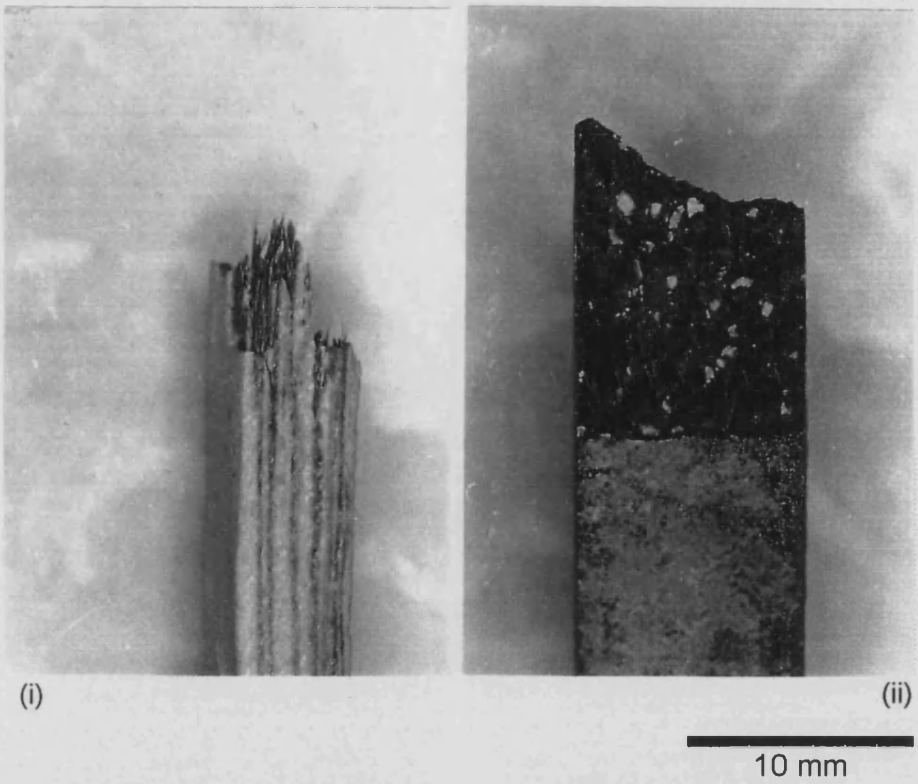

Figure 3.44 Macroscopic appearance of flexural test specimens.
(i) 'HC' composite sintered at 750 °C showing tough fracture behaviour.
(ii) 'HC' composite sintered at 1100 °C showing brittle fracture behaviour.

Figure 3.45 Fibre pull-out in tensile region of a flexural fracture surface.
Sample: Series 'HC' composite sintered at 750 °C.

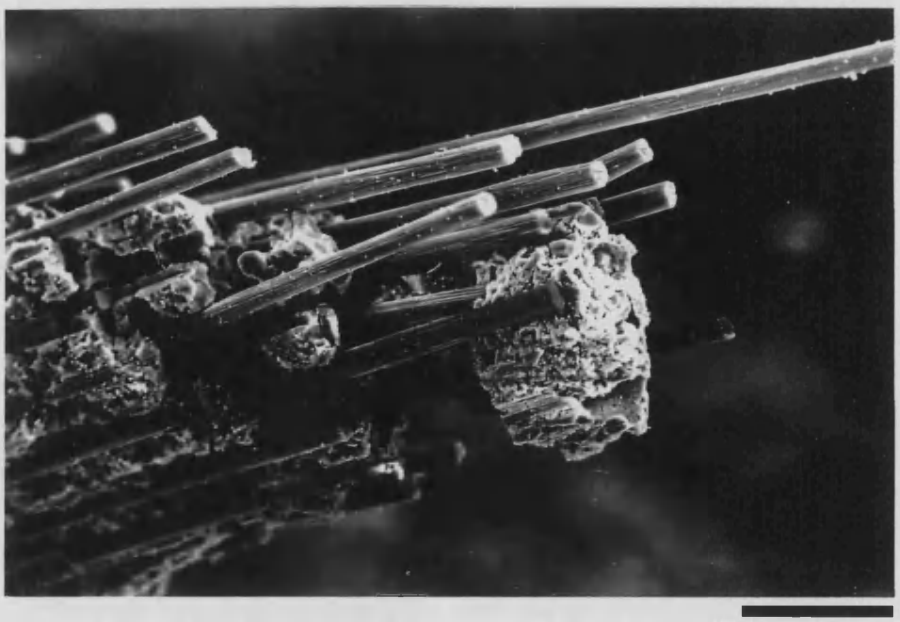

Figure 3.46 Matrix debris adhering to pulled-out fibre bundle.
Sample: Series 'HC' composite sintered at 750 °C.

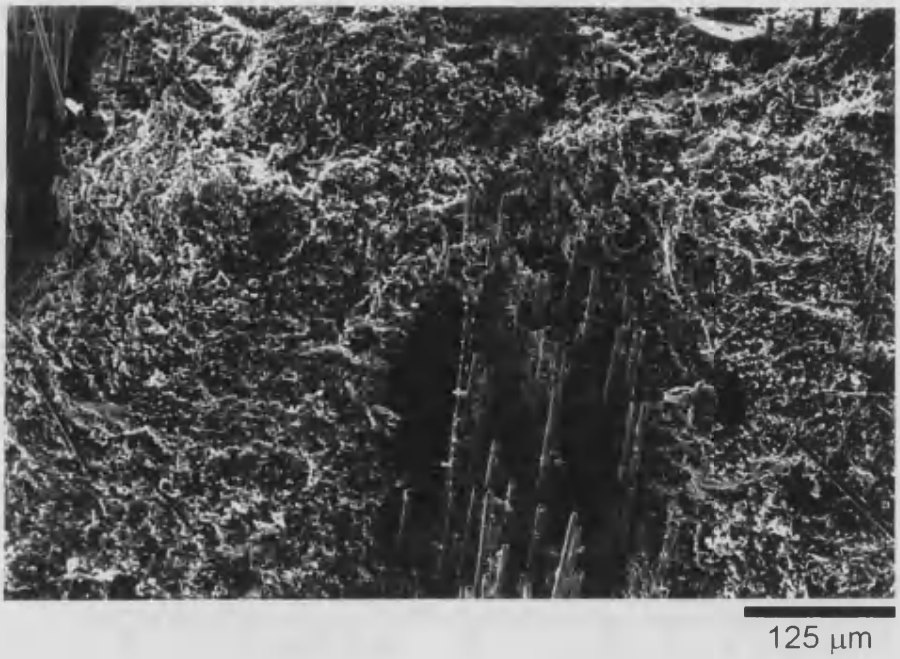

Figure 3.47 Poor fibre dispersion during filament winding led to fibres being pulled-out in bundles rather than individually.
Sample: Series 'HC' composite sintered at 900 °C.

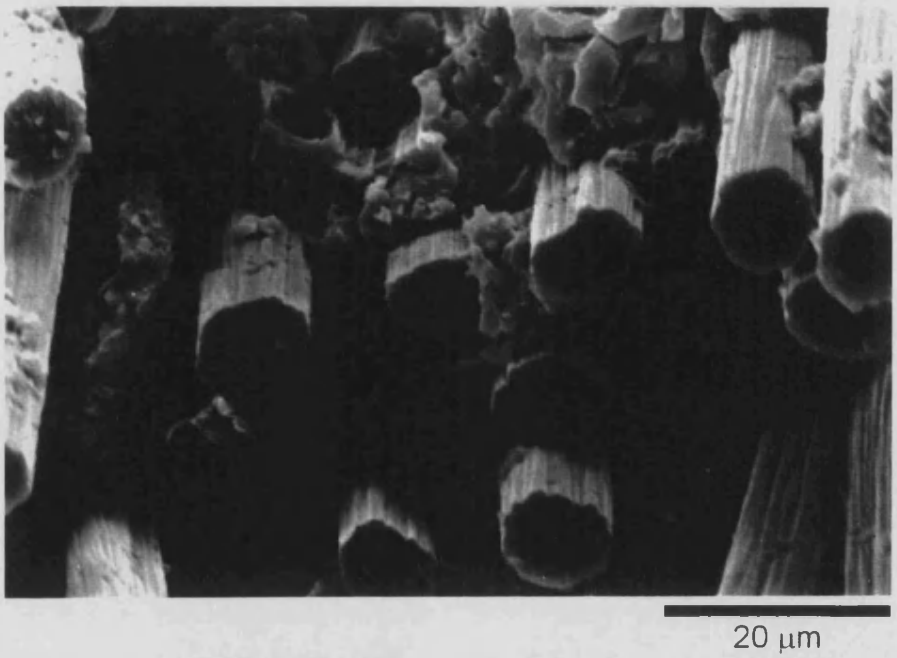

Figure 3.48 Fracture surface in a brittle specimen showing limited fibre pull-out.
Sample: Series 'HC' composite sintered at 1400 °C.

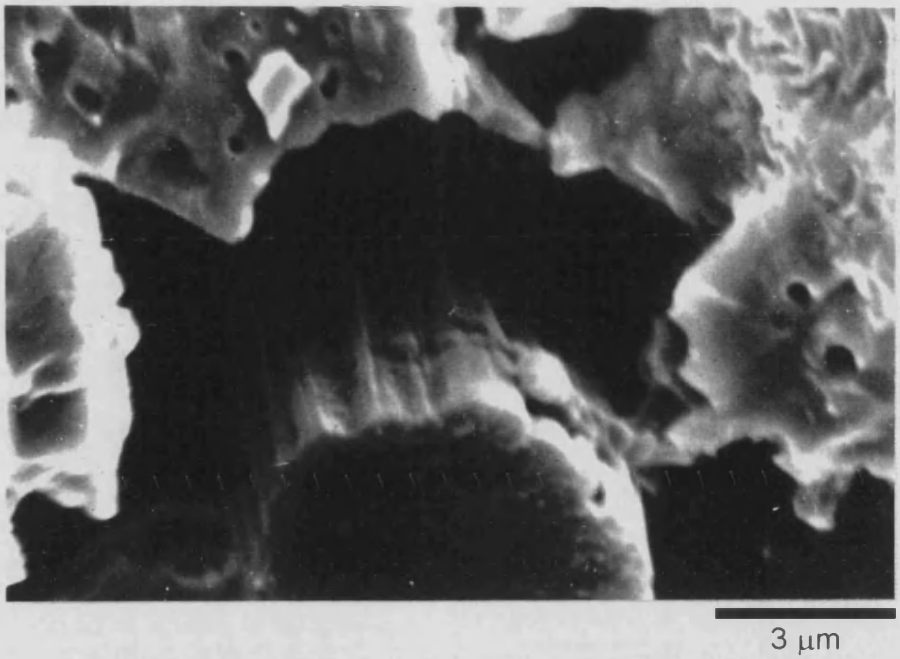

Figure 3.49 Low fibre-matrix bond strength indicated in fracture surface.
Sample: Series 'HC' composite sintered at 900 °C.

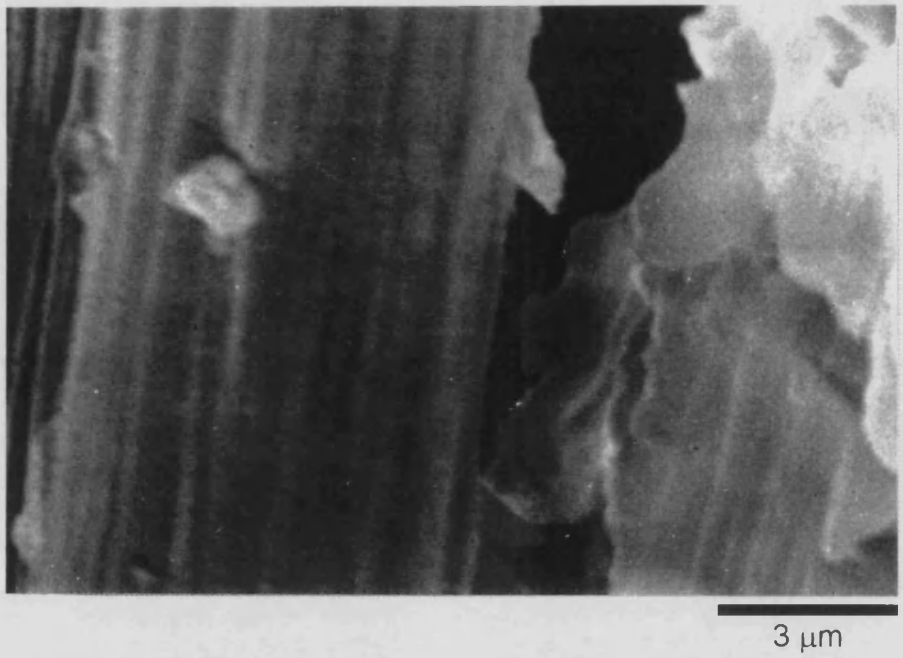

Figure 3.50 High fibre-matrix bond strength indicated in fracture surface.
Sample: Series 'HC' composite sintered at 1400 °C.

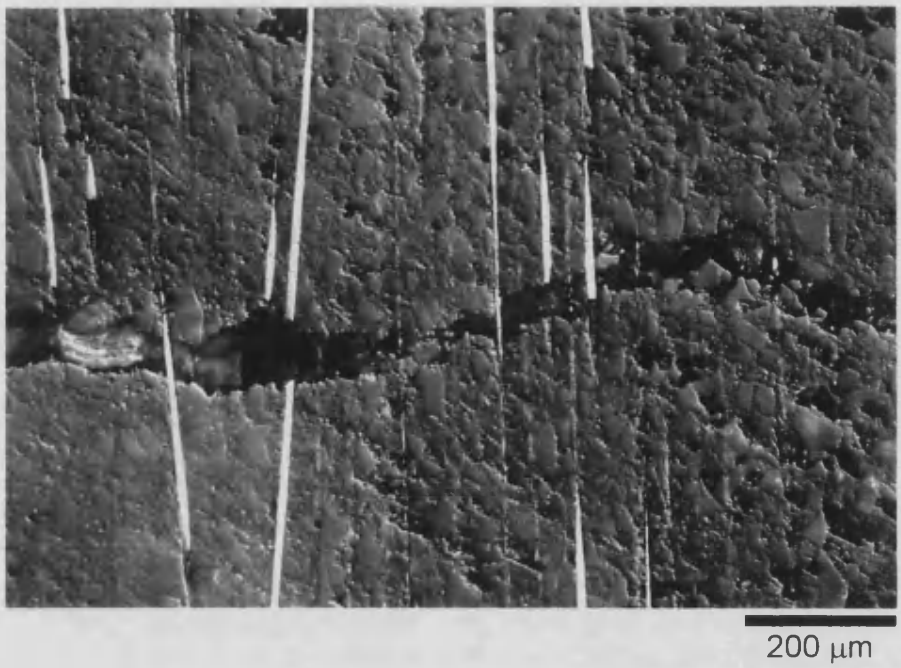

Figure 3.51 Fibres bridging a matrix crack in the tensile region of a flexural test specimen. Sample: Series 'HQ' composite sintered at 750 °C.

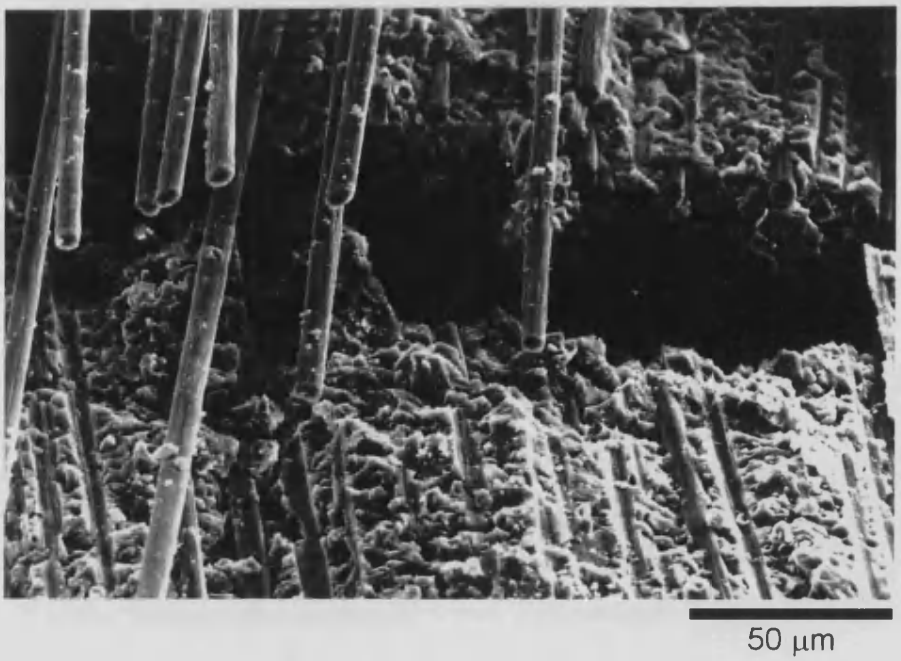

Figure 3.52 Absence of fibre-bridging and fibre-pullout in a brittle flexural specimen. Sample: Series 'HQ' composite sintered at 1400 °C.

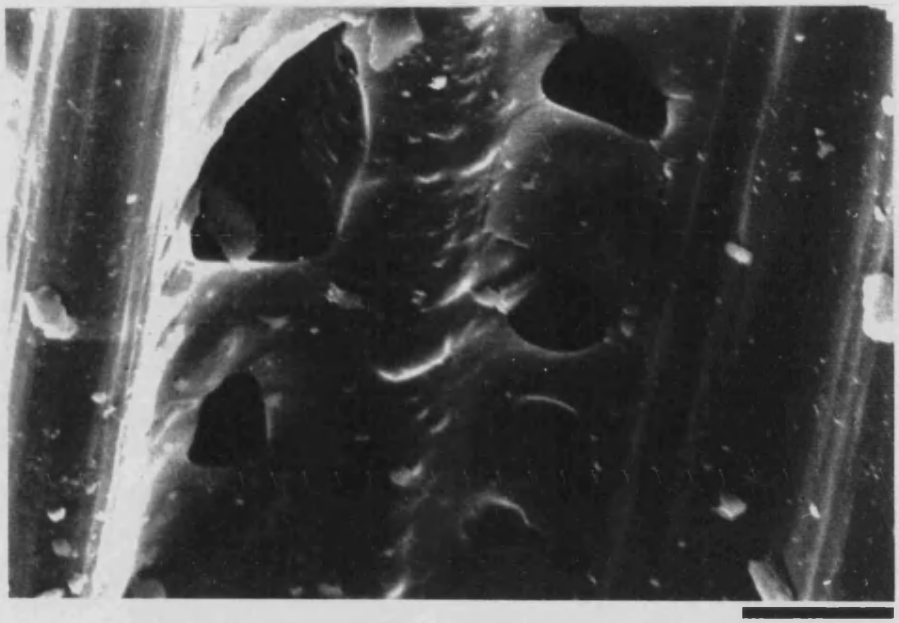

i)

ii)

Figure 3.53 Matrix porosity may link up (i) and lead to debonding at the fibre-matrix interface (ii).

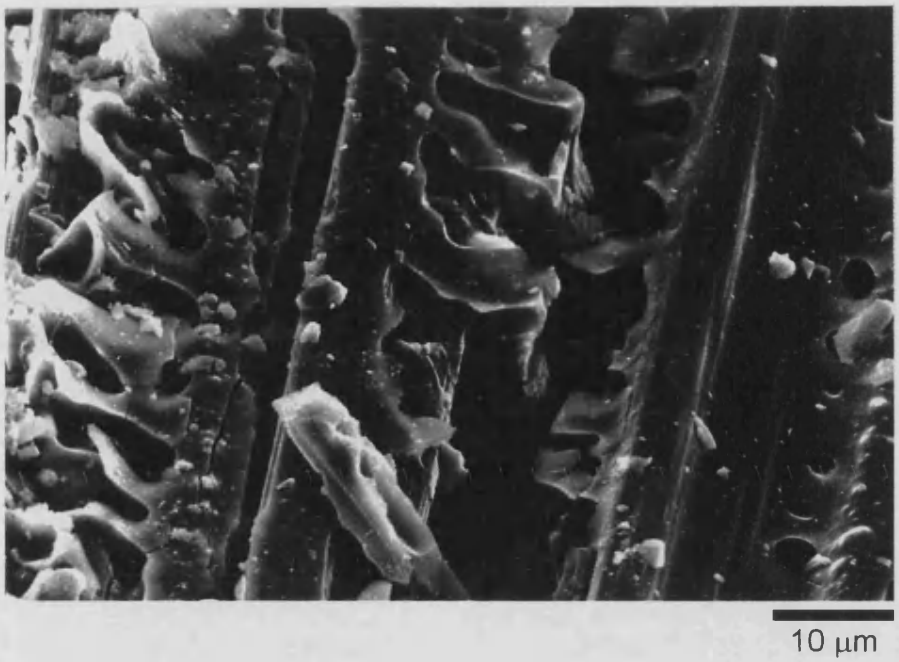

Figure 3.54 Damage in porous matrix regions in a flexural test specimen. Pores have linked and the matrix has split parallel to the fibres.

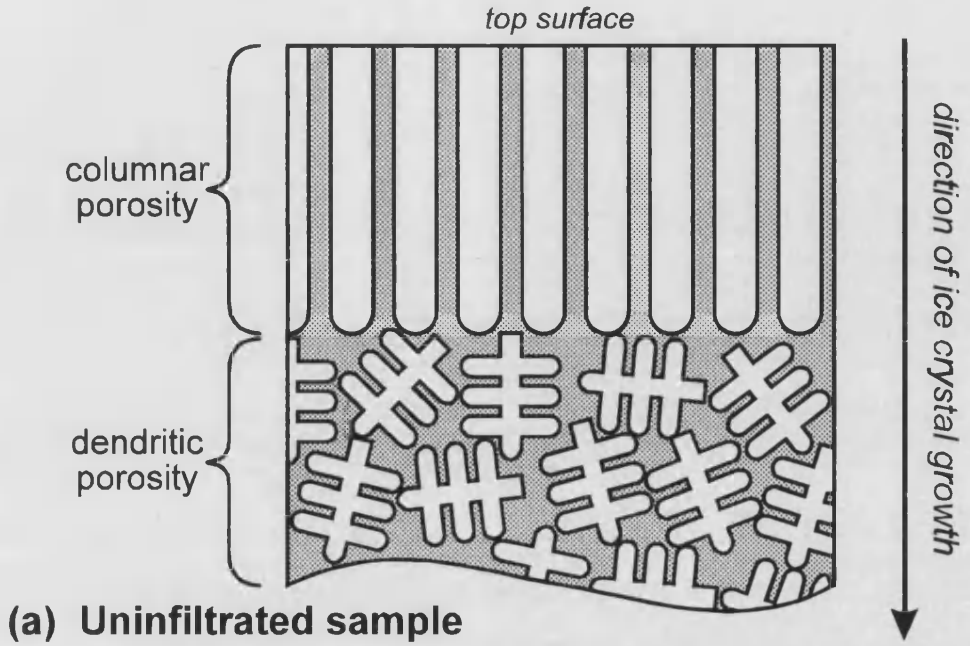

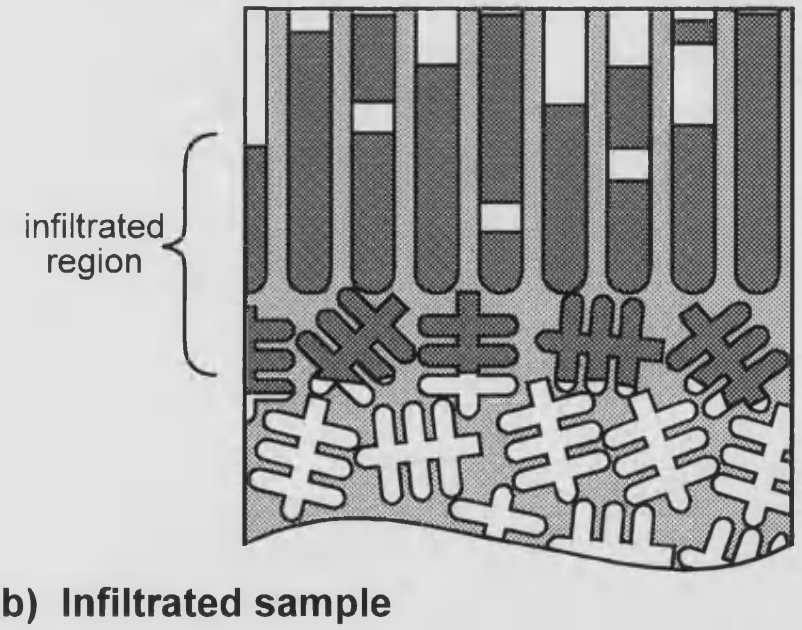

Figure 3.55 Schematic representation of the porosity patterns in freeze-gelled materials. The pores in the uninfiltrated samples (a) are replicas of the ice crystals which grew during the freeze-gelation process. The pores (shown white in the diagram) are continuous and open. The relatively fine, dendritic pores filter infiltrant sols and restrict effective liquid-phase infiltration to the outer layers of the samples (b).

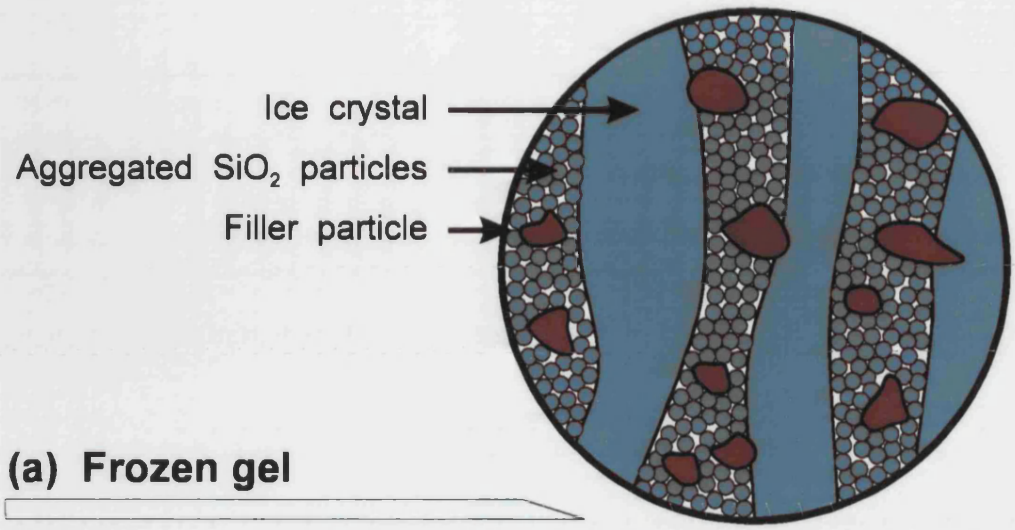

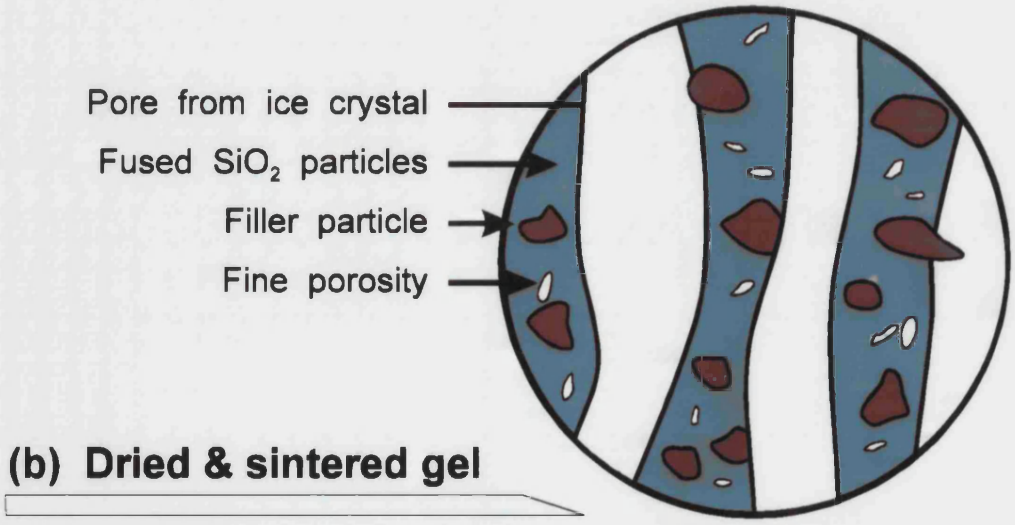

Figure 3.56 The presence of filler particles in a colloidal silica sol does not affect the freeze-gelation process. In a frozen gel (a) the filler particles are channelled into the regions between ice crystals with the aggregated colloidal particles. This arrangement is retained when the gel is dried and sintered (b).

1 Fibre tows are desized and impregnated with sol + filler mixture (refer to figure 3.2) then wound onto mandrel.

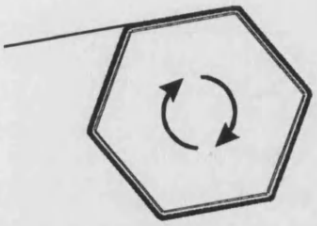

2 Wound composite sheets are sandwiched between steel plates.

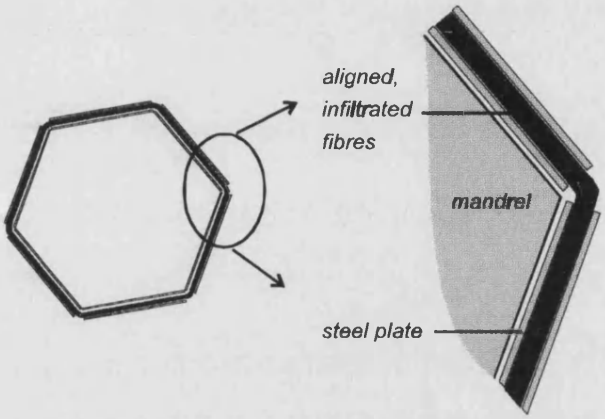

3 The composite 'sandwiches' are stacked, pressed and immersed in a bath of N_2 to cause freeze-gelation.

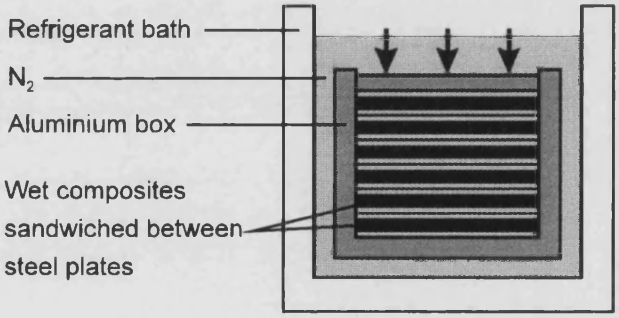

4 The green composites are thawed and dried whilst still supported on the lower plates.

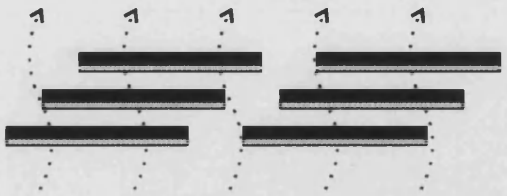

5 The composites are infiltrated with colloidal silica 5 times, sintered in argon at typically 750°C, reinfiltrated 3 times, cut into strips of width 10mm and resintered at 500°C.

Figure 4.1 Schematic representation of the filament winding/freeze-gelation processing route used to fabricate composite samples.

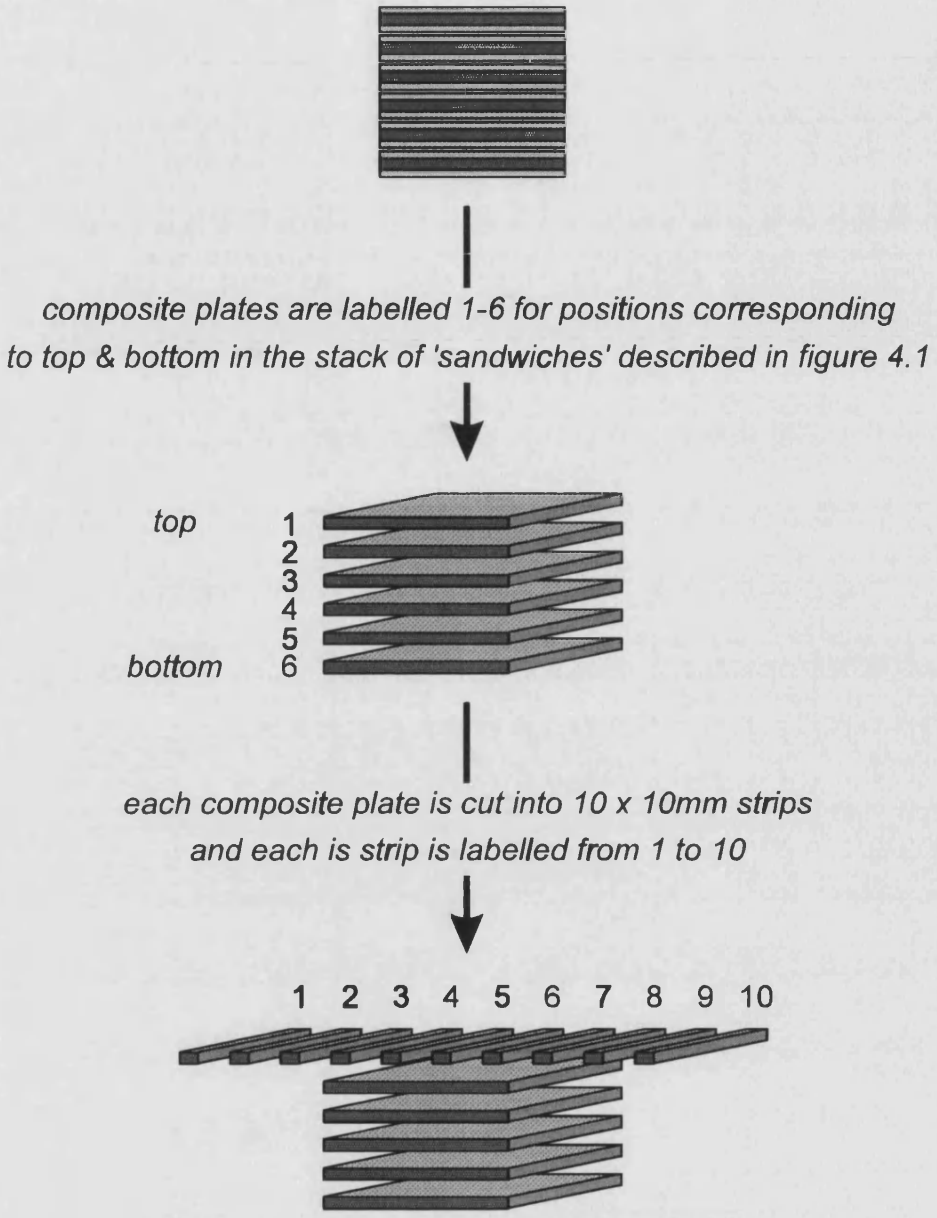

Figure 4.2 Details of the labelling scheme used to identify composite specimens from their position during fabrication.

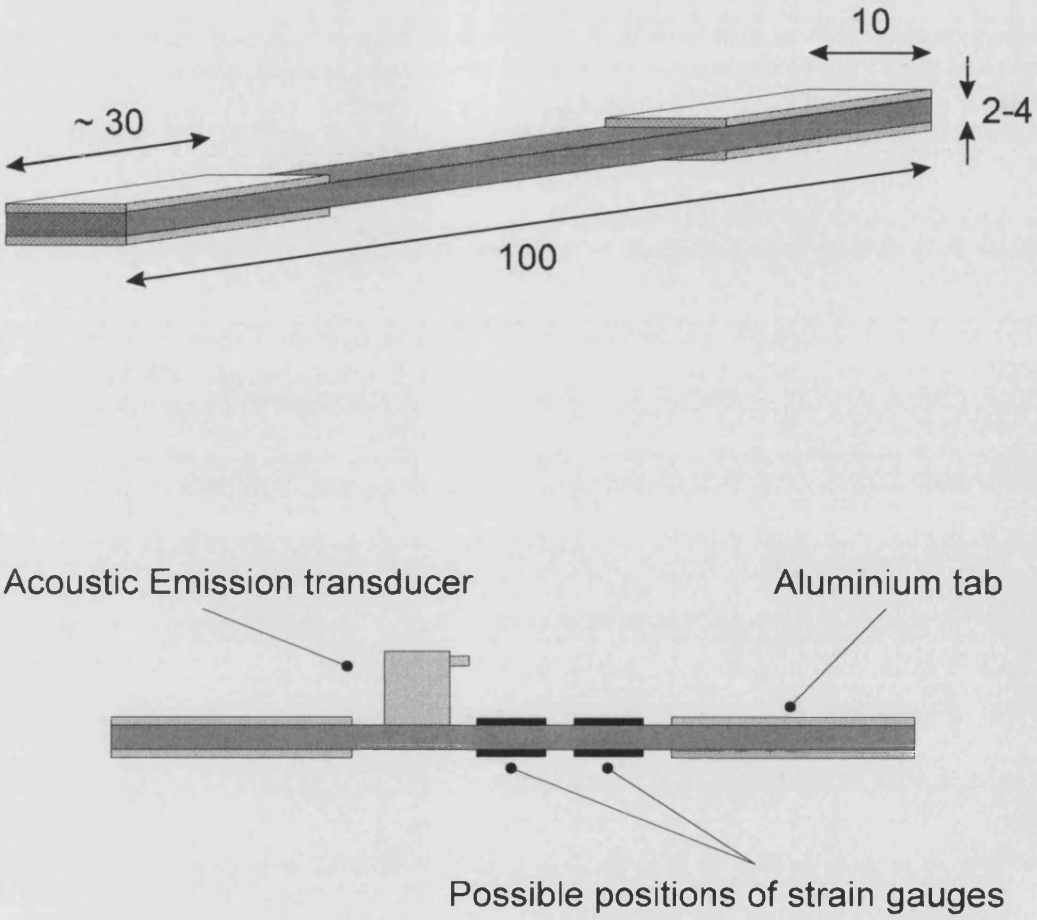

Figure 4.3 Geometry of tensile test specimens used during this study. A dimensions shown are in mm. The bottom figure shows the location of the acoustic emission transducer and the positions of strain gauges and/or contact pads.

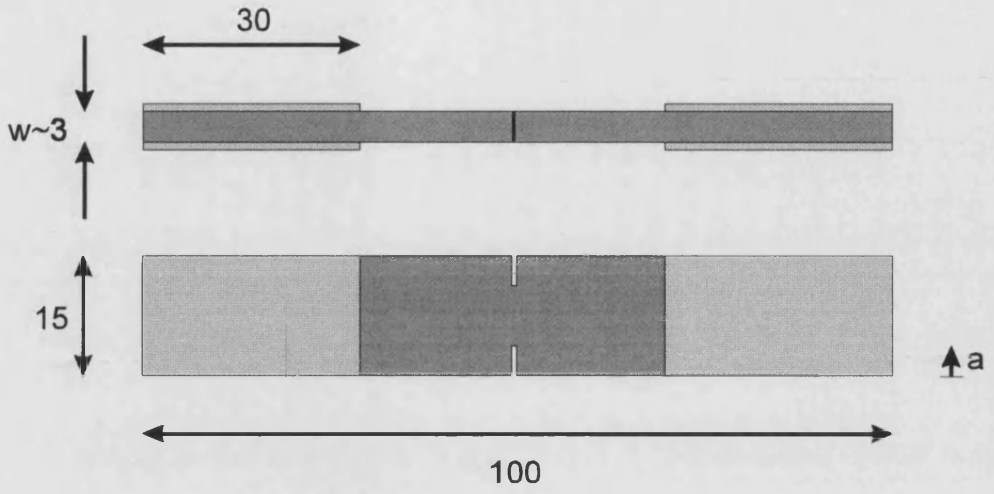

a) Notched tension

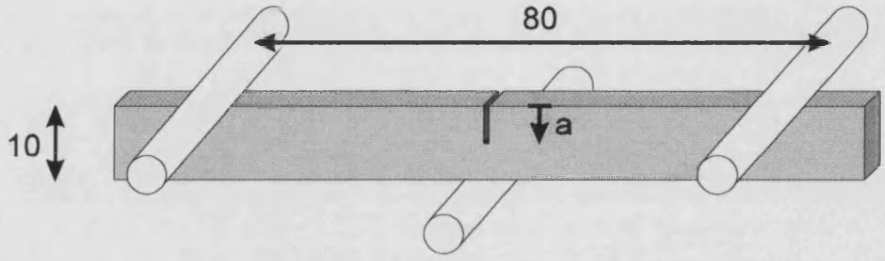

(i) through-width configuration

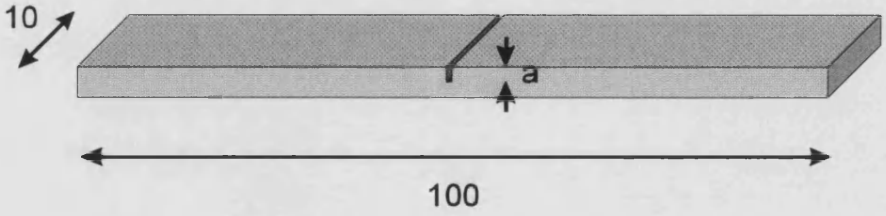

(ii) through-thickness configuration

b) Single-edge-notched beam

Figure 4.4 Geometries of (a) double-edge-notched tension and (b) single-edge-notched bend (SENB) specimens used to measure nominal stress intensity factor, K^*. SENB specimens were tested at a loading span of 80 mm and were designed to measure crack growth resistance through the (i) widths and (ii) thicknesses of samples. All dimensions shown are in mm.

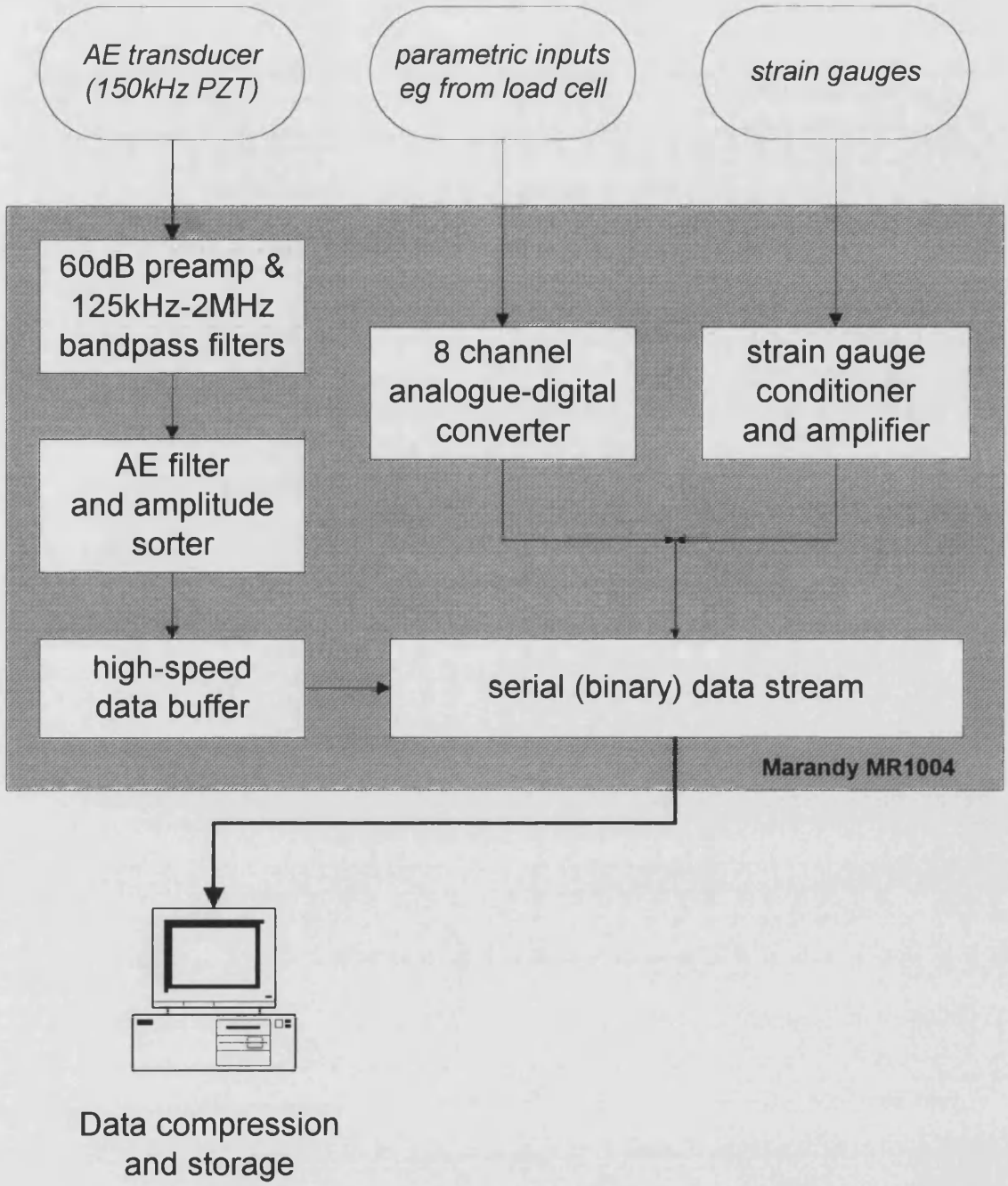

Figure 4.5 Schematic representation of the Marandy MR1004 acoustic-emission-detection/data-logging system.

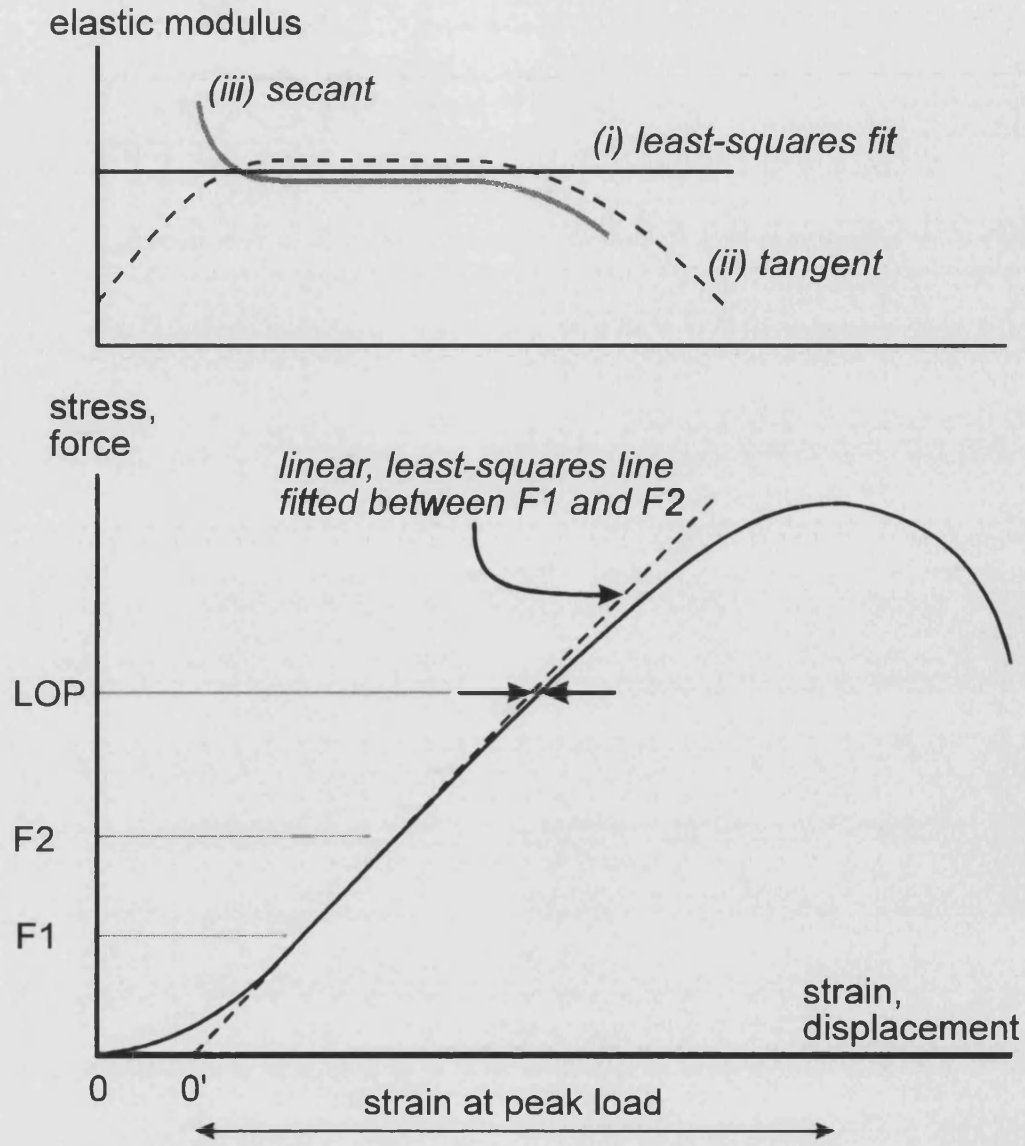

Figure 4.6 Schematic representation of the method used to calculate elastic moduli and proportional limits from stress-strain/force-displacement curves. The dashed line in the lower diagram represents a linear, least-squares fit performed between F1 and F2. Extrapolation of this line to zero force identifies a nominal zero strain (0'). The limit of proportionality (LOP) was defined to be the point where the actual strain/displacement exceeded the predicted value by a factor of 1.02.

The upper diagram shows the superposition of instantaneous elastic moduli which were calculated from (i) the least-squares line; (ii) tangents (*i.e.* running differentials) and (iii) secants to 0'. Good agreement of these lines was taken to be indicative that a valid value of modulus had been determined.

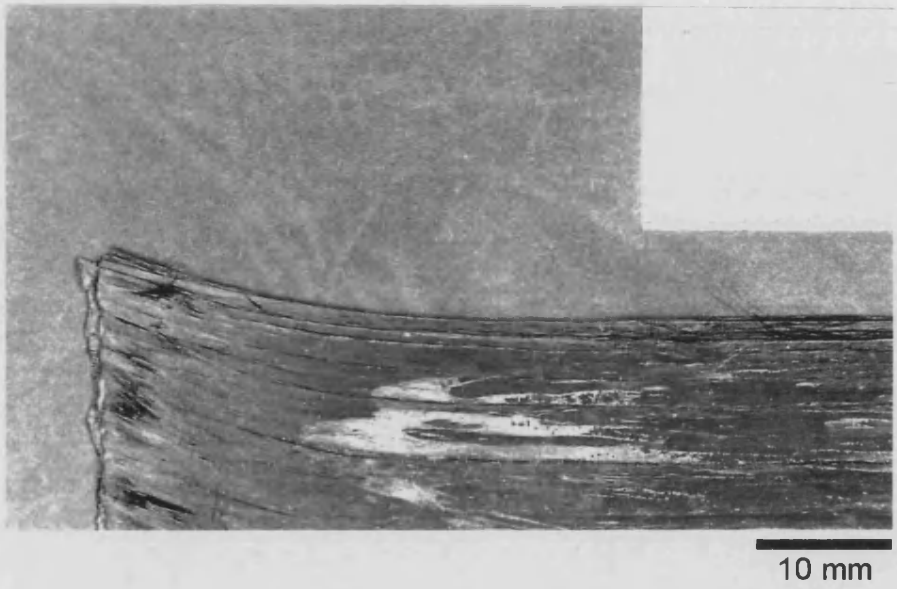

Figure 4.7 Fibre slippage during stacking of wet plates led to poor fibre orientations in this green plate.

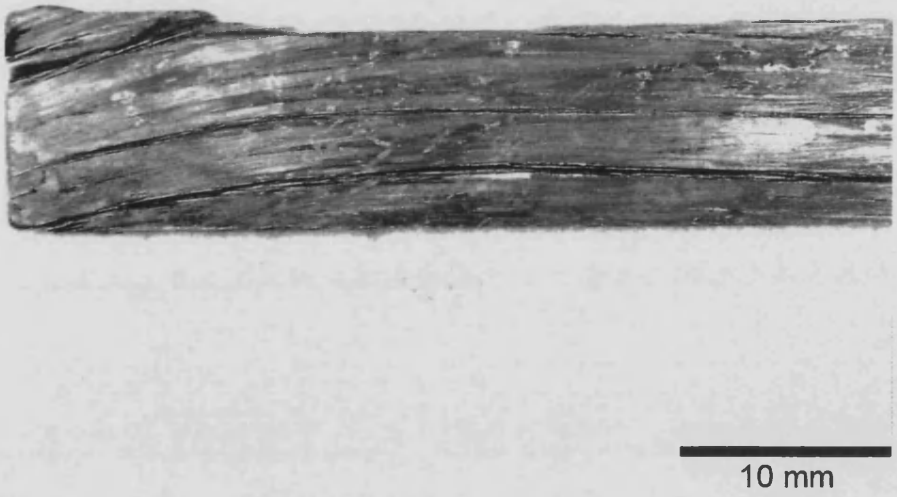

Figure 4.8 Poor fibre orientation and cracking in a test specimen which resulted from fibre slippage during stacking of wet plates.

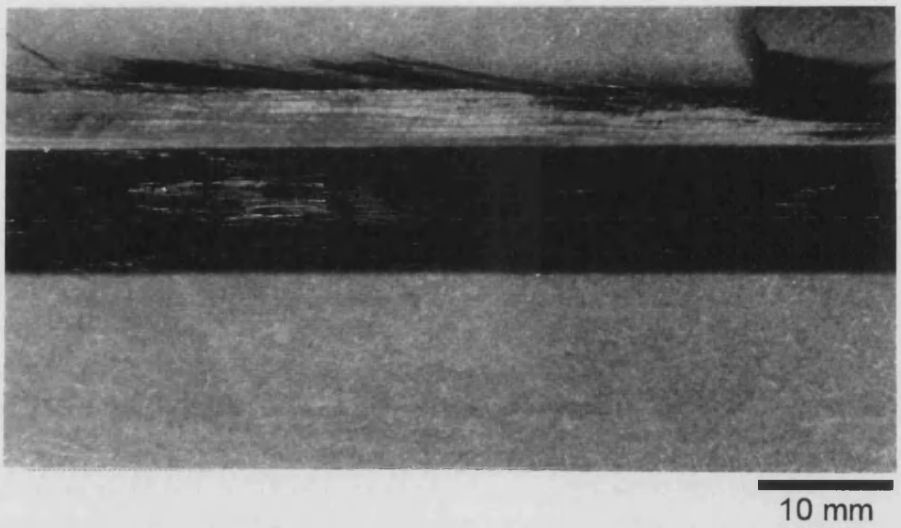

Figure 4.9 "Fluffy" cut edge in sample with no matrix filler.

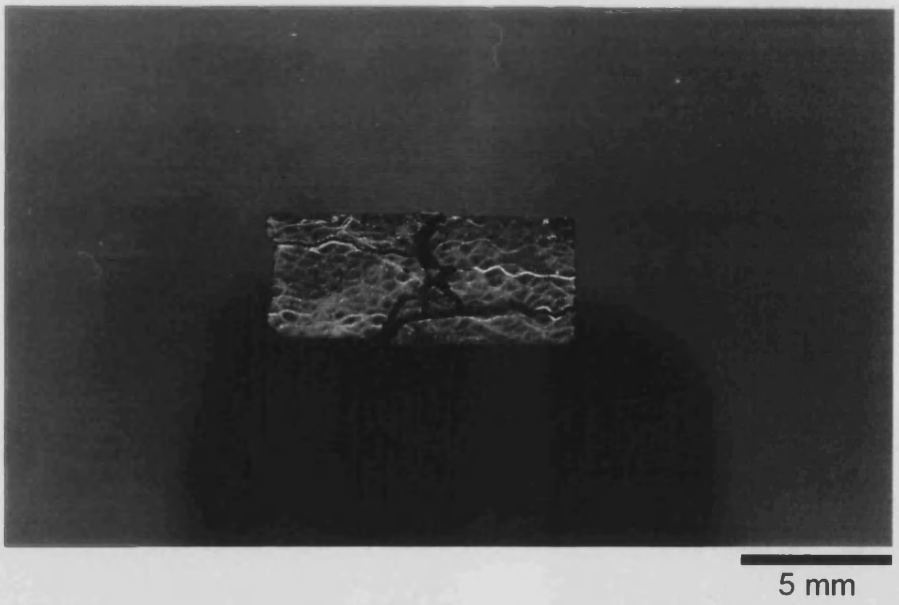

Figure 4.10 Interply and inter fibre bundle cracking was observed in samples with low filler content. This example is from a sample with matrix composition HT50 / 0.02 V_{NLAS} .

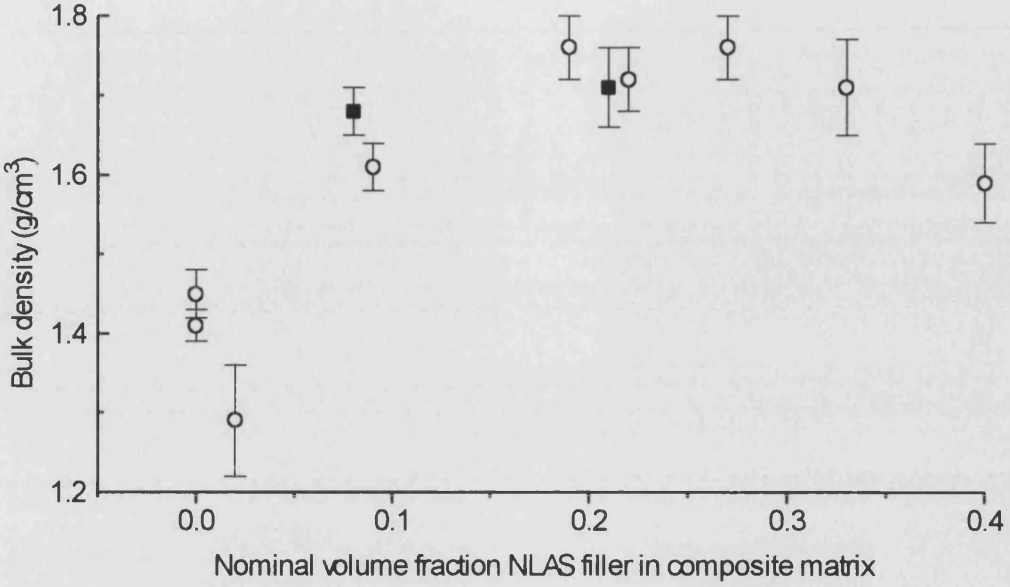

Figure 4.11 Variation of composite bulk density with NLAS filler content in matrix.
○ : HT50-derived matrix. ■ : X30-derived.
The error bars indicate standard deviations.

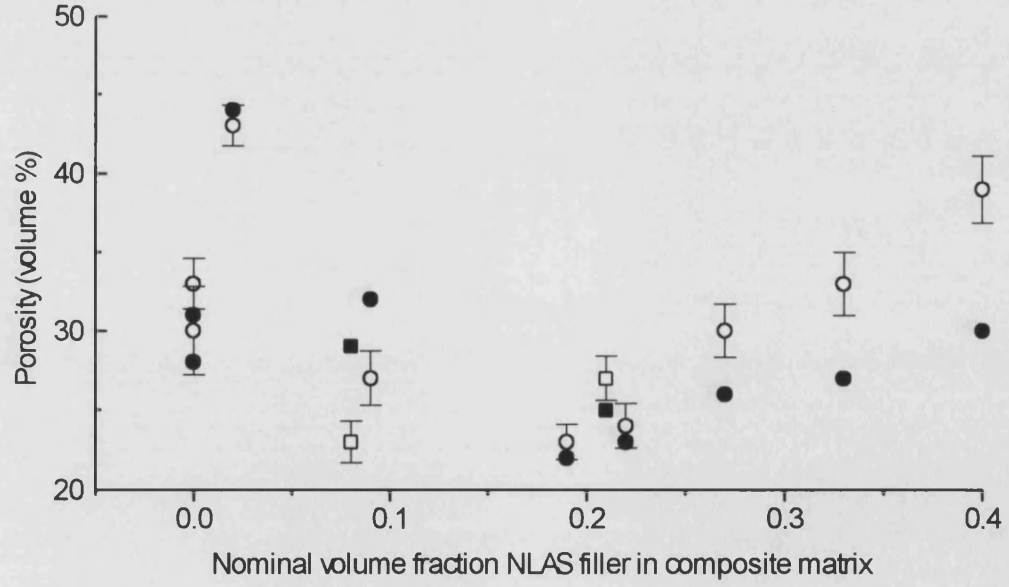

Figure 4.12 Variation of composite porosity with NLAS filler content in matrix.
○,● : HT50-derived matrix. □,■ : X30-derived. Data were obtained by measurement (open symbols) and calculated from density values (closed symbols). The error bars indicate standard deviations.

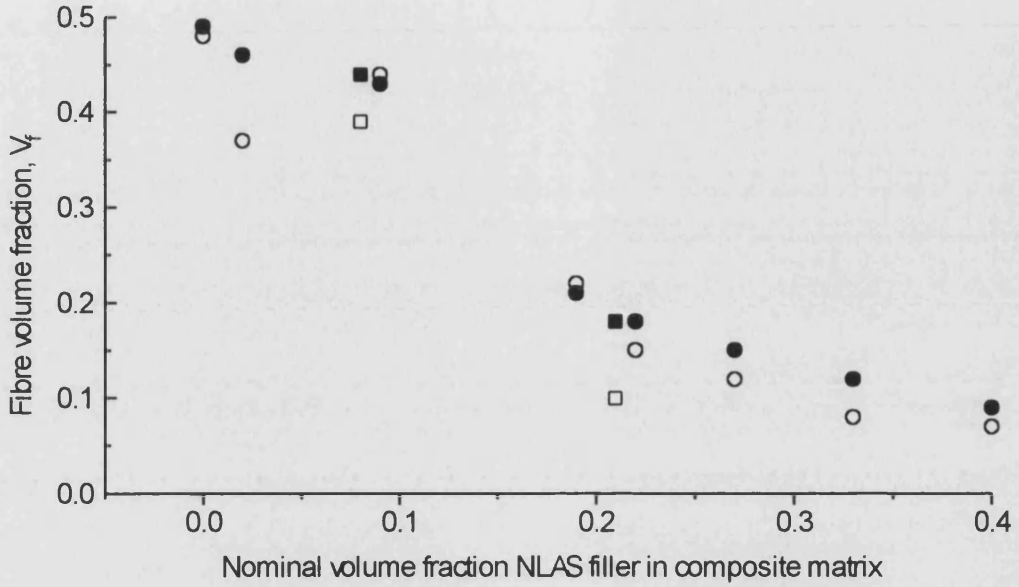

Figure 4.13 Variation of fibre volume fraction (V_f) with NLAS filler content in matrix. ○,● : HT50-derived matrix. □,■ : X30-derived. Data were obtained by image analysis (open symbols) and by pyrolysis (closed symbols).

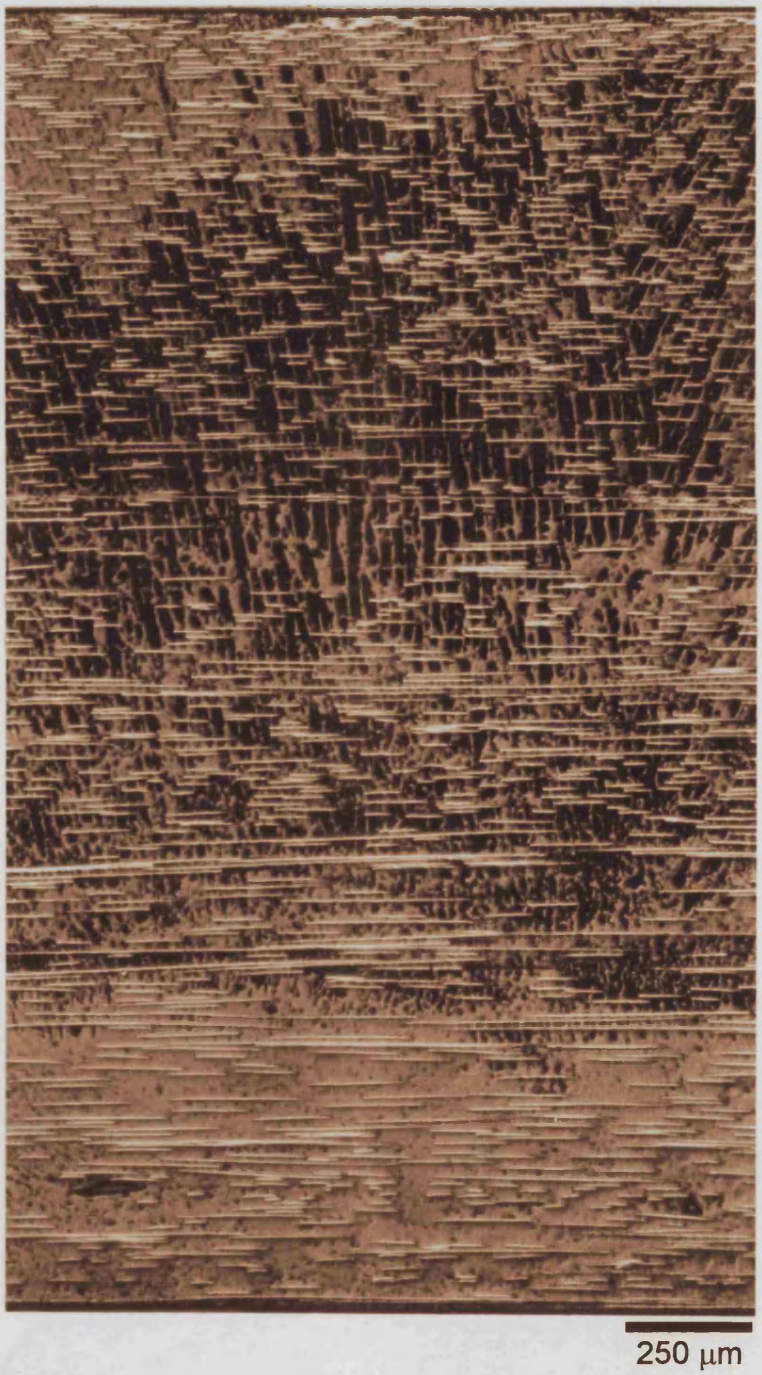

Figure 4.14 Through-section optical micrograph of sample with matrix composition HT50 / 0.19 V_{NLAS} .

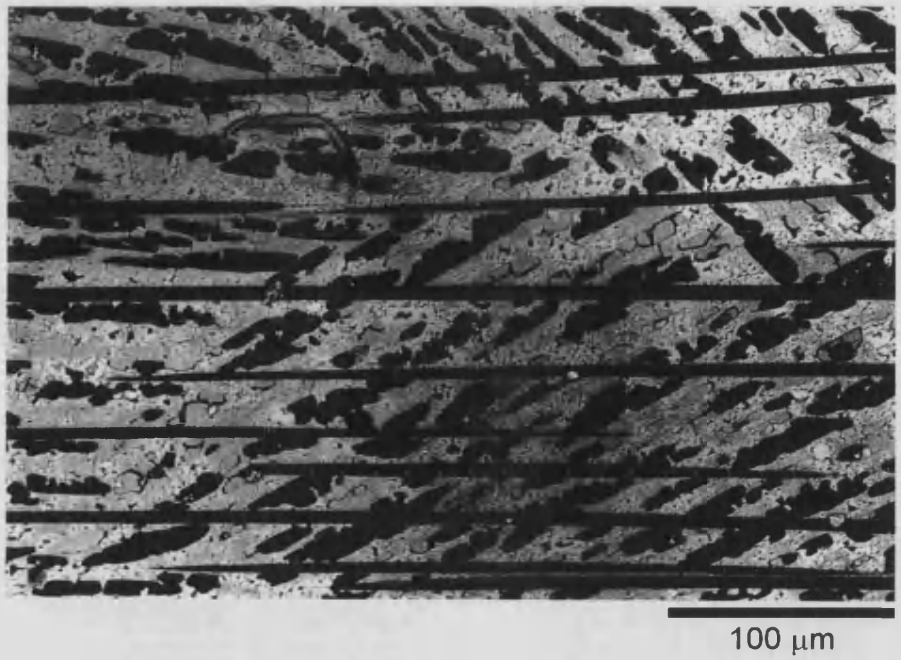

Figure 4.15 Variable orientation of columnar pores due to thermal fluctuations during the freeze-gelation process.

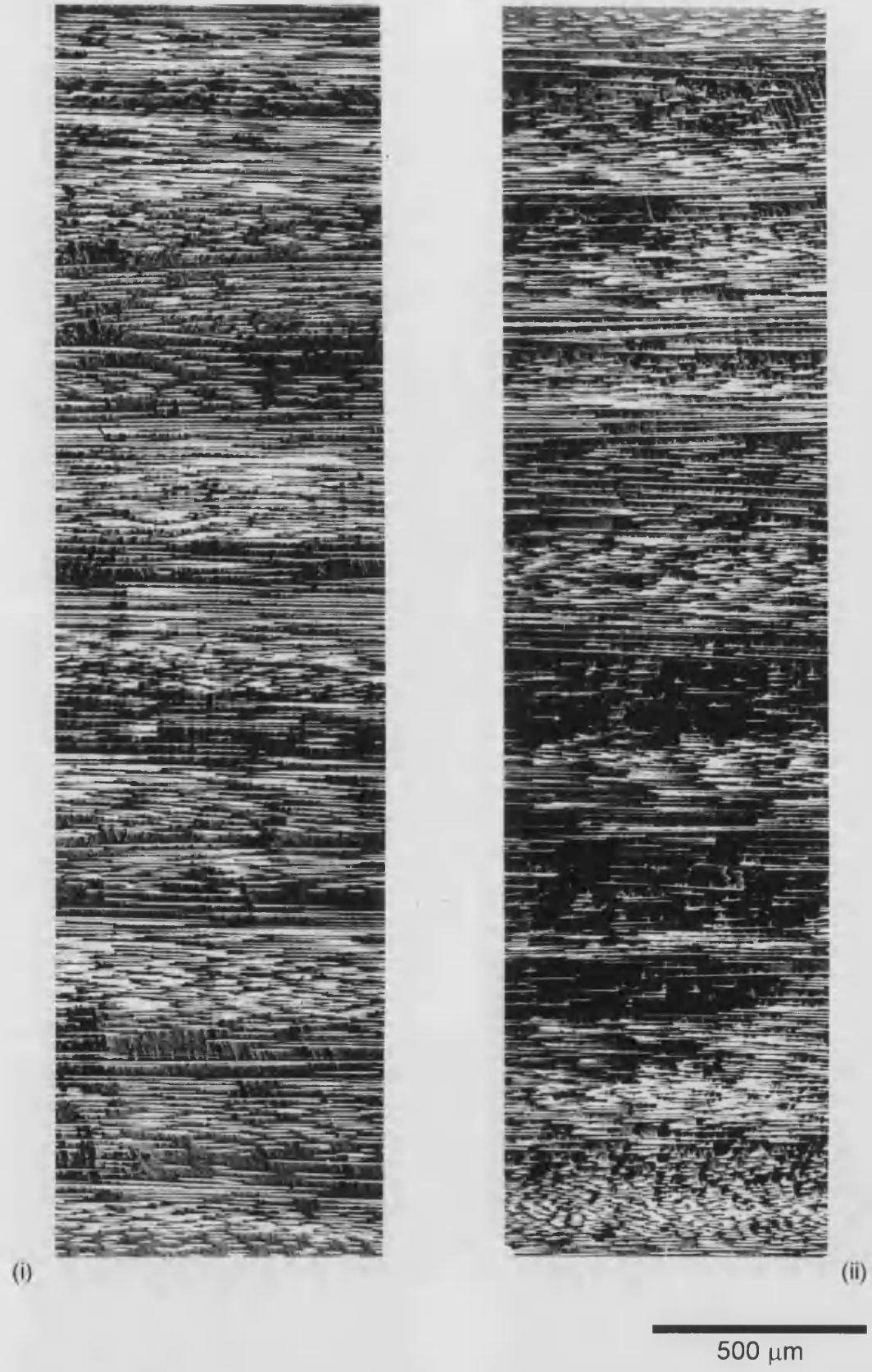

Figure 4.16 Pair of through-section optical micrographs from adjoining regions of a sample with matrix composition HT50 / 0.08 V_{NLAS} showing (i) clearly defined columnar pores running through the entire thickness and (ii) undefined pore structure in the centre of the specimen.

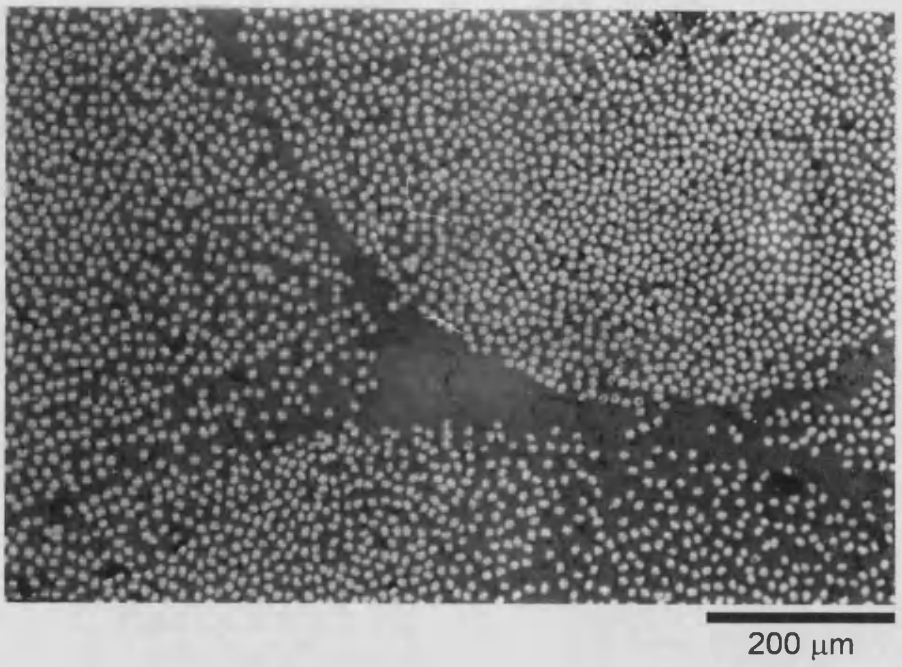

Figure 4.17 Fibres often remained in bundles. The junction of three bundles is seen clearly in this example.

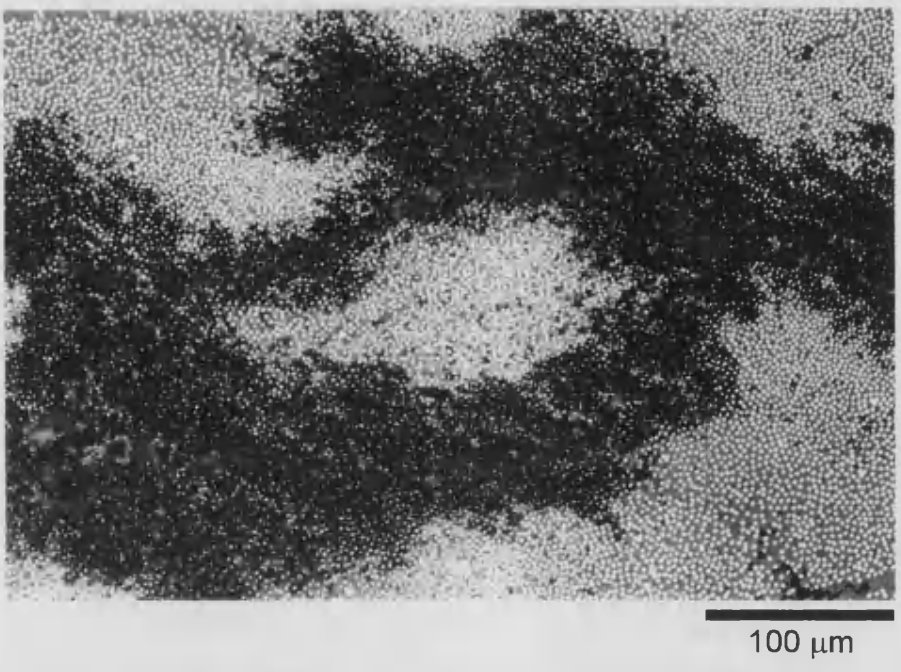

Figure 4.18 In some instances, matrix appeared to be denser within fibre tows.

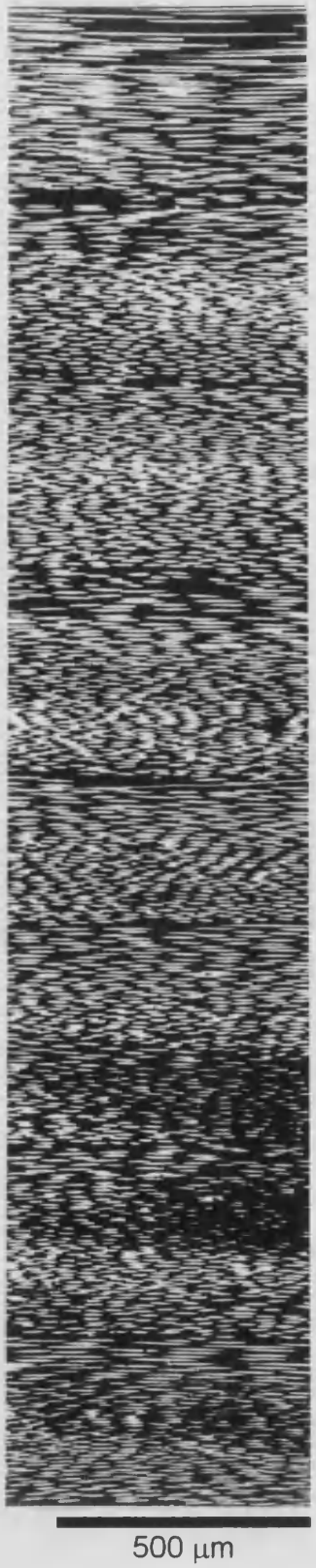

Figure 4.19 Through-section micrograph of a sample with matrix HT50 / 0.02 V_{NLAS} showing variability in fibre orientations.

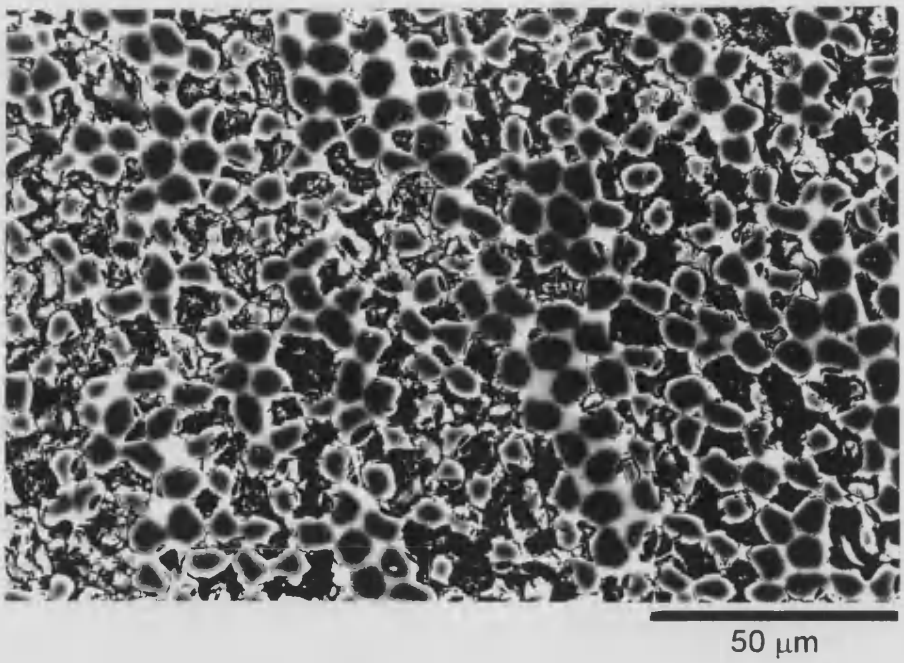

Figure 4.20 Porous regions of composites could not be polished satisfactorily, leading to problems in establishing reliable thresholds for image analysis.

Figure 4.21 SEM micrograph of sample with matrix HT50 / 0.22 V_{NLAS} demonstrating how regions of columnar porosity appear as parallel plates of solid material.

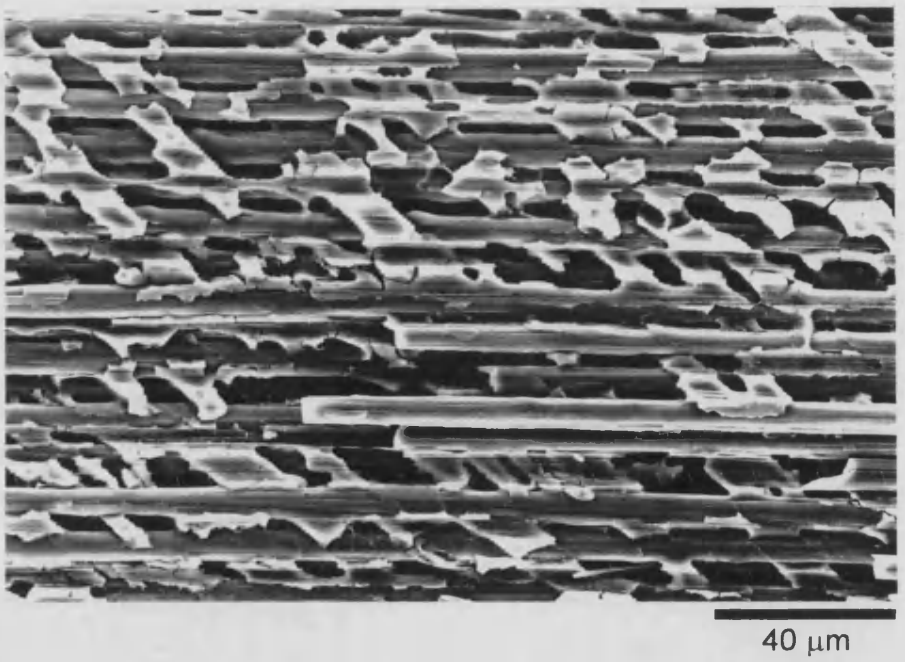

Figure 4.22 Samples with unfilled HT50 matrix exhibited high fibre volume fraction and very high porosity.

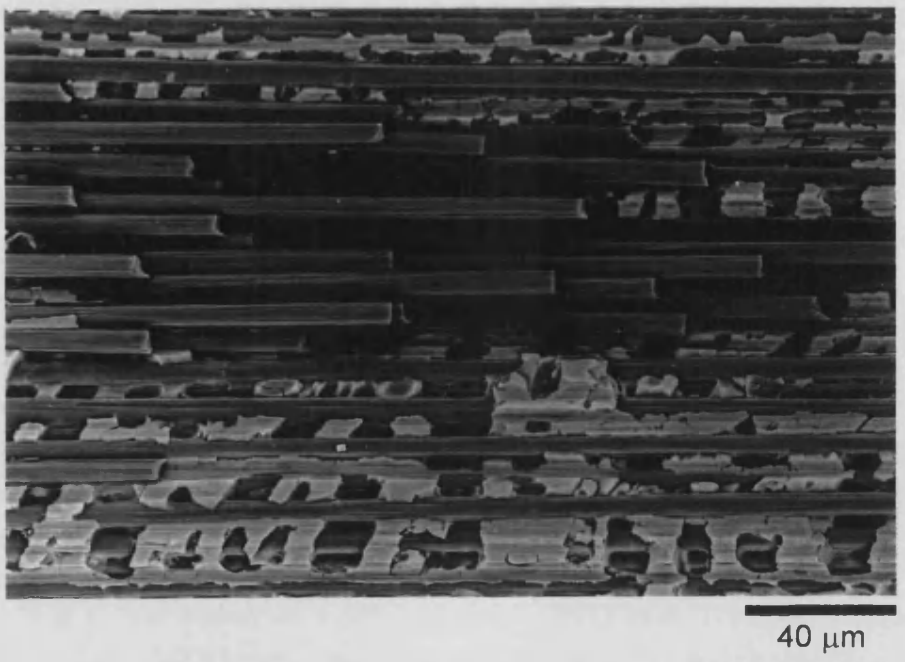

Figure 4.23 Extreme example of porosity in a composite with unfilled HT50 matrix.

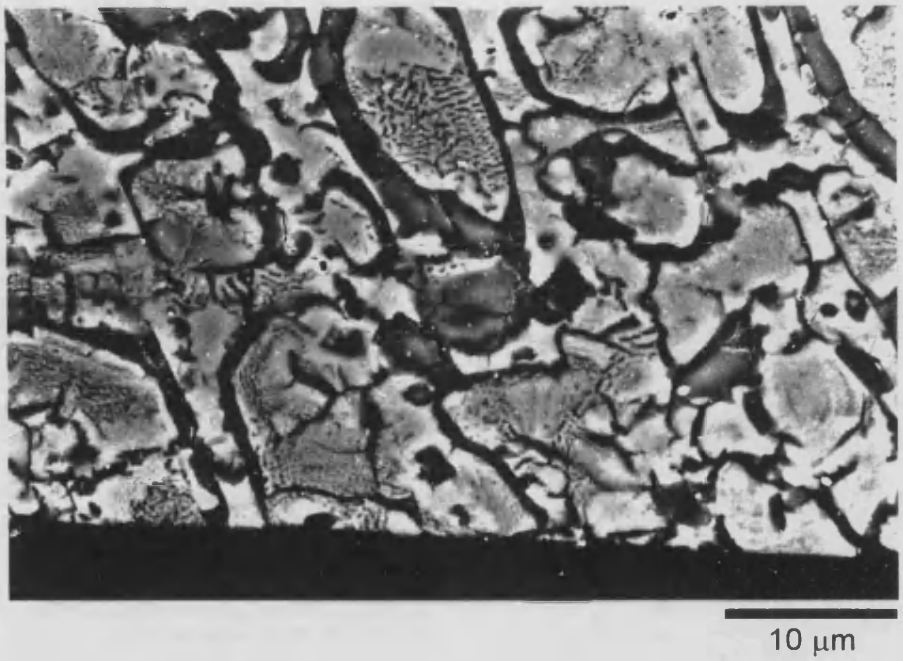

Figure 4.24 SEM micrograph of sample with matrix composition HT50 / 0.09 V_{NLAS} showing regions of fine-scale porosity. This porosity appears mottled against light grey regions of matrix. Infiltrated pores appear dark grey.

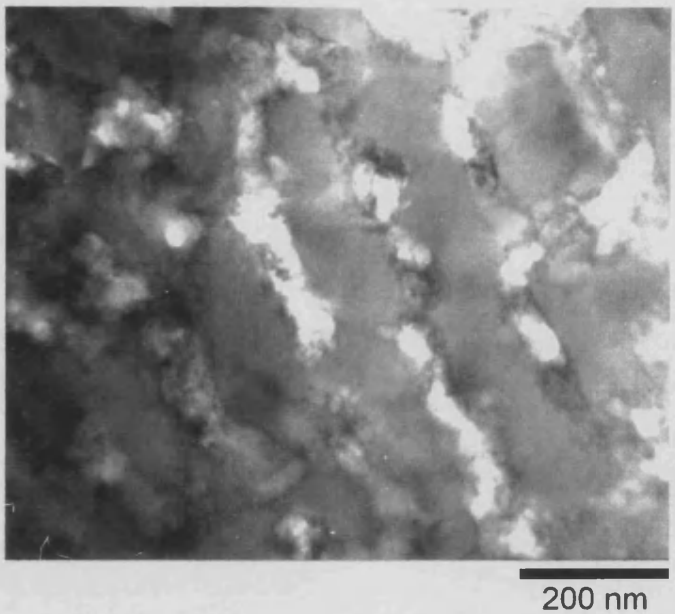

Figure 4.25 TEM micrograph of sample with matrix composition HT50 / 0.09 V_{NLAS} showing a region where colloidal silica particles have only partly fused. ED showed the region to be amorphous and EDS showed that no NLAS filler was present.

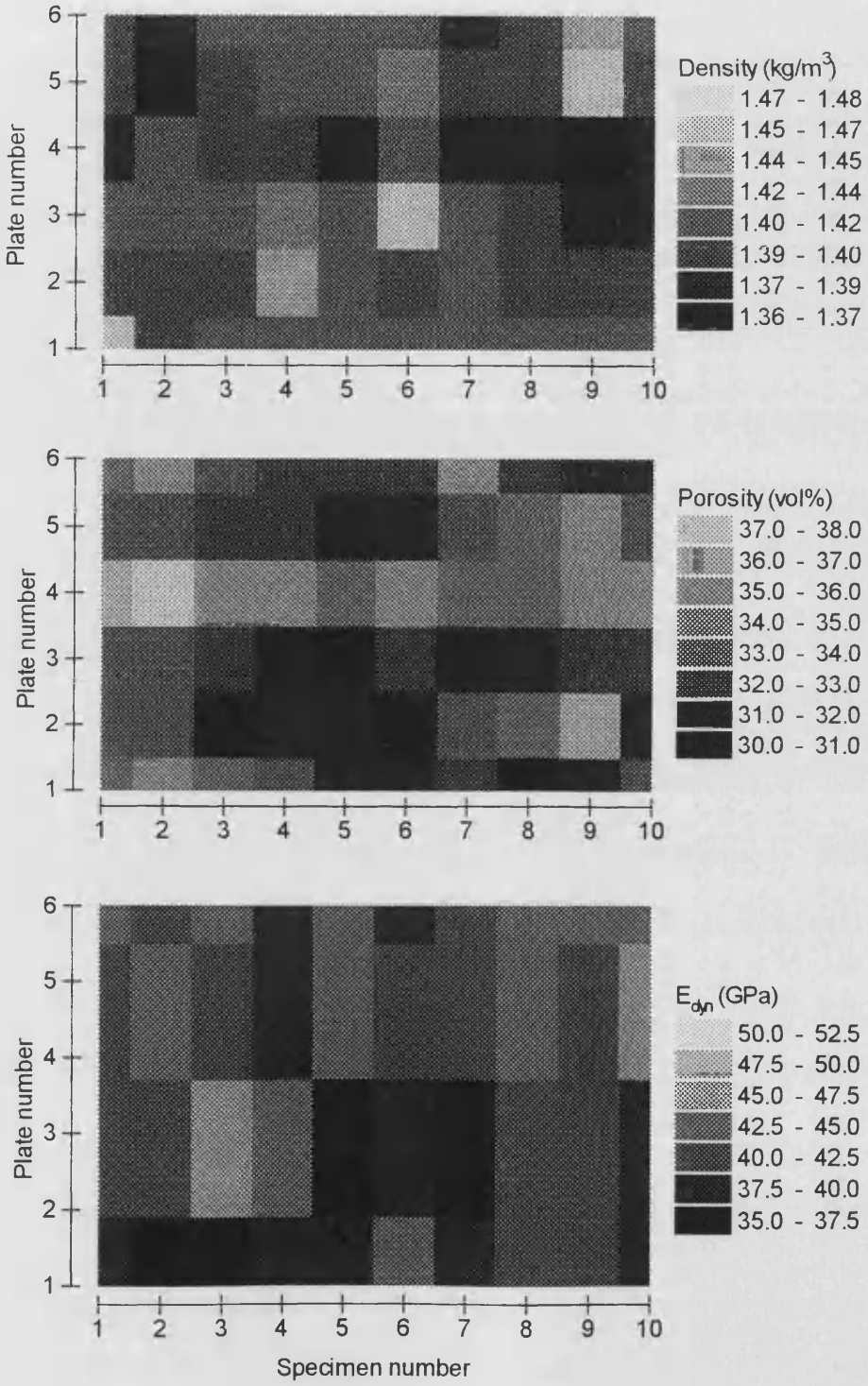

Figure 4.26 Variation of composite density (*top*), porosity (*middle*) and dynamic modulus, E_{dyn} (*bottom*) with specimen position during fabrication for a composite having an unfilled HT50 matrix. The different shades correspond to the keys shown right.

Figure 4.27 Through-section optical micrograph of a sample with matrix composition HT50 / 0.09 V_{NLAS} showing how liquid-phase infiltration was effective to a depth of only ~ ½ mm.

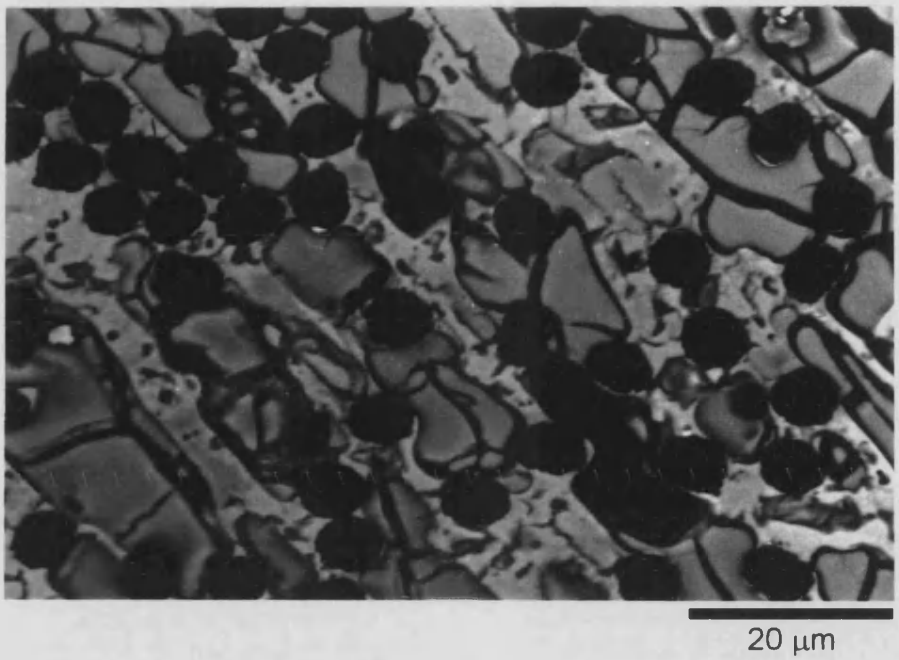

Figure 4.28 Within infiltrated regions, infiltrant silica sol (dark grey) was extensively cracked due to shrinkage. This example is taken from a sample with matrix composition HT50 / 0.27 V_{NLAS} .

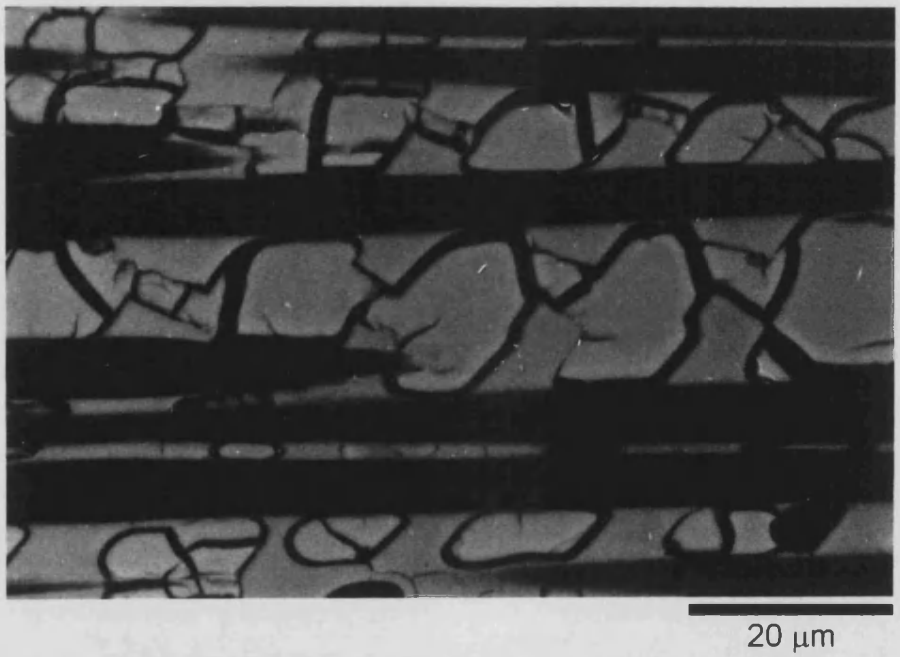

Figure 4.29 Appearance of infiltrant shrinkage cracking in transverse orientation. This example is taken from a sample with matrix composition HT50 / 0.09 V_{NLAS} .

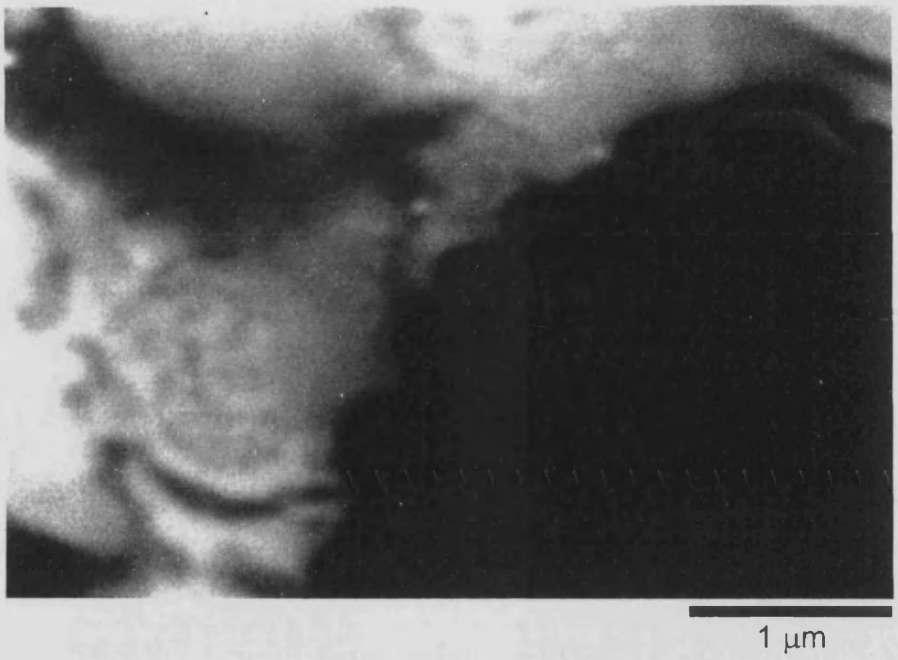

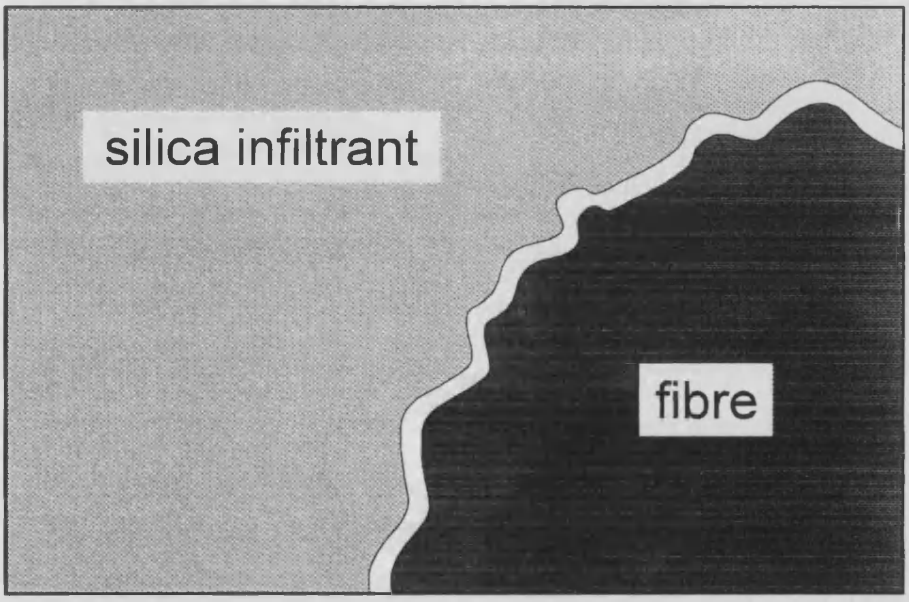

Figure 4.30 Infiltrant shrinkage cracking led locally to poor contact between fibres and infiltrant.

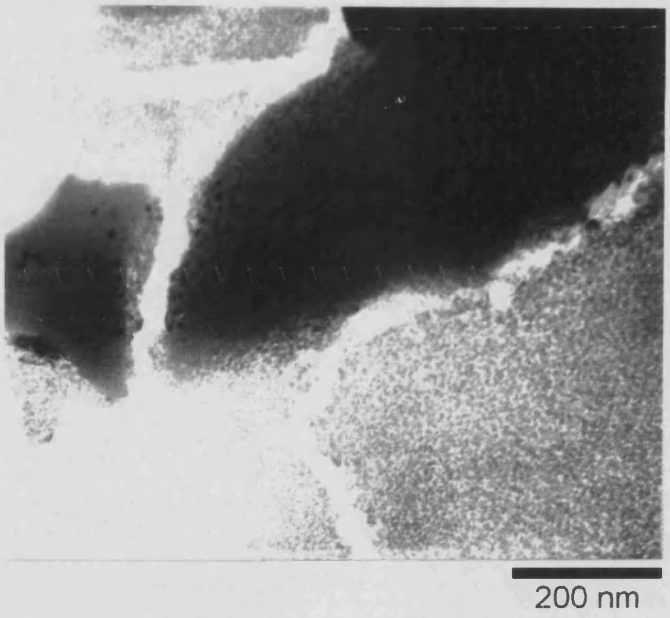

Figure 4.31 TEM micrograph from a sample with matrix composition HT50 / 0.19 V_{NLAS} showing limited fusing between infiltrant silica (7nm D30) particles, cracking within infiltrant regions and lack of integrity between infiltrant and the primary matrix material.

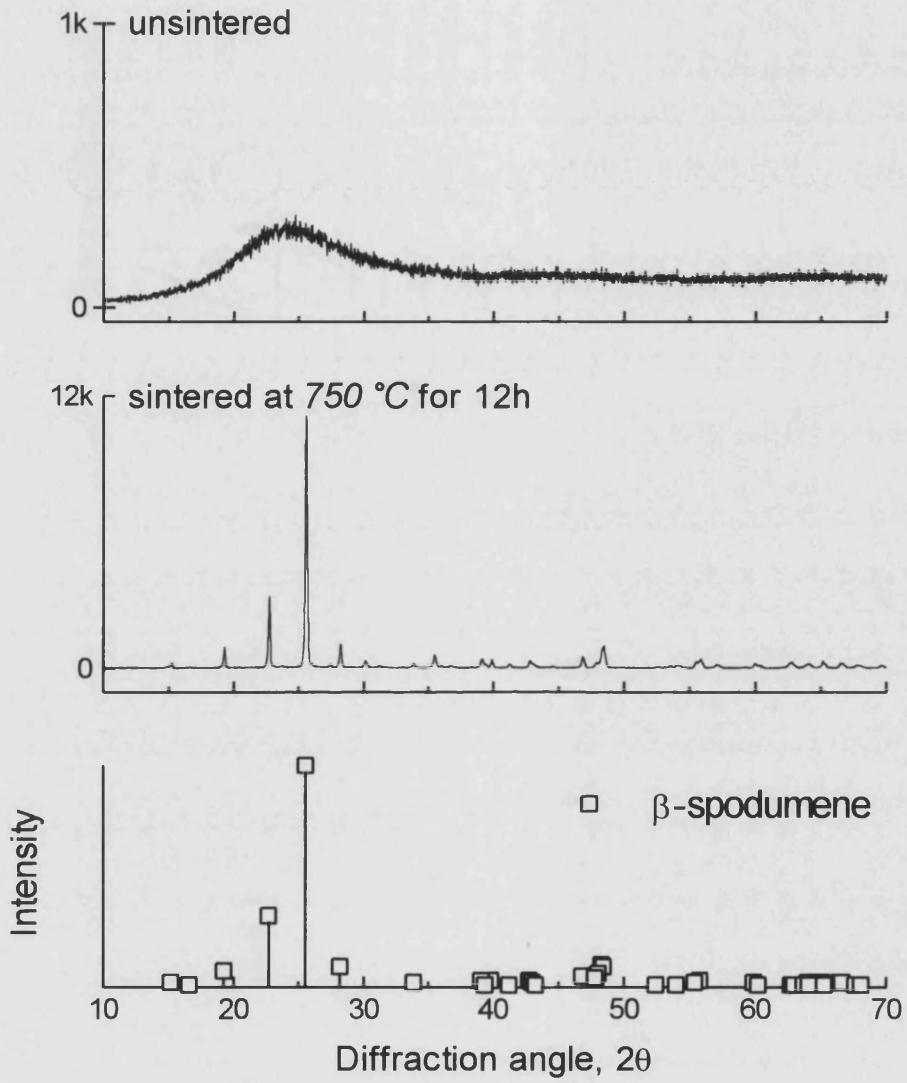

Figure 4.32 XRD data from NLAS powder in the as-received condition and following sintering at 750 °C. The lower graph gives the standard data for β-spodumene [123].

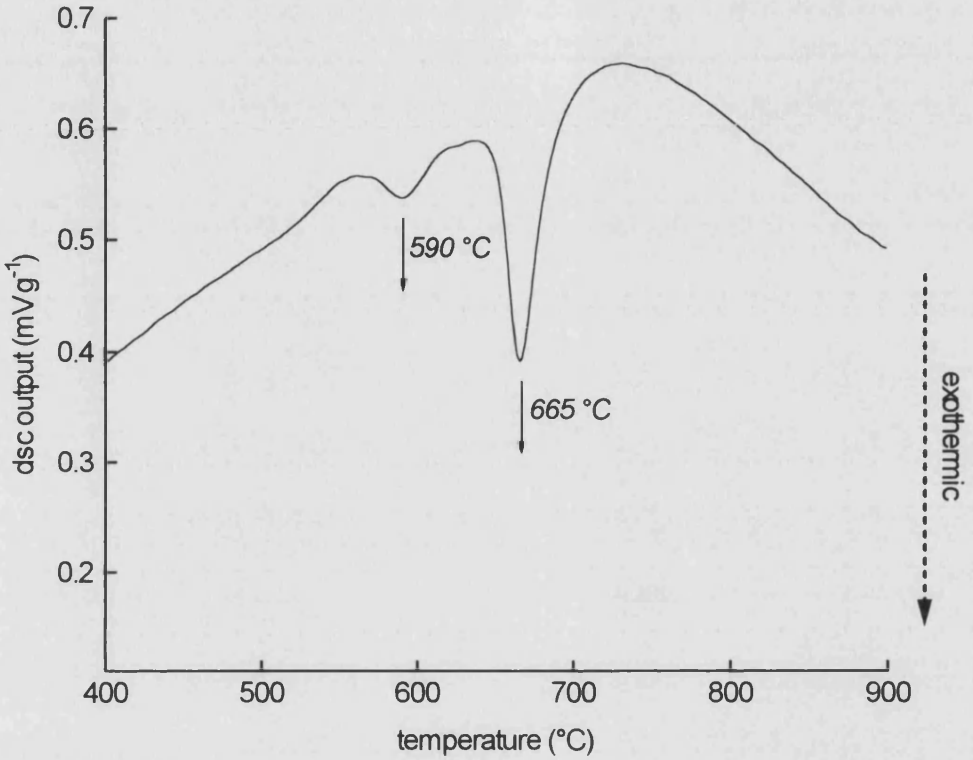

Figure 4.33 Differential scanning calorimetry trace of as-received NLAS powder. Exotherms were detected at 590 °C and 665 °C.

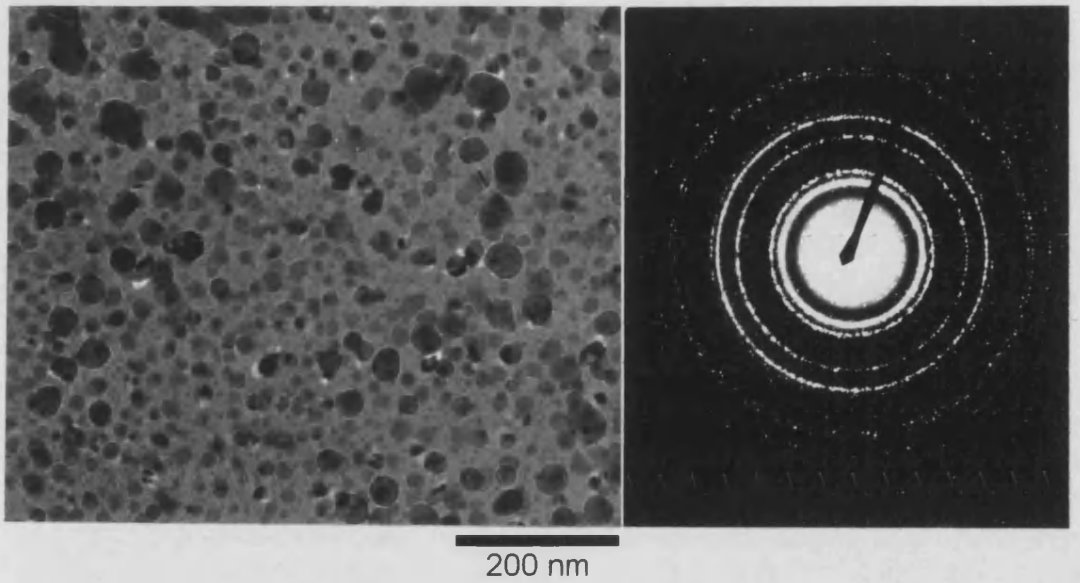

Figure 4.34 TEM micrograph of NLAS matrix filler cerammed at 750 °C for 12 hours showing crystallites in a glassy matrix (*left*). The electron diffraction pattern of this region (*right*) corresponds with that of β-spodumene.

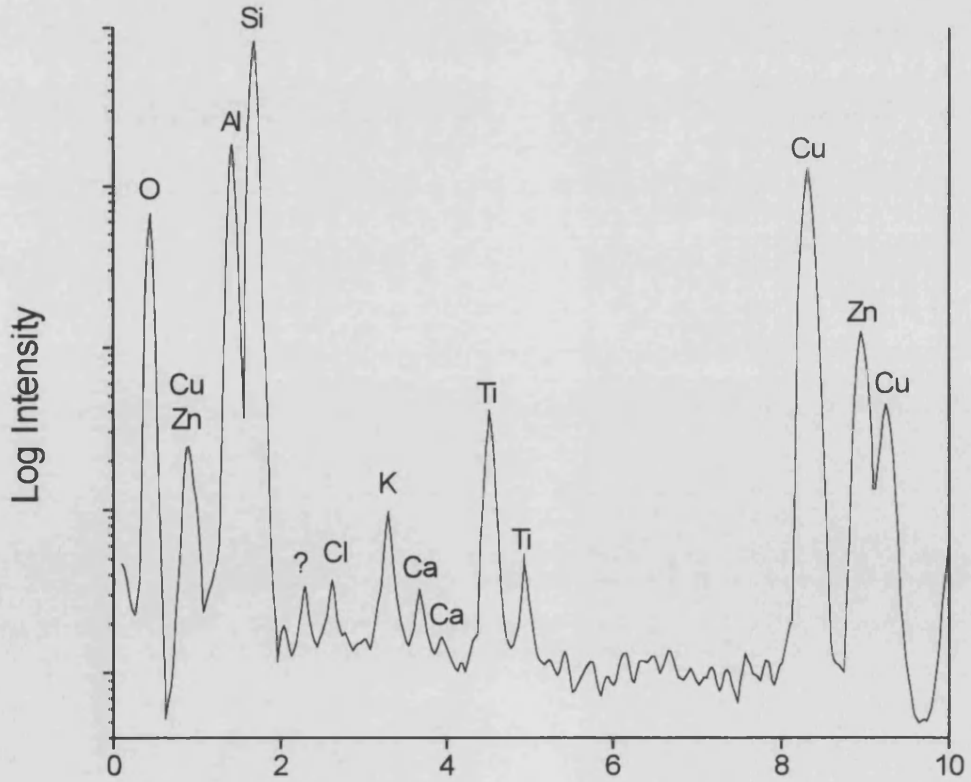

Figure 4.35 TEM EDS trace of NLAS sample cerammed at 750 °C for 12 hours.

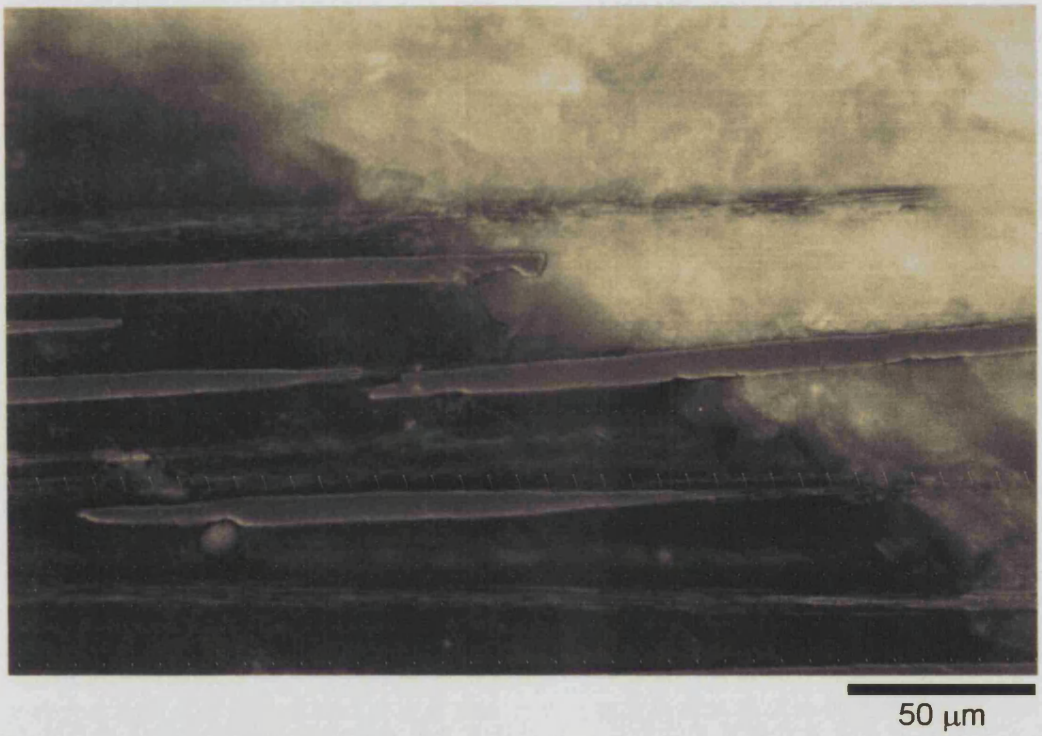

Figure 4.36 Optical micrograph (DIC) of a sample with matrix composition HT50 / 0.19 V_{NLAS}. A discrete boundary is seen between uniformly dull regions and bright, apparently crystalline regions.

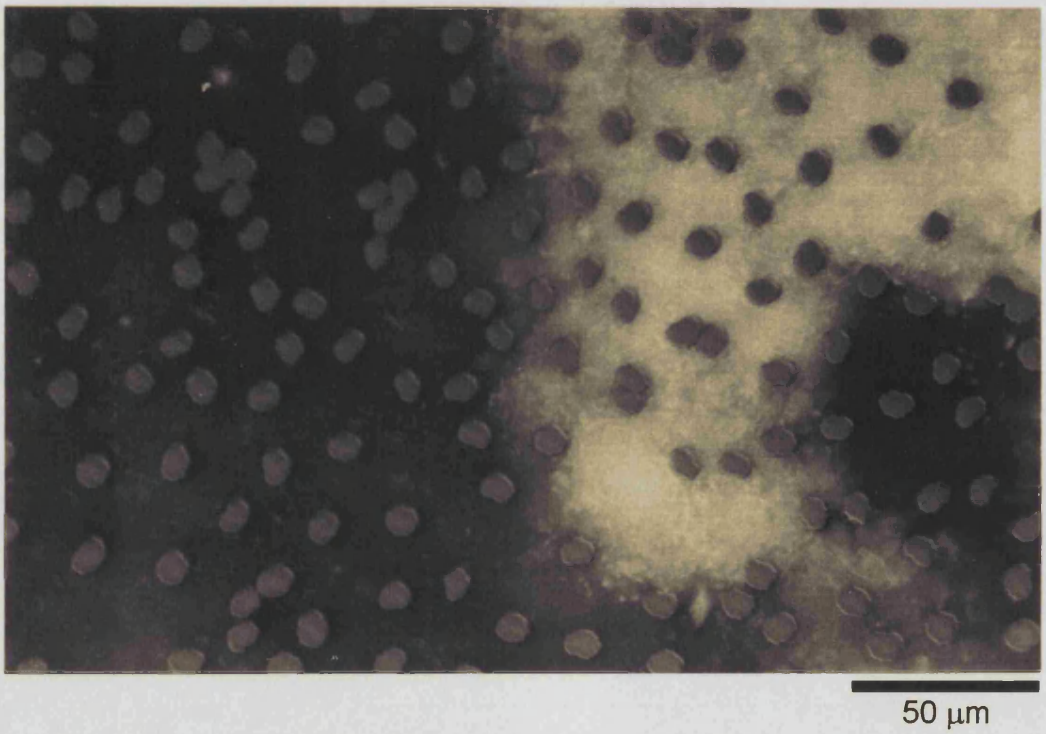

Figure 4.37 The two types of matrix appearance described in figure 4.36 were seen also in the transverse orientation. This example is from a sample with matrix HT50 / 0.22 V_{NLAS}.

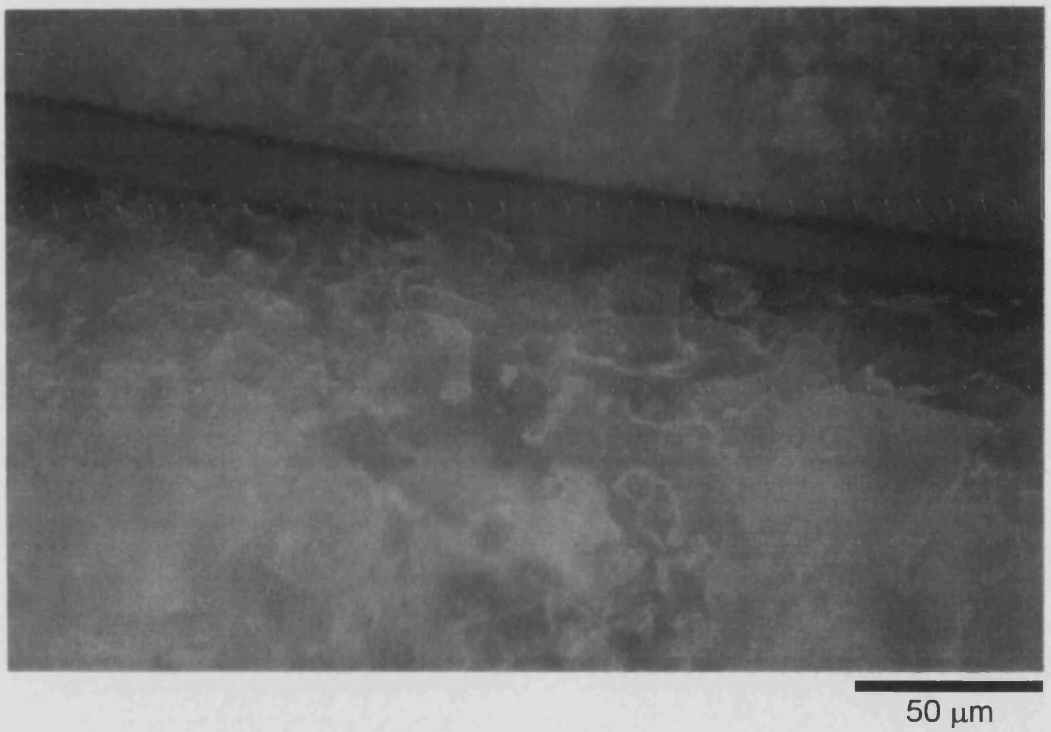

Figure 4.38 Optical micrograph (DIC) from the dense region of a sample with matrix composition HT50 / 0.27 V_{NLAS}. The matrix appears uniformly bright and crystalline.

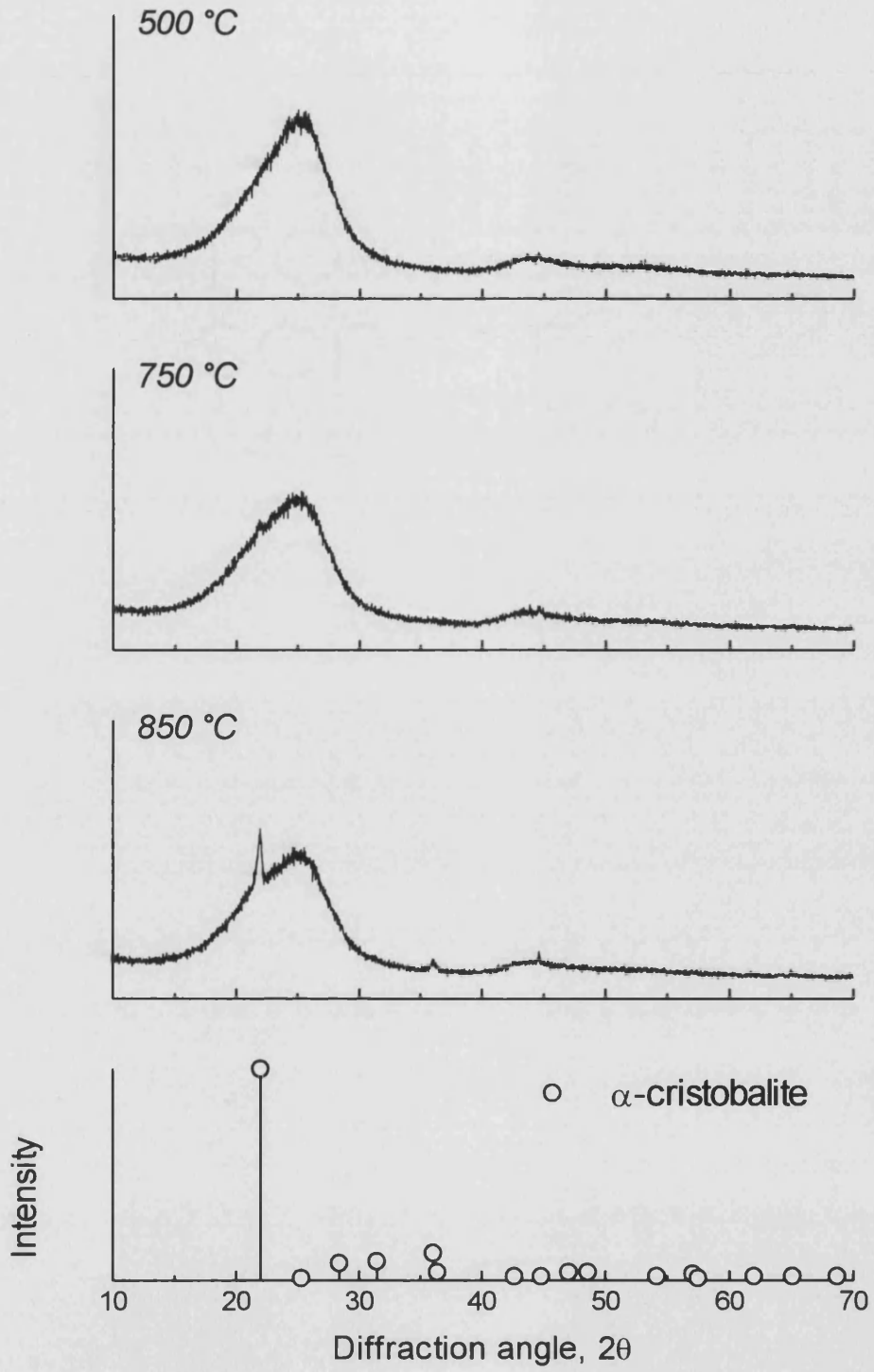

Figure 4.39 Effect of sintering temperature on the crystallography of composites with unfilled HT50 matrices. The lower graph gives pattern data for α-cristobalite.

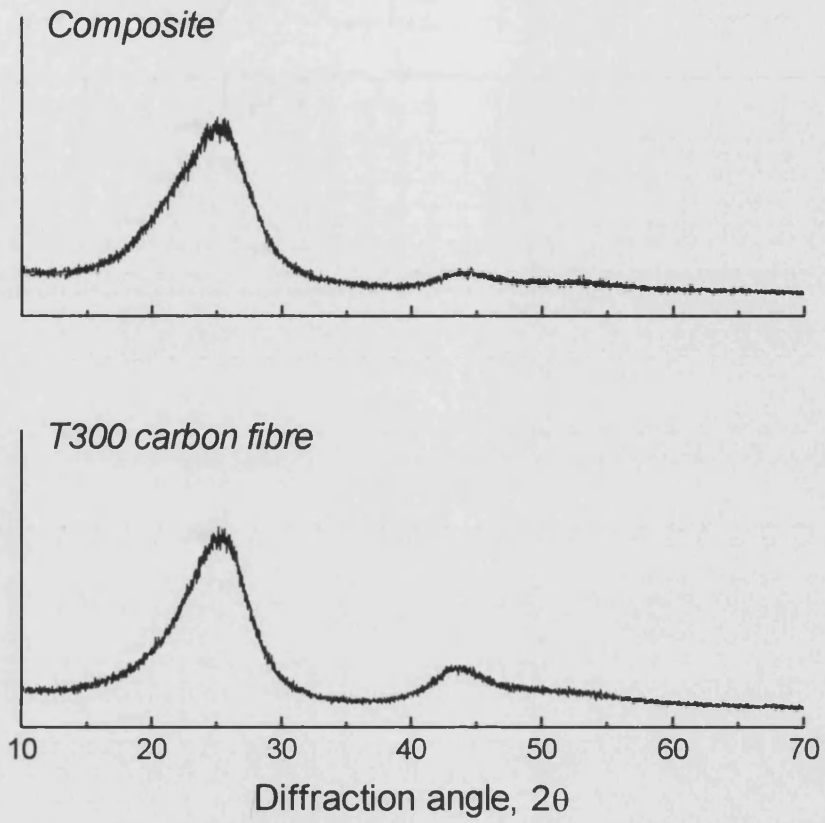

Figure 4.40 Composites with unfilled silica matrices exhibit a 'double hump' X-ray diffraction trace (*top graph*). The lower graph demonstrates how these two broad peaks are attributable to the T300 carbon fibres (*lower graph*).

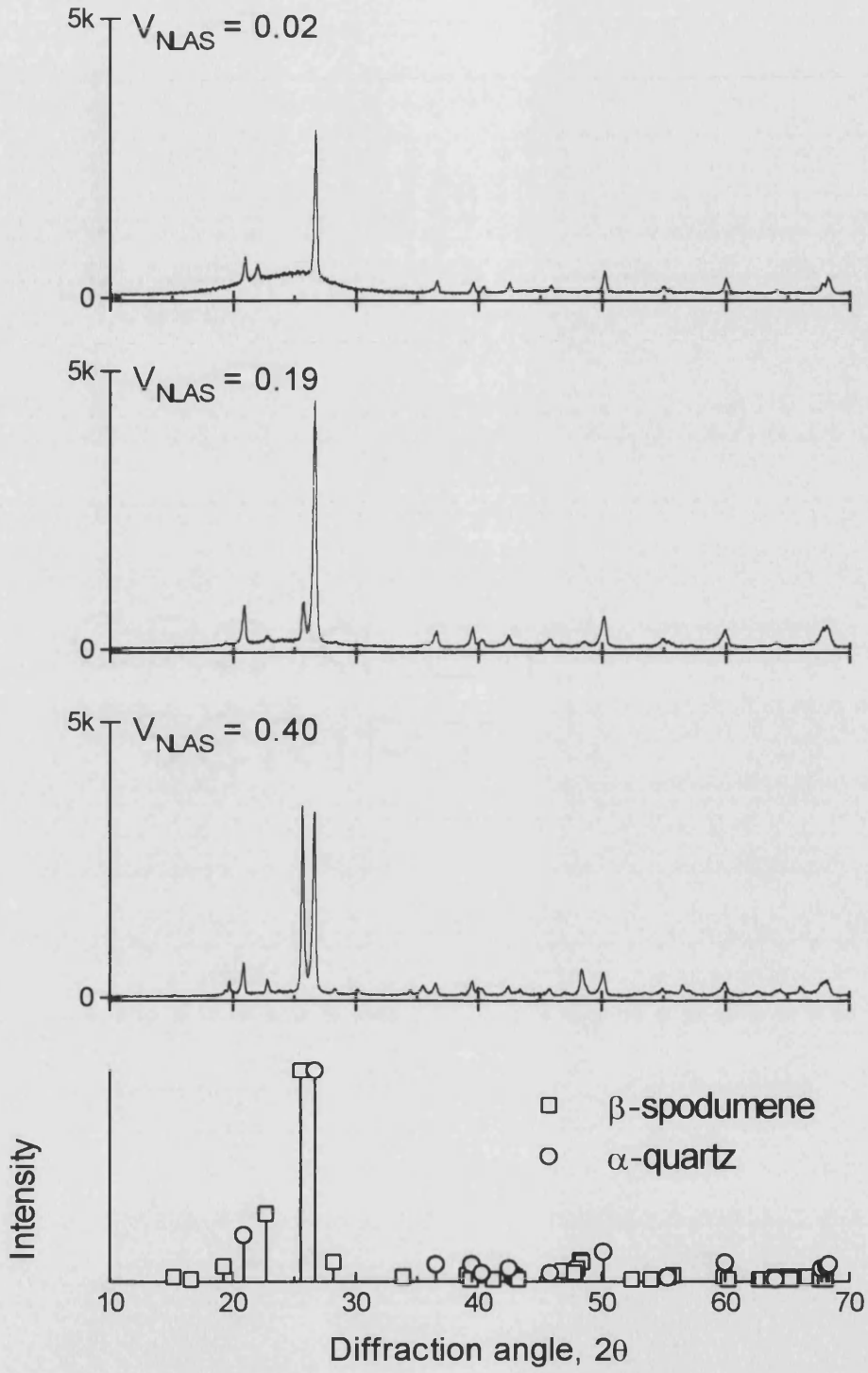

Figure 4.41 XRD traces from composites with HT50-derived matrices containing 0.02, 0.19 and 0.40 volume fractions of NLAS glass-ceramic filler. The pattern data for α-quartz [116] and β-spodumene [123] (*lower graph*) are shown normalised to the same peak height.

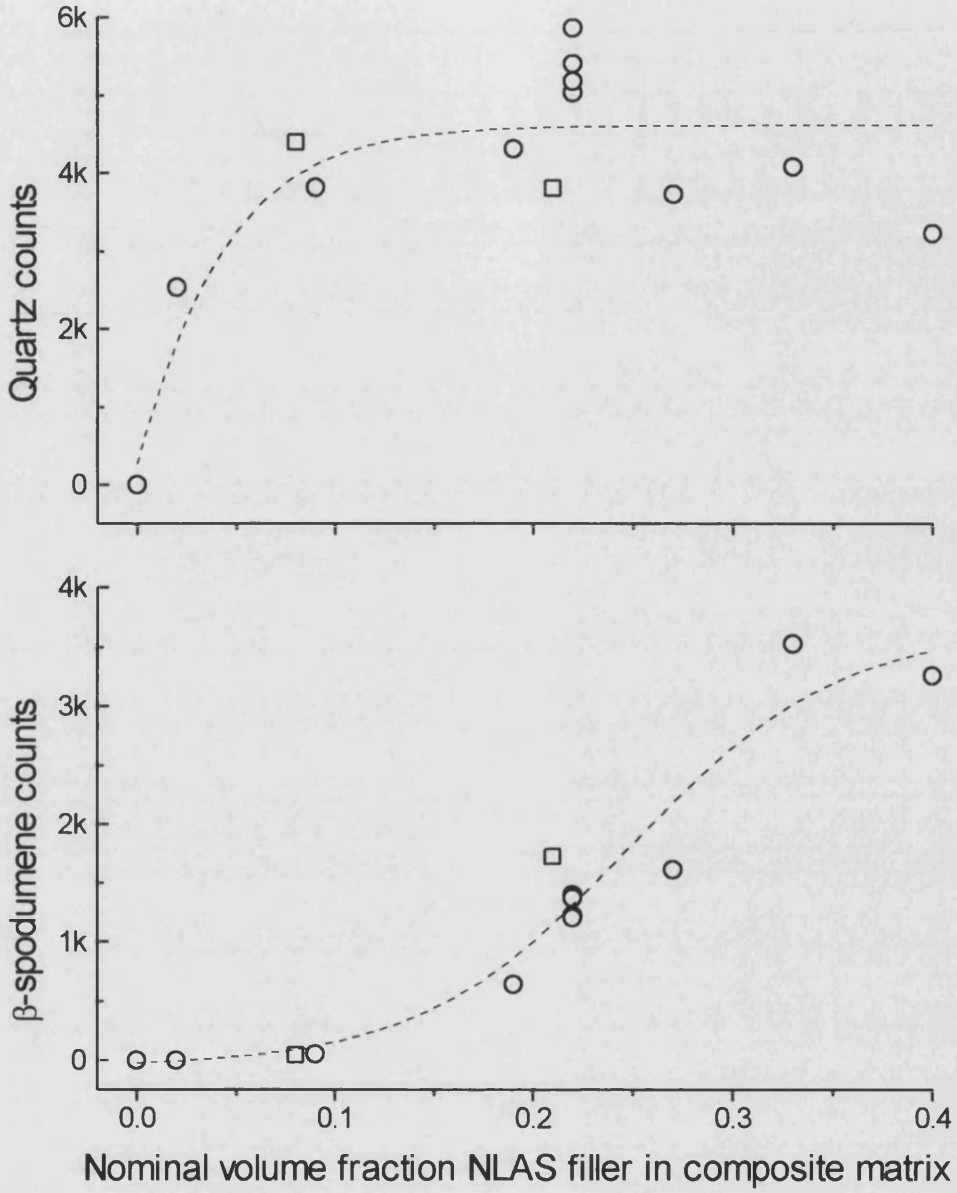

Figure 4.42 Variation of X-ray diffraction data with volume fraction NLAS filler in composite matrix. ○: HT50-derived matrix; □: X30-derived matrix.

TOP: ordinate axis shows counts at $2\theta = 26.67°$, *i.e.* the principal peak of quartz.

BOTTOM: ordinate axis shows counts at $2\theta = 25.55°$, *i.e.* the principal peak of β-spodumene

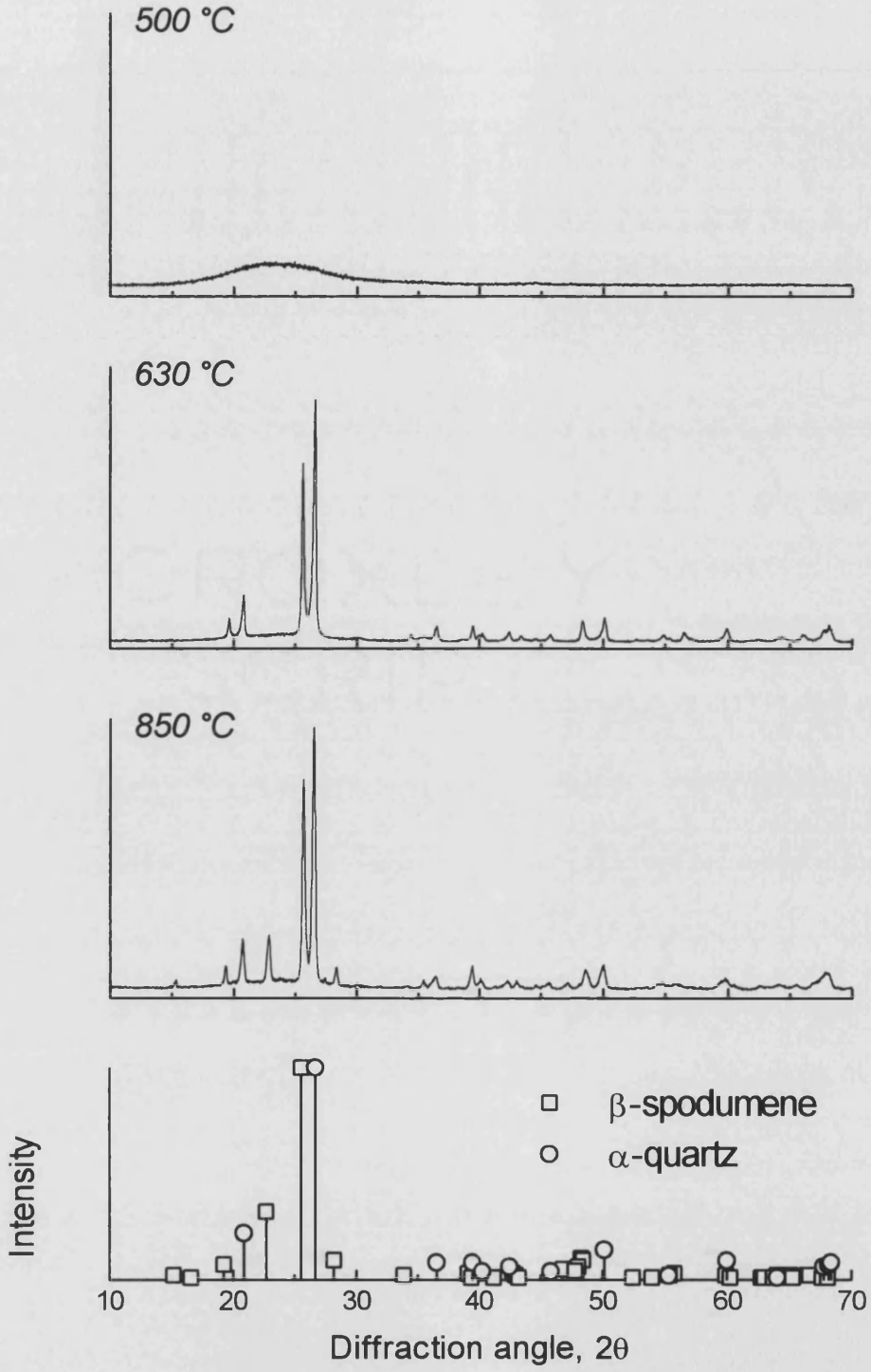

Figure 4.43 Effect of sintering temperature on the XRD response of samples with matrix composition HT50 / 0.33 V_{NLAS}. The lower graph gives pattern data for α-quartz [116] and β-spodumene [123] normalised to the same peak height.

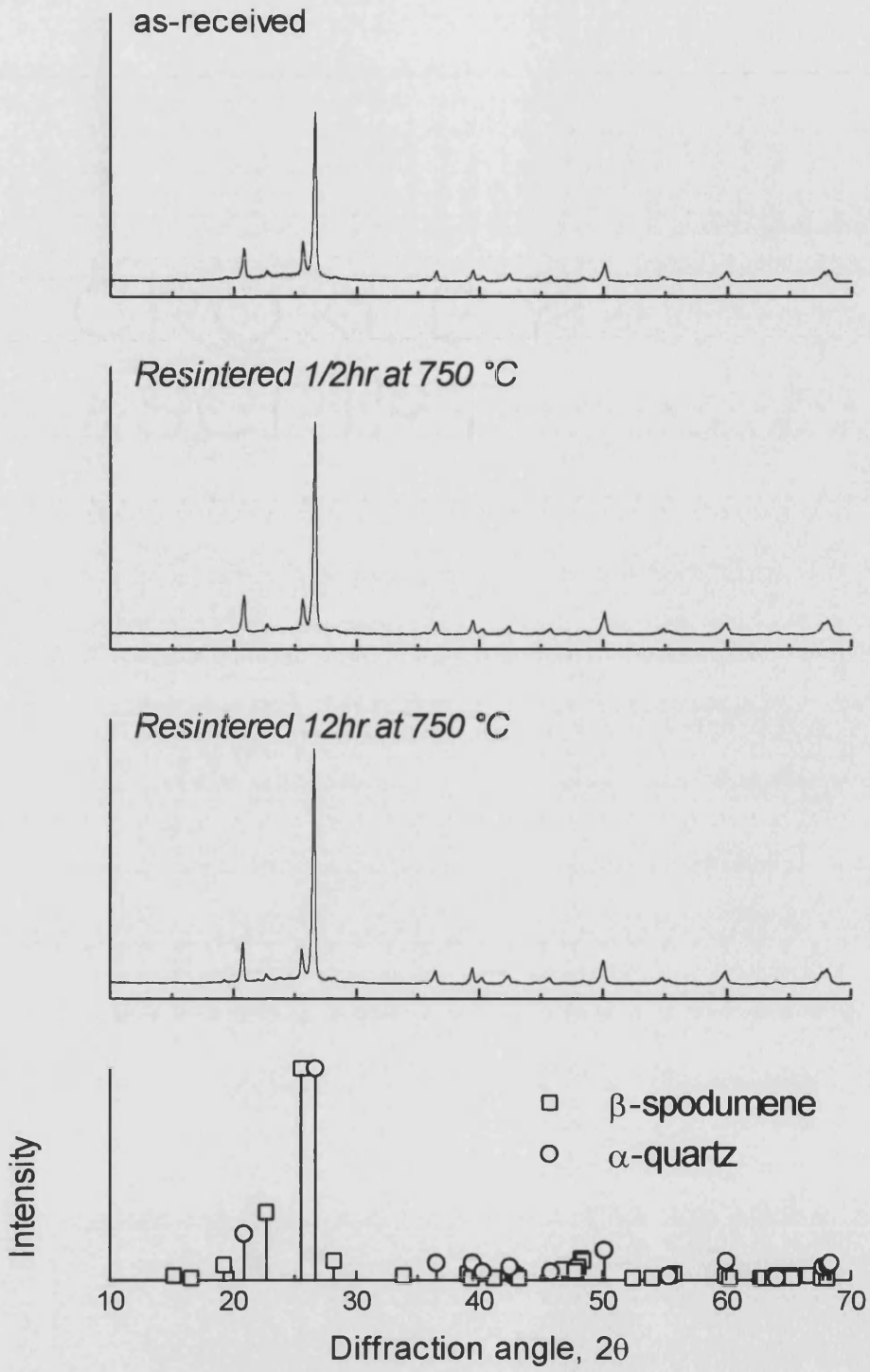

Figure 4.44 Effect of resintering on the XRD spectra of composites with matrix composition HT50 / 0.19 V_{NLAS}. The lower graph gives pattern data for α-quartz [116] and β-spodumene [123] normalised to the same peak height. The quartz content increases during resintering whilst the β–spodumene peak remains constant.

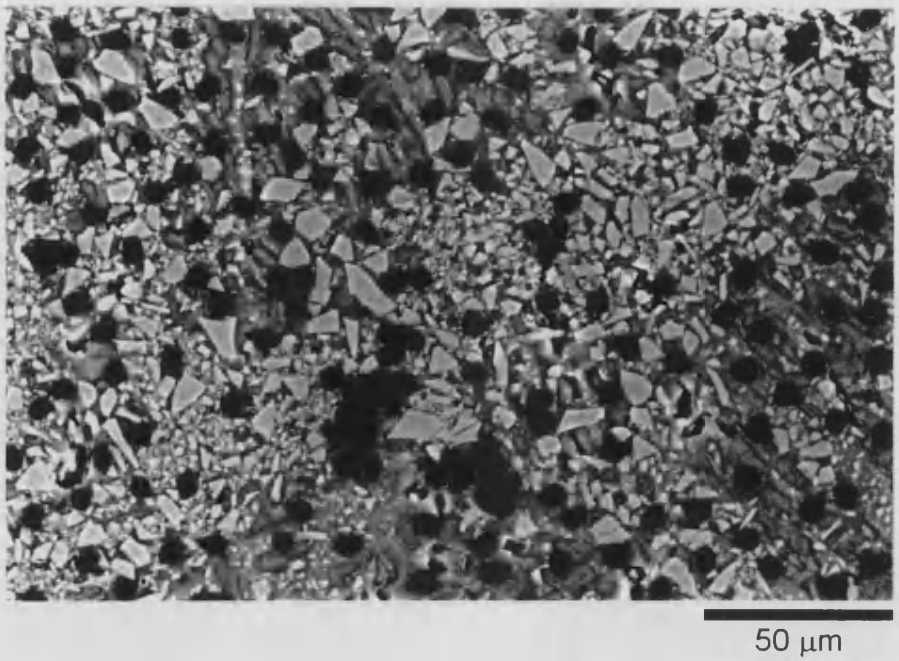

Figure 4.46 SEM micrograph of sample having matrix composition HT50 / 0.33 V_{NLAS} and sintered at 500 °C. NLAS filler particles (light grey) are clearly visible.

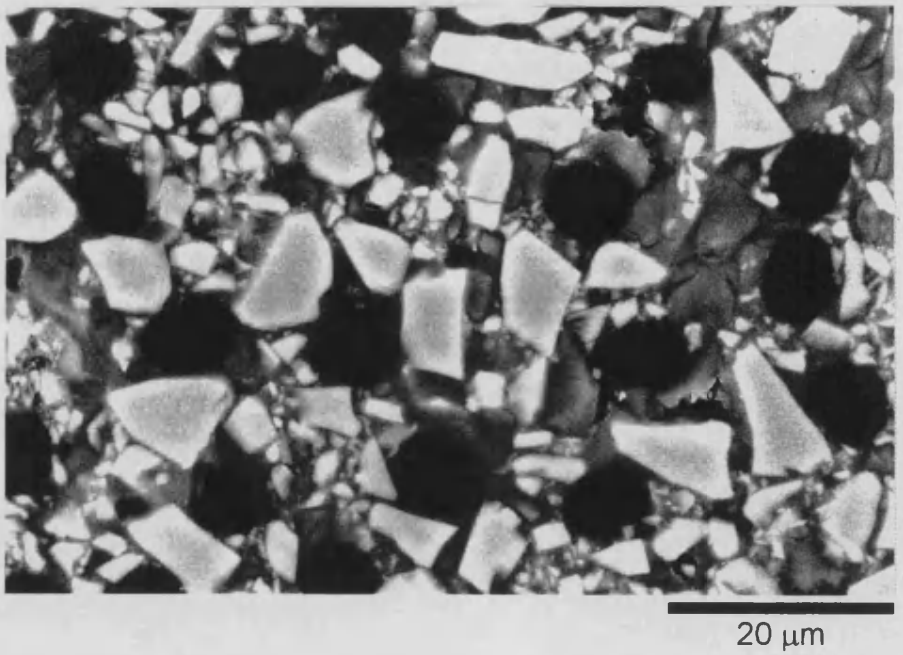

Figure 4.47 SEM micrograph of sample having matrix composition HT50 / 0.33 V_{NLAS} and sintered at 500 °C. NLAS filler particles (light grey) are clearly visible.

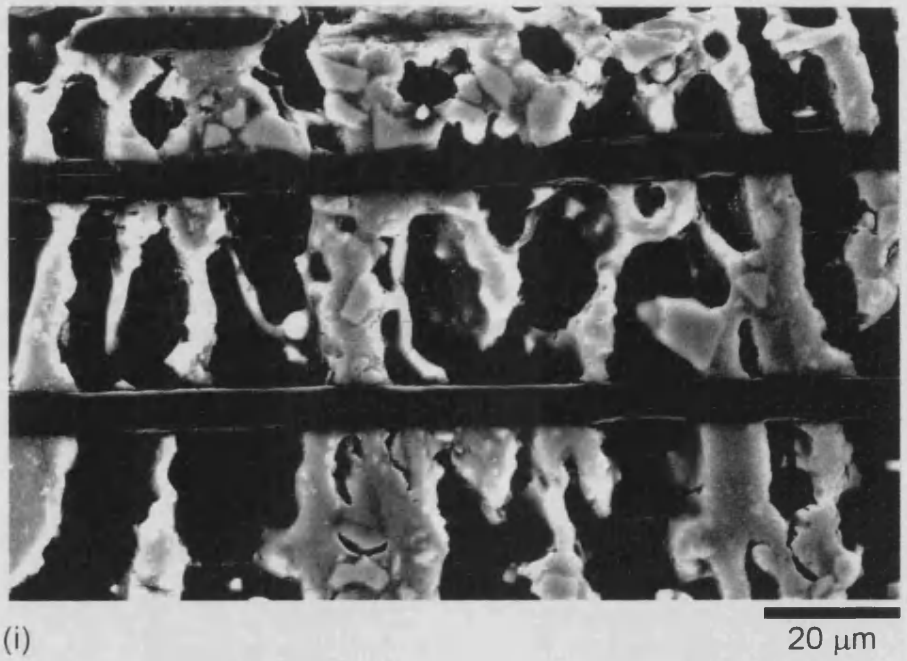

Figure 4.48 SEM micrograph of sample having matrix composition HT50 / 0.33 V_{NLAS} and sintered at 500 °C. NLAS filler particles (light grey) are situated in the threads of matrix material which bound open, columnar pores.

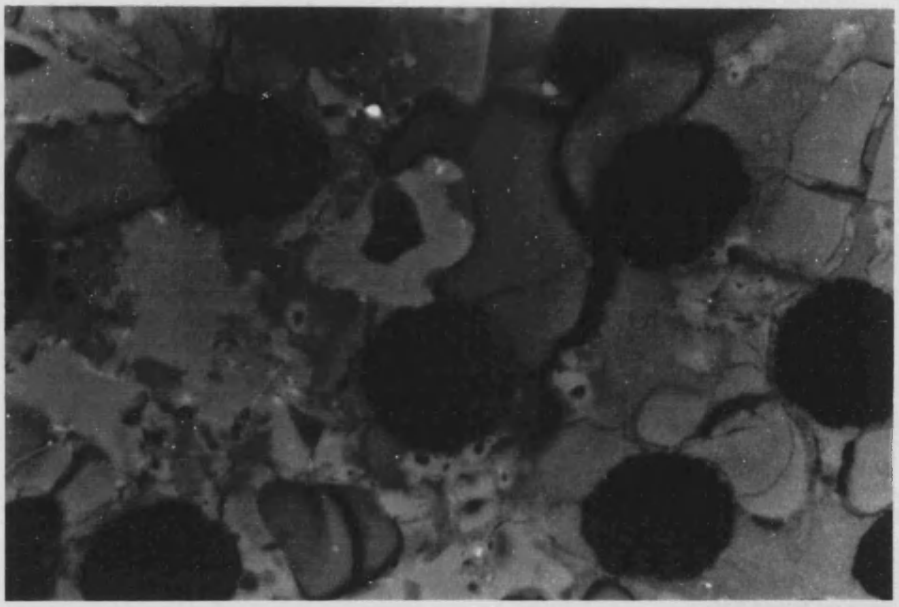

Figure 4.49 SEM micrograph of sample having matrix composition HT50 / 0.33 V_{NLAS} and sintered at 630 °C. NLAS filler particles (light grey) have clearly flowed and are only partly visible against the colloidal silica matrix (dark grey).

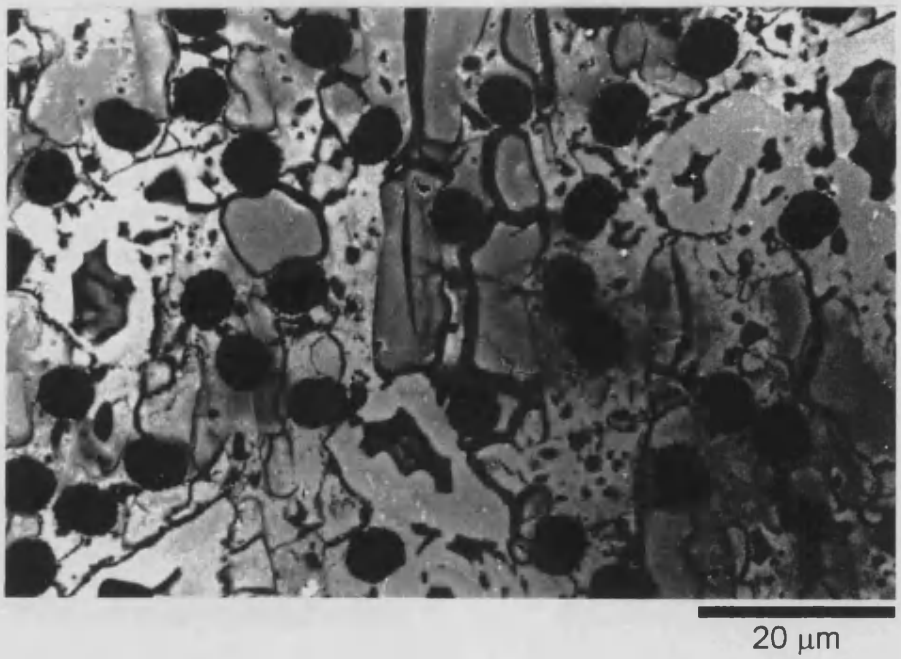

Figure 4.50 SEM micrograph of sample having matrix composition HT50 / 0.33 V_{NLAS} and sintered at 750 °C. NLAS filler particles are no longer clearly visible against the colloidal silica matrix.

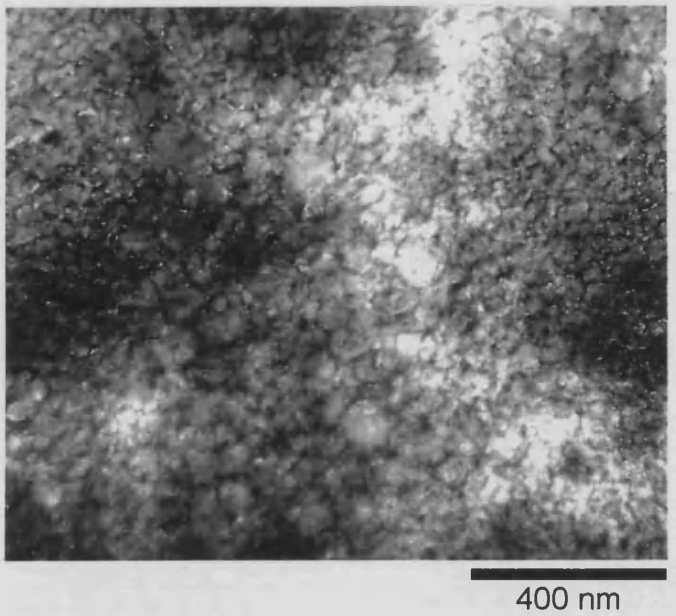

Figure 4.51 TEM micrograph showing partially fused 125nm colloidal silica particles in a region shown by EDS to contain no NLAS filler particles. ED confirmed that this region was amorphous. Matrix composition: HT50 / 0.09 V_{NLAS}.

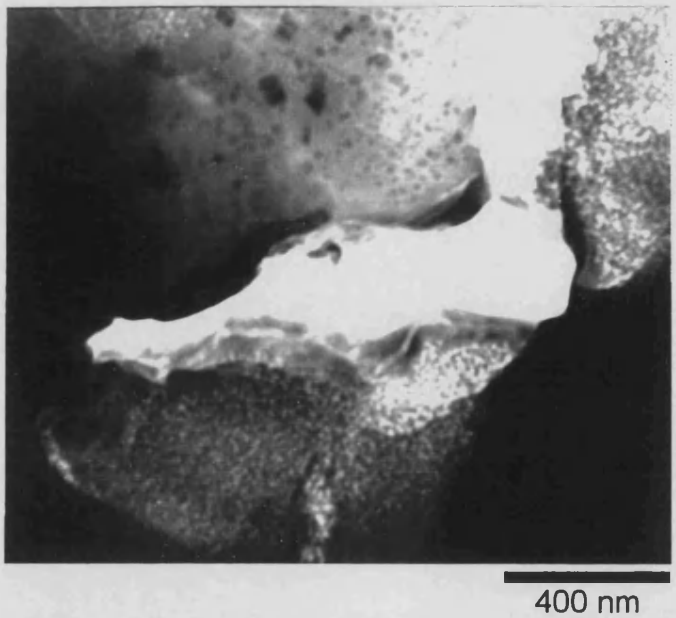

Figure 4.52 TEM micrograph of sample with matrix X30 / 0.21 V_{NLAS}. The matrix in the lower right corner contains NLAS filler particles an appears to be dense. ED showed that this whole region was crystalline.

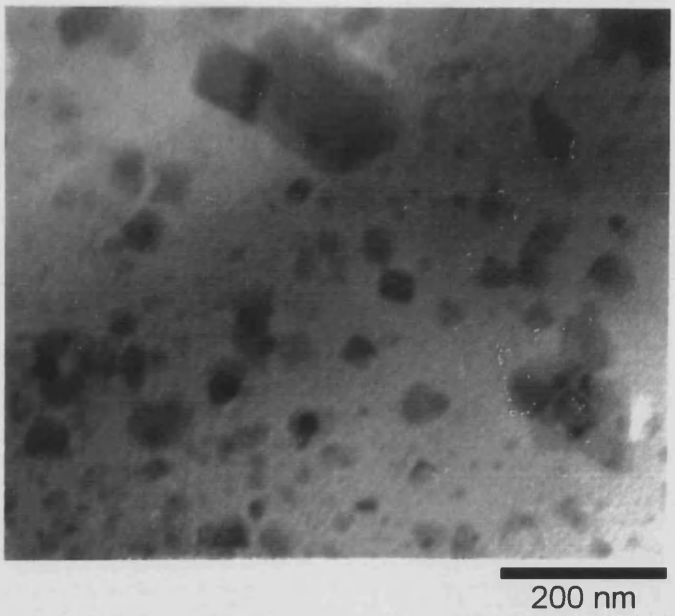

Figure 4.53 TEM micrograph showing detail of a matrix region with high filler content. β-spodumene crystals are clearly defined.
Matrix composition: HT50 / 0.27 V_{NLAS}.

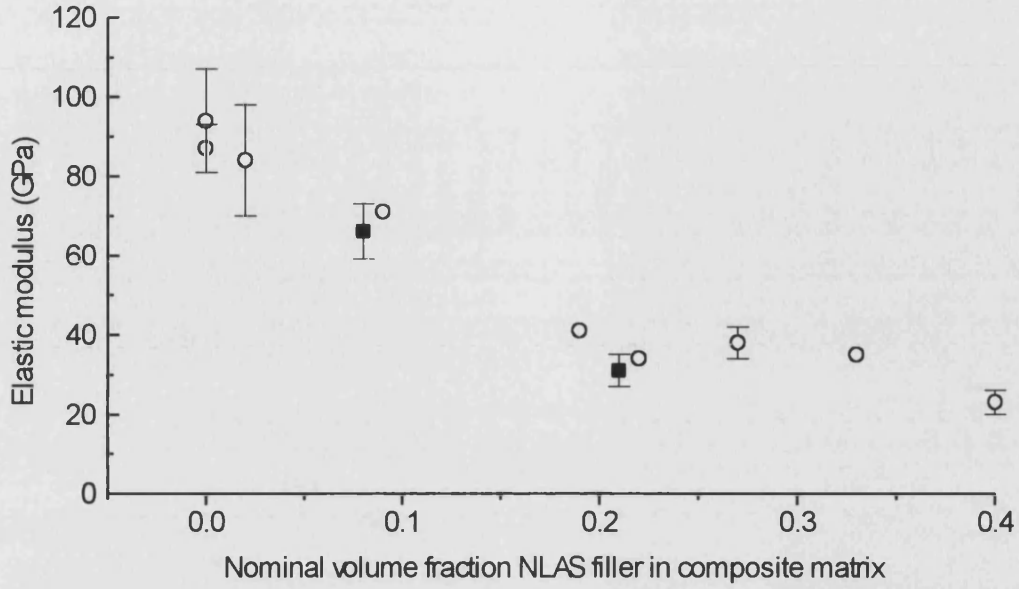

Figure 4.54 Variation of composite flexural modulus with NLAS filler content in matrix.
○ : HT50-derived matrix. ■ : X30-derived.
The error bars indicate standard deviations.

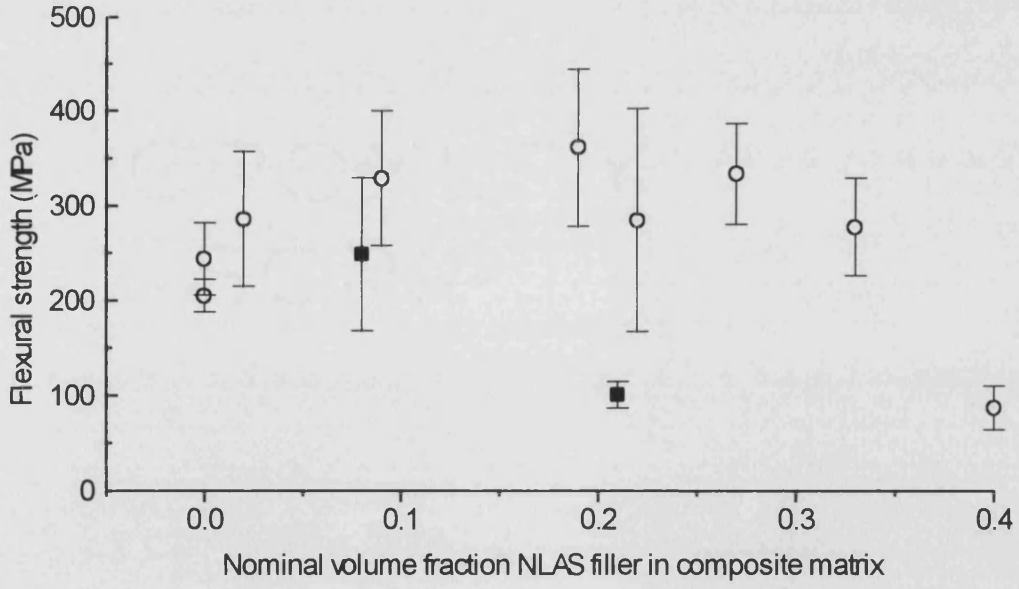

Figure 4.55 Variation of composite flexural strength with NLAS filler content in matrix.
○ : HT50-derived matrix. ■ : X30-derived.
The error bars indicate standard deviations.

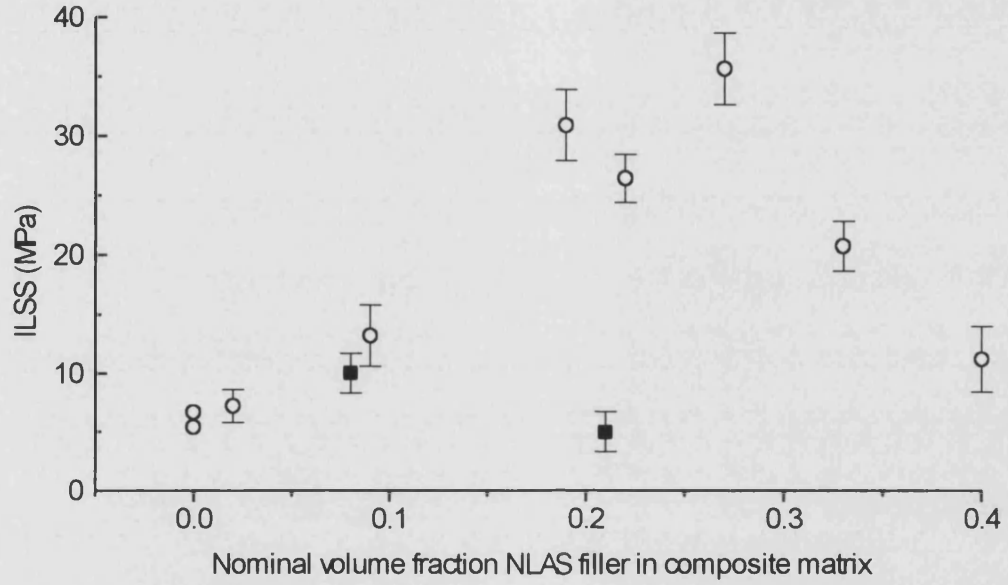

Figure 4.56 Variation of interlaminar shear strength with NLAS filler content in matrix.
○ : HT50-derived matrix. ■ : X30-derived.
The error bars indicate standard deviations.

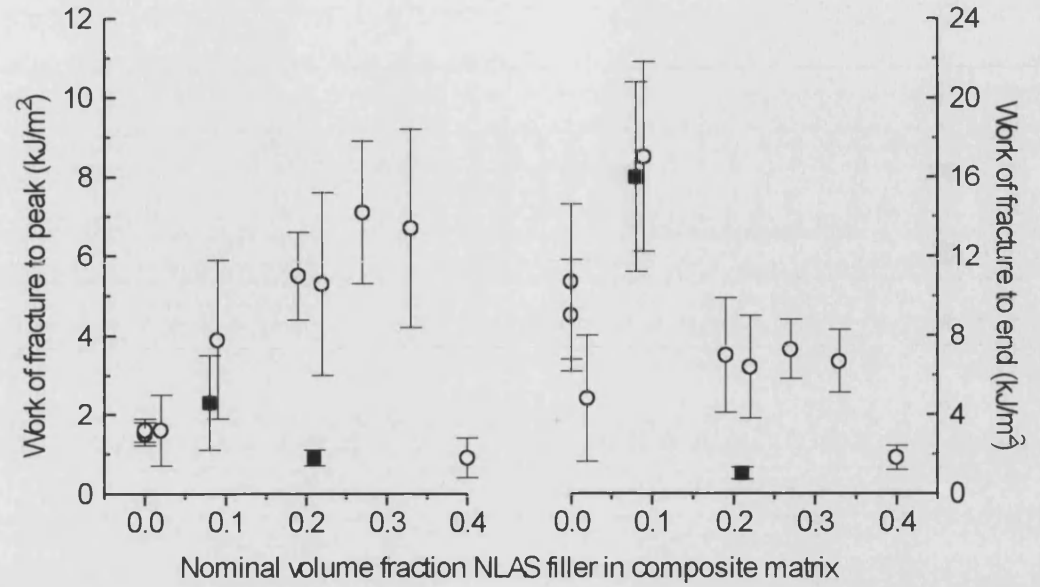

Figure 4.57 Variation of composite flexural work of fracture with NLAS filler content in matrix. ○ : HT50-derived matrix. ■ : X30-derived. The error bars indicate standard deviations.

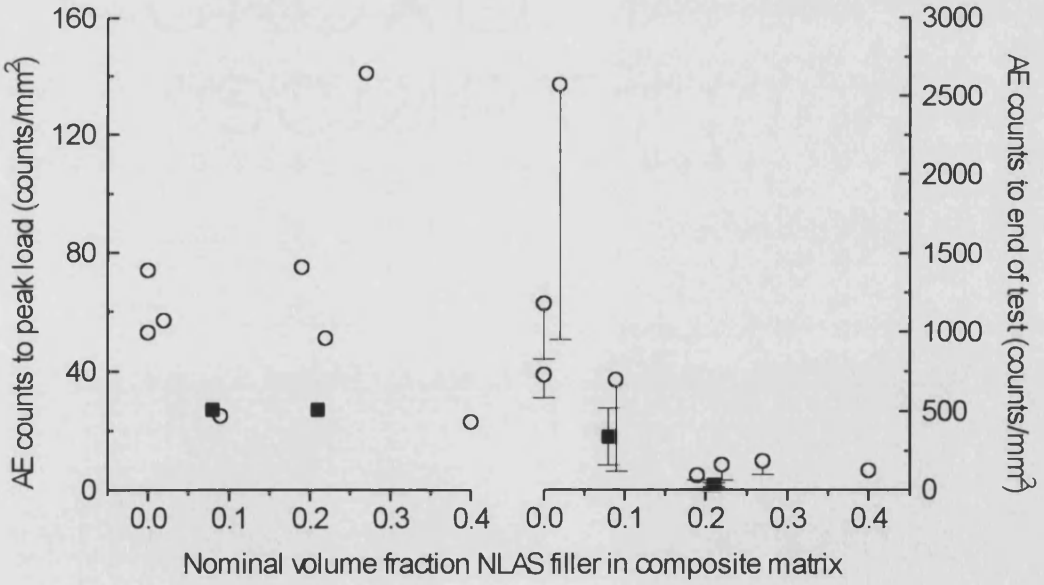

Figure 4.58 Variation of acoustic emission counts detected during flexural testing of composites with NLAS filler content in matrix. ○ : HT50-derived matrix; ■ : X30-derived. The error bars indicate standard deviations.

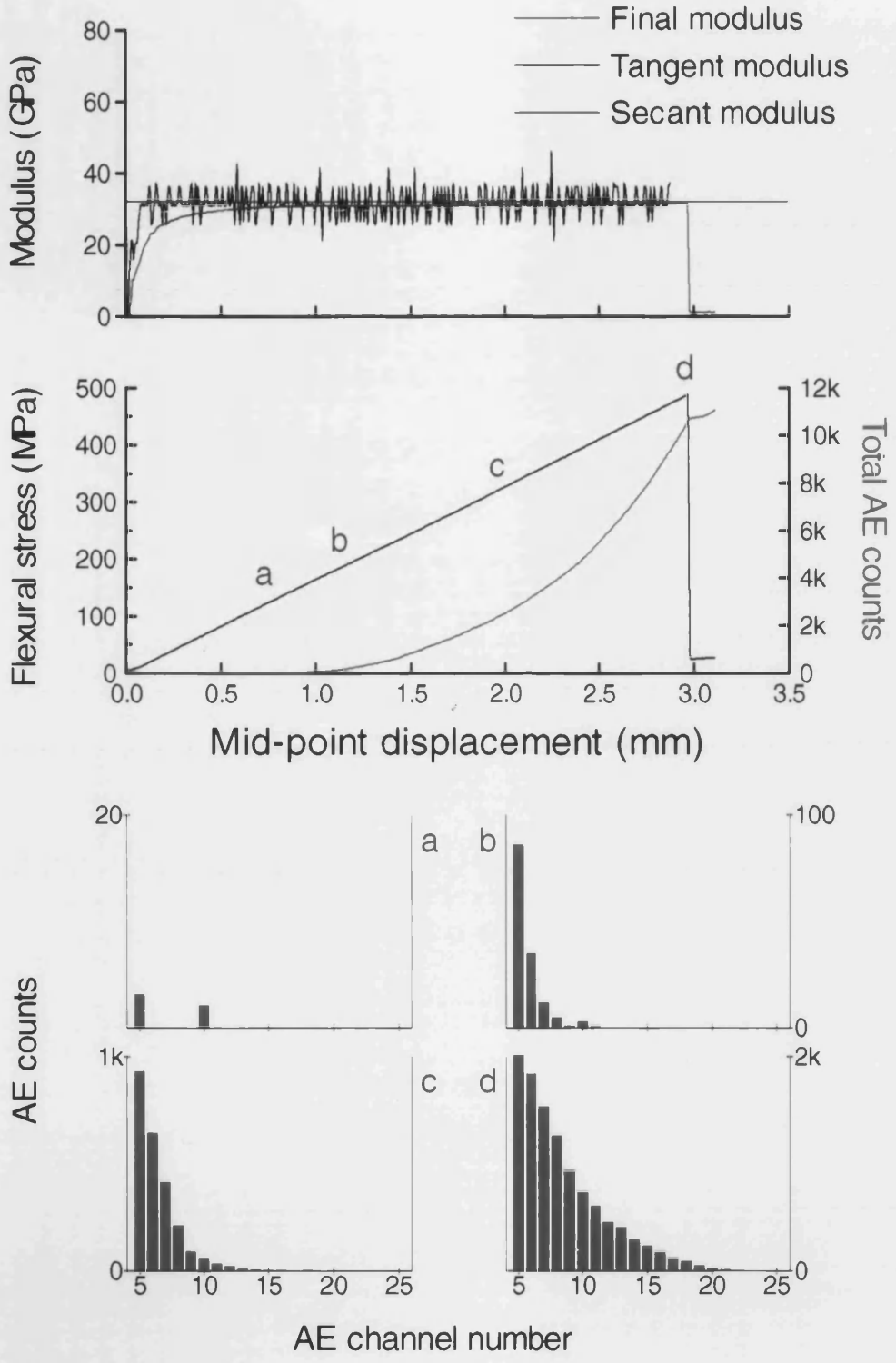

Figure 4.59 Typical flexural response of composite with HT50 / 0.19 V_{NLAS} matrix. *TOP*: Determination of elastic modulus; *MIDDLE*: force-displacement curve and total acoustic emission generation; *BOTTOM*: Acoustic emission amplitude distributions at displacements corresponding to points a,b,c and d.

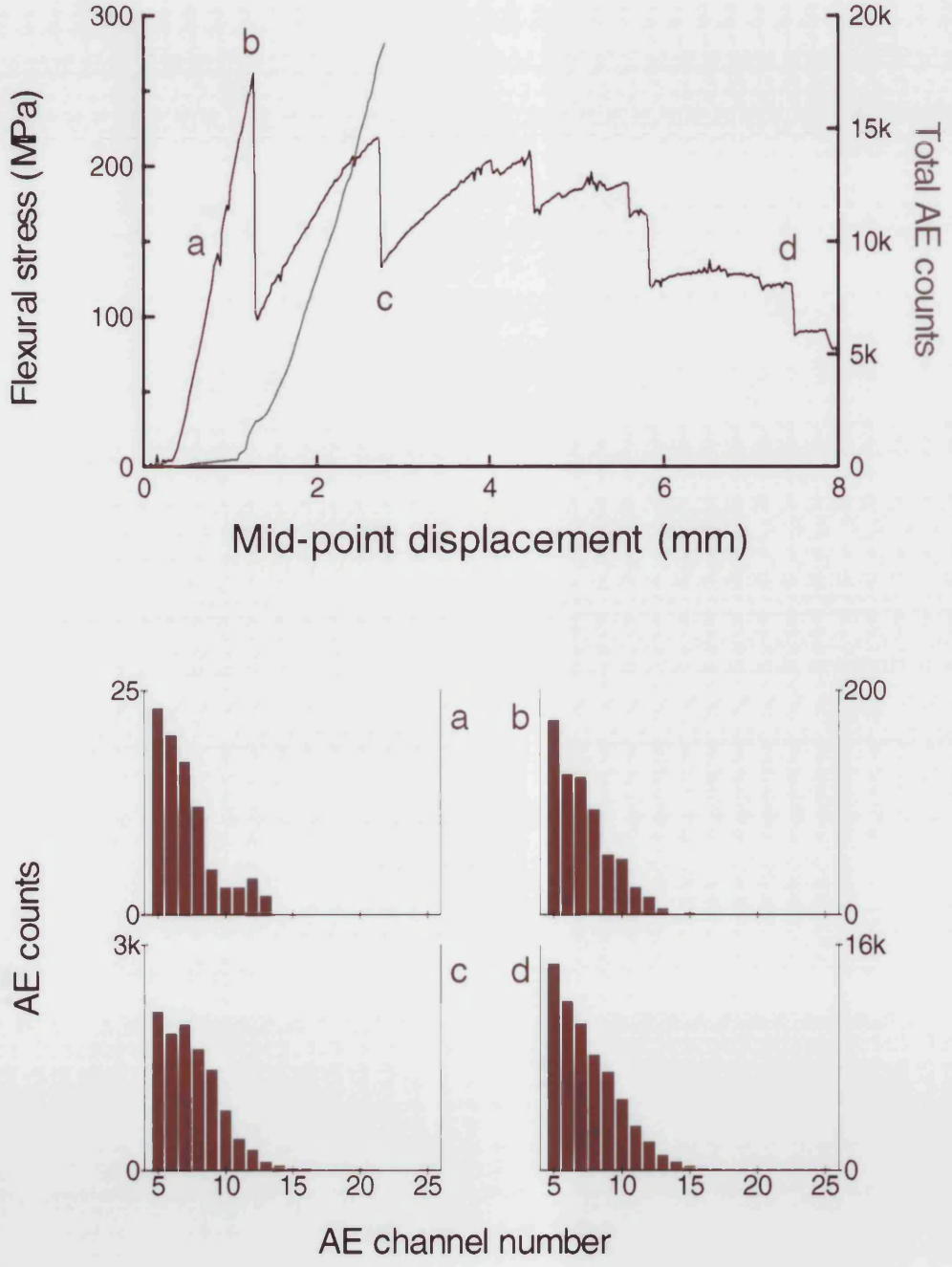

Figure 4.60 Typical flexural response of composite with HT50 / 0.09 V_{NLAS} matrix. *TOP*: Determination of elastic modulus; *MIDDLE*: force-displacement curve and total acoustic emission generation; *BOTTOM*: Acoustic emission amplitude distributions at displacements corresponding to points a,b,c and d.

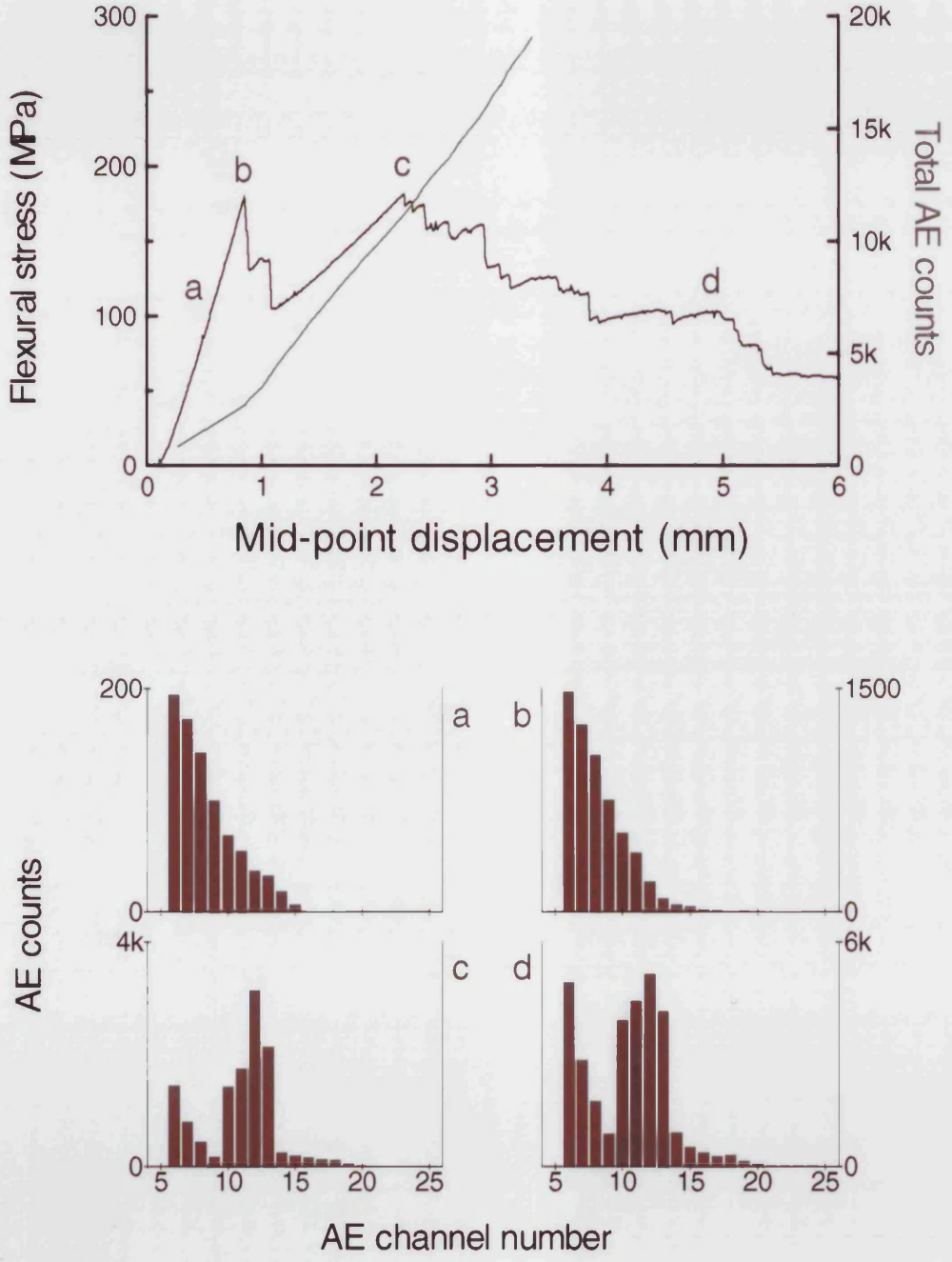

Figure 4.61 Typical flexural response of composite with unfilled HT50 matrix. *TOP*: Determination of elastic modulus; *MIDDLE*: force-displacement curve and total acoustic emission generation; *BOTTOM*: Acoustic emission amplitude distributions at displacements corresponding to points a,b,c and d.

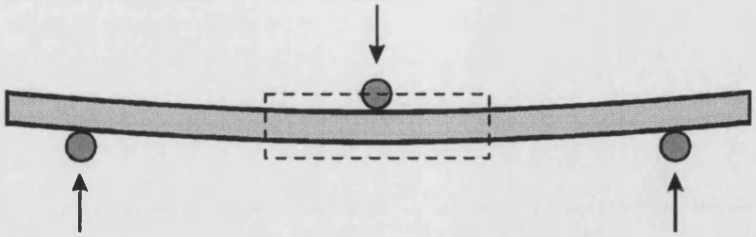

mode 1

- partial delaminating on tensile side of specimen
- large load drops on force-displacement curve
- no evidence of compressive damage

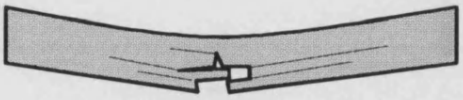

mode 2

- extensive delaminating throughout entire specimen
- many small load drops on force-displacement curve
- limited compressive damage (esp. fibre buckling)

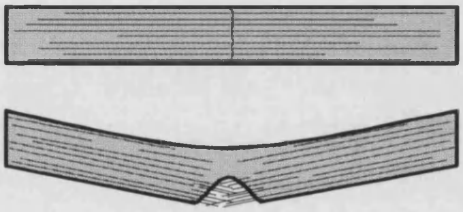

mode 3

- brittle
- no delaminating
- no compressive damage

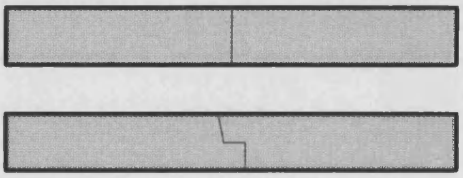

Figure 4.62 Schematic diagrams of the principal flexural damage modes which were observed in carbon-fibre-reinforced silica and silica/NLAS composites. These idealised representations summarise the main features which were observed, although categorising individual specimens was frequently difficult.

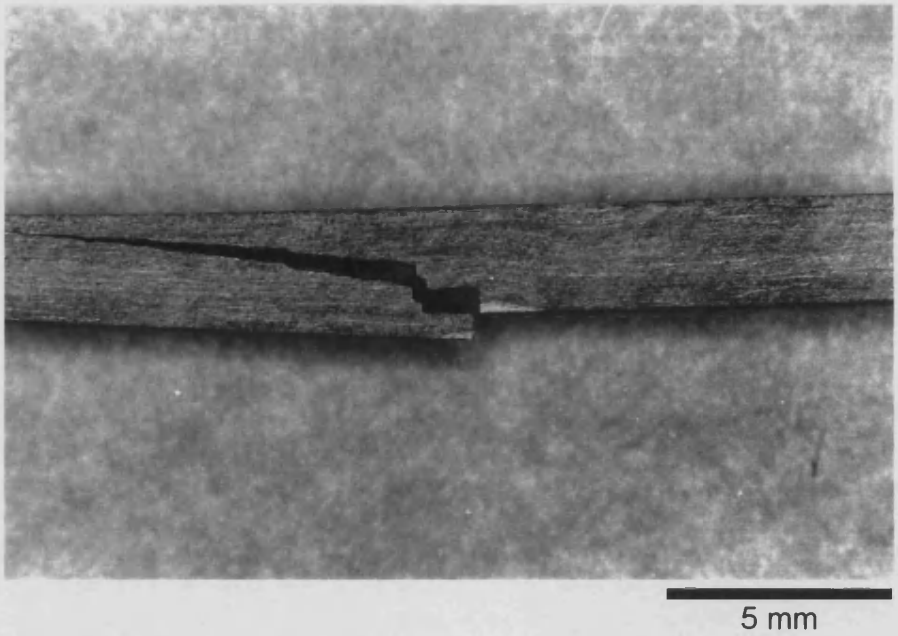

Figure 4.63 Brittle failure mode in flexural sample with matrix composition HT50 / 0.27 V_{NLAS}

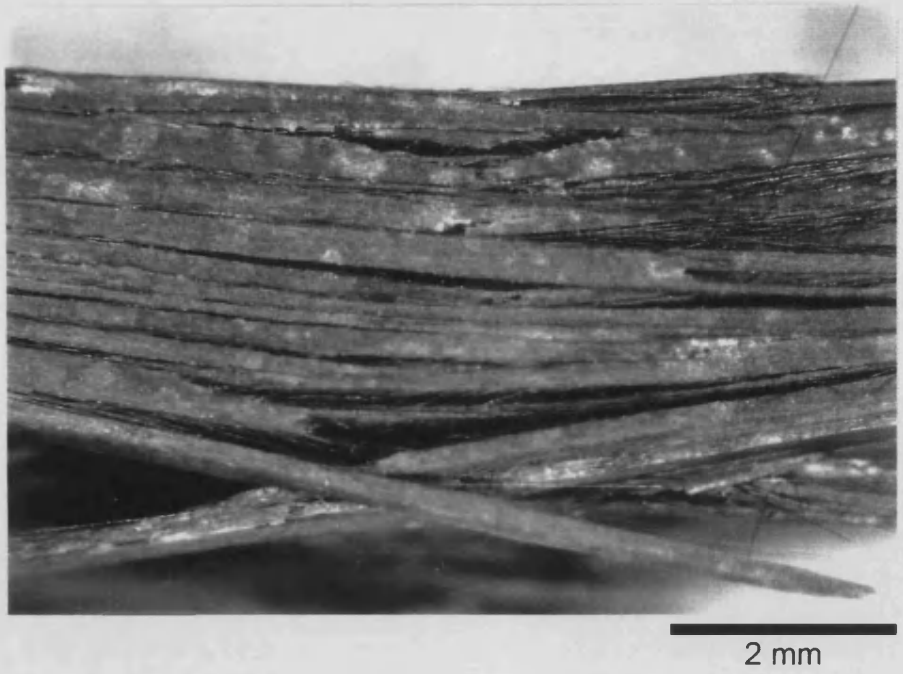

Figure 4.64 Extensive delamination in flexural sample with matrix composition HT50 / 0.02 V_{NLAS}.

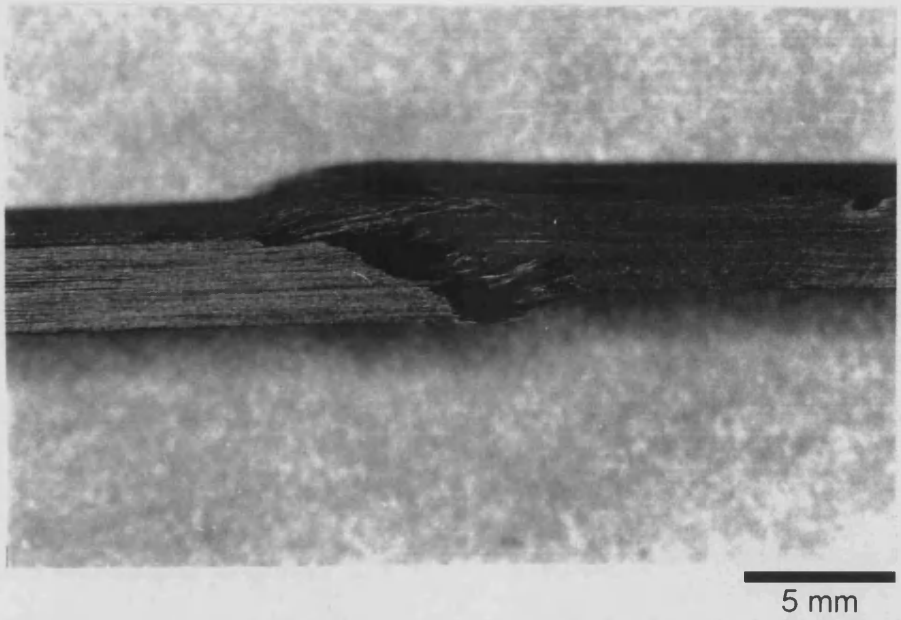

Figure 4.65 Side view of flexural sample with unfilled HT50 matrix showing extensive compression damage (bottom of picture).

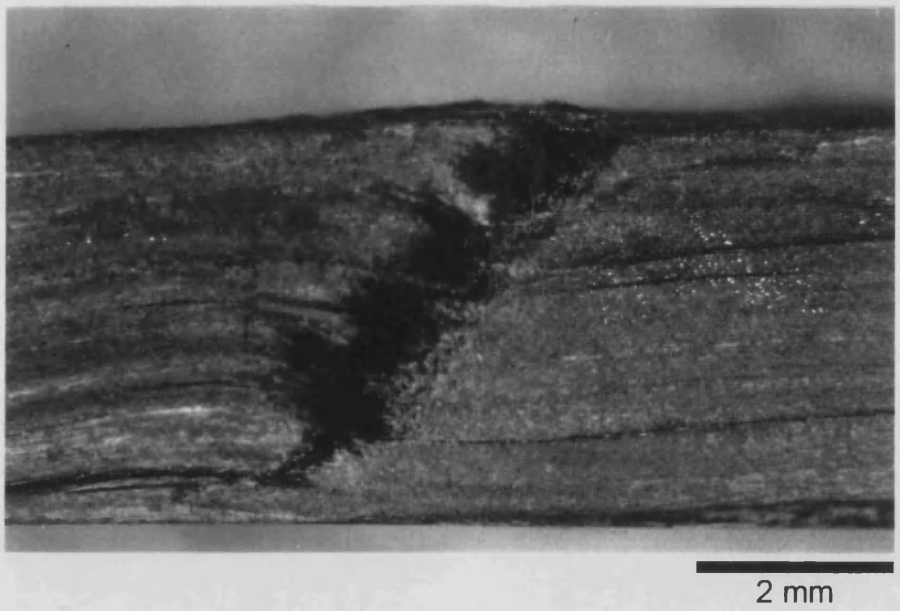

Figure 4.66 Detail of compression damage on the compressive face of a flexural sample with matrix composition X30 / 0.08 V_{NLAS}.

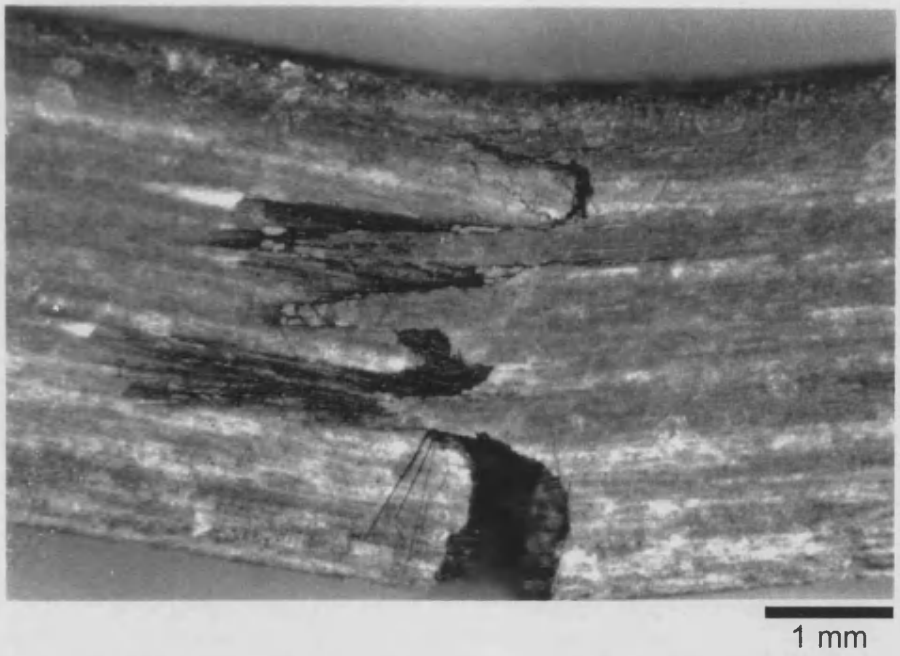

Figure 4.67 Partial interlocking of delaminated planes in flexural sample with matrix composition HT50 / 0.09 V_{NLAS}

Figure 4.68 Extensive interlocking of delaminated planes in flexural sample with matrix composition HT50 / 0.09 V_{NLAS}

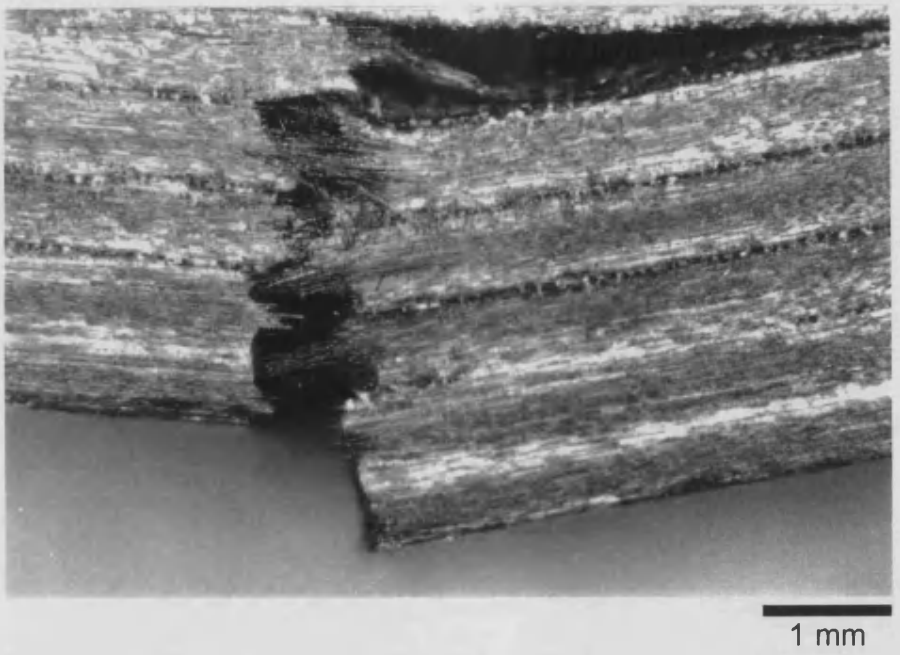

Figure 4.69 Fibre bridging and shear damage in flexural sample with matrix composition HT50 / 0.02 V_{NLAS}

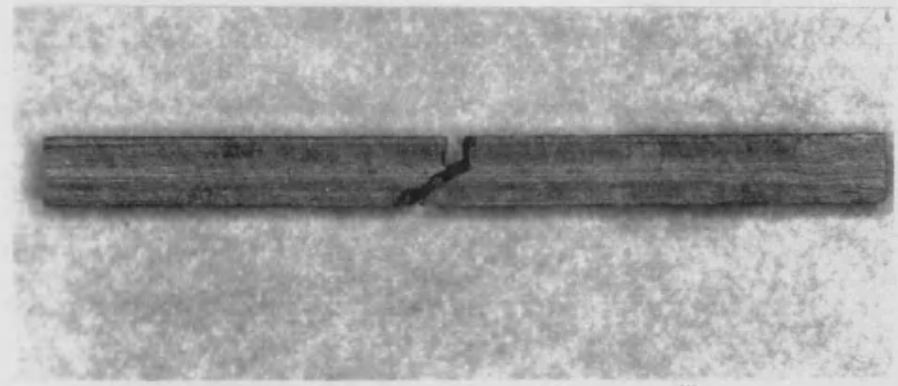

(i)

(ii)

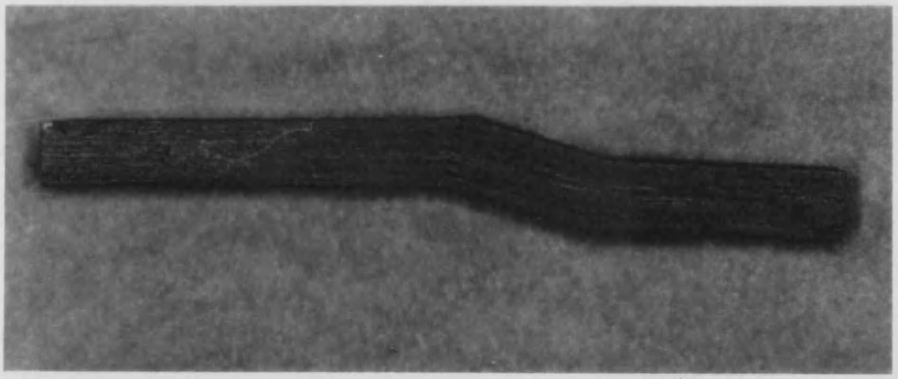

(iii)

Figure 4.70 Failure modes in interlaminar shear specimens.

(i) Brittle

(ii) Delaminating

(iii) Kinking

Figure 4.71 Brittle fracture surface in flexural specimen with matrix composition HT50 / 0.27 V_{NLAS} . Note the absence of any fibre pullout.

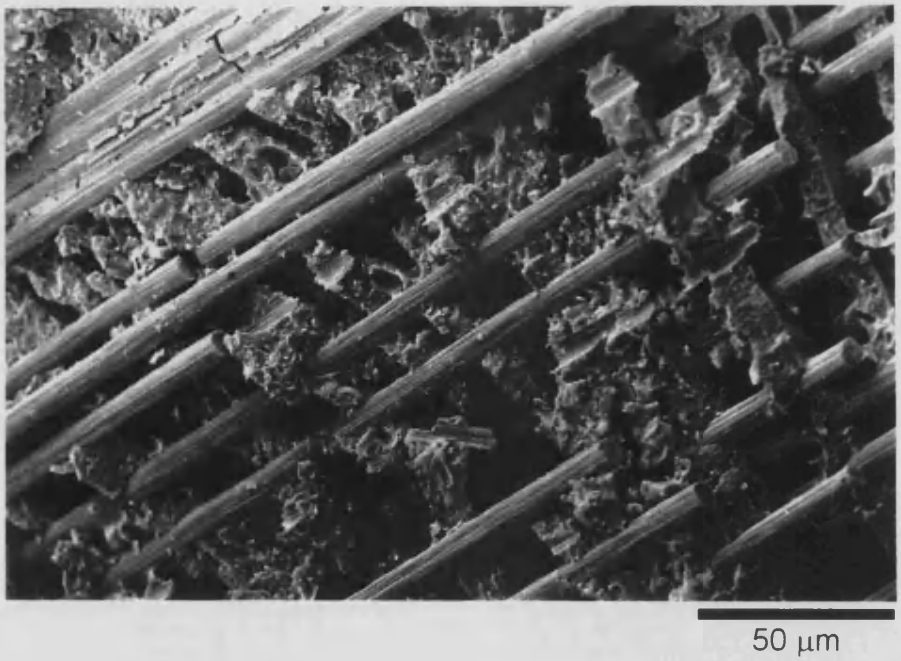

Figure 4.72 View of a delaminated plane taken from the tensile side of a flexural specimen with matrix composition HT50 / 0.09 V_{NLAS}. The plane is orientation is 'c' in the notation of figure 3.4.

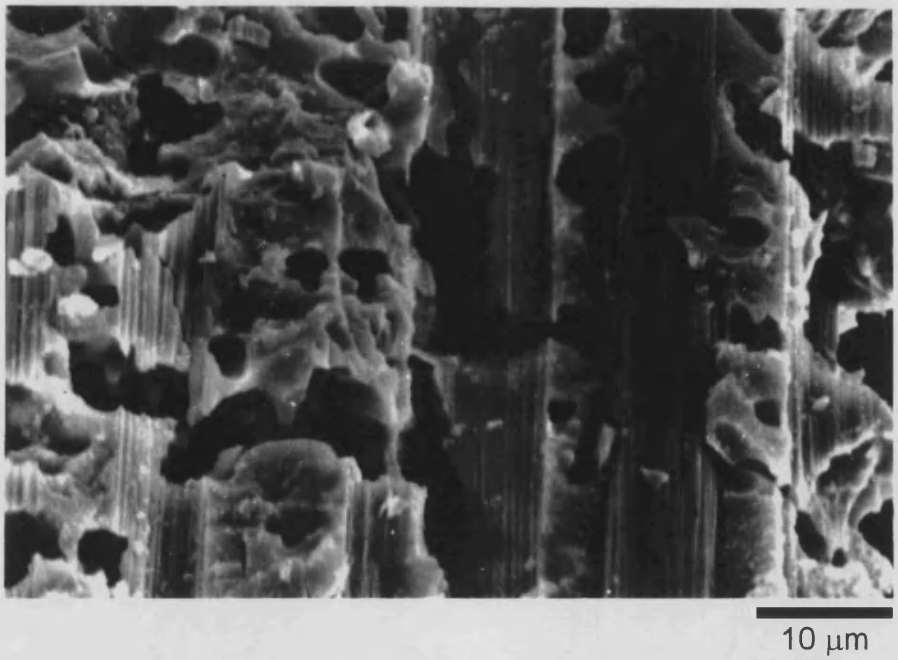

Figure 4.73 View of a delaminated plane taken from the central region of a flexural specimen with matrix composition HT50 / 0.09 V_{NLAS}. The plane is orientation is 'c' in the notation of figure 3.4.

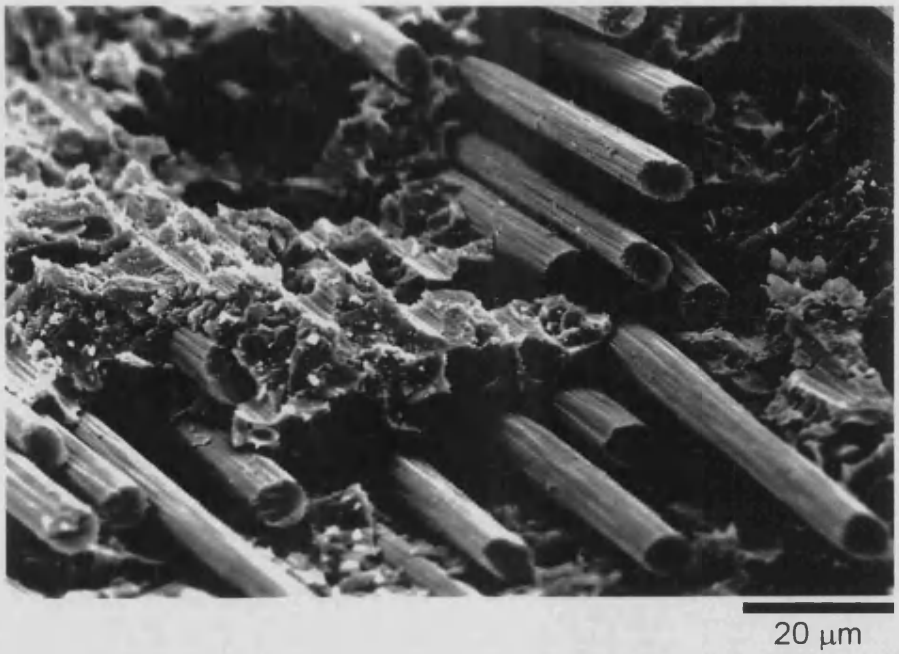

Figure 4.74 Where fibre-matrix bond strength was locally high, tearing of matrix and fibre clumps occurred within laminae apparently subject to tensile loads. This example is taken from the tensile side of a flexural specimen with matrix composition HT50 / 0.09 V_{NLAS}.

Figure 4.75 Parallel planes of material were observed to have become detached within separated laminae in flexural specimens. This example is from a specimen with matrix composition X30 / 0.08 V_{NLAS}.

Figure 4.76 View of flexural damage in a specimen with matrix composition HT50 / 0.22 V_{NLAS} demonstrating limited fibre bridging and fibre pullout in an individual lamina apparently subject to tensile loads.

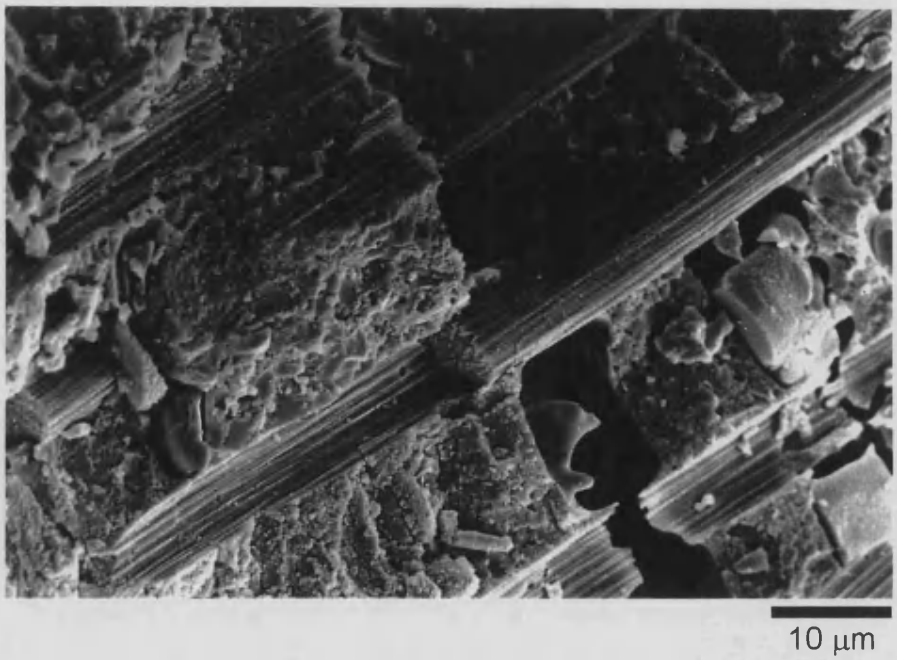

Figure 4.77 Direct evidence of crack bridging and fibre pullout in a flexural specimen with matrix composition HT50 / 0.09 V_{NLAS}. Note that the fibre appears to be constrained by the matrix.

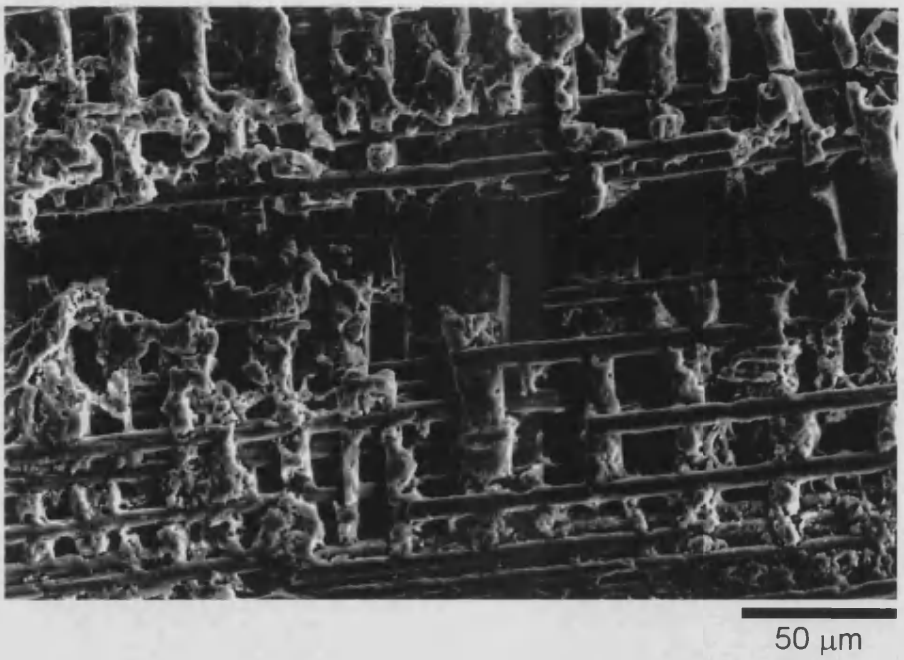

Figure 4.78 Example of a delamination crack in a highly porous (uninfiltrated) region of a flexural specimen with matrix composition X30 / 0.08 V_{NLAS}.

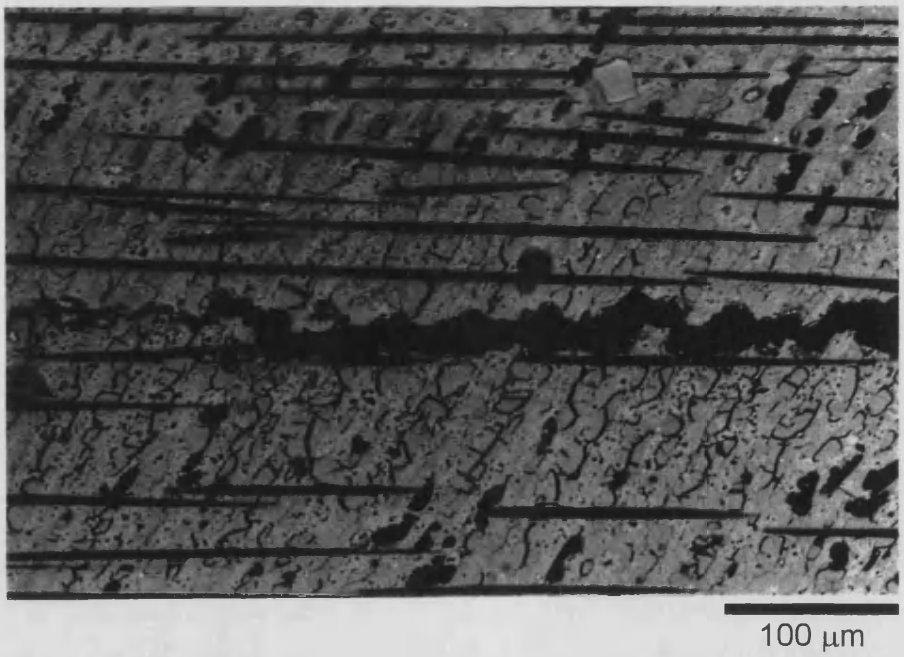

Figure 4.79 The form of matrix cracking described in figure 4.bx was unaffcctcd by the presence of infiltrated porosity. The matrix composition of this flexural specimen was HT50 / 0.19 V_{NLAS}.

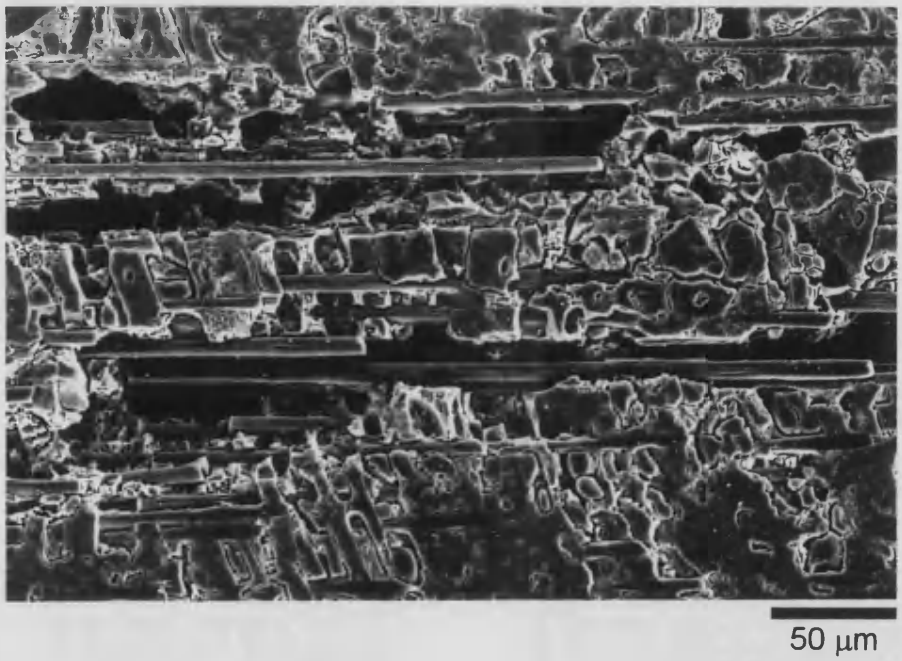

Figure 4.80 Intersection of delamination cracks in a flexural specimen with matrix composition X30 / 0.08 V_{NLAS}.

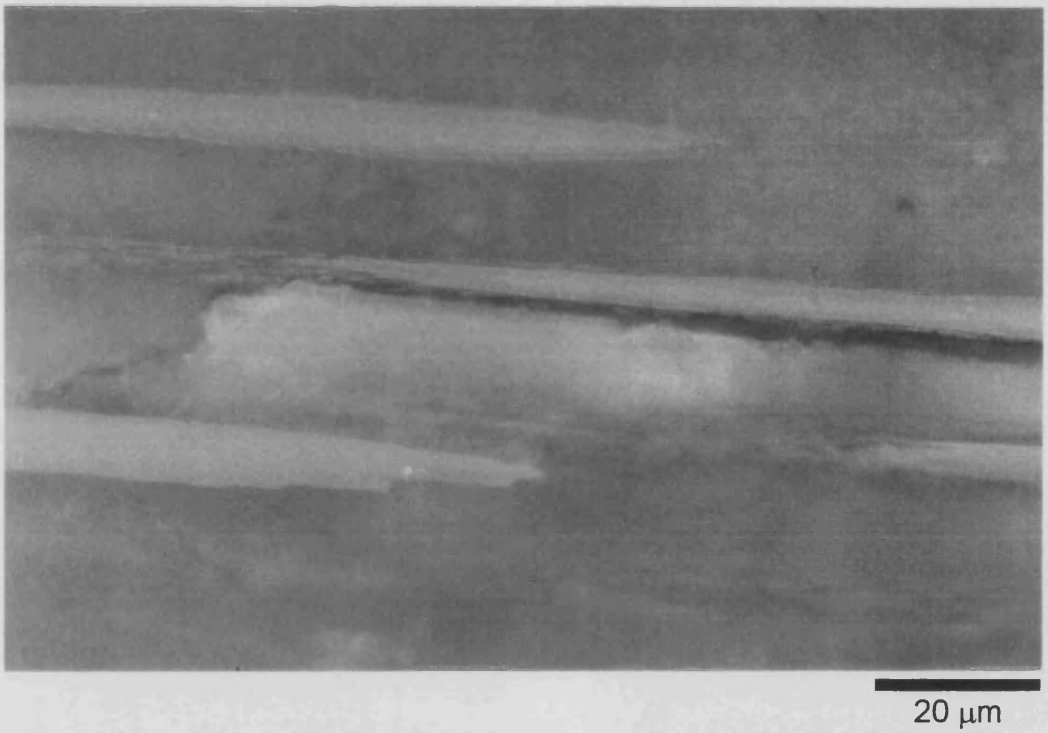

Figure 4.81 Optical (DIC) micrograph of damage in a flexural specimen with matrix composition HT50 / 0.22 V_{NLAS}. Note that the interface between bright and dull regions (*e.g.* see figures 4.36 and 4.37) provides a preferred path for matrix cracking.

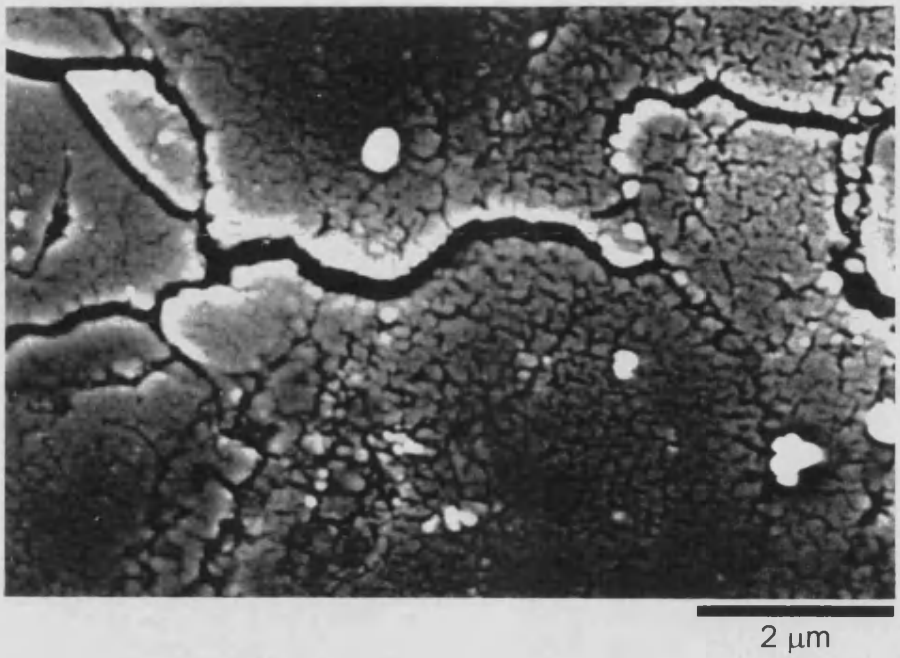

Figure 4.82 Matrix cracking in a matrix-rich interlaminar region in a flexural specimen with matrix composition X30 / 0.08 V_{NLAS}.

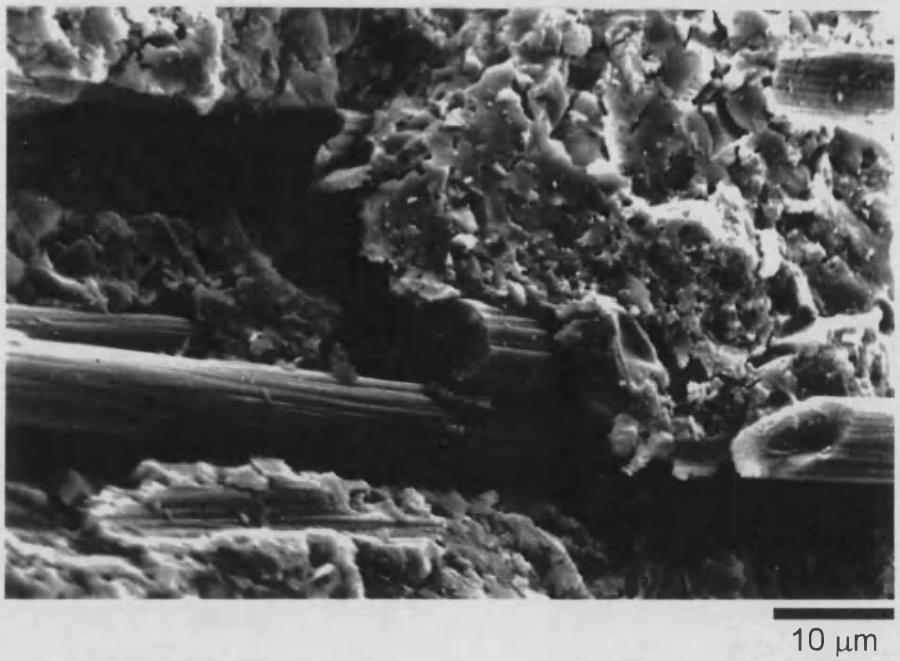

Figure 4.83 Intersection of two sliding laminae in the central region of a flexural specimen with matrix composition HT50 / 0.22 V_{NLAS}.

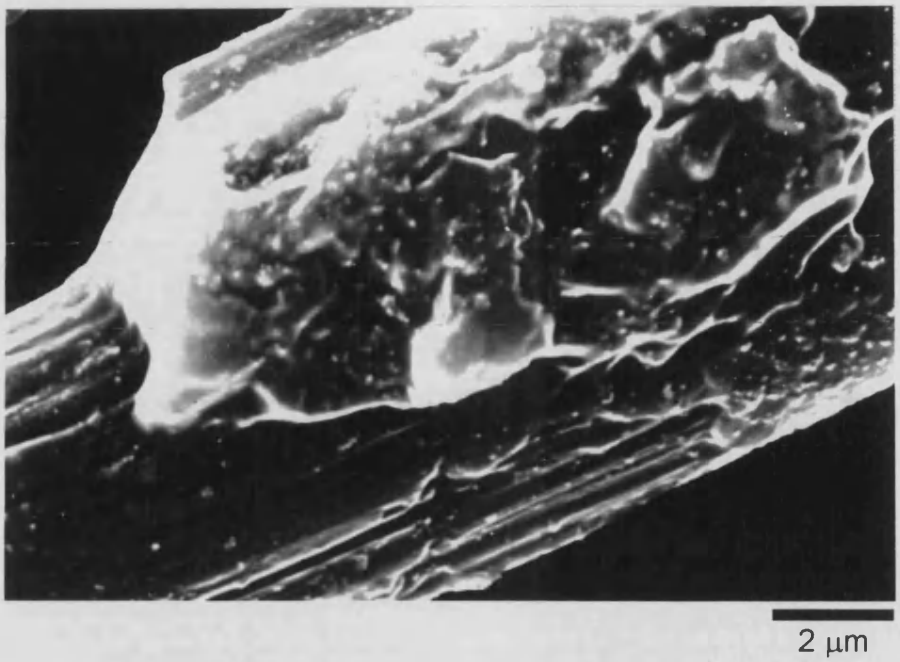

Figure 4.84 Matrix material adhering to a fibre in a flexural specimen with matrix composition HT50 / 0.22 V_{NLAS}.

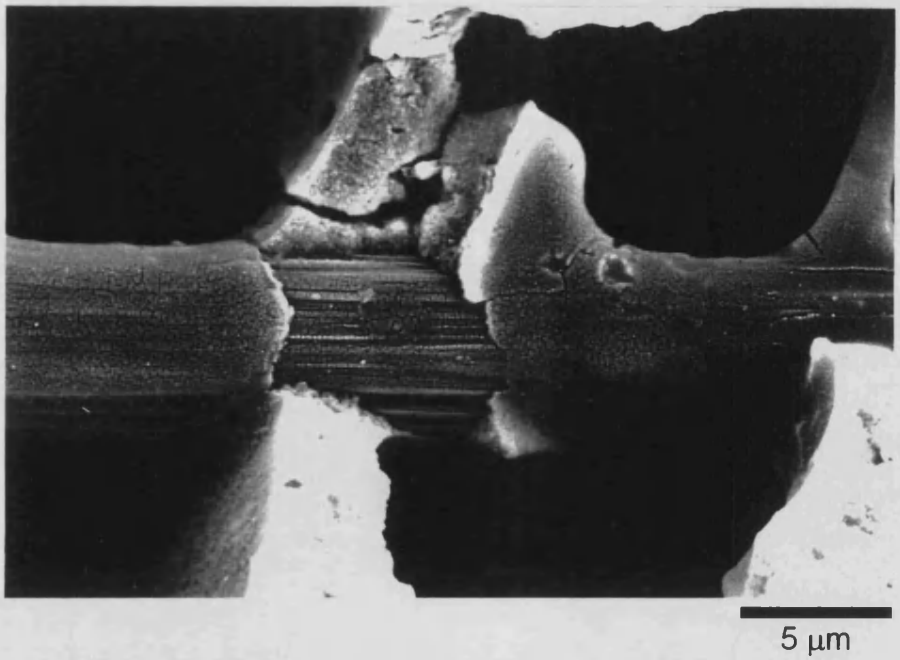

Figure 4.85 Evidence that strong fibre-matrix bonding encouraged intra-matrix fracture (rather than fibre-matrix separation) in a flexural specimen with matrix composition HT50 / 0.09 V_{NLAS}.

Figure 4.86 Evidence that strong fibre-matrix bonding encouraged matrix tearing in an interlaminar shear plane of a flexural specimen with matrix composition HT50 / 0.22 V_{NLAS}.

Figure 4.87 Strong fibre-matrix bonding caused widespread matrix damage as clumps of matrix material were sheared between intact planes moving in opposite directions. This example is taken from central region of a flexural specimen with matrix composition X30 / 0.08 V_{NLAS}.

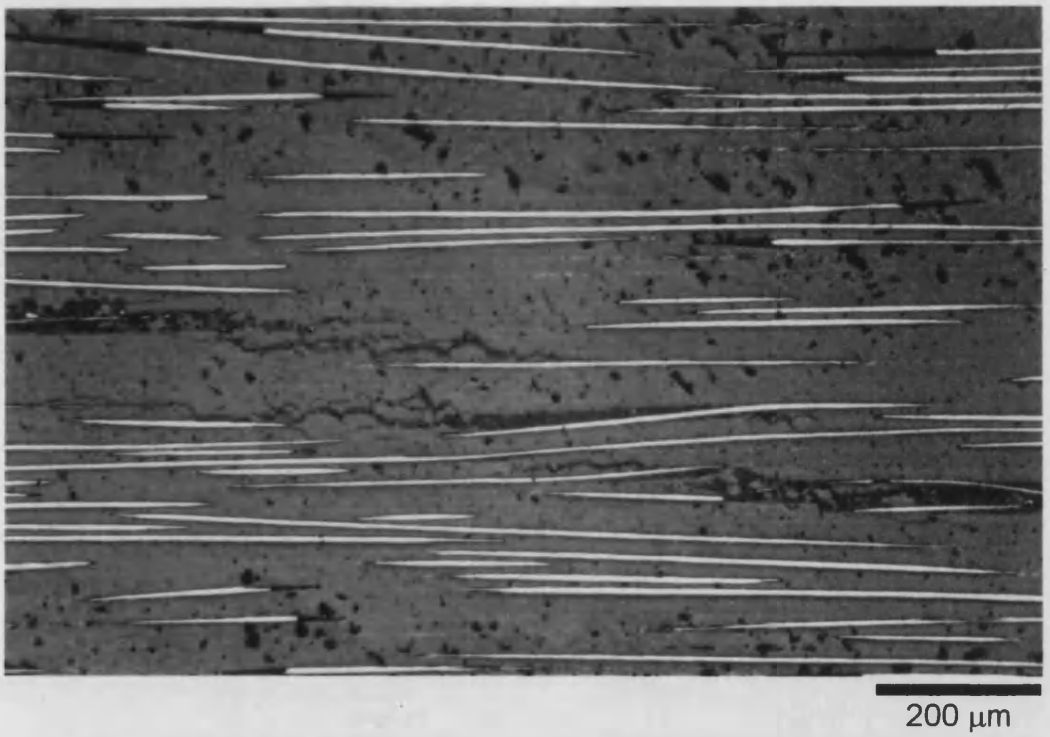

Figure 4.88 Optical micrograph showing a delamination plane of a flexural specimen with matrix composition HT50 / 0.19 V_{NLAS}. Fibres kink as they bridge the growing interlaminar cracks.

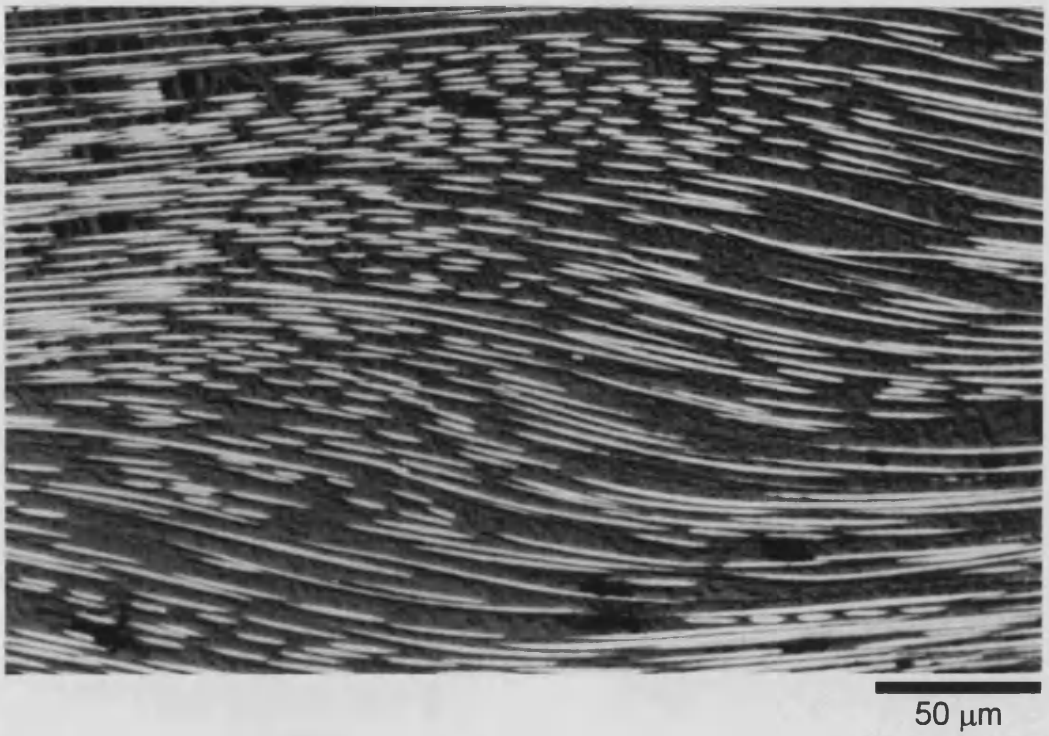

Figure 4.89 Optical micrograph showing extensive fibre kinking in the compression region of a flexural specimen with matrix composition HT50 / 0.09 V_{NLAS}.

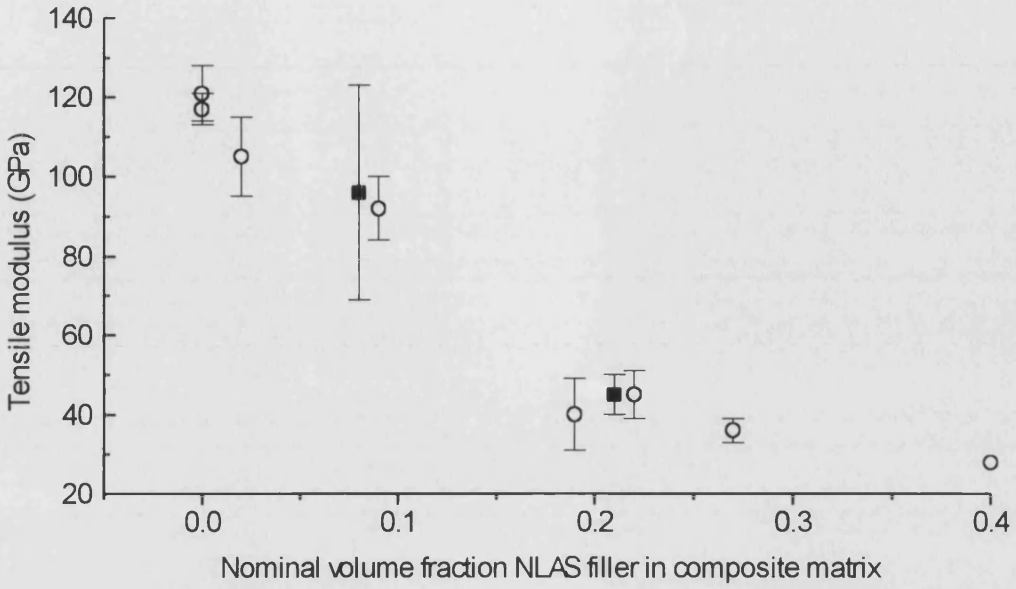

Figure 4.90 Variation of tensile elastic modulus with NLAS filler content in matrix.
○ : HT50-derived matrix. ■ : X30-derived.
The error bars indicate standard deviations.

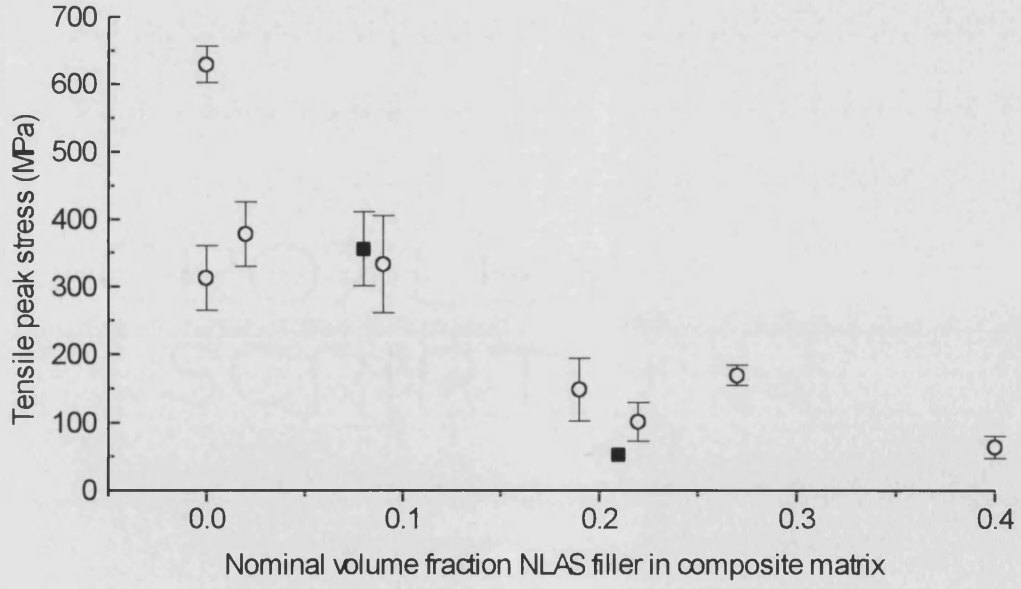

Figure 4.91 Variation of tensile peak stress with NLAS filler content in matrix.
○ : HT50-derived matrix. ■ : X30-derived.
The error bars indicate standard deviations.

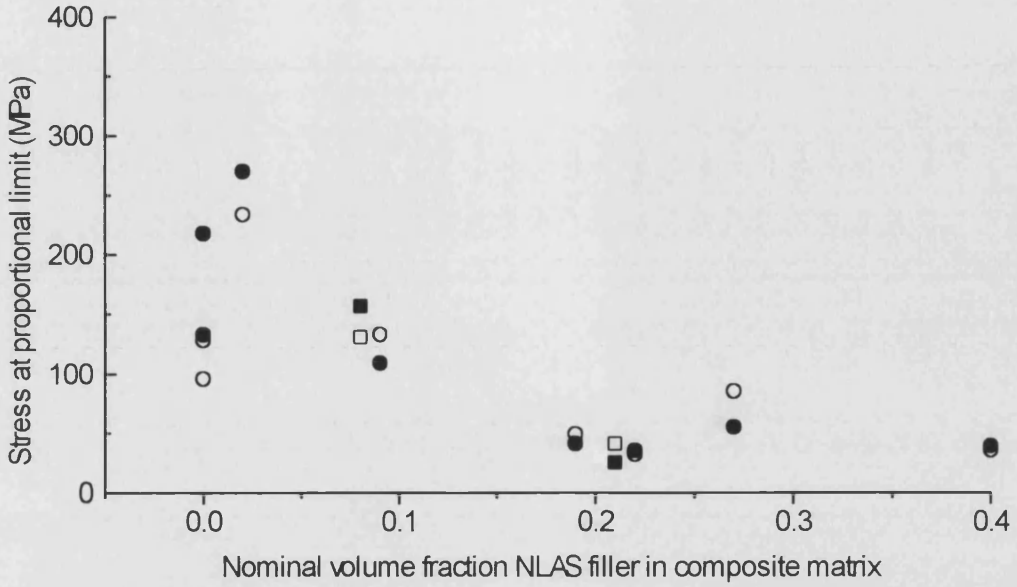

Figure 4.92 Variation of tensile proportional limit stress with NLAS filler content in matrix. ○,● : HT50-derived matrix. □,■ : X30-derived. Proportional limits were discerned from mechanical data (open symbols) and from acoustic emission response (closed symbols).

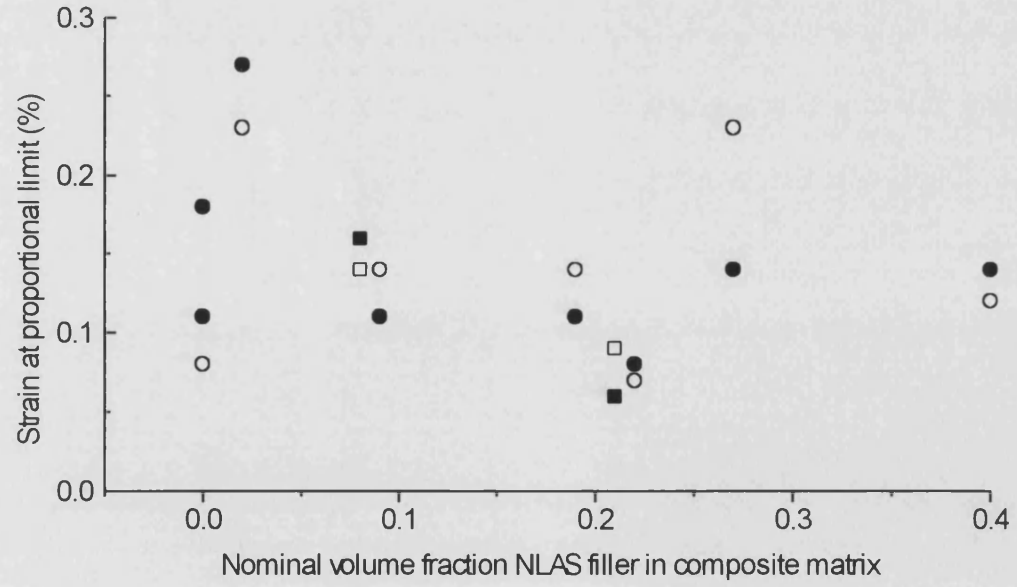

Figure 4.93 Variation of tensile proportional limit strain with NLAS filler content in matrix. ○,● : HT50-derived matrix. □,■ : X30-derived. Proportional limits were discerned from mechanical data (open symbols) and from acoustic emission response (closed symbols).

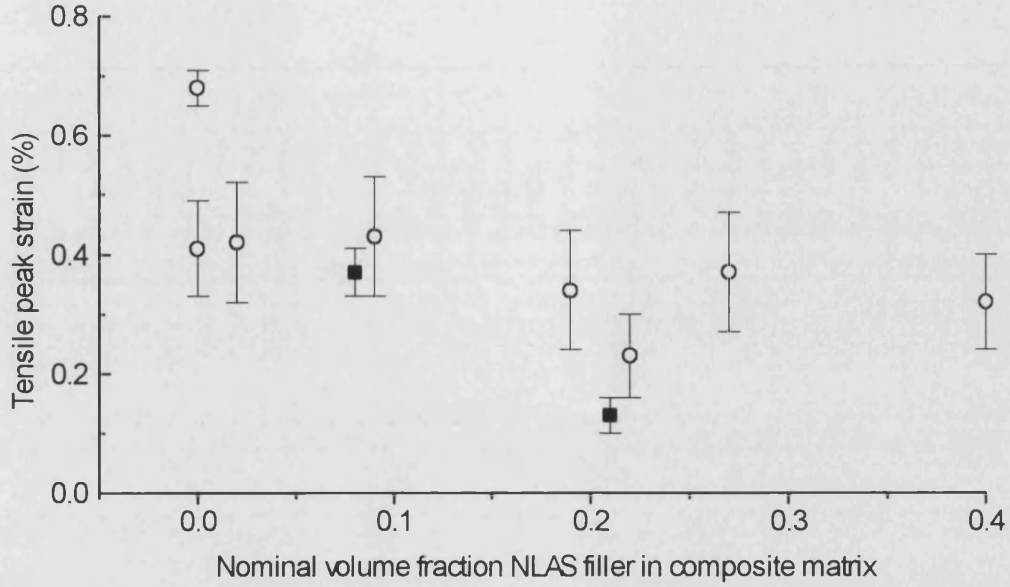

Figure 4.94 Variation of tensile peak strain with NLAS filler content in matrix.
○ : HT50-derived matrix. ■ : X30-derived.
The error bars indicate standard deviations.

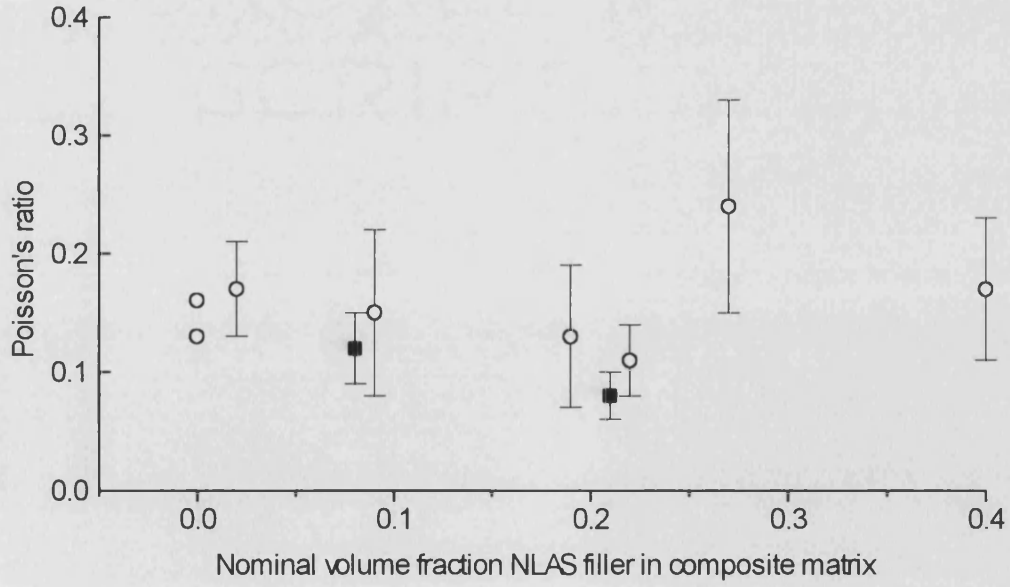

Figure 4.95 Variation of tensile Poisson's ratio with NLAS filler content in matrix.
○ : HT50-derived matrix. ■ : X30-derived.
The error bars indicate standard deviations.

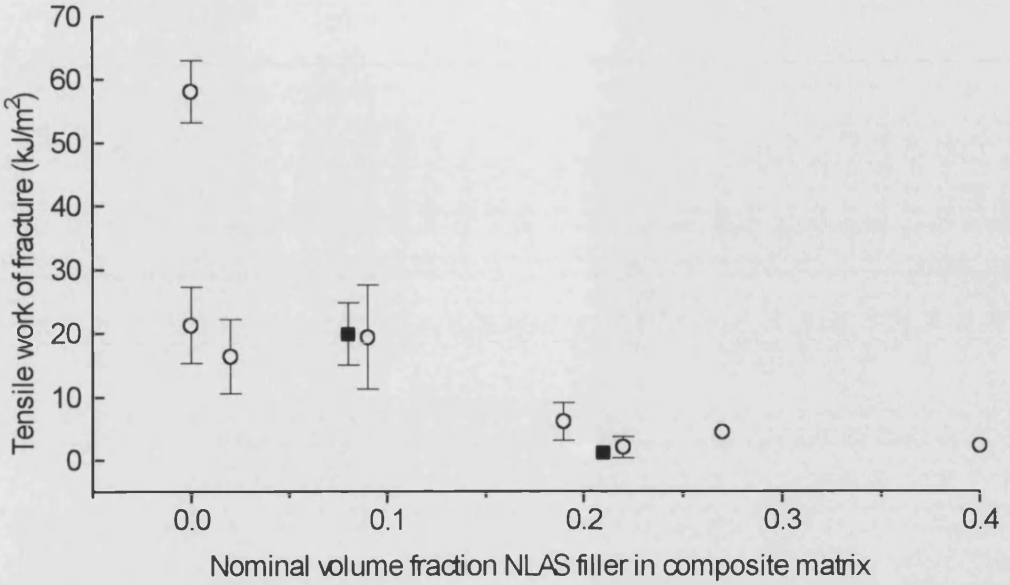

Figure 4.96 Variation of tensile work of fracture with NLAS filler content in matrix. Integrated stress-strain data are normalised with respect to 2 x specimen cross-sectional area. The error bars indicate standard deviations.

○ : HT50-derived matrix. ■ : X30-derived.

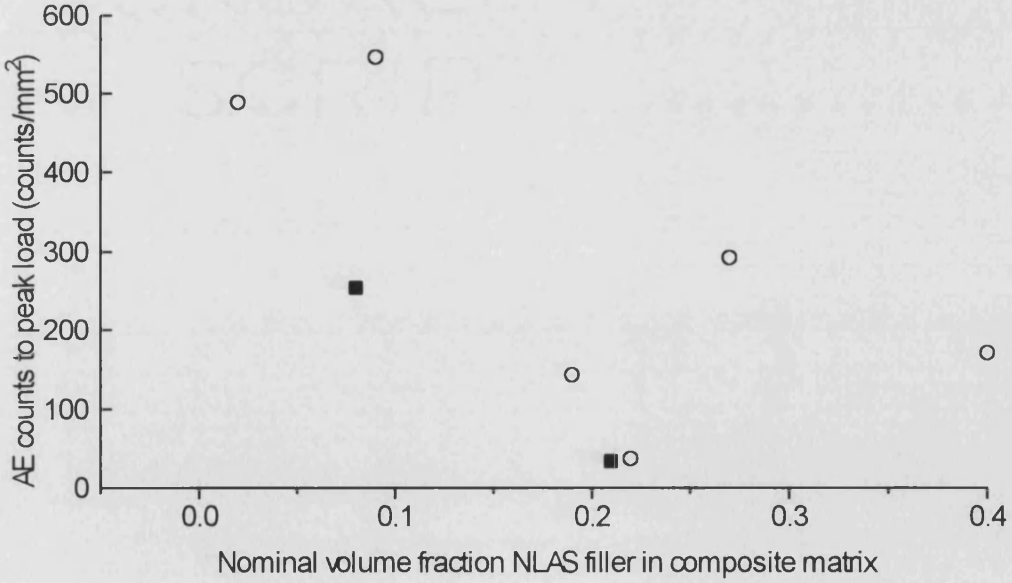

Figure 4.97 Variation of acoustic emission generated during tensile testing of composites with NLAS filler content in matrix.

○ : HT50-derived matrix. ■ : X30-derived.

The error bars indicate standard deviations.

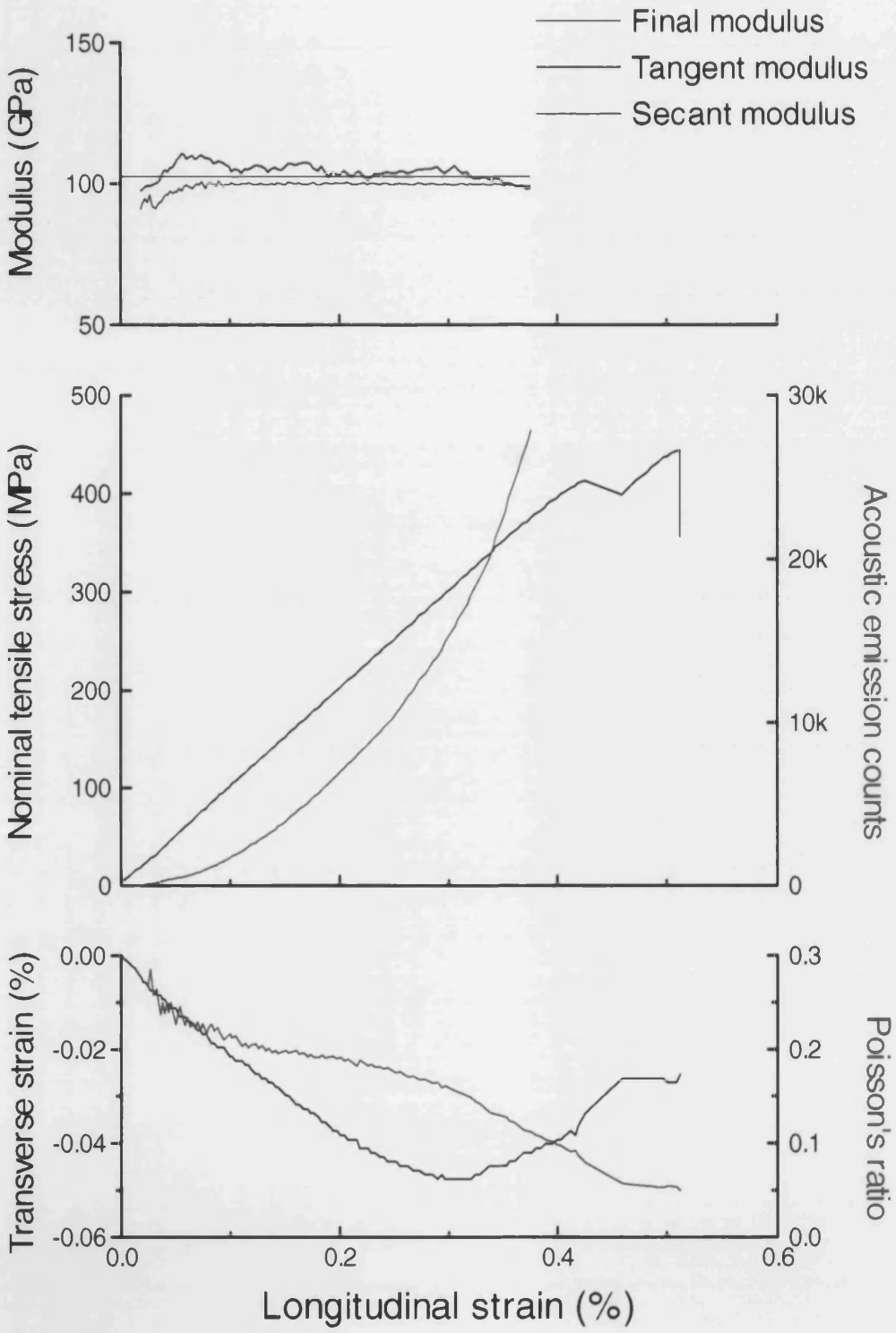

Figure 4.98 Typical tensile response of composite with HT50 / 0.02 V_{NLAS} matrix. *TOP*: Determination of elastic modulus; *MIDDLE*: $\sigma - \varepsilon$ curve and acoustic emission generation; *BOTTOM*: Transverse response and determination of Poisson's ratio.

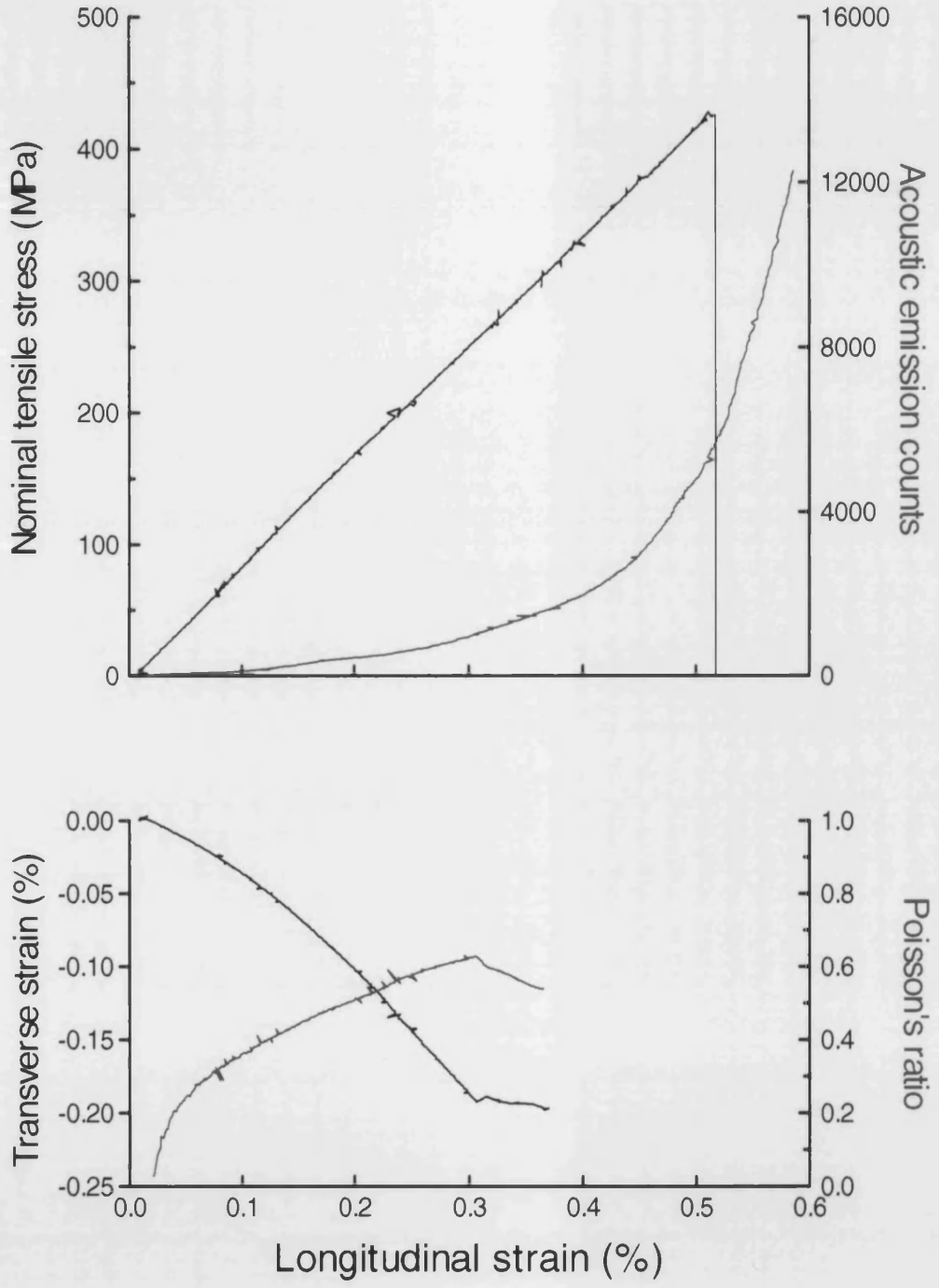

Figure 4.99 Typical tensile response of composite with HT50 / 0.09 V_{NLAS} matrix.

TOP: $\sigma - \varepsilon$ curve and acoustic emission generation;

BOTTOM: Transverse response and determination of Poisson's ratio.

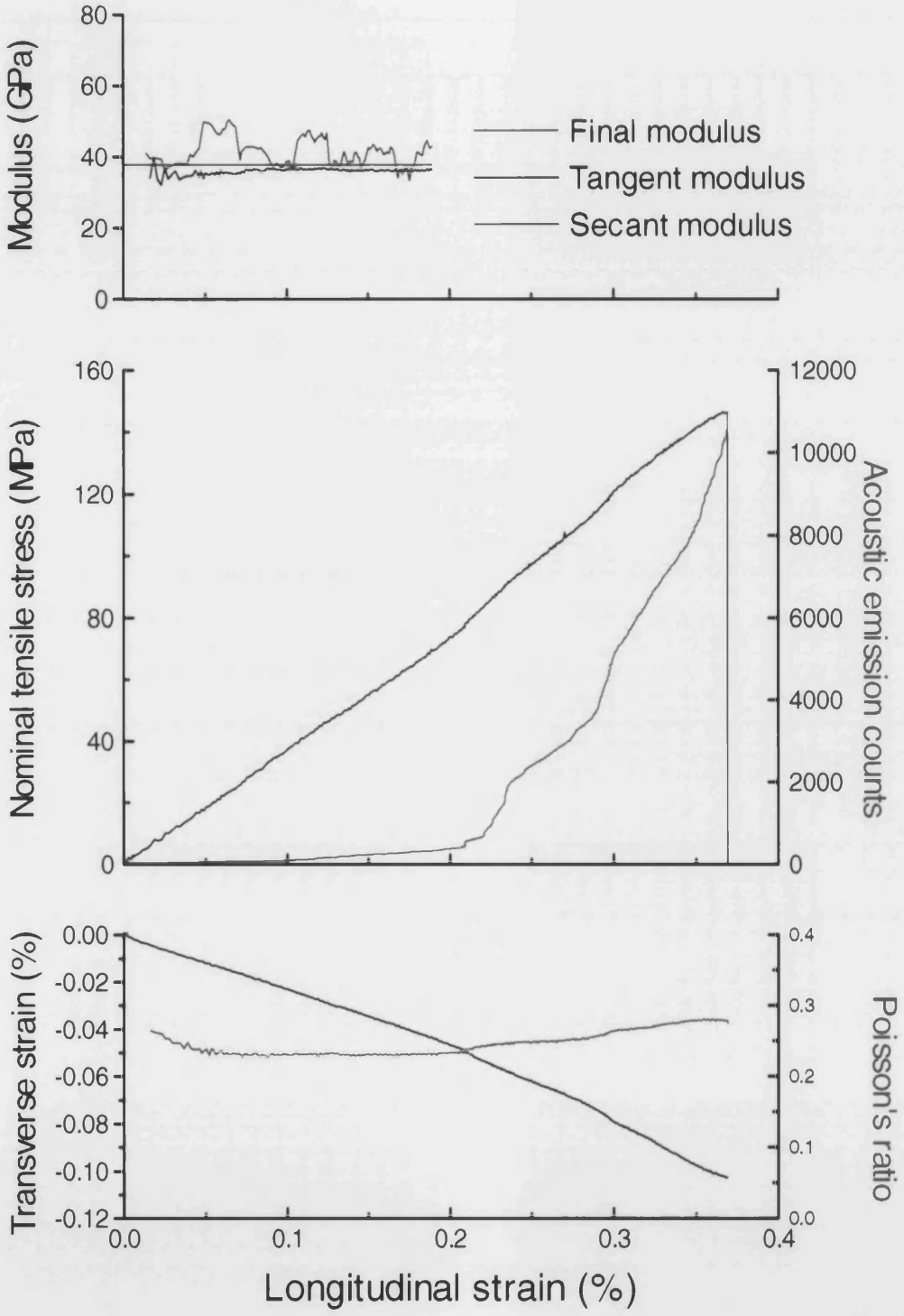

Figure 4.100 Typical tensile response of composite with HT50 / 0.27 V_{NLAS} matrix. *TOP*: Determination of elastic modulus; MIDDLE: σ - ε curve and acoustic emission generation; *BOTTOM*: Transverse response and determination of Poisson's ratio.

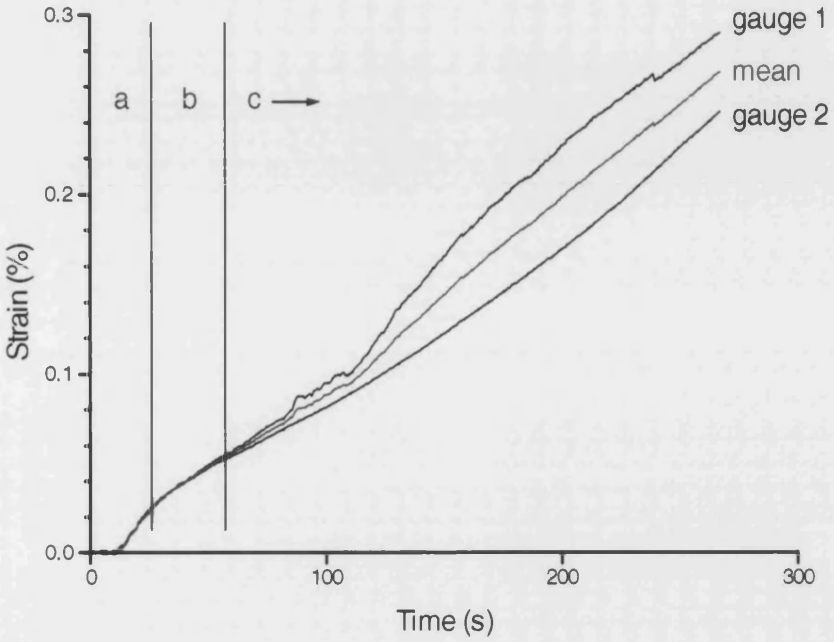

Figure 4.101 Typical strain gauge outputs from opposite specimen faces during a tensile test. Region 'a' corresponds to the 'bedding in' zone of the test during which the apparatus grips become embedded into the specimen's aluminium end tabs. Elastic moduli and Poisson's ratios are determined from region 'b' which corresponds to the linear region of the stress-strain curve. Note that the strain gauge outputs coincide over this range. Permanent damage accumulates within region 'c' and final failure occurs at around 260 seconds. The measured strains differ within region 'c' which indicates that damage occurs non-uniformly through the specimen.

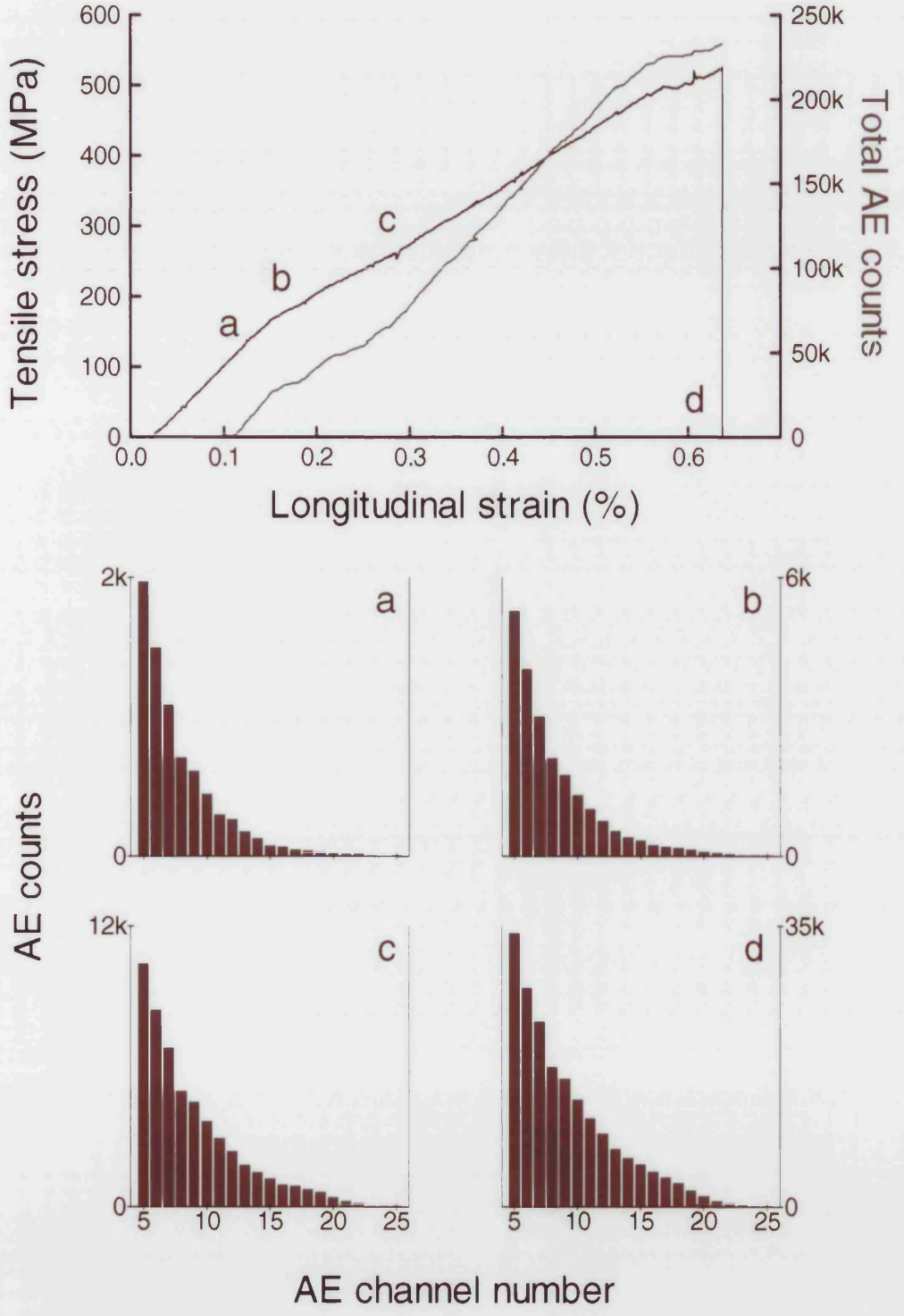

Figure 4.102 Typical tensile response of composite with unfilled HT50 matrix.
TOP: $\sigma - \varepsilon$ curve and total acoustic emission counts;
BOTTOM: Acoustic emission amplitude distributions at strains corresponding to points a,b,c and d in the top graph.

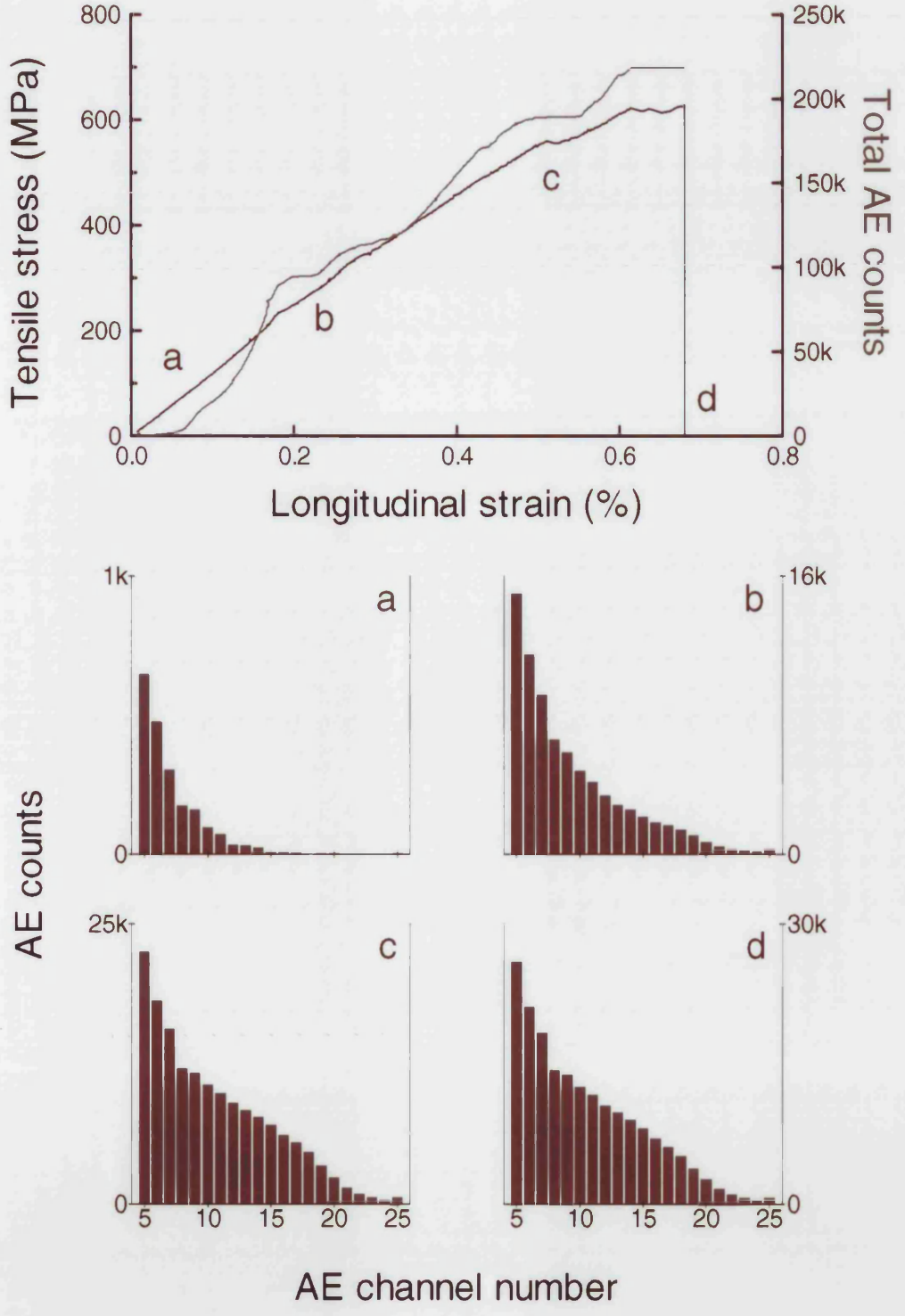

Figure 4.103 Typical tensile response of composite with unfilled HT50 matrix.
TOP: $\sigma - \varepsilon$ curve and total acoustic emission counts;
BOTTOM: Acoustic emission amplitude distributions at strains corresponding to points a,b,c and d in the top graph.

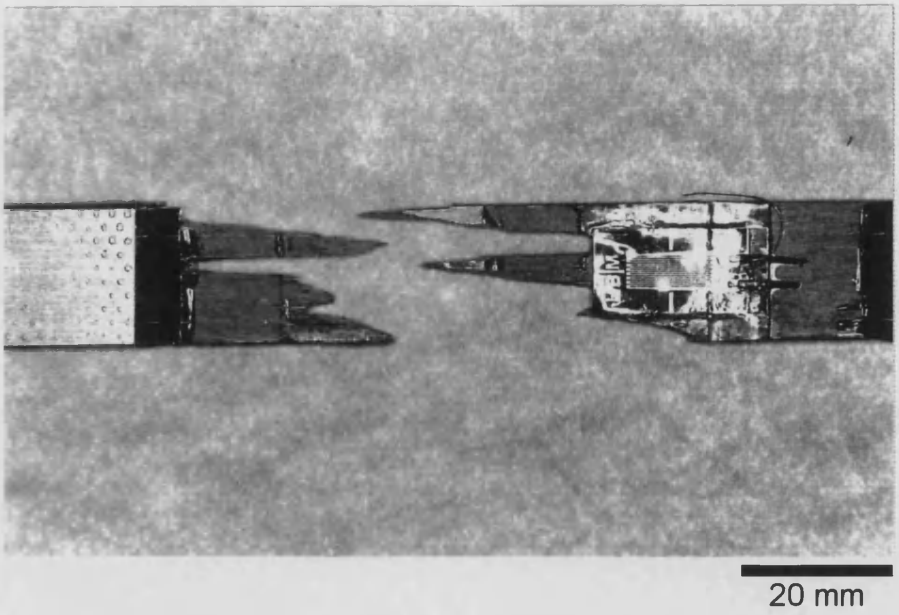

Figure 4.104 Crenellated, brittle failure in a tensile specimen with matrix composition HT50 / 0.27 V_{NLAS}.

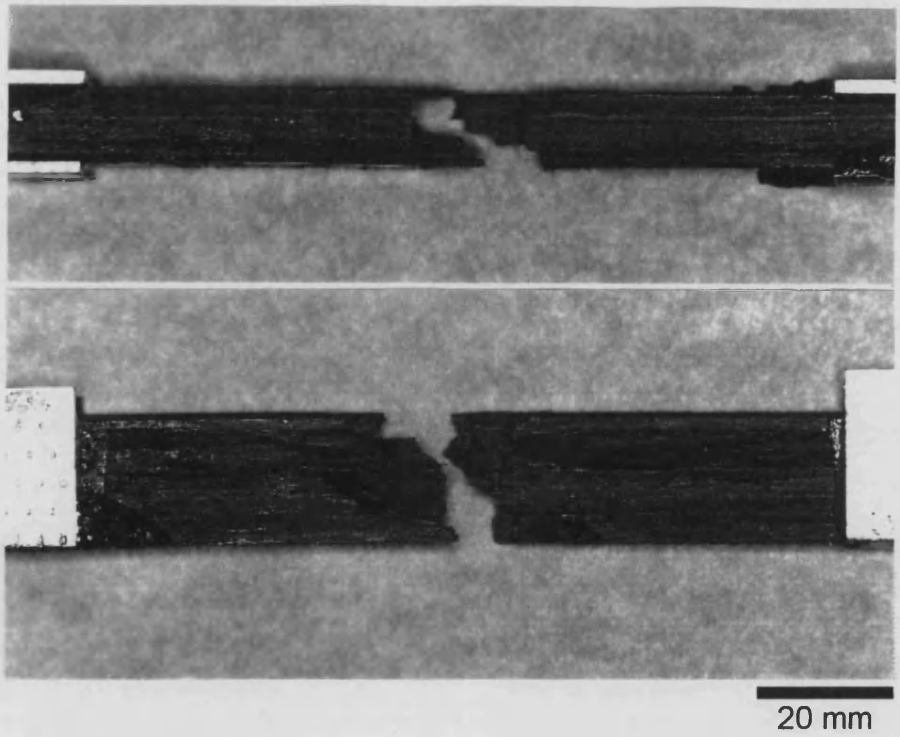

Figure 4.105 Tougher, fibrous fracture mode in a tensile specimen with matrix composition HT50 / 0.09 V_{NLAS}.

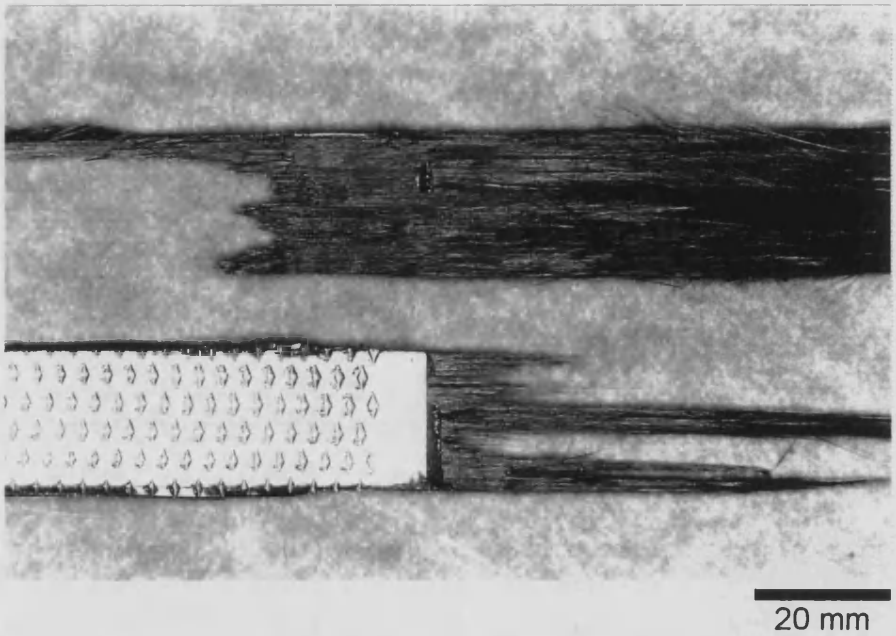

Figure 4.106 Extensive delamination and longitudinal splitting in a tensile specimen with matrix composition HT50 / 0.02 V_{NLAS}.

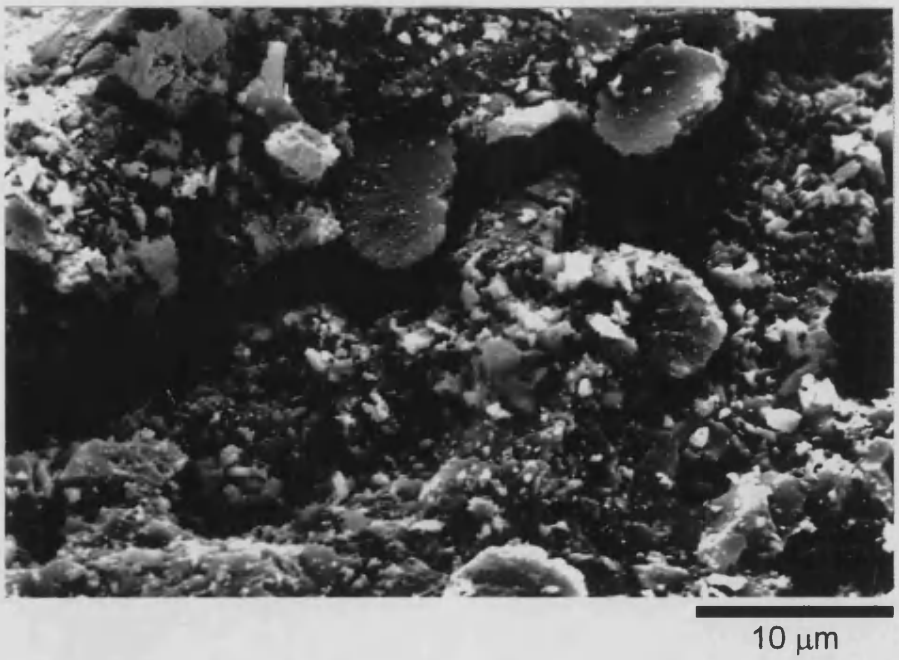

Figure 4.107 Brittle fracture surface and delamination crack in a tensile sample with matrix composition HT50 / 0.27 V_{NLAS}

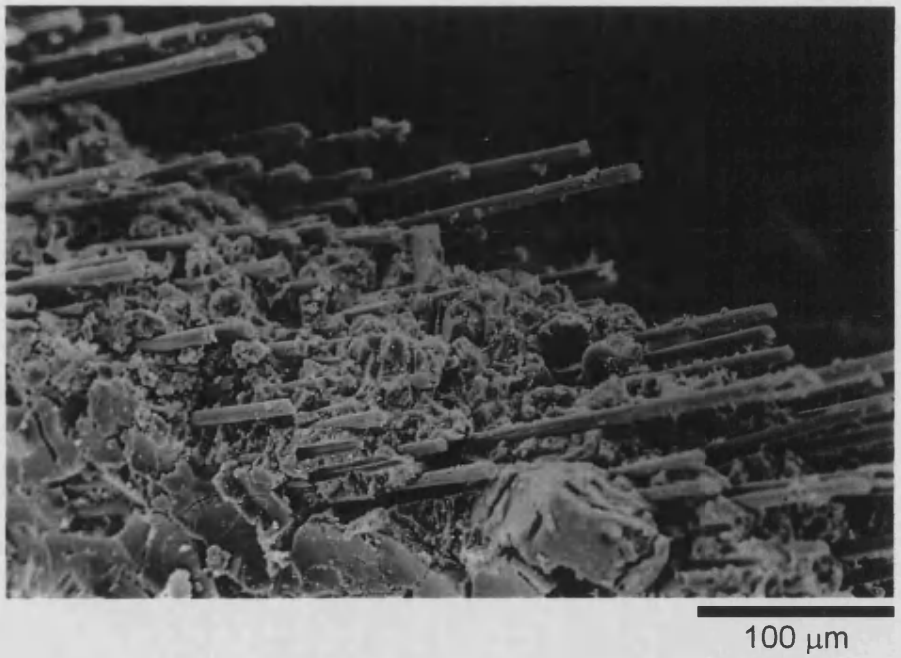

Figure 4.108 Fibrous fracture surface at the edge of an intact clump of composite in a tensile sample with matrix composition HT50 / 0.09 V_{NLAS}

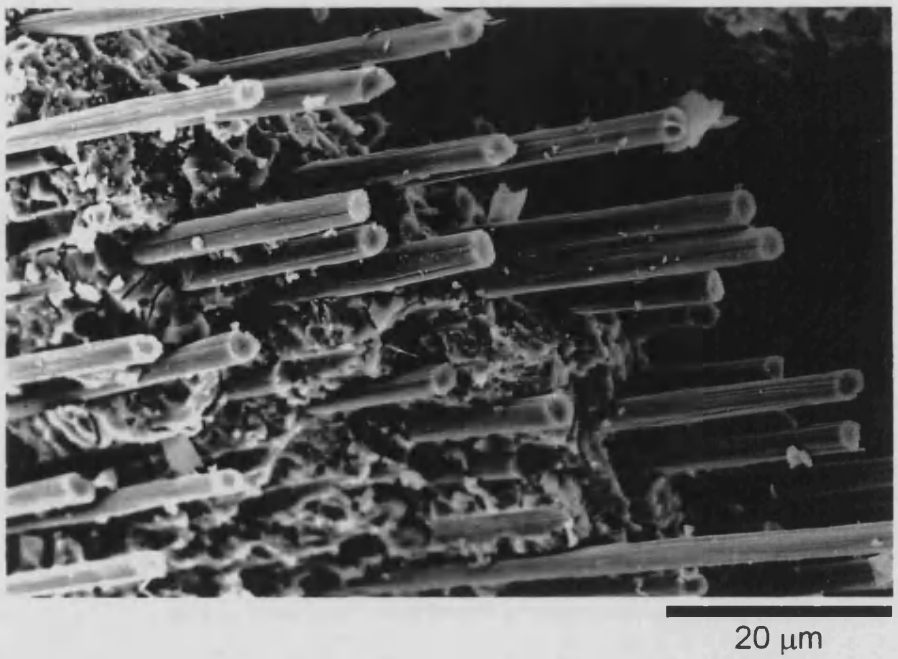

Figure 4.109 Fibrous fracture surface on the exterior face of a tensile sample with matrix composition X30 / 0.08 V_{NLAS}.

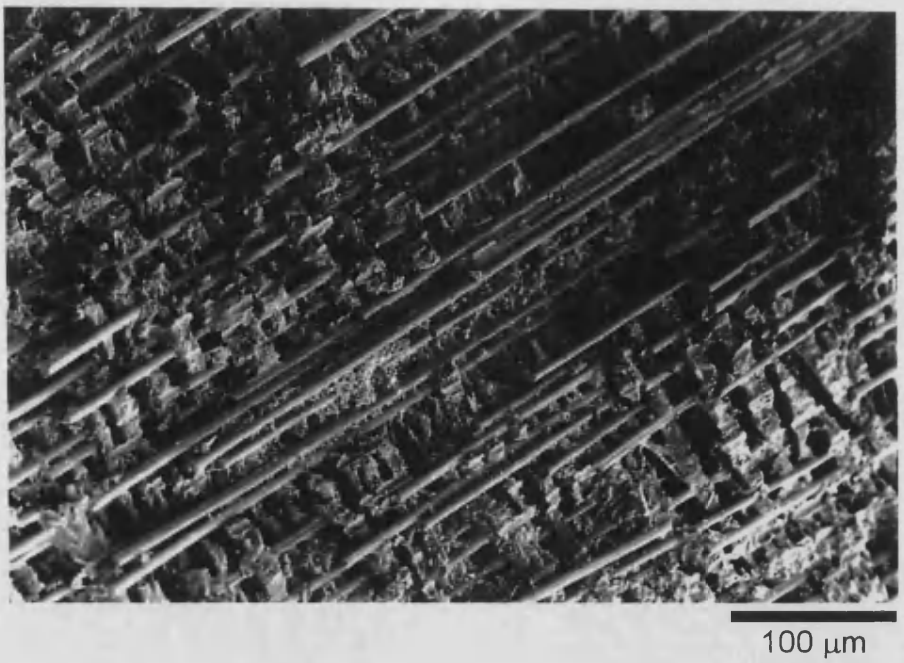

Figure 4.110 View of a delaminated plane of an intact clump of composite in a tensile sample with matrix composition HT50 / 0.09 V_{NLAS}

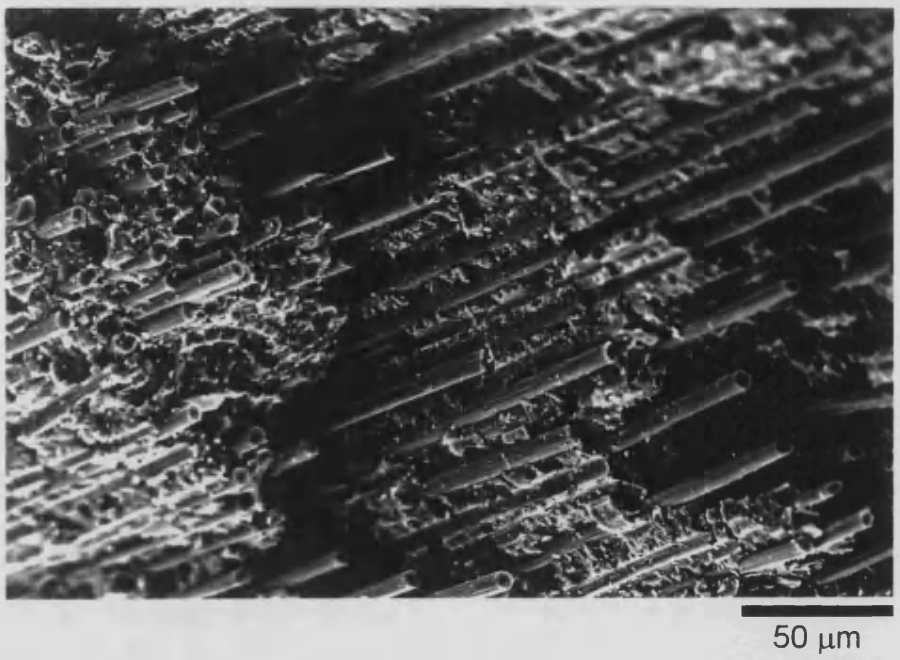

Figure 4.111 View of intact composite clumps which have failed by shear. The three clumps are shown by the arrows. The matrix composition of this tensile sample was HT50 / 0.19 V_{NLAS}.

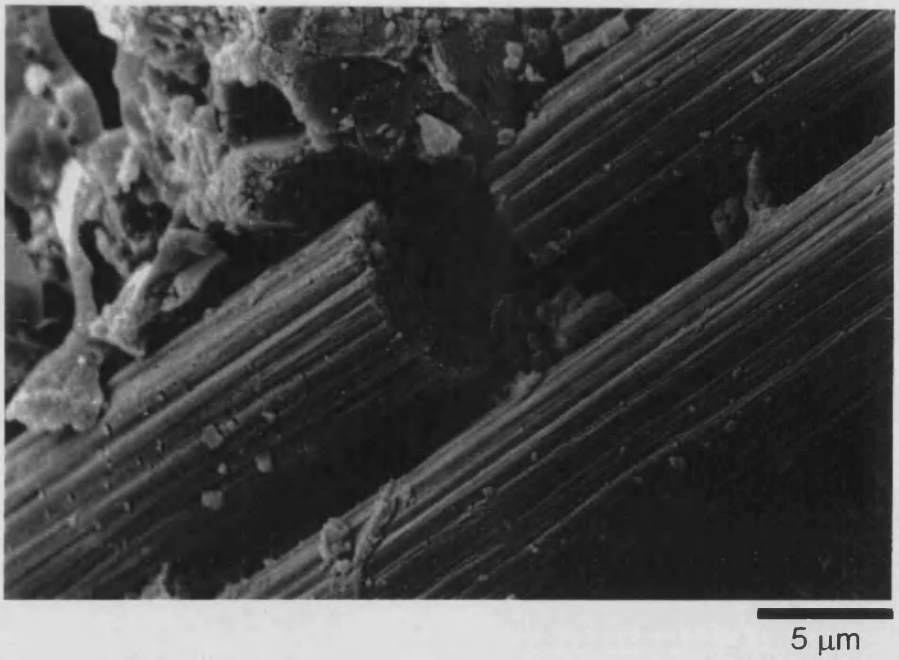

Figure 4.112 Fibre fracture in an intact clump of material in a tensile sample with matrix composition HT50 / 0.19 V_{NLAS}.

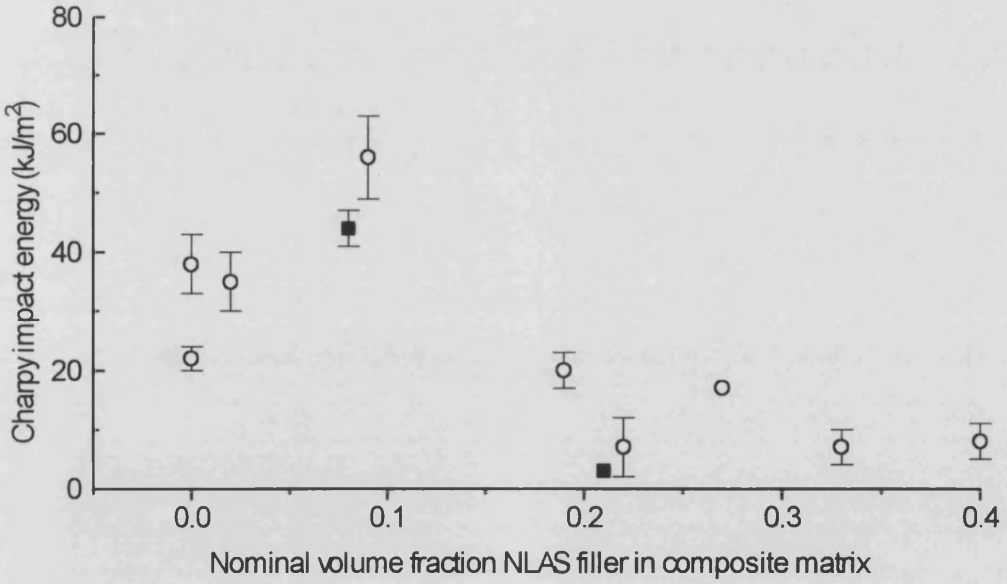

Figure 4.113 Variation of un-notched Charpy impact toughness with NLAS filler content in matrix. ○ : HT50-derived matrix. ■ : X30-derived. The error bars indicate standard deviations.

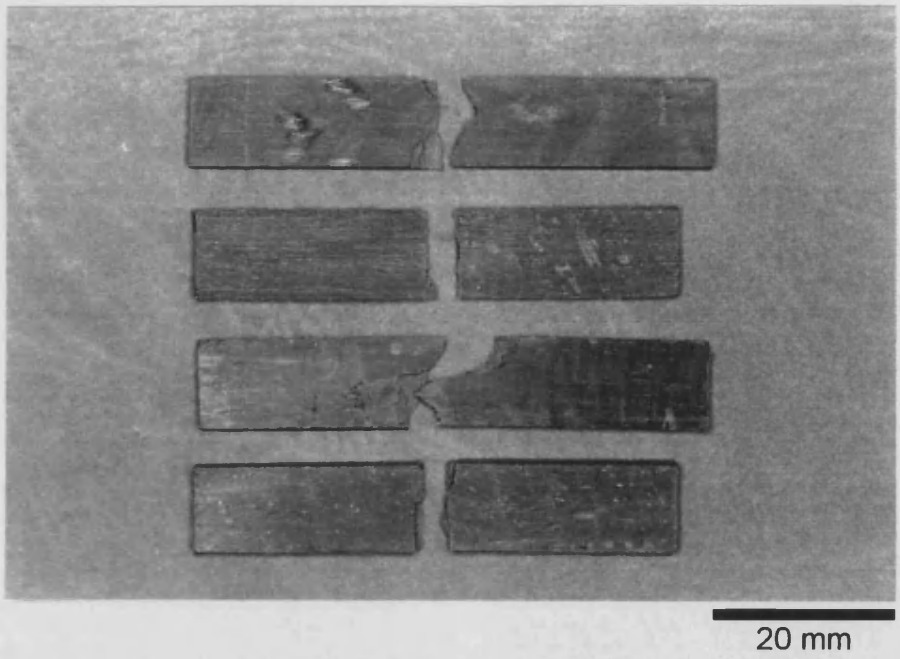

Figure 4.114 Brittle failure mode exhibited by Charpy specimens with matrix composition HT50 / 0.22 $VNLA_S$.

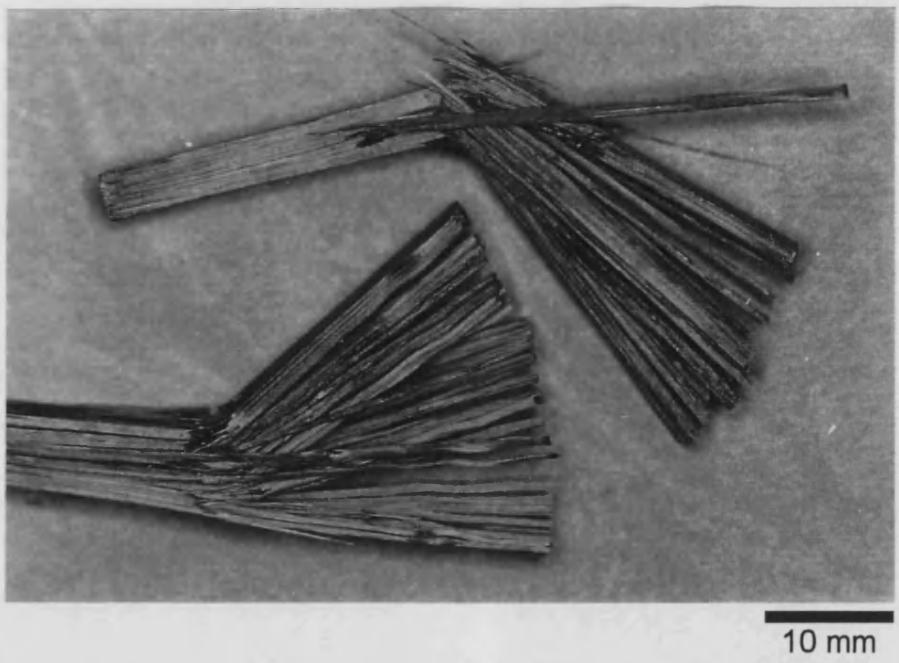

Figure 4.115 Charpy specimens with matrix composition HT50 / 0.09 V_{NLAS} failed by extensive delamination and longitudinal splitting.

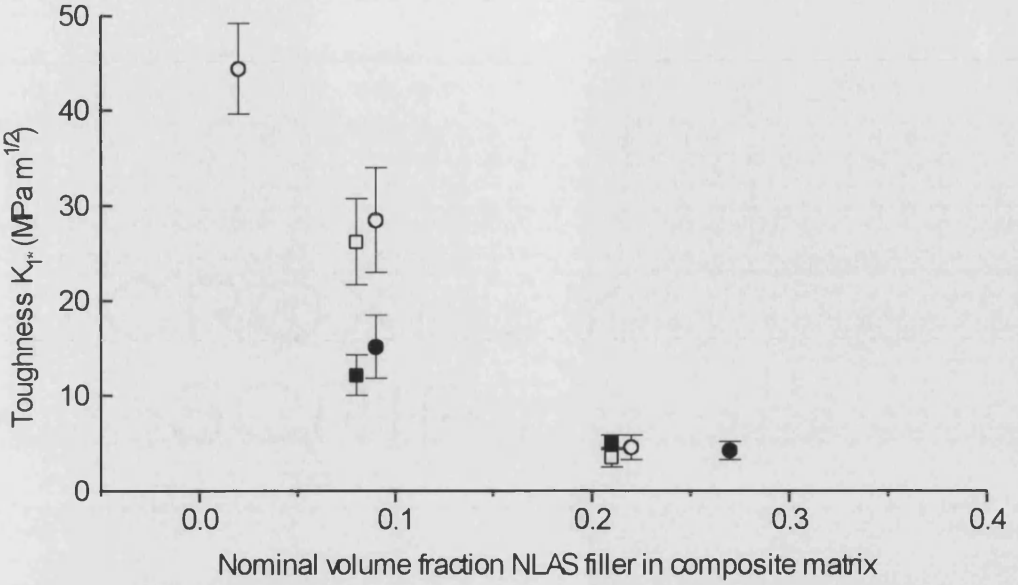

Figure 4.116 Variation of "toughness" (K^*) with NLAS filler content in matrix.
○,● : HT50-derived matrix. □,■ : X30-derived. Values of K^* were measured with notched tensile (open symbols) and SENB (closed symbols) configurations. The error bars indicate standard deviations.

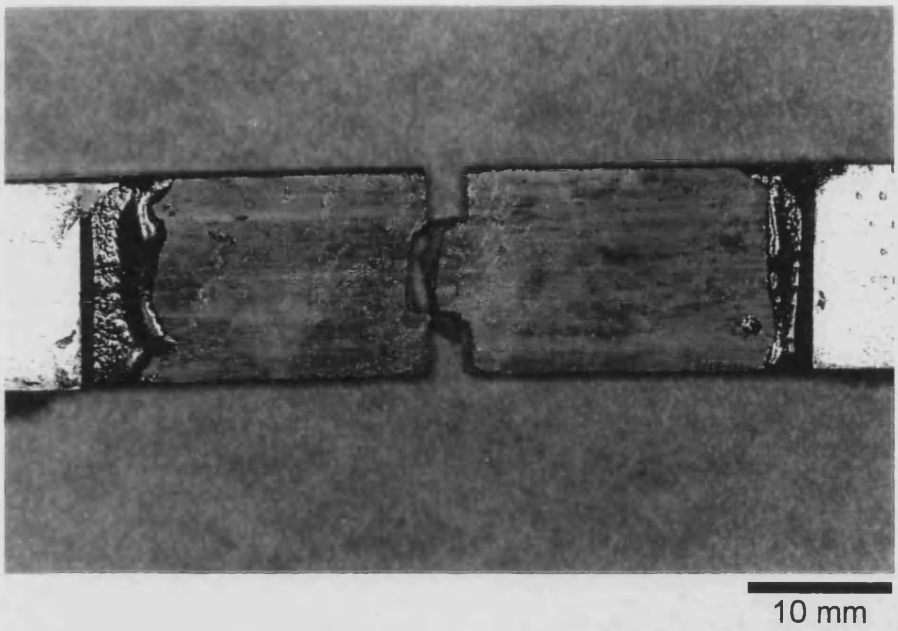

Figure 4.117 Brittle failure mode exhibited by notched tension (K_{I*} determination) specimen with matrix composition HT50 / 0.22 V_{NLAS}.

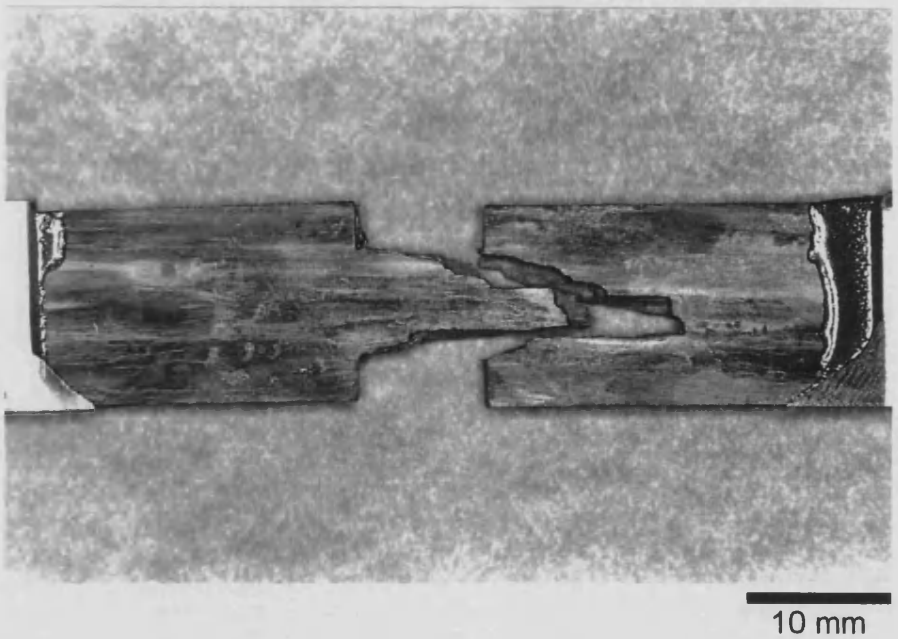

Figure 4.118 Notched tension (K_{I*} determination) specimen with matrix composition HT50 / 0.22 V_{NLAS} showing some shear damage in an otherwise brittle specimen.

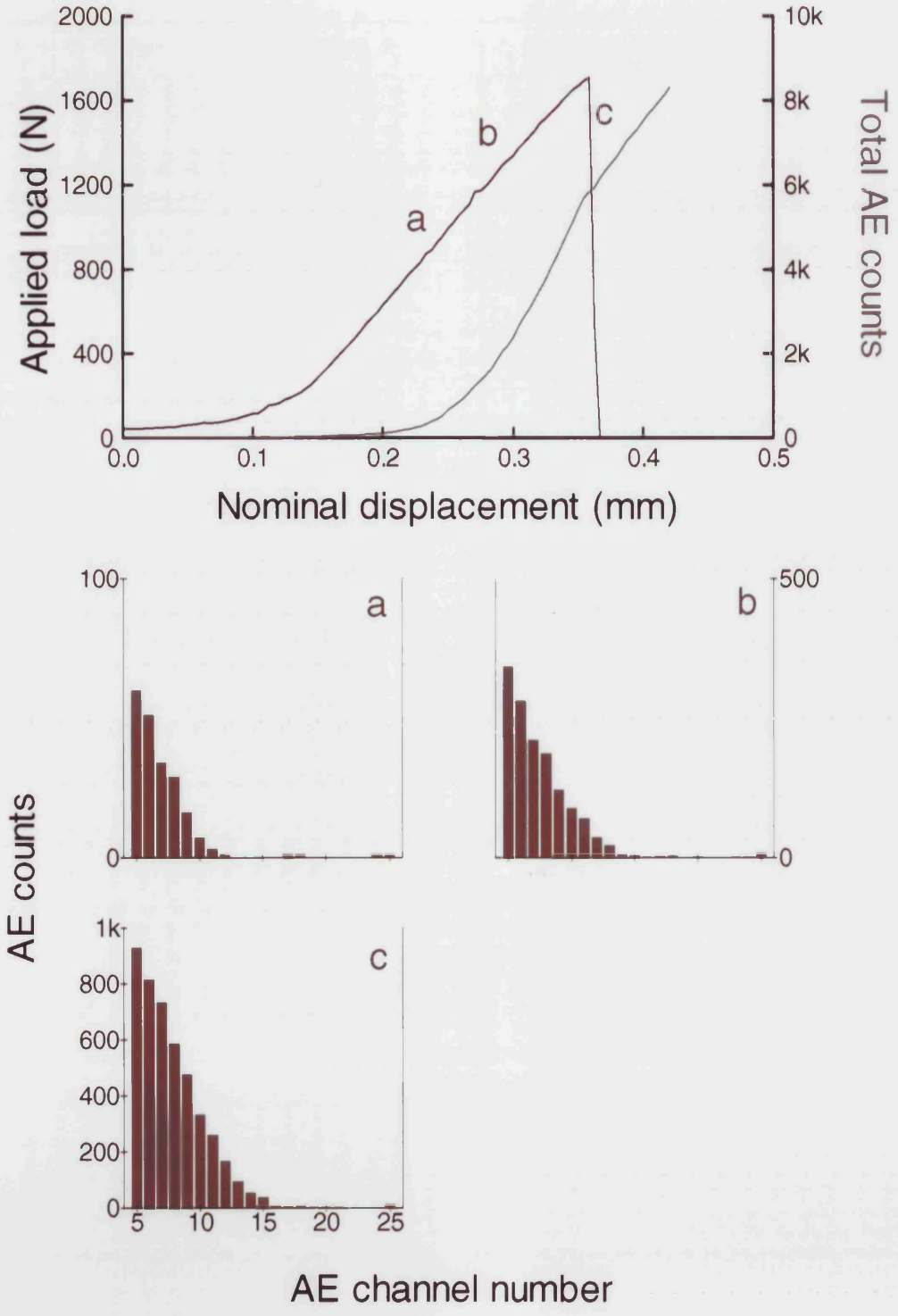

Figure 4.119 K^* determination by notched tensile test. This example is from a composite with HT50 / 0.22 V_{NLAS} matrix. *TOP*: Force-displacement curve and total acoustic emission generation; *BOTTOM*: AE amplitude distributions at displacements corresponding to points a,b and d.

Figure 4.120 SENB specimen with matrix composition X30 / 0.21 V_{NLAS} showing tearing at the notch tip of an otherwise brittle specimen. This specimen configuration measured K_{I*} in 'through-width' mode (ii - see figure 4.4).

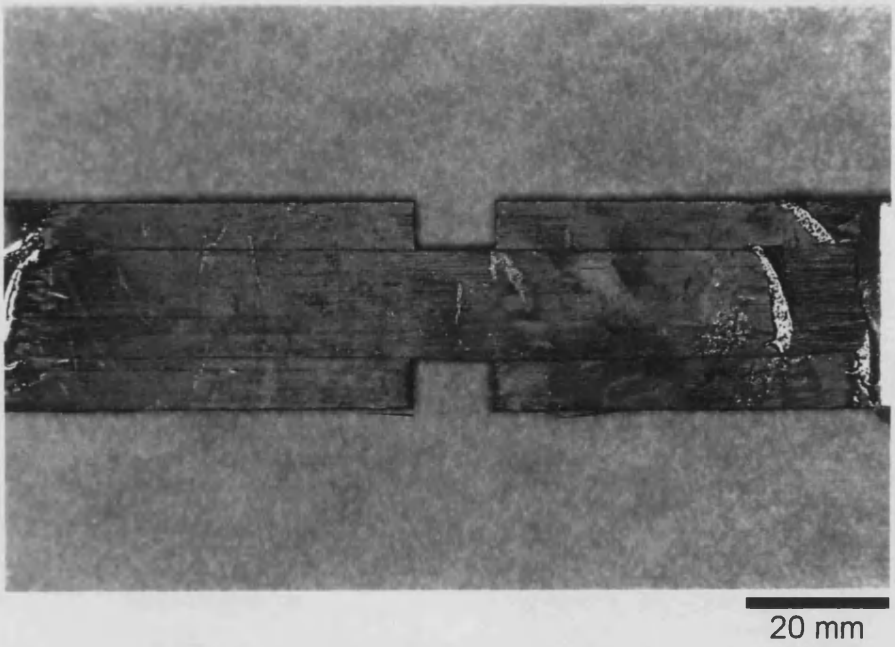

Figure 4.121 Notched tension specimen (K_{I*} determination) with matrix composition HT50 / 0.02 V_{NLAS} showing extensive delamination at the notch tip.

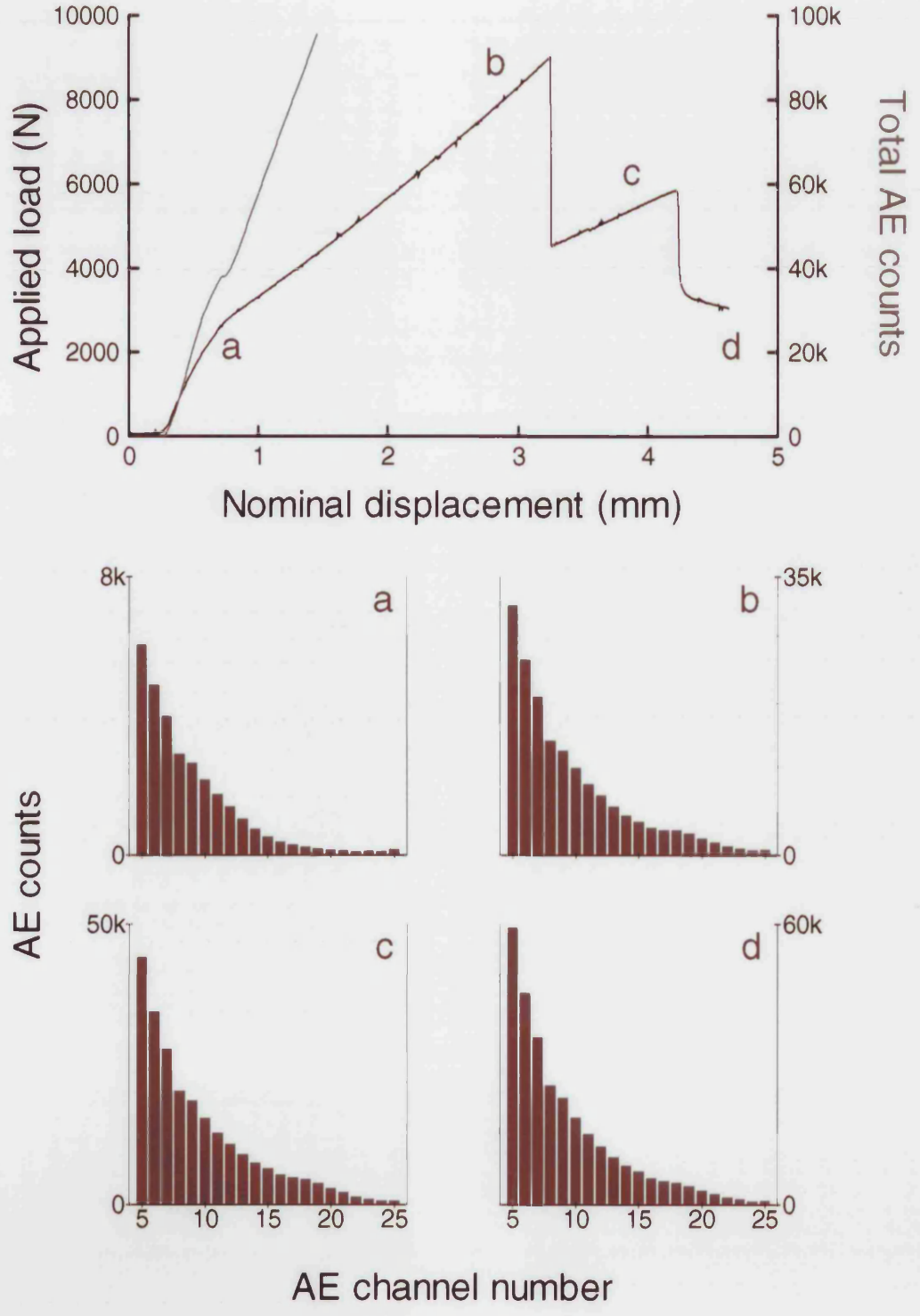

Figure 4.122 K^* determination by notched tensile test. This example is from a composite with HT50 / 0.02 V_{NLAS} matrix. *TOP*: Force-displacement curve and total acoustic emission generation; *BOTTOM*: AE amplitude distributions at displacements corresponding to points a,b,c and d.

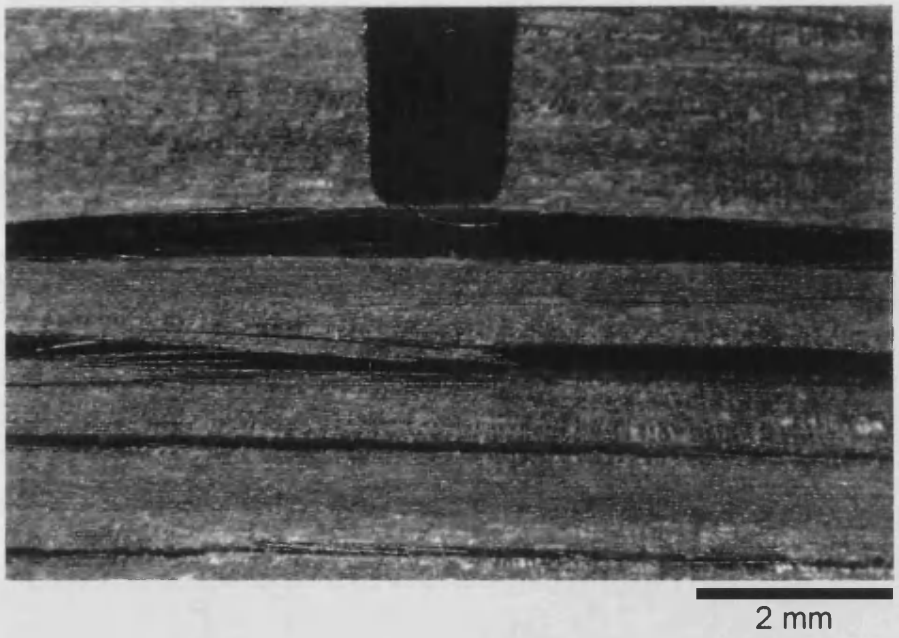

Figure 4.123 Extensive delamination in SENB specimen with unfilled HT50 matrix.

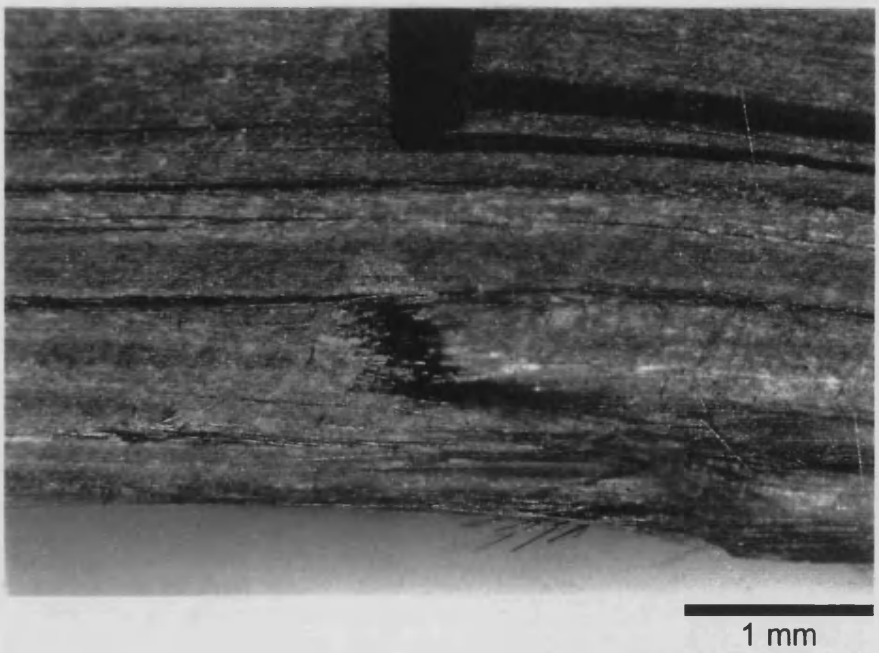

Figure 4.124 Compression damage and delamination in SENB specimen with matrix composition HT50 / 0.02 V_{NLAS}.

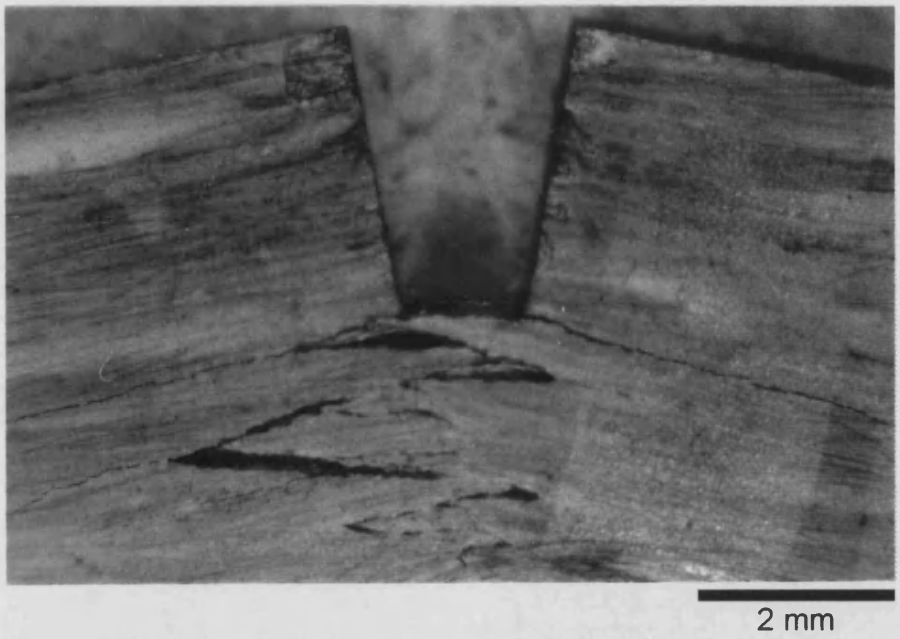

Figure 4.125 Ligament bridging in SENB specimen with matrix composition X30 / 0.08 V_{NLAS}.

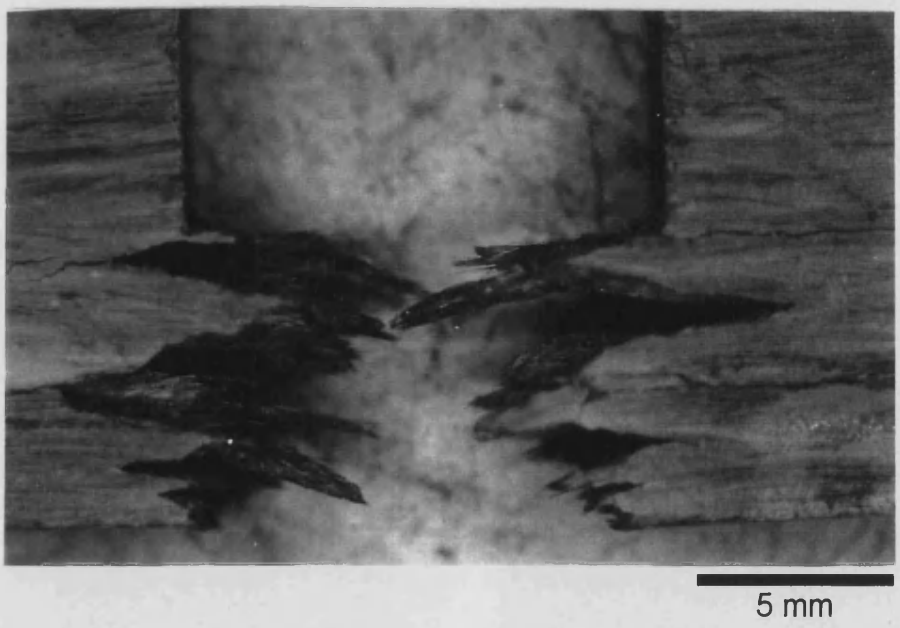

Figure 4.126 Detail of fibrous fracture surface in SENB specimen which failed by ligament bridging. Specimen matrix composition: HT50 / 0.09 V_{NLAS}.

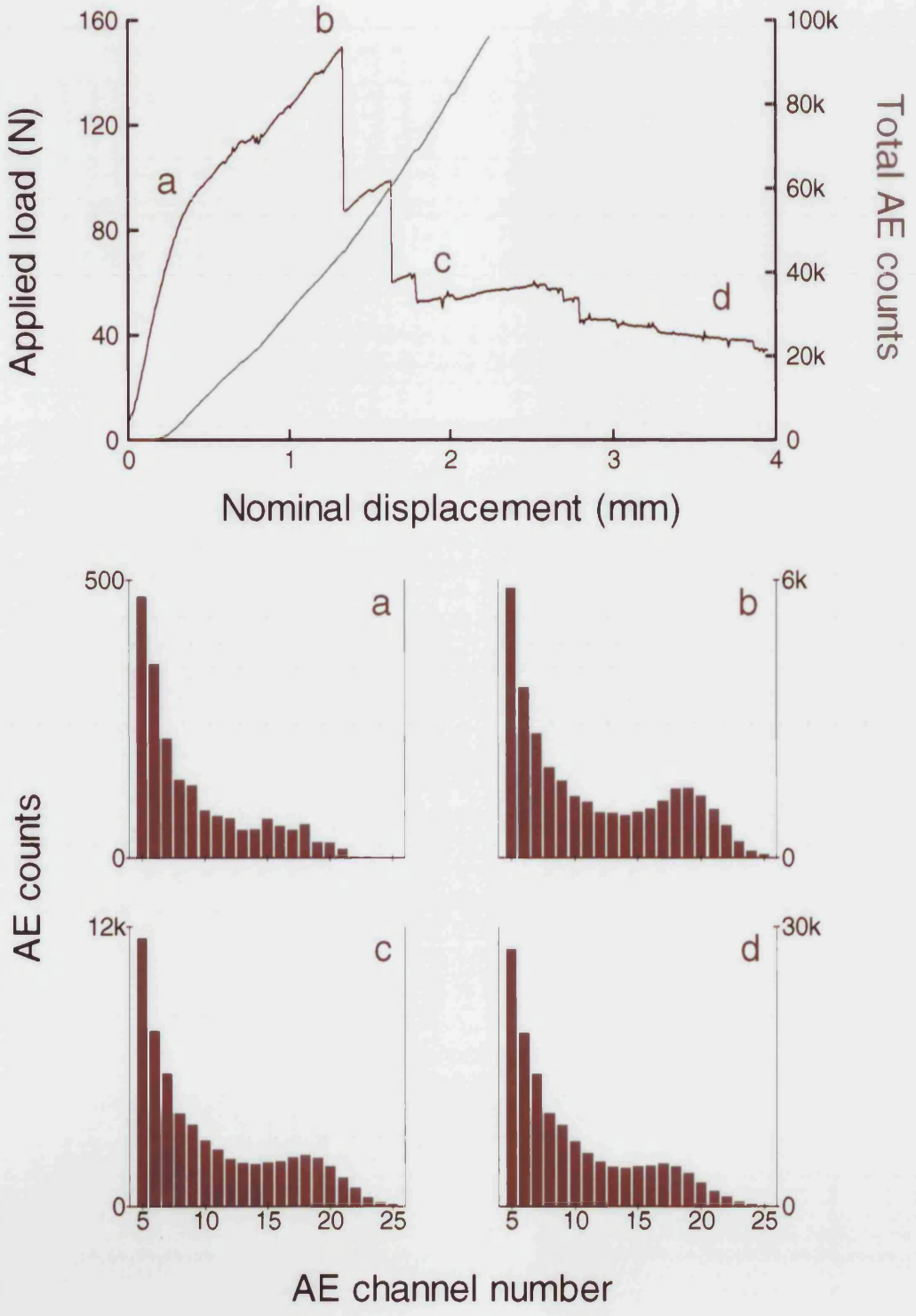

Figure 4.127 K^* determination by notched tensile test. This example is from a composite with HT50/0.09 V_{NLAS} matrix. *TOP*: Force-displacement curve and total acoustic emission generation; *BOTTOM*: AE amplitude distributions at displacements corresponding to points a,b and d.

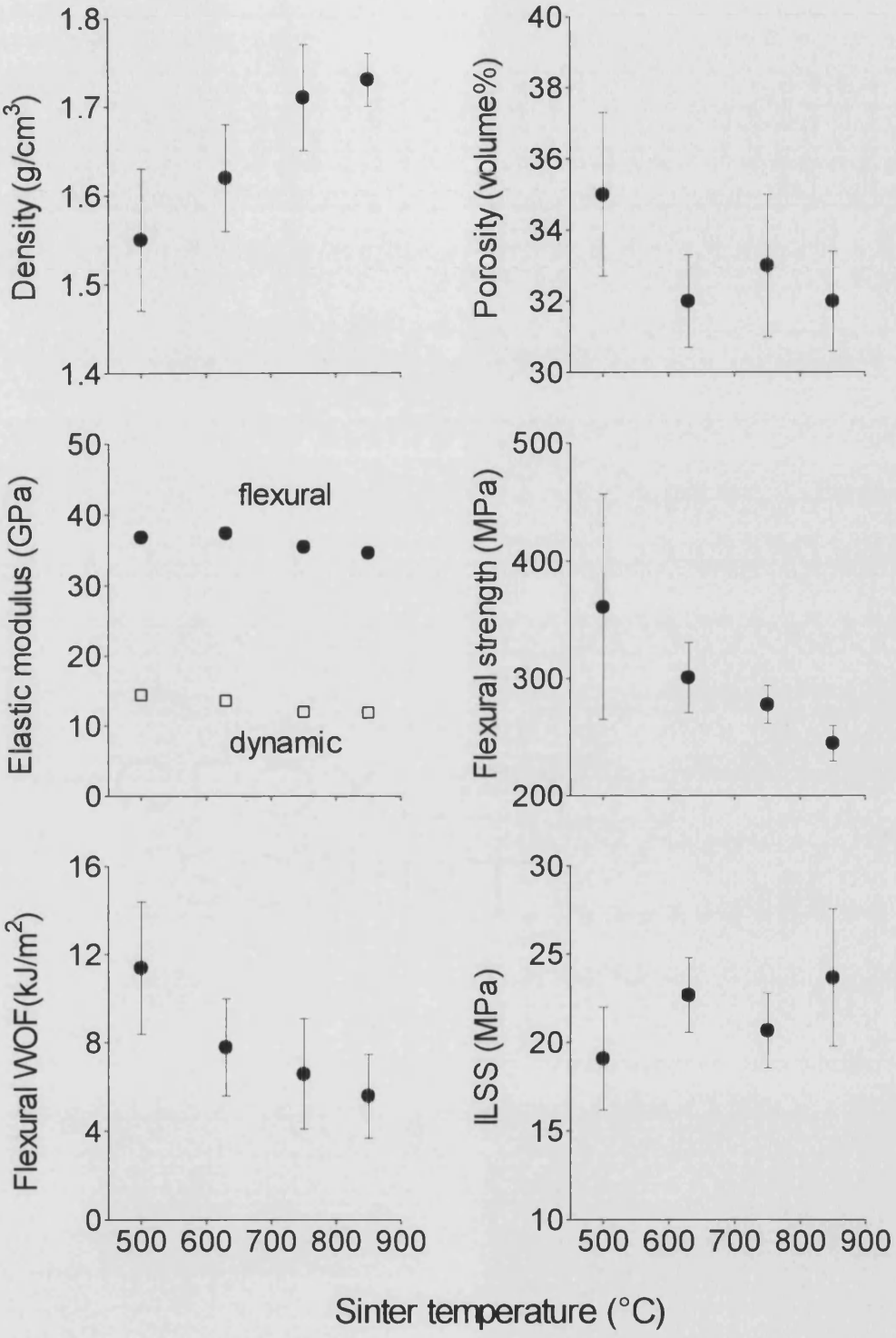

Figure 4.128 Variation of microstructural and flexural properties with sintering temperature for composites with HT50 / 0.33 V_{NLAS} matrix. Error bars indicate standard deviations from at least 9 measurements.

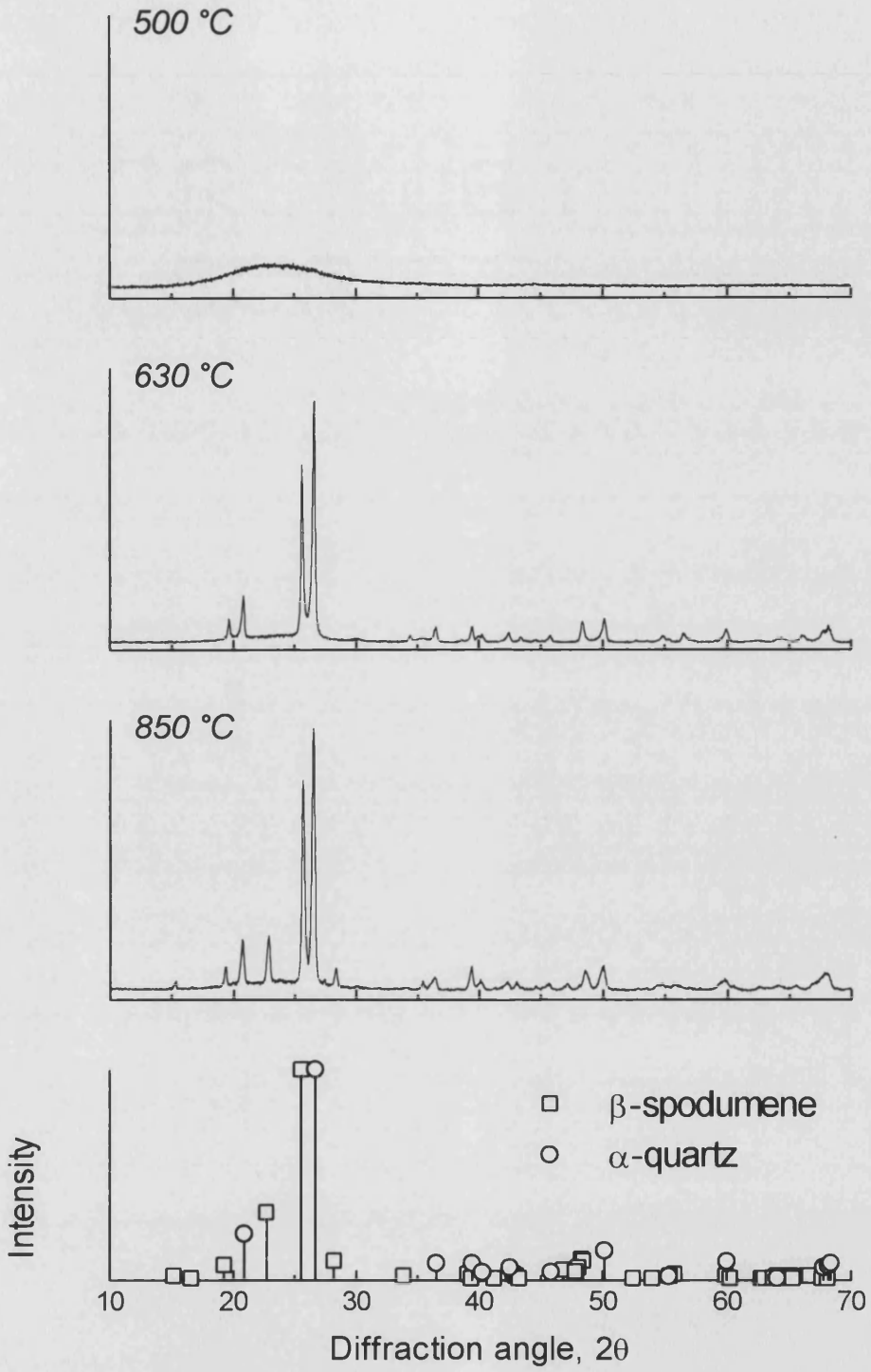

Figure 4.129 Effect of sintering temperature on the XRD response of samples with matrix composition HT50 / 0.33 V_{NLAS} .

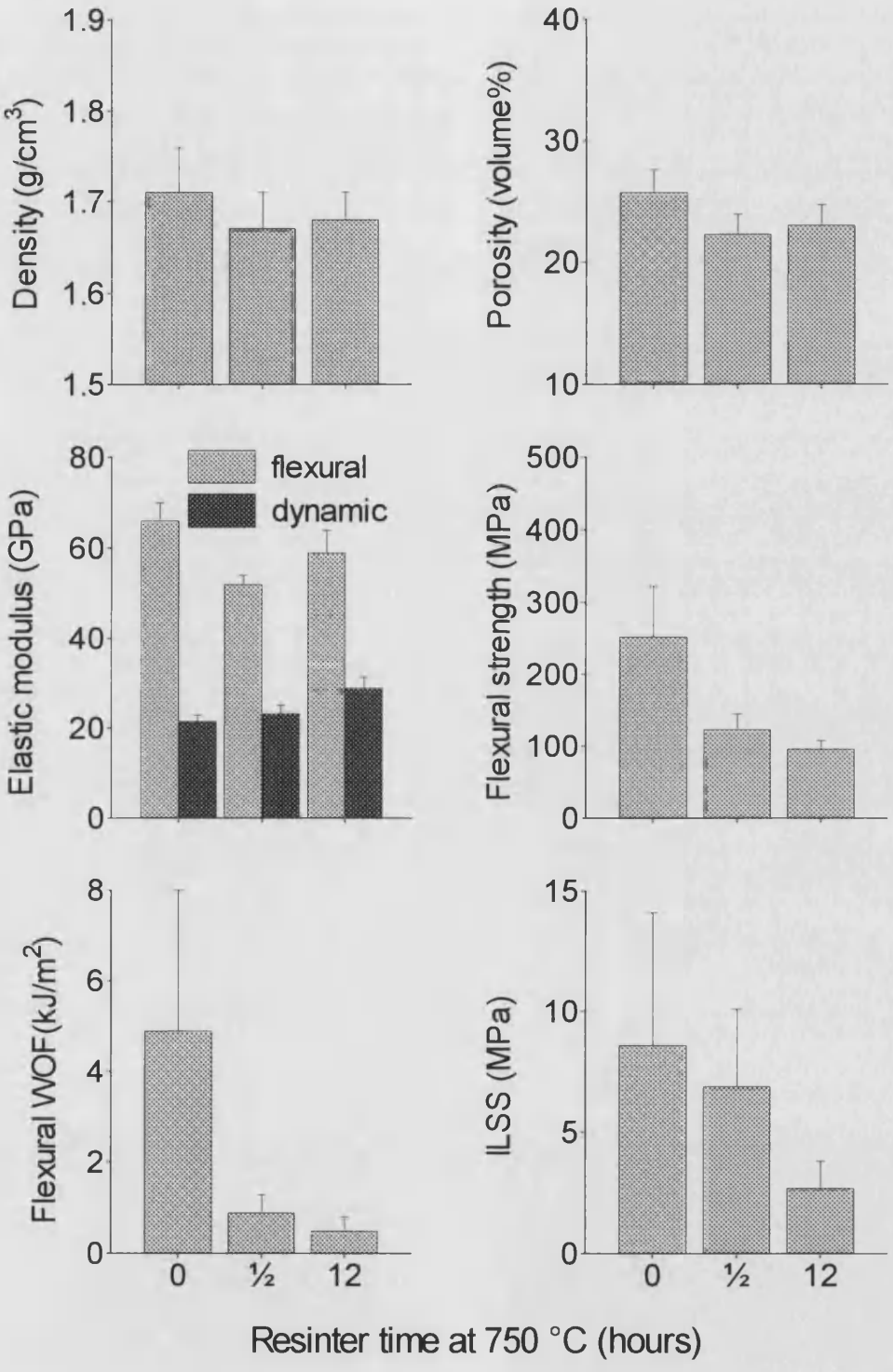

Figure 4.130 Effect of resintering at 750 °C on the microstructural and flexural properties of composites with matrix composition HT50 / 0.22 V_{NLAS}.

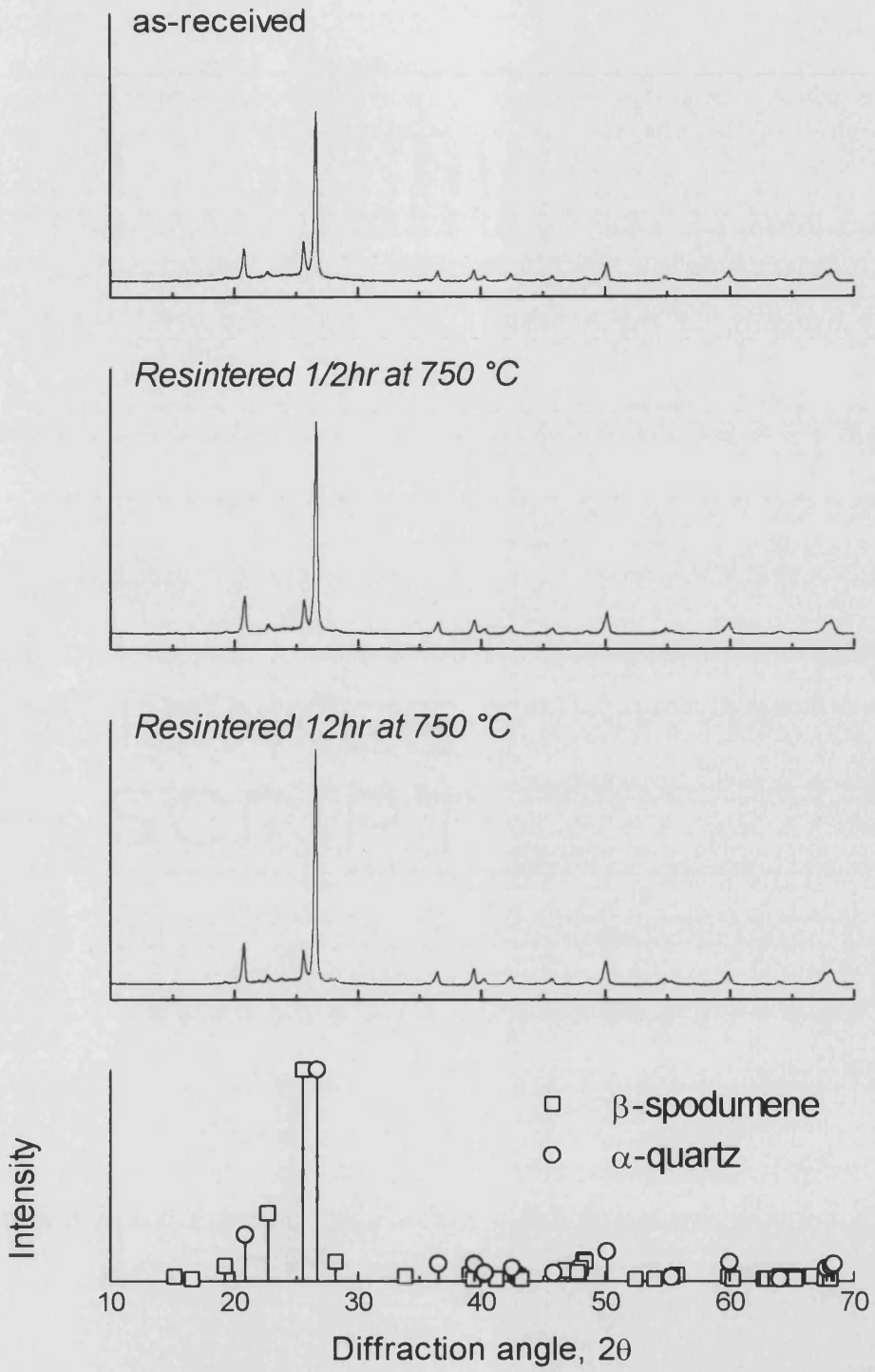

Figure 4.131 Resintering HT50 / 0.22 V_{NLAS} composite samples for ½ hour and 12 hours at 750 °C did not affect the amount of β–spodumene detected by XRD, although slightly more α-quartz was detected in samples sintered for longer periods.

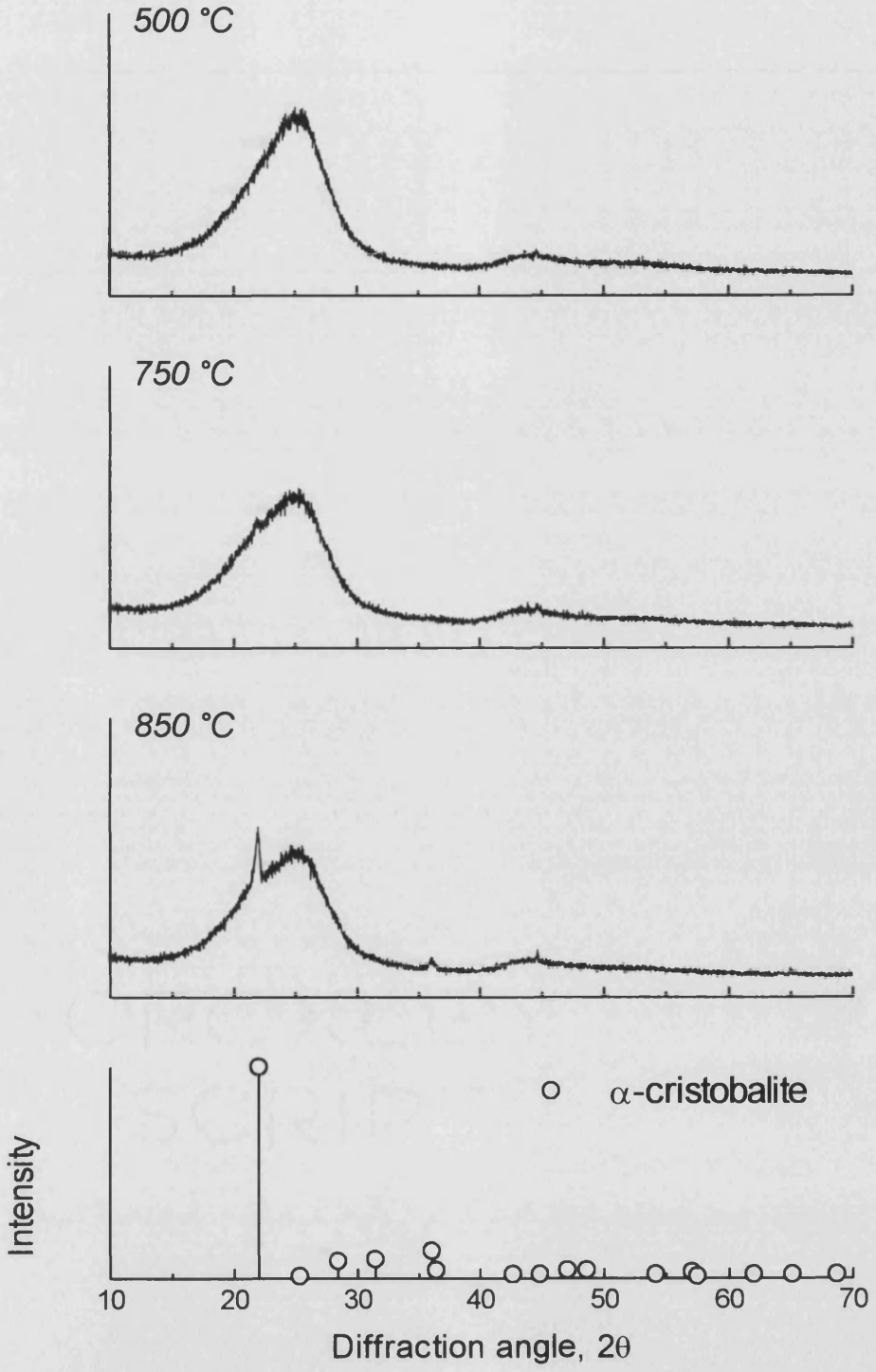

Figure 4.132 Effect of sintering temperature on the crystallography of composites with unfilled HT50 matrices. The lower graph gives pattern data for α-cristobalite [114].

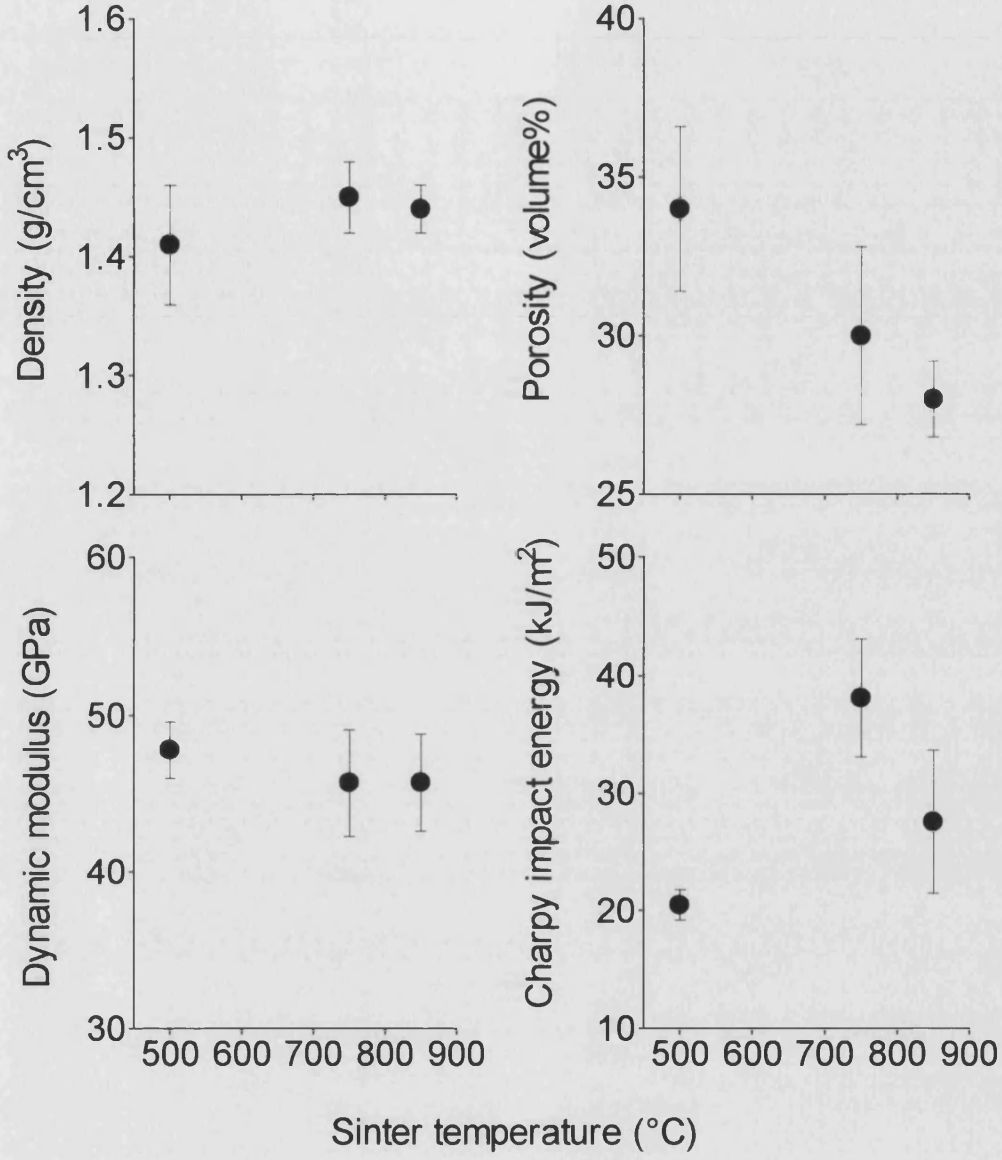

Figure 4.133 Effect of sintering temperature on density, porosity, dynamic modulus and Charpy impact energy of composites with unfilled HT50 matrices. The data are the means of at least 10 measurements, and error bars indicate standard deviations.

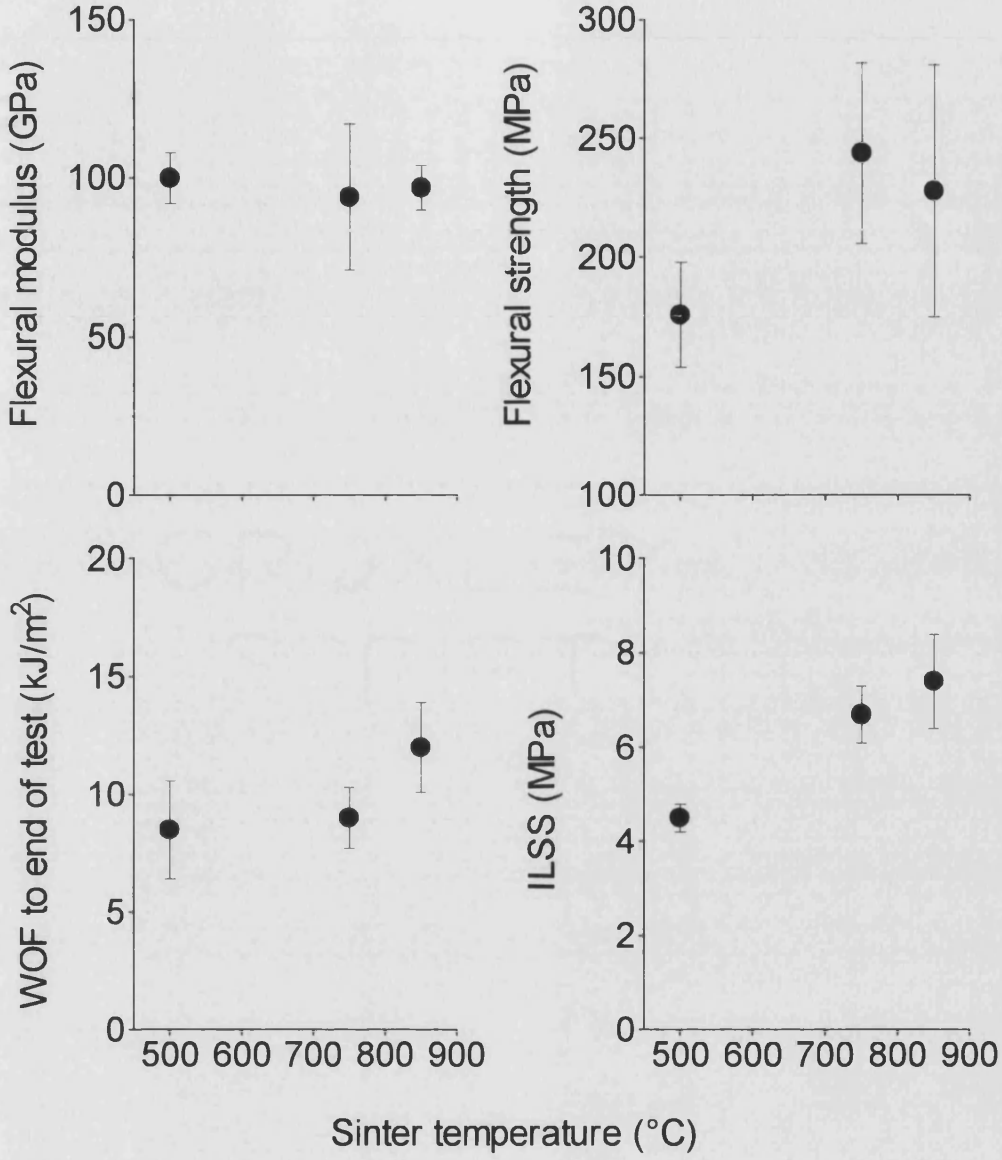

Figure 4.134 Effect of sintering temperature on the flexural mechanical properties and interlaminar shear strength of composites with unfilled HT50 matrices. The data are the means of at least 10 measurements, and error bars indicate standard deviations.

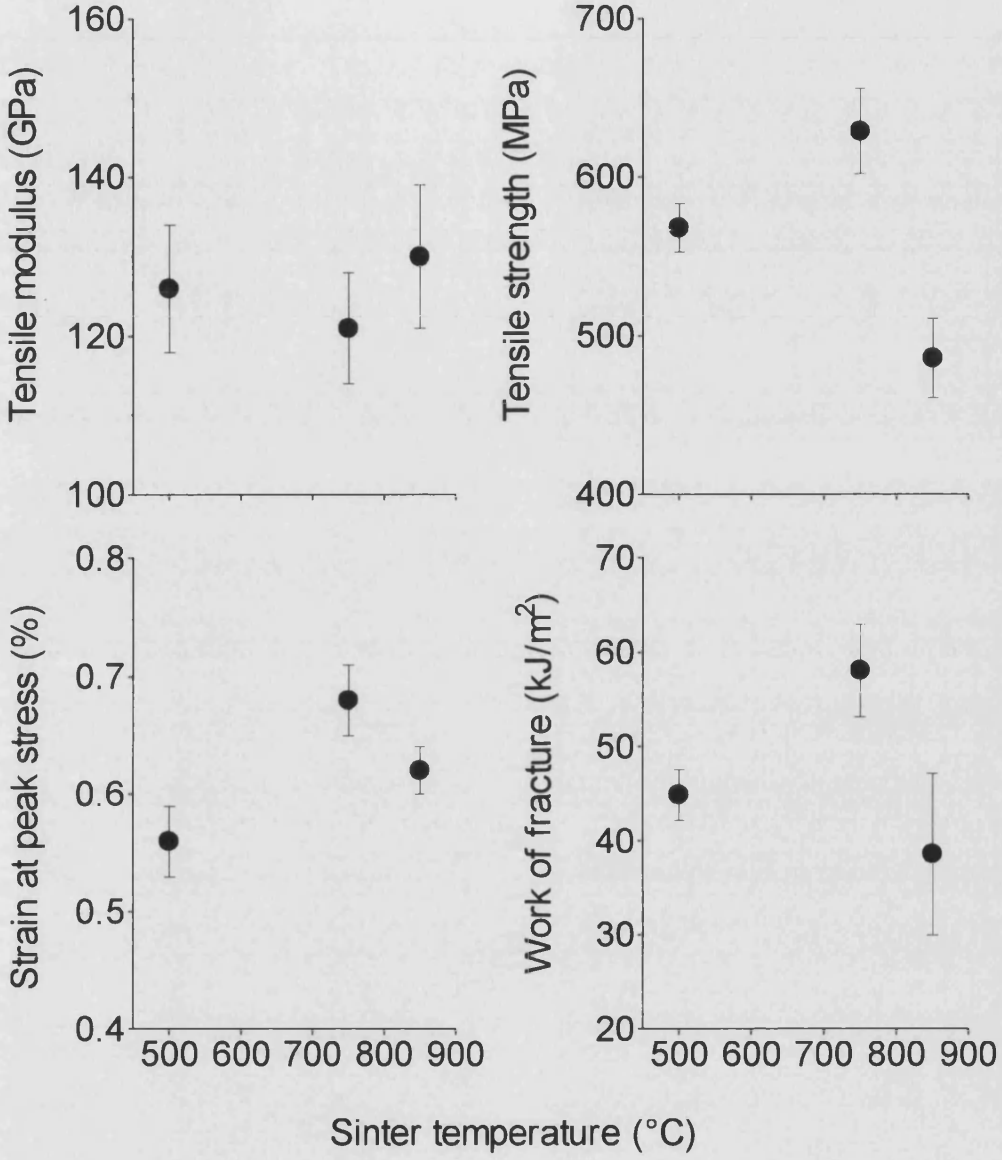

Figure 4.135 Effect of sintering temperature on the tensile properties of composites with unfilled HT50 matrices. The data are the means of at least 10 measurements, and error bars indicate standard deviations.

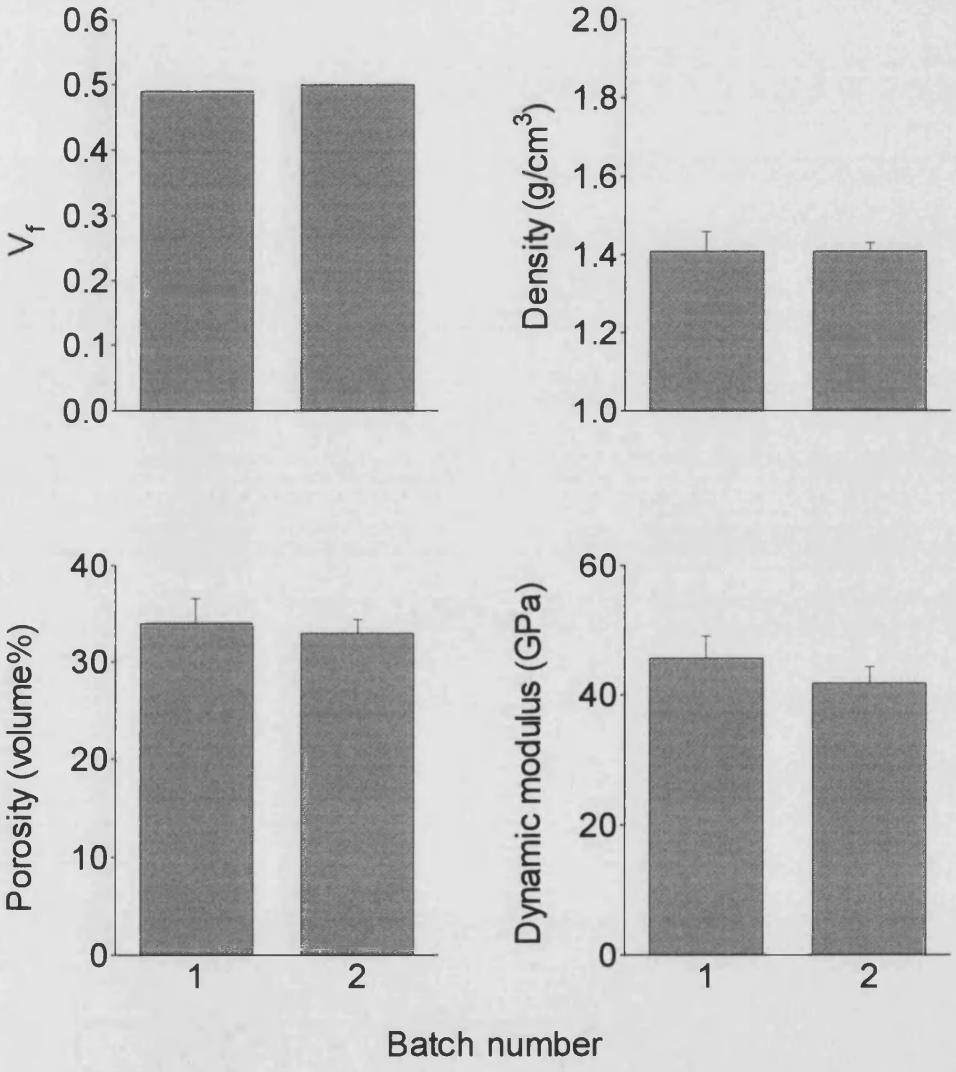

Figure 4.136 Reproducibility of microstructural parameters of composites with unfilled HT50 matrices.

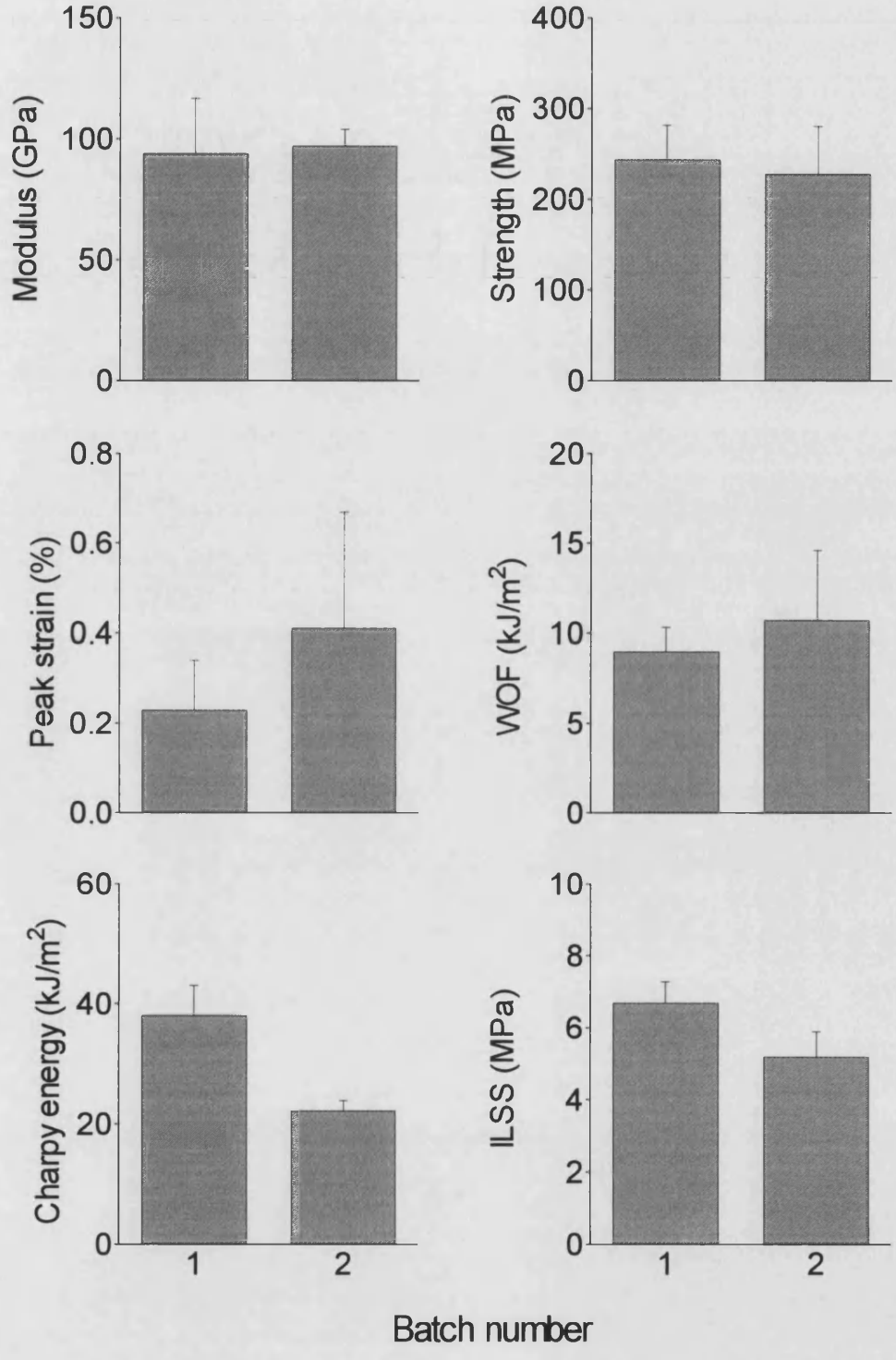

Figure 4.137 Reproducibility of flexural properties of composites with unfilled HT50 matrices.

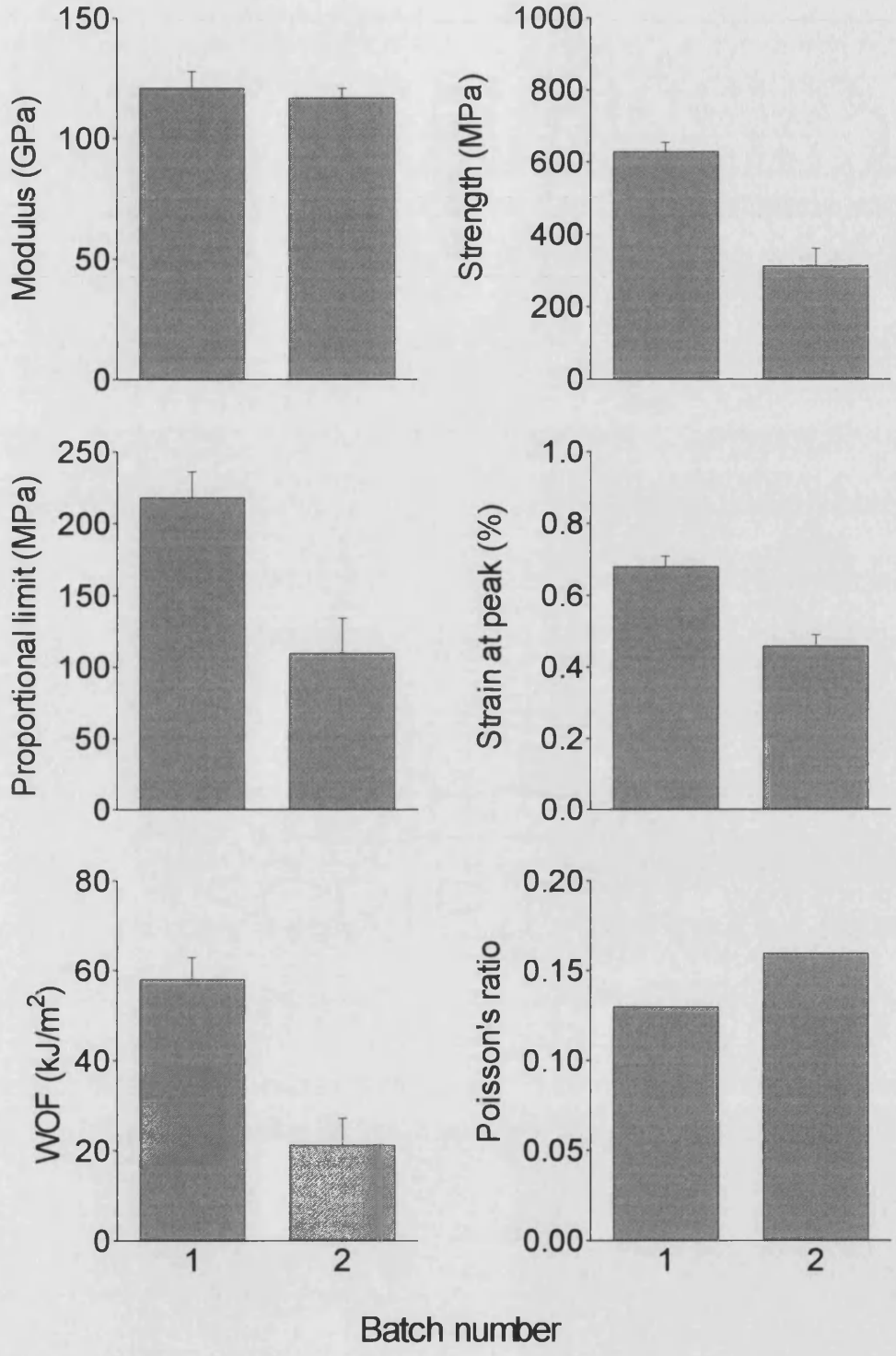

Figure 4.138 Reproducibility of tensile properties of composites with unfilled HT50 matrices.

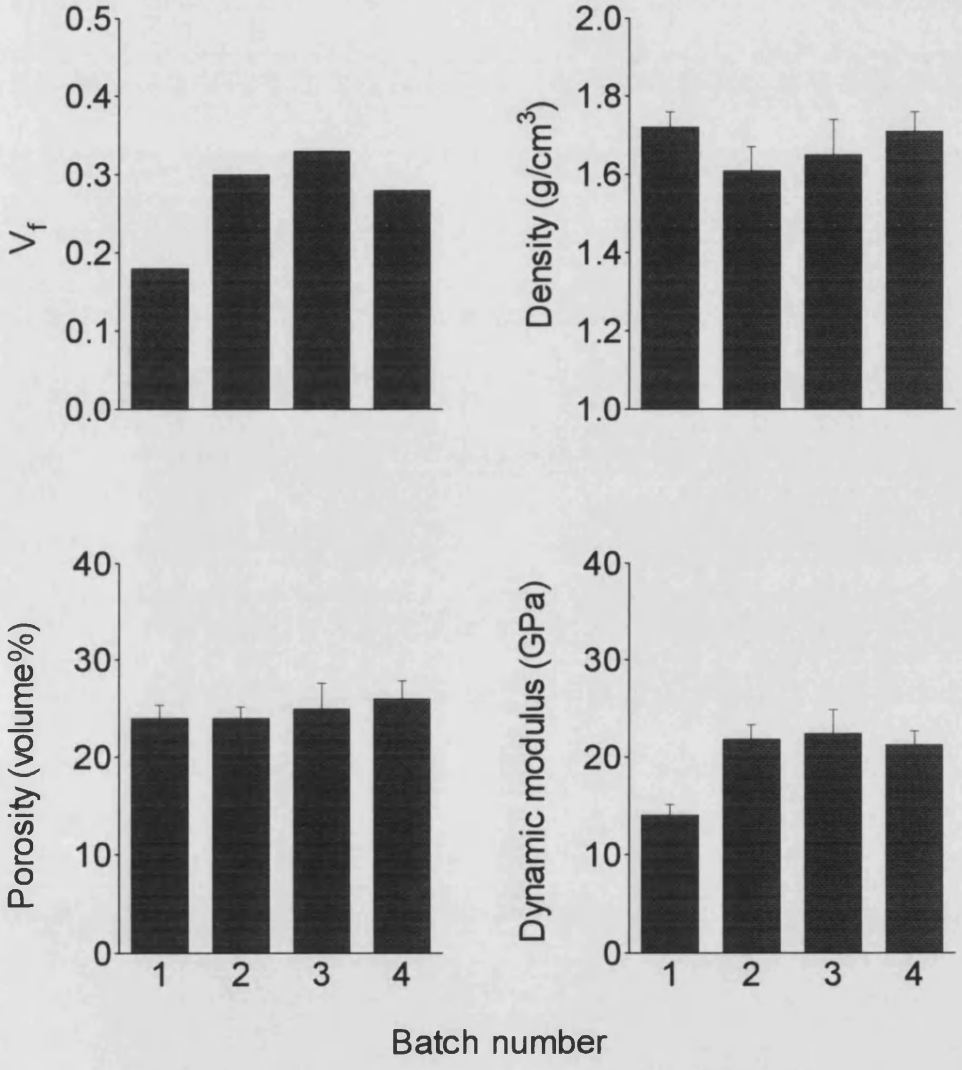

Figure 4.139 Reproducibility of microstructural parameters of composites with matrix composition HT50 / 0.22 V_{NLAS}.

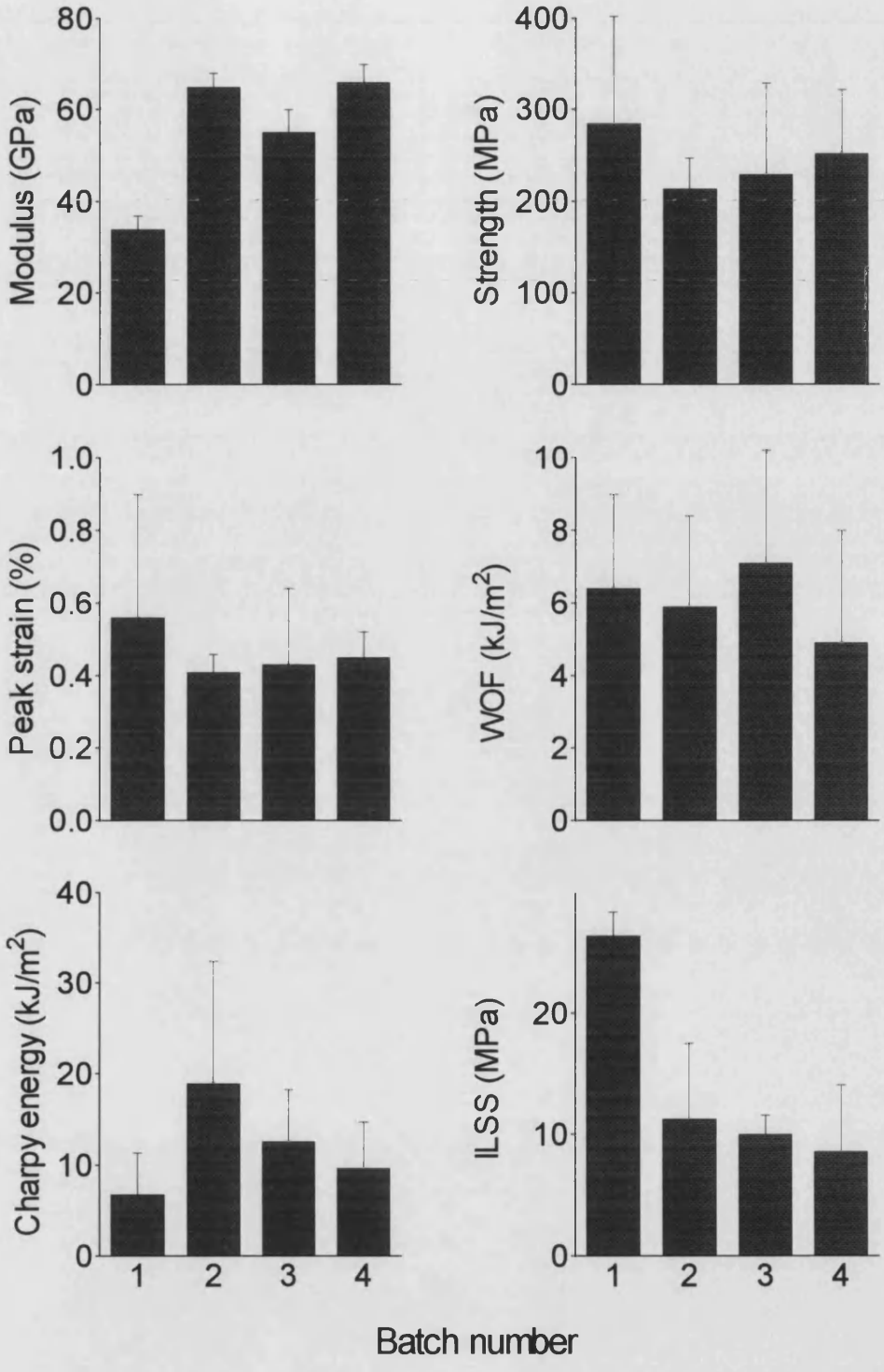

Figure 4.140 Reproducibility of flexural properties of composites with matrix composition HT50 / 0.22 V_{NLAS}.

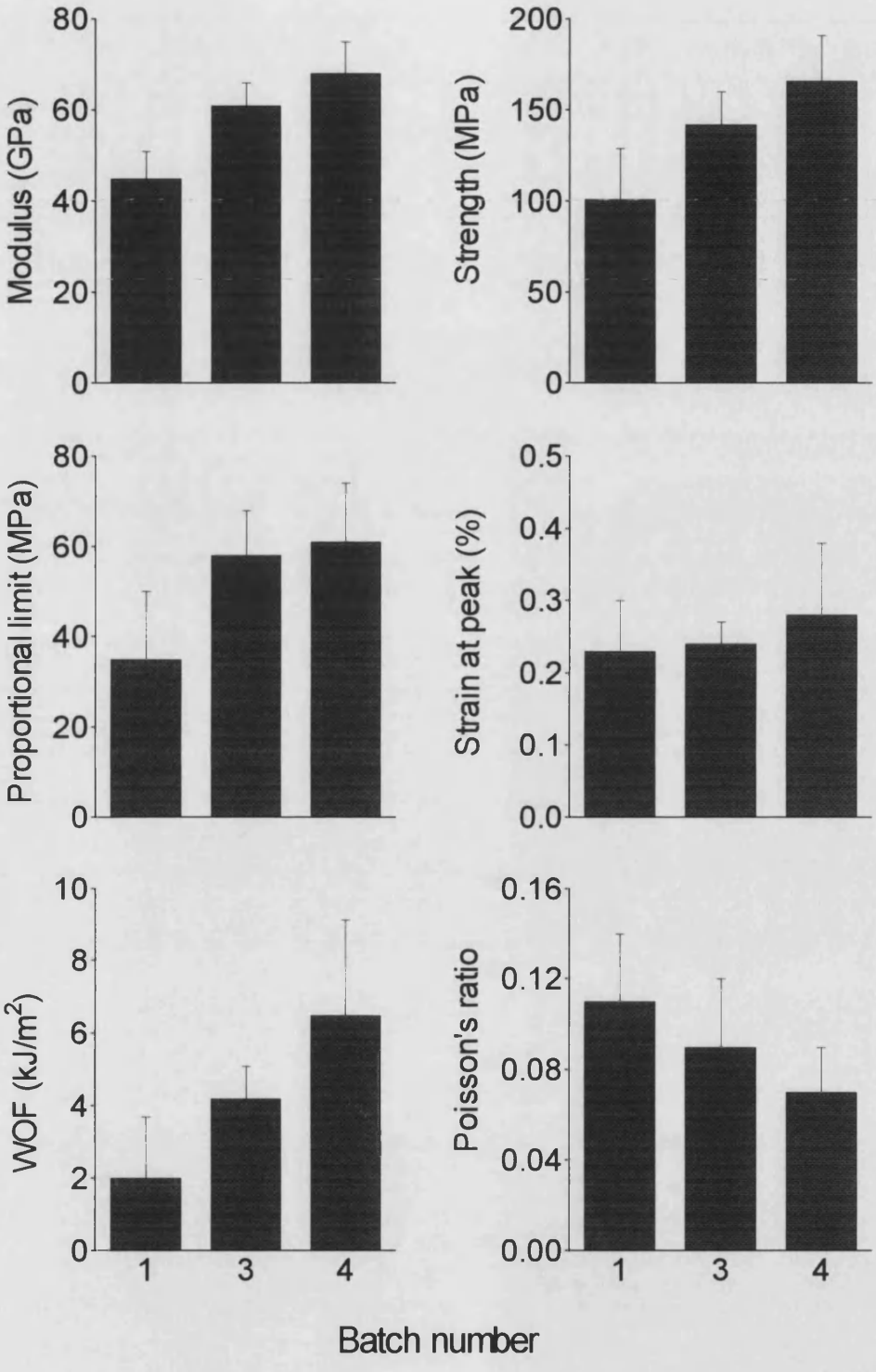

Figure 4.141 Reproducibility of tensile properties of composites with matrix composition HT50 / 0.22 V_{NLAS}.

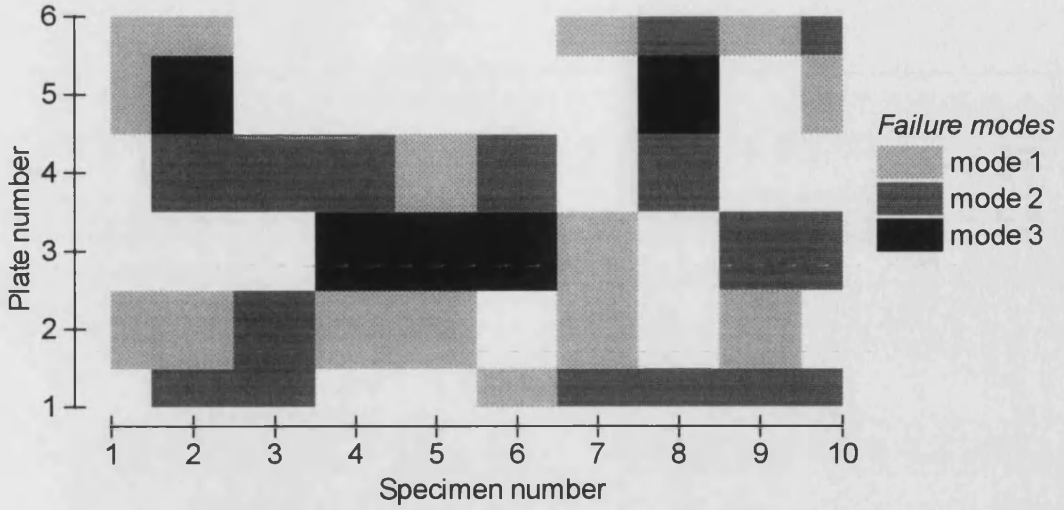

Figure 4.142 Distribution of flexural failure modes in a single batch of composite with matrix composition HT50 / 0.22 V_{NLAS}. Modes 1, 2, and 3 correspond to failure by partial delamination, extensive delamination and brittle fracture respectively (see figure 4.62).

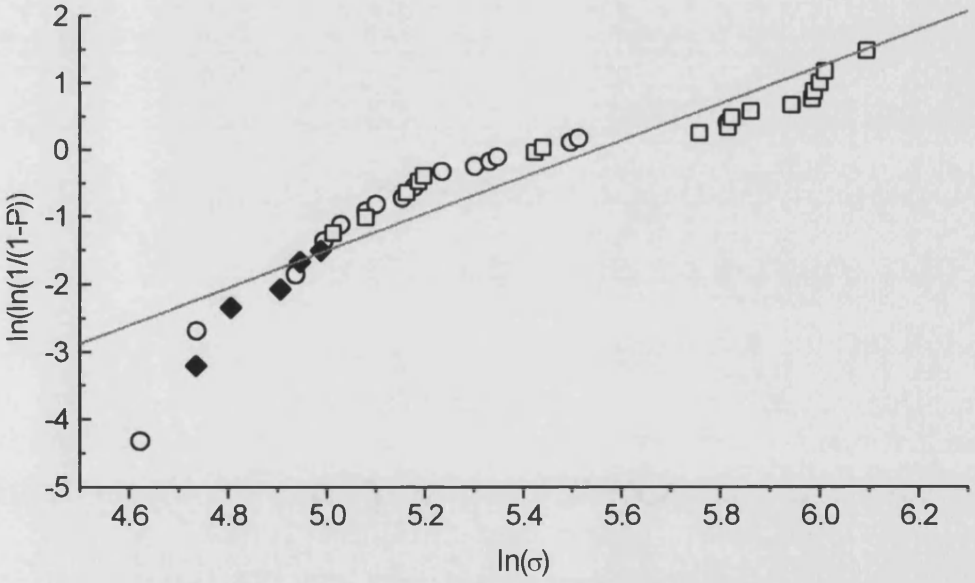

$$\ln\left[\ln\left[\frac{1}{1-P_f}\right]\right] = m\ln(\sigma) - m\ln(S_0)$$

m	2.74
σ_0	258
r	0.93

Figure 4.143 Determination of Weibull modulus from flexural strengths of a single batch of composite with matrix composition HT50 / 0.22 V_{NLAS}. The datum points are categorised by the failure modes described in figure 4.62;
○ = mode 1; □ = mode 2; ◆ = mode 3. The solid line gives the linear regression fit through all the data from which m and σ_0 are calculated.

Figure 4.144 Optical micrograph of HT50 / 0.22 V_{NLAS} composite sample heated at 450 °C for 72 hours. The carbon fibres were completely pyrolysed to leave replica pores.

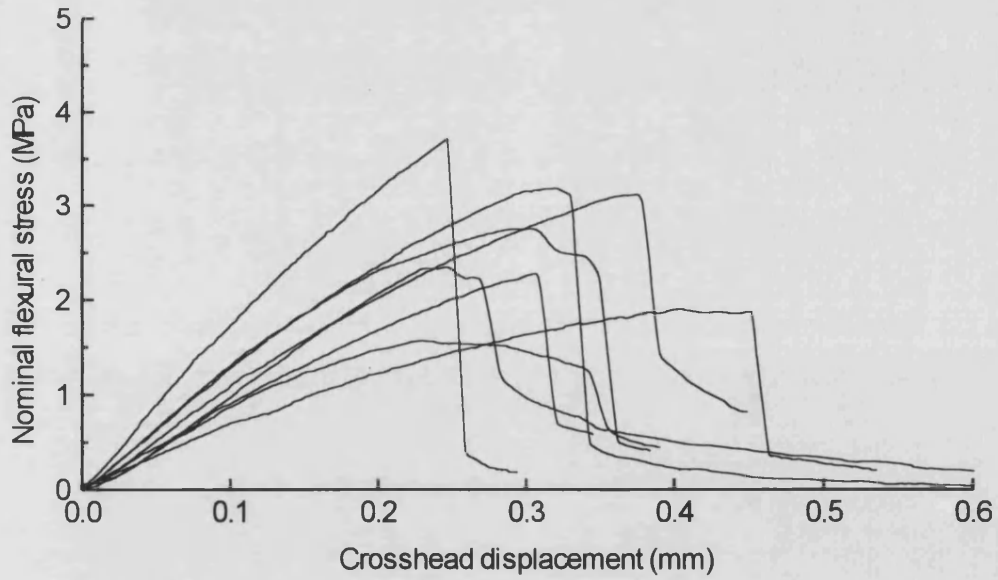

Figure 4.145 Typical flexural response curves of pyrolysed composite samples with HT50 / 0.22 NLAS matrix. The carbon fibres in the composites were completely removed by heating the samples in air at 450 °C for 72 hours.

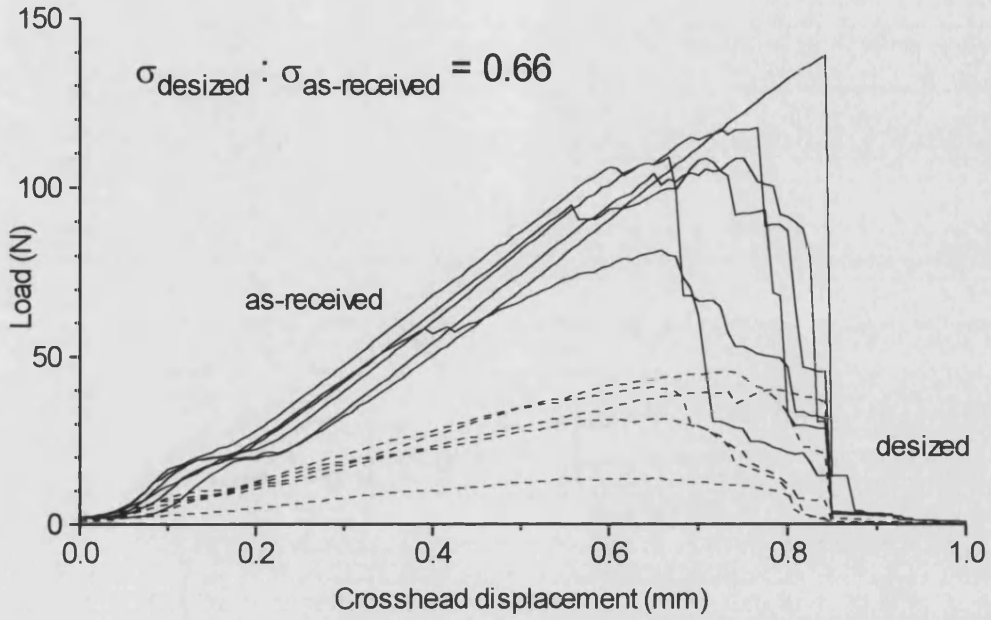

Figure 4.146 Effect of desizing and handling on the bundle breaking load of T300 carbon fibres. Fibres were tested (i) in the as-received condition and (ii) after having been desized at 750 °C, and wound dry onto the composite-forming mandrel in order to emulate the damage the fibres would acquire during composite forming.

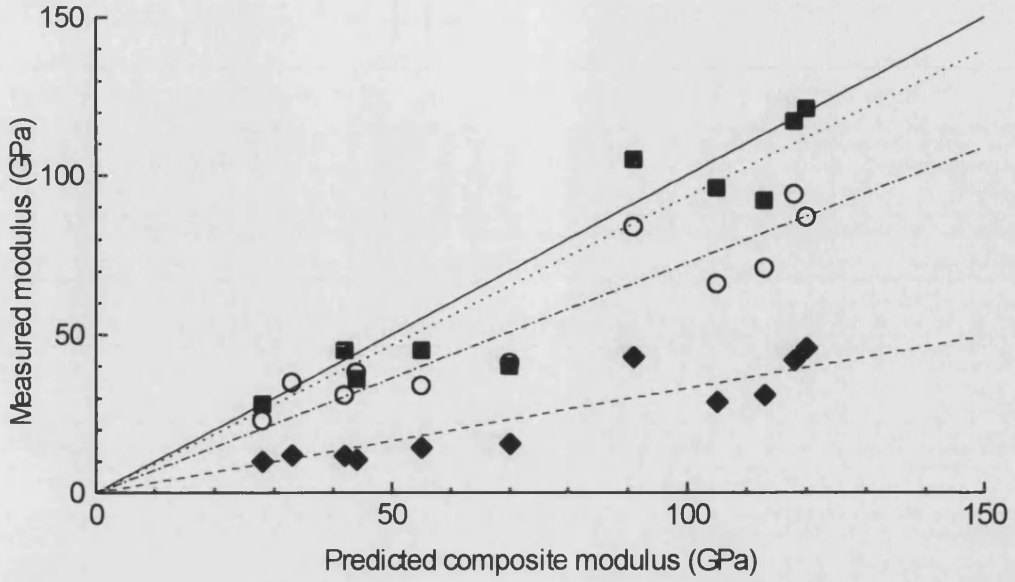

Figure 4.147 Comparison of measured elastic moduli with values predicted from a modified rule of mixtures. The solid line represents a 1:1 relation between actual and predicted values. ■ : tensile, dotted line corresponds to 93% of theoretical;
○ : flexural, line corresponds to 73% of theoretical;
◆ : dynamic, dashed line corresponds to 33% of theoretical.

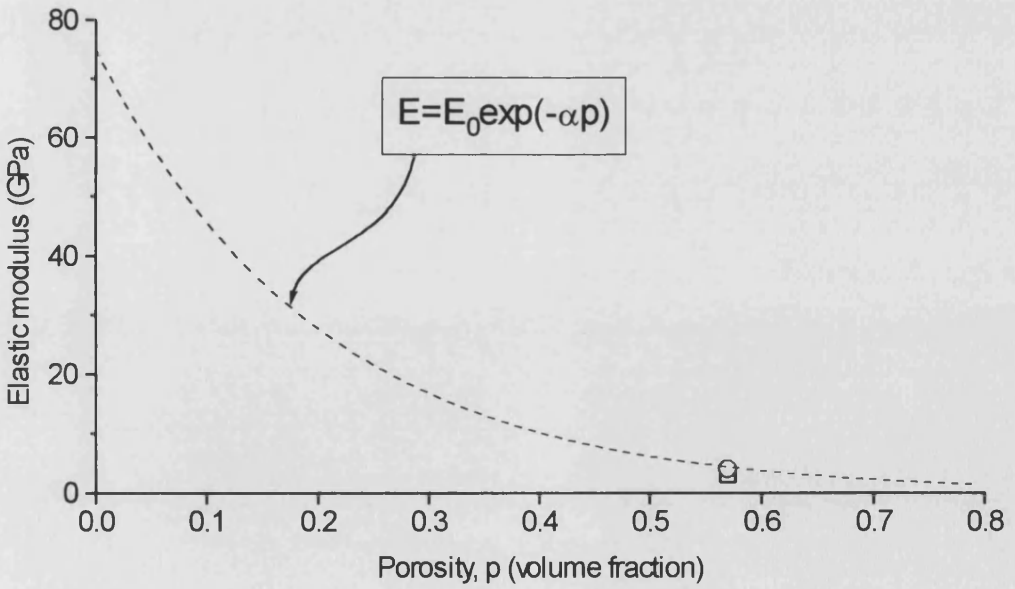

Figure 4.148 Flexural (□) and dynamic (○) elastic moduli of pyrolysed composite samples with HT50 / 0.22 V_{NLAS} matrix are adequately described by the relation $E = E_0\exp(-\alpha p)$ where $E_0 = 75$ GPa and $\alpha = 5$.

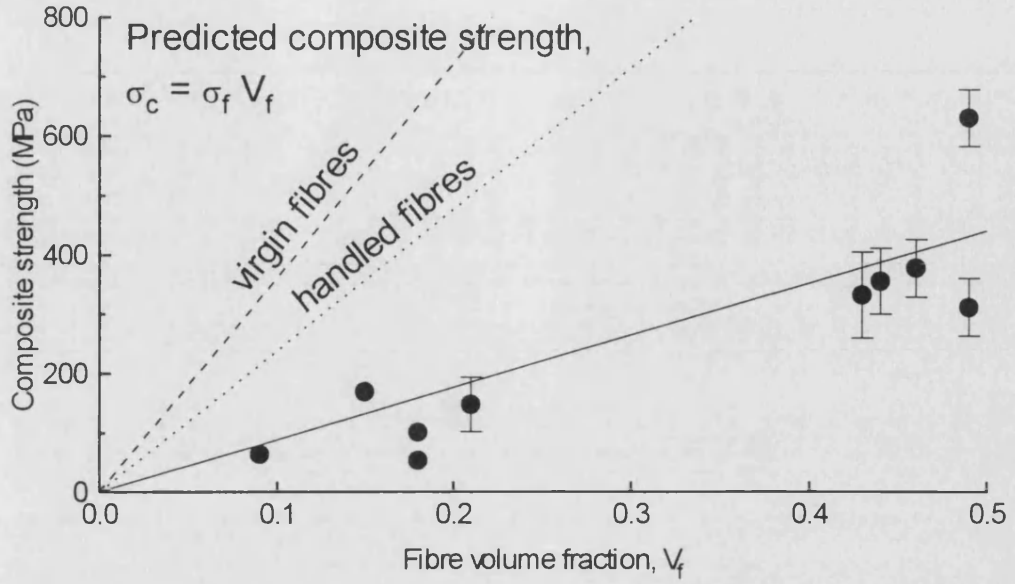

Figure 4.149 Comparison of measured tensile strengths (●) with values predicted from a modified rule of mixtures.

Solid line: linear fit (indicates an apparent fibre strength (σ_f) of 1760 MPa)

Dashed line: prediction based on σ_f = 3600 MPa (virgin fibres)

Dotted line: prediction based on σ_f = 2375 MPa (handled fibres)

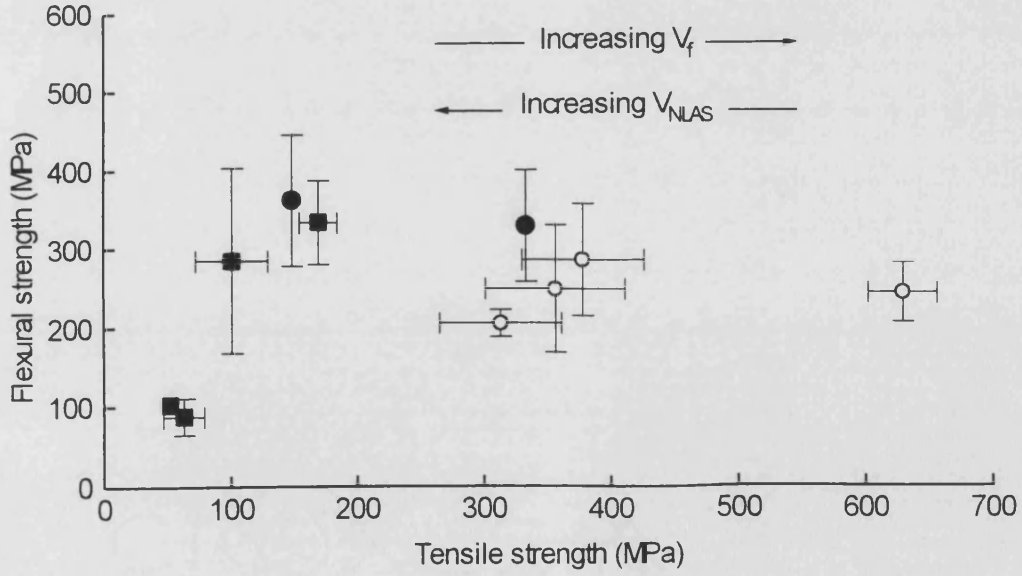

Figure 4.150 Poor correlation between tensile and flexural strengths of all composites tested in chapter 4. The symbols represent different failure modes in flexure:

○ : mode 1 (extensive delamination); ● : mode 2 (partial delamination); ■ : mode 3 (brittle) (refer to figure 4.62).

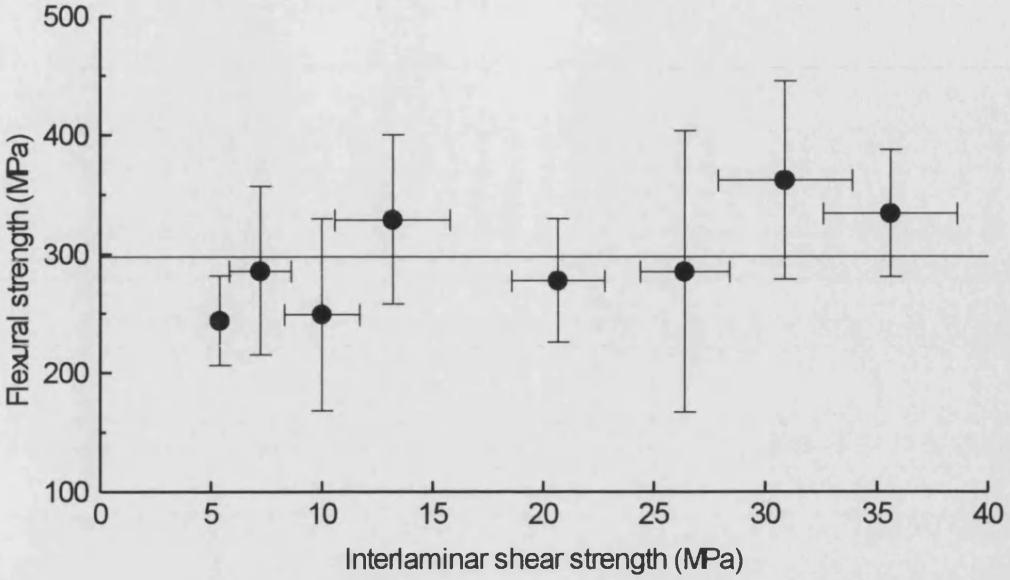

Figure 4.151 Comparison of flexural strengths and interlaminar shear strengths of composite samples which failed by delamination when tested in flexure (*i.e.* those containing up to ~ 0.22 V_{NLAS} in the matrix). Error bars indicate standard deviations.

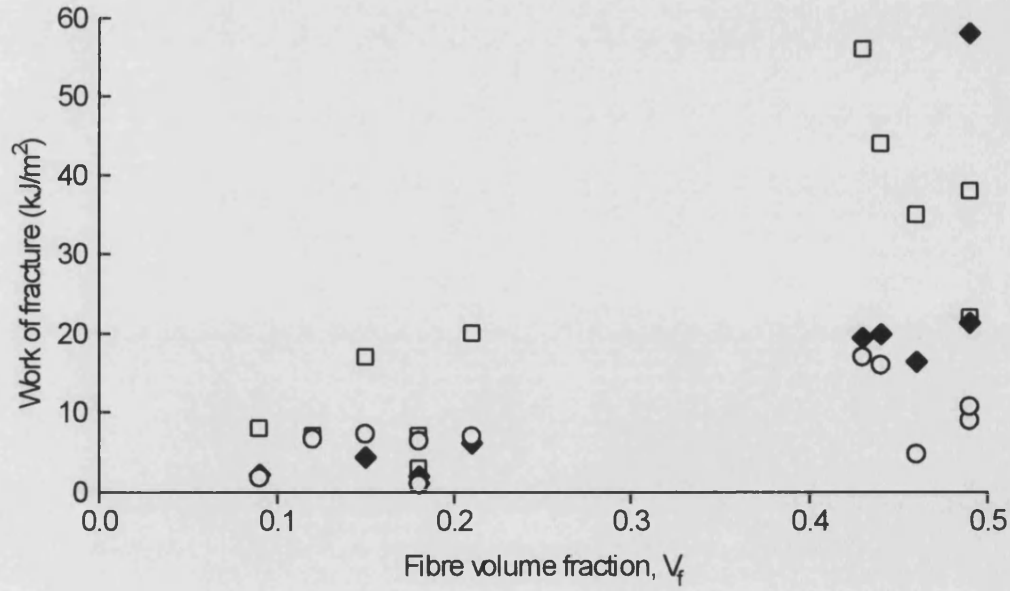

Figure 4.152 Comparison of the variations of flexural (○), tensile (□) and Charpy (◆) works of fracture with fibre volume fraction. These data are taken from figures 4.57, 4.96 and 4.113 respectively.

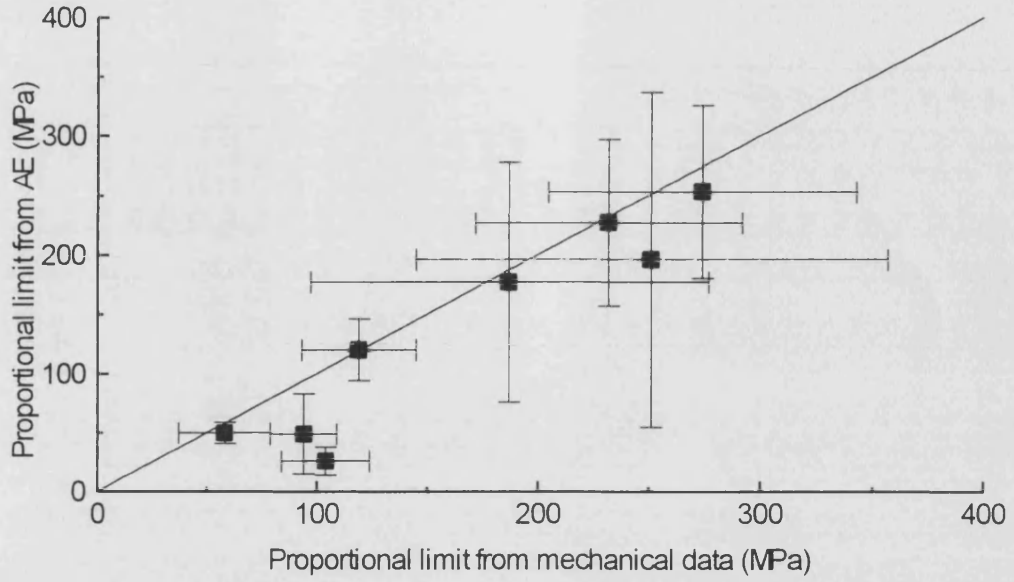

Figure 4.153 Correlation between flexural proportional limits determined from mechanical data (horizontal axis) and from the onset of acoustic emission activity (vertical axis). These data are taken from tables 4.13 & 4.14). The straight line indicates a 1:1 (ideal) relation between the two measurements.

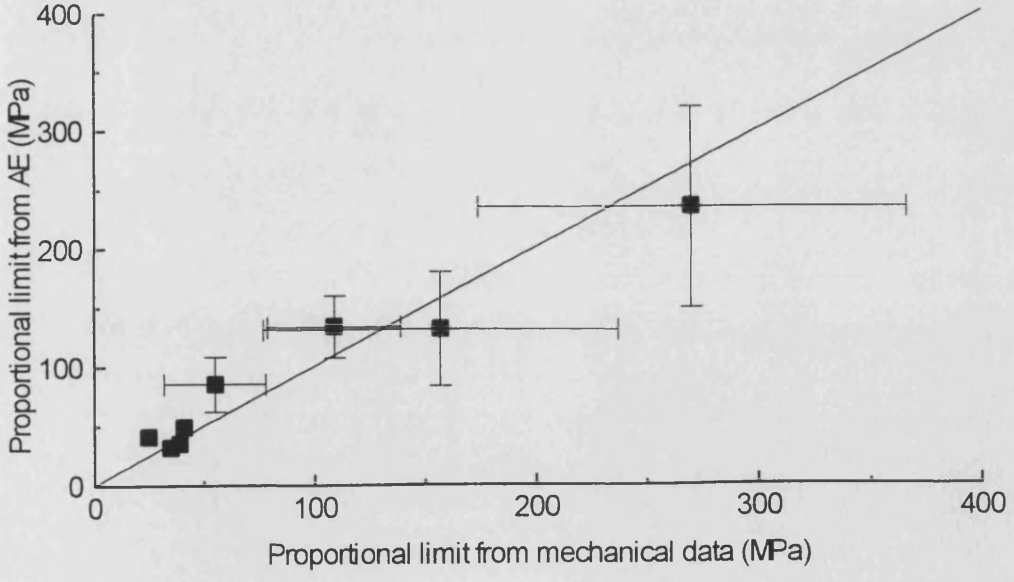

Figure 4.154 Correlation between tensile proportional limits determined from mechanical data (horizontal axis) and from the onset of acoustic emission activity (vertical axis). These data are taken from tables 4.17 & 4.18). The straight line indicates a 1:1 (ideal) relation between the two measurements.

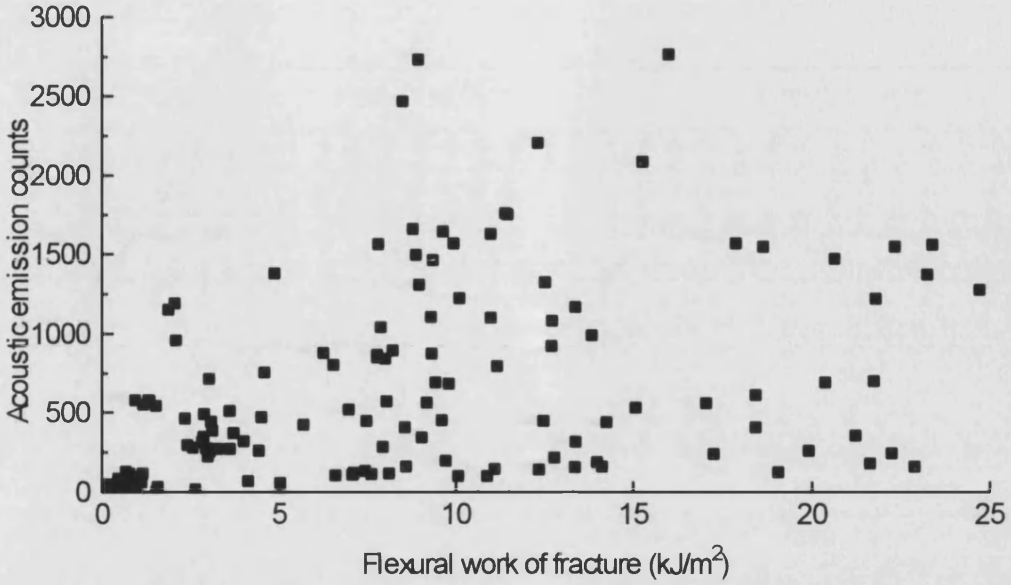

Figure 4.155 There was a poor correlation between work of fracture (to end of test) and the number of acoustic emission counts generated for flexural data.

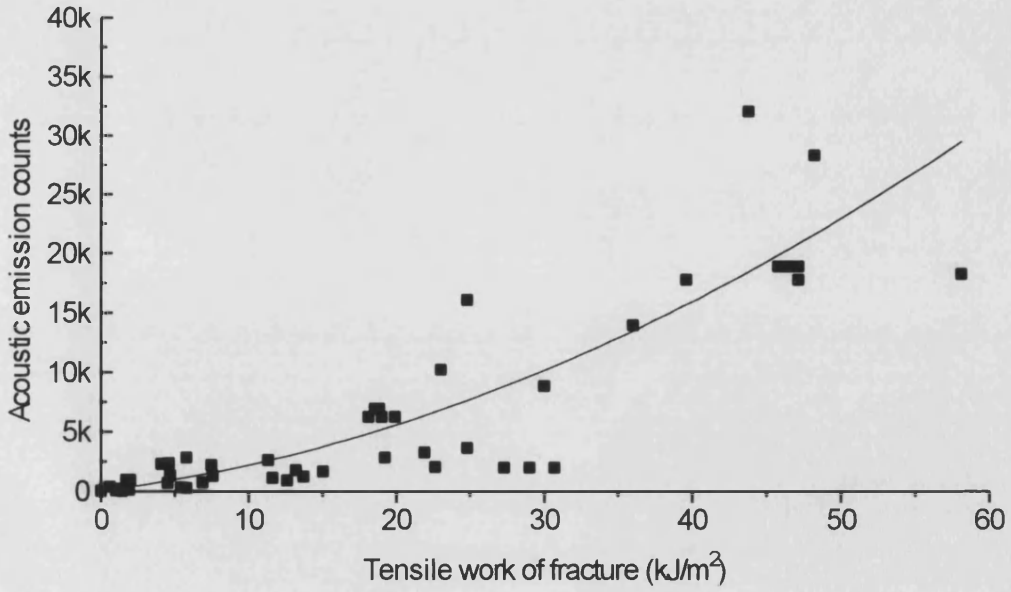

Figure 4.156 There was a reasonable correlation between tensile work of fracture and the number of acoustic emission counts.

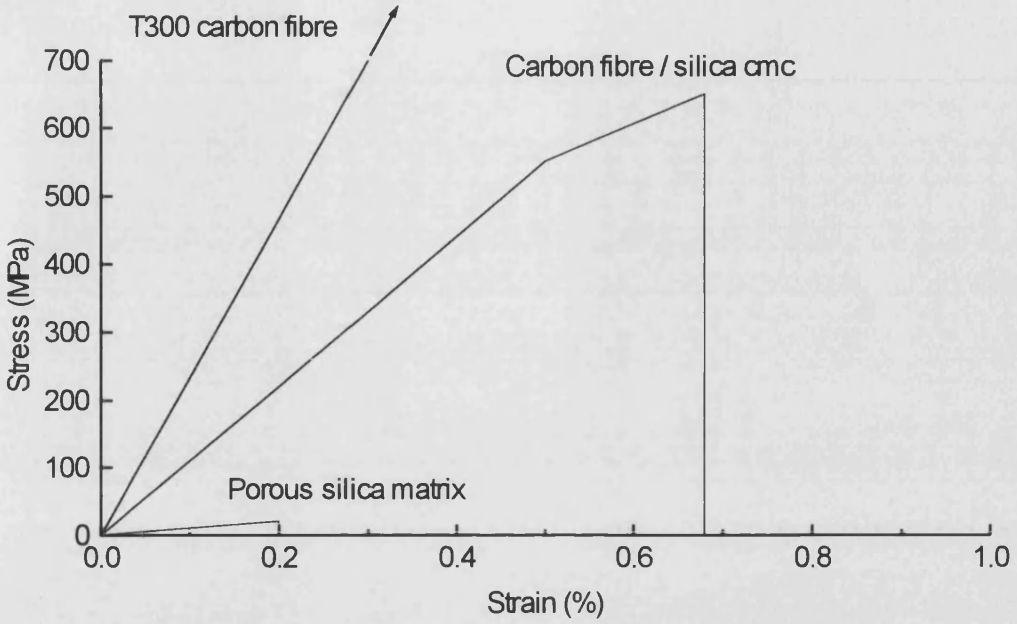

Figure 4.157 Illustration of the effectiveness of composite materials fabricated by freeze-gelation. The figure compares the tensile properties of:

(i) T300 carbon fibres (manufacturer's data);

(ii) CF/silica composite fabricated by freeze-gelation (idealised data);

(iii) porous, silica matrix prepared by freeze-gelation (from flexure tests).